



SAPIENZA  
UNIVERSITÀ DI ROMA

Measurement of the properties of the new particle  
observed within the search for the Standard Model  
Higgs Boson in the  $H \rightarrow ZZ^{(*)} \rightarrow 4\ell$  decay chan-  
nel at ATLAS

Scuola di dottorato in Fisica  
Dottorato di Ricerca in Fisica – XXVI Ciclo

Candidate

Valerio Ippolito  
ID number 1090818

Thesis Advisors

Prof. Carlo Dionisi  
Prof. Stefano Giagu  
Dr. Marco Rescigno

A thesis submitted in partial fulfillment of the requirements  
for the degree of Doctor of Philosophy in Physics

October 2013

Thesis defended on February 18th, 2014  
in front of a Board of Examiners composed by:  
Prof. Antonio di Domenico (chairman)  
Prof. Mauro Dell'Orso  
Prof. Vittorio Lubicz

---

**Measurement of the properties of the new particle observed within the search for the Standard Model Higgs Boson in the  $H \rightarrow ZZ^{(*)} \rightarrow 4\ell$  decay channel at ATLAS**

Ph.D. thesis. Sapienza – University of Rome

© 2013 Valerio Ippolito. All rights reserved

This thesis has been typeset by L<sup>A</sup>T<sub>E</sub>X and the Sapthesis class.

Version: January 30, 2014

Author's email: [valerio.ippolito@cern.ch](mailto:valerio.ippolito@cern.ch)

*To my grandmother, Maria Maccario,  
who always believed it was worth.*



## Abstract

The discovery of a new particle within the search for the Standard Model Higgs boson in the  $H \rightarrow ZZ^{(*)} \rightarrow 4\ell$  channel at ATLAS, with about  $25\text{ fb}^{-1}$  of data collected in  $pp$  collisions at the LHC, is discussed. Different hypotheses on the quantum numbers of the new boson are tested, by means of spin–parity studies based on a matrix element description of the  $H \rightarrow ZZ$  decay amplitude. Prospects for the measurement of the tensor structure of the  $HZZ$  vertex in the spin zero hypothesis at a high–luminosity LHC are also presented.



## Acknowledgments

*The day we discovered the Higgs boson (or whatever it is) was actually early night — or late night for Geneva standards — and after an hour of quiet excitement I was really aware for the first (and maybe last) thirty minutes that I would have needed a thesis, and an acknowledgements section, way longer than expected. I am deeply indebted to Carlo Dionisi, who taught me everything I know about particle physics and most of all taught me how to tackle what I would have wanted or been asked to know. He has been a guide and example, the someone I trusted and appreciated most since we practically met in a parking at CERN in Summer 2009, and a good director, too.*

*None of this work would have been possible without the guidance of Stefano Giagu and Marco Rescigno, their clever and attentive way of doing physics and teaching what a physicist should be, or learn, or in any case do. Thank you for all the support, whatever analysis we worked on and whatever goal, challenge and solution we aimed for. Thank you for sustaining (and bearing with) me from the early  $J/\psi$   $d_0$  disputes to the Higgs and beyond, thank you for being so different and so complementary.*

*Thank you to Kostas Nikolopoulos, who led the  $H \rightarrow ZZ^{(*)} \rightarrow 4\ell$  effort and taught me how to discover a particle and be cool with that. For taking care and supporting me, through all those hard and exciting months and beyond; for melomakarona, a challenge for the spell-checker and my pastry-making skills. Thank you to Christos Anastopoulos, for all the nights and days of discussions and for always seeing the point. Thank you to Fabien Tarrade, whose caring and support were invaluable beyond he could even imagine.*

*Thank you to Elvira and Francesco for sharing more and more during the last four years, however difficult sometimes things turned out to be; for dinners and teachings and for missed dinners and teachings, and a couple of things I still have to do. Thank you to Francesco and Giacomo, with whom I shared the pleasure of being eventually awarded an office with sight. Thank you to Francesco, who was a noisy roommate and a quiet housemate and a friend I am delighted to have earned. To Giacomo, who eventually married Eleonora making it more difficult to write consistent acknowledgments between paragraphs, for his support and rare but remarkable cooking. Thank you to Camilla, for useful discussions in the last three years and all the nice time we worked together in the spin-parity months.*

*Thank you to Eleonora, who made it worth to spend two weeks in deep Transilvania and who still has to decipher some of my words, for her precious friendship. Thank you to my friend Vieri, with whom I started and with whom apparently I will never agree on some fundamental topics like Midnight in Paris and the meaning of life; thank you for everything, including James Joyce's statue and Rome with the snow. Thank you to Attilio and Chiara, for late night discussions and having made living in Geneva agreeable and funny (!) and having proven that you can have good taste and still an awful sense of humour. Thank you to Lidia, for caring for me and proving to be an invaluable and supporting friend, despite whatever poor parking skills and late night trigger coding life chose to saddle us with.*

*Thank you to David, for useful discussions and proofreading and for everything else including supportive climbing and successful blogging. Thank you to Daniele, for*

*his supporting friendship which included slow-motion car crashes, counseling, writing (yes, I will start back properly after this thesis), cinema and music, complaining and everything else, and for being more important than he thinks he is (and for changing his name). To Jacopo, for everything we shared (and share, but I am obliged to use the past tense throughout these acknowledgments), for being still able to ask for a change and fight for it, for invaluable support despite the fact that we still miss a tunnel connecting our cities. Thank you to Pierfrancesco and Piermarco, who themselves share half of their names and with whom I shared useful discussions. To Thiago, for his friendship and cleverness, for his attitude towards physics and life and for having made Windy and Warm the soundtrack of the last two years. To Alessia, whom I am glad to have shared the complex deep side of last year with, for having taught me what is really worth, and for struggling for that way more than I do.*

*Thank you to Elisa and Stefano (and Anna!) for, in random order: catamaran sailing, Sardinia, two weeks of humour, Paris, thrown stuff, support, a number of dinners involving hand-made pasta and foie gras, C.I., macroeconomics, Paris again and everything I will not state here but it's obvious I am indebted for. More than three years of my life would have not been the same without Natalia, who therefore I will thank for three representative events i.e. for cooking a dinner in late August 2011, for the tiramisoup and for making me smile, and laugh, and think almost whenever I needed it. Thank you to Martina, Arianna and Marianna, who are special persons. (Martina, for everything since those birthday greetings, for her continuous support and care, for her friendship, her wisdom, for all that she gave me and for neglecting some vending machine and driving-back-home crisis. Arianna, who should not live so far away, for her being deep and funny and crazy as one is supposed to be. Marianna, for her support and her caring empathy, for Sardinia, for knowing what's right.)*

*To those who are not in this list, but still made it possible and, often, worth. To my family, to my father and my mother, who have always been there.*

# Contents

<b>1</b>	<b>The Higgs Boson</b>	<b>1</b>
1.1	The Standard Model of Particle Physics . . . . .	1
1.1.1	The Role of Symmetries . . . . .	1
1.1.2	Quantum Electrodynamics . . . . .	2
1.1.3	Strong Interactions . . . . .	3
1.1.4	Electroweak Interactions . . . . .	4
1.2	Giving Mass to Particles: the Higgs–Brout–Englert Mechanism . . . . .	6
1.2.1	Electroweak Symmetry Breaking . . . . .	6
1.2.2	Gauge Bosons . . . . .	8
1.2.3	Fermions . . . . .	9
1.2.4	Theoretical Constraints on $m_H$ . . . . .	9
1.3	Looking for the Higgs Boson . . . . .	10
1.3.1	Production Mechanisms . . . . .	11
1.3.2	Decay Channels . . . . .	12
1.3.3	Where do We Stand? . . . . .	14
<b>2</b>	<b>The ATLAS Experiment at the LHC</b>	<b>21</b>
2.1	The Large Hadron Collider . . . . .	21
2.1.1	The High Luminosity LHC . . . . .	23
2.2	ATLAS, a Particle Physics Experiment . . . . .	26
2.2.1	Detecting Particles . . . . .	26
2.2.2	A Toroidal LHC ApparatuS . . . . .	27
2.2.3	The Magnet System . . . . .	31
2.2.4	The Inner Detector . . . . .	32
2.2.5	Calorimeters . . . . .	35
2.2.6	The Muon Spectrometer . . . . .	38
2.2.7	Taking Data: the Trigger System . . . . .	40
<b>3</b>	<b>Lepton Reconstruction</b>	<b>43</b>
3.1	Tracking Charged Particles . . . . .	43
3.1.1	Inside–out Algorithm . . . . .	43
3.1.2	Outside–in Algorithm . . . . .	44
3.1.3	Primary Vertices . . . . .	44
3.2	Muons . . . . .	47
3.2.1	Muon Spectrometer . . . . .	47

3.2.2	Combining Inner Detector and Muon Spectrometer Measurements	48
3.2.3	Combining Calorimeter and Muon Spectrometer Measurements	49
3.2.4	Performance	49
3.3	Electrons	53
3.3.1	The Gaussian Sum Filter	53
3.3.2	Electron Reconstruction	55
3.3.3	Electron Identification	58
<b>4</b>	<b><math>H \rightarrow ZZ \rightarrow 4\ell</math>: the Golden Channel</b>	<b>63</b>
4.1	The Standard Model Signature	63
4.1.1	Low and High Mass Searches	64
4.1.2	The Irreducible Background	66
4.1.3	Reducible Backgrounds	67
4.2	Probing the $HZZ$ Vertex	70
4.2.1	Kinematic Observables	71
4.2.2	Angular Distributions	72
4.2.3	Decay Amplitudes	73
4.2.4	$CP$ Admixtures	76
<b>5</b>	<b>Signal Extraction</b>	<b>77</b>
5.1	Data Samples	77
5.1.1	Collision Data	77
5.1.2	Monte Carlo Simulation	77
5.2	Event Selection	79
5.2.1	Trigger	79
5.2.2	Leptons	80
5.2.3	Candidates	81
5.3	Mass Resolution	82
5.3.1	Final State Radiation Recovery	84
5.3.2	The $Z$ Mass Constraint Fit	84
5.3.3	Results	91
5.4	Reducible Background Estimation	95
5.4.1	$\ell\ell + \mu\mu$ Background	95
5.4.2	$\ell\ell + ee$ Background	96
5.4.3	Summary of Reducible Background Estimates	97
5.5	Systematic Uncertainties	100
5.6	Results	100
5.6.1	Upper Limit and Signal Significance	101
5.6.2	Mass Measurement	107
5.6.3	Signal Strength	107
5.7	Combination with Other Channels	107
5.7.1	Mass Measurement	107
5.7.2	Signal Strengths	109

<b>6</b>	<b>Spin–parity Measurements</b>	<b>111</b>
6.1	Analysis Method	111
6.1.1	Hypothesis Testing	111
6.1.2	Data and Monte Carlo Samples	112
6.1.3	Event Selection	112
6.1.4	Kinematic Distributions	116
6.2	The $J^P$ -MELA Discriminant	116
6.2.1	Signal Description	118
6.2.2	Closure Tests	119
6.2.3	Spin Two: Admixtures between $gg$ and $q\bar{q}$ Production	119
6.3	Signal and Background Parametrization	124
6.3.1	Likelihood Model	125
6.3.2	Discriminant Distributions	125
6.3.3	Systematic Uncertainties	129
6.4	Hypothesis Testing Results	132
6.4.1	Expected Separations	132
6.4.2	Observed Separations	132
6.4.3	Summary	137
6.5	Combination with Other Channels	137
<b>7</b>	<b>Probing the <math>HZZ</math> Tensor Structure</b>	<b>139</b>
7.1	Decay Amplitude in the Scalar Boson Assumption	139
7.1.1	Measurement Strategy	140
7.1.2	Interpretation of $g_4/g_1$ vs $\langle f_{CP} \rangle$	140
7.1.3	Sensitivity on $g_4/g_1, g_2/g_1$	141
7.1.4	Analysis Techniques	144
7.2	8D Fit	150
7.2.1	Likelihood Model	151
7.2.2	Background Description	151
7.2.3	Statistical Procedure	151
7.2.4	Closure Tests	151
7.2.5	Results	156
7.3	2D Discriminant Analysis	159
7.3.1	Likelihood Model	159
7.3.2	Statistical Procedure	159
7.3.3	Results	161
7.4	Summary	161
<b>8</b>	<b>Conclusions</b>	<b>167</b>
<b>A</b>	<b>Decay Amplitudes and Differential Distributions</b>	<b>169</b>
A.1	Spin One	169
A.2	Spin Two	169
A.3	Differential Distributions	171
A.3.1	The Effect of the Production Mechanism	173

---

<b>B</b>	<b>Closure Tests for Signal Parametrization</b>	<b>175</b>
B.1	Closure Tests	175
B.1.1	$J^P = 0^-$	175
B.1.2	$J^P = 1^+$	177
B.1.3	$J^P = 1^-$	179
B.1.4	$J^P = 2^+$	181
B.1.5	$J^P = 2^-$	183
B.1.6	$J^P = 2^+$ (25% $qq$ production)	185
B.1.7	$J^P = 2^+$ (50% $qq$ production)	187
B.1.8	$J^P = 2^+$ (75% $qq$ production)	189
B.1.9	$J^P = 2^+$ (100% $qq$ production)	191
B.1.10	$J^P = 2^-$ (25% $qq$ production)	193
B.1.11	$J^P = 2^-$ (50% $qq$ production)	195
B.1.12	$J^P = 2^-$ (75% $qq$ production)	197
B.1.13	$J^P = 2^-$ (100% $qq$ production)	199

# Introduction

The last decades of high energy experiments have verified to an impressive level of accuracy the predictions of the Standard Model of particle physics. The question on how particles acquire mass has in the Standard Model an answer — the Higgs–Brout–Englert mechanism — which remained for a long time still to be confirmed by observations. The existence of a scalar field is predicted to give mass to fermions and vector bosons via Yukawa couplings and spontaneous breaking of the underlying symmetry of the standard theory, leading to the emergence of a physical scalar particle, the Higgs boson.

The fact that the mass of this particle,  $m_H$ , is a free parameter of the Standard Model has motivated the construction of the Large Hadron Collider (LHC), colliding proton beams at unprecedented center-of-mass energies. High precision detectors like ATLAS have been designed to obtain the broadest sensitivity to a possible Higgs signal in the full mass range. Different reconstruction strategies have been designed for different values of  $m_H$ , at which different decay channels become more interesting than others. Among them, the  $H \rightarrow ZZ^{(*)} \rightarrow 4\ell$  channel provides high signal sensitivity, giving a significant contribution to the discovery potential for masses from 100 GeV to the TeV region, with a high signal to background ratio despite the low cross-section times branching ratio. Lepton momentum reconstruction performance leads to an excellent four-lepton mass resolution, of the order of  $2 \div 4$  GeV, which allows a high precision measurement of  $m_H$ . Moreover, the fact that the decay chain is fully reconstructed provides a clean and clear signature from which information about the inner structure of the Higgs decay can be extracted.

This thesis work started after the HCP conference in November 2011, where combined data from the ATLAS and CMS experiments excluded a wide range of Higgs masses with up to  $2.3 \text{ fb}^{-1}$  of  $pp$  collision data at  $\sqrt{s} = 7 \text{ TeV}$ , leaving only the  $114 \text{ GeV} < m_H < 141 \text{ GeV}$  region as a viable one for the observation of a low mass Higgs boson consistent with electroweak precision measurements. The author has been a core developer of the  $H \rightarrow ZZ^{(*)} \rightarrow 4\ell$  analysis, and has contributed to optimize both for the searches at low and high values of  $m_H$ . He worked first to the introduction of the  $Z$  mass constraint fit method in the 2011 data analysis, which brought an  $\mathcal{O}(10\%)$  improvement in mass resolution and consequently a  $\mathcal{O}(5\%)$  improvement in signal sensitivity. He then focused on the optimization of lepton selection and isolation criteria, to maximize signal efficiency thus keeping under control contamination from irreducible and reducible backgrounds, with particular attention on event pile-up effects which became more and more relevant with the increasing instantaneous luminosity in 2012.

The Higgs search culminated in July 4th, 2012, with the public announcement of

the observation of a new particle in the search for the Higgs boson in the  $H \rightarrow \gamma\gamma$  and  $H \rightarrow ZZ^{(*)} \rightarrow 4\ell$  decay channels with the first  $\approx 11 \text{ fb}^{-1}$  collected at  $\sqrt{s} = 7 \text{ TeV}$  and  $8 \text{ TeV}$ , for a combined significance against background of more than  $5\sigma$ . Naturally the question arised on whether the new particle observed *searching for* the Higgs boson actually *is* the Standard Model Higgs boson, or not. The study of its quantum numbers by means of the determination of its spin–parity state  $J^{PC}$  is a crucial step for the understanding of the properties of the new boson: the observed particle could be a pseudo–scalar boson, a graviton–like  $2^+$  state, a spin 1 state or also a spin 0 state which is not eigenstate of  $CP$  or shows deviations in the decay amplitude from the Standard Model expectation, which might hint to new physics. The  $H \rightarrow ZZ^{(*)} \rightarrow 4\ell$  decay channel is the most suitable instrument to achieve this goal, as one can reconstruct the full decay chain and derive the intrinsic properties of the  $H \rightarrow ZZ$  decay amplitude from angular and invariant mass distributions of the final state. The author developed a matrix–element based technique which allowed the exclusion with the full  $\approx 25 \text{ fb}^{-1}$  statistics of many alternative  $J^P$  hypotheses against the Standard Model expectation, and will allow in the near future to further investigate the tensor structure of the  $HZZ$  vertex in the  $J = 0$  assumption.

This thesis is organized as follows. In Chapter 1, a brief introduction to Higgs boson physics is presented, together with the current status of the Higgs boson searches. In Chapter 2, a description of the scope and features of the LHC and the ATLAS experiment is provided. In Chapter 3, a description of lepton identification and reconstruction techniques used for the analyses presented in this thesis is provided. In Chapter 4, a general introduction on the main features of the  $H \rightarrow ZZ^{(*)} \rightarrow 4\ell$  channel is presented, together with the instruments which exploit the four–lepton signature to investigate the  $HZZ$  vertex with matrix element techniques. In Chapter 5, the results of the  $H \rightarrow ZZ^{(*)} \rightarrow 4\ell$  search with the most recent analysis of the full 2011 and 2012 combined datasets are discussed. In Chapter 6, the  $J^P$ –MELA technique is introduced, and results on hypothesis testing of different specific models against the Standard Model hypothesis are shown. In Chapter 7, two techniques based on the same matrix element approach are presented, which allow to probe coupling parameters describing the most general  $H \rightarrow ZZ$  decay amplitude. Prospects on the sensitivity which can be reached with a High Luminosity LHC are discussed. Conclusions are drawn in Chapter 8.

# Chapter 1

## The Higgs Boson

The Standard Model of Particle Physics is currently the best description of the strong and electroweak interactions between elementary particles. Many high energy physics experiments have shown the impressive level of agreement between its predictions and precision measurements, culminating with the recent discovery of a new particle within Higgs boson searches by ATLAS and CMS. In this chapter, an introduction to the theoretical framework of the Standard Model is provided, with particular focus on the role of the spontaneous symmetry breaking and the Higgs mechanism.

### 1.1 The Standard Model of Particle Physics

Among the four known forces which occur in nature – the electromagnetic force, the weak interactions, the strong nuclear force and the gravitational force, the first three are the dominant ones in the scale of particle physics<sup>1</sup>. The aim of the Standard Model (SM) is to provide an unified theoretical description of these three forces, using the language of Quantum Field Theory (QFT).

#### 1.1.1 The Role of Symmetries

QFT arises as a solution to the problem of unifying quantum mechanics and relativity. Particles in QFT are described by local fields  $\psi(x)$ , evaluated in the space–time point  $x$ . Dynamics can be described using a lagrangian density  $\mathcal{L}$ , which is a function of the field  $\psi$  and its space–time derivatives  $\partial_\mu\psi$ ; classical equations of motion are determined by the requirement of the action

$$S = \int d^4x \mathcal{L}(\psi, \partial_\mu\psi)$$

---

<sup>1</sup>Gravitational force is negligible up to an energy scale for which the Compton wave length  $\lambda$  of a particle is comparable to its Schwarzschild radius, i.e.

$$\lambda = \frac{\hbar}{mc} = G_N \frac{m}{c^2},$$

where  $\hbar$  is the Planck constant divided by  $2\pi$ ,  $c$  is the speed of light in vacuum and  $G_N$  the gravitational constant. This happens when the particle mass  $m$  is at the order of  $1 \times 10^{19}$  GeV, which is called *Planck mass*.

to be stationary, i.e.  $\delta S = 0$ . The gauge group of the theory is the continuous group of local transformations of the fields for which the variation  $\delta S$  remains unchanged.

Symmetries observed in Nature motivate the gauge structure of the lagrangian density of the SM,  $\mathcal{L}_{SM}$ . Since, by Noether's theorem, each continuous symmetry of the lagrangian density yields to a conserved current and hence a conserved charge, observed symmetries are accounted for by symmetries of  $\mathcal{L}_{SM}$  under transformations of fields,  $U^2$ .

The SM is a gauge theory with lagrangian density

$$\mathcal{L}_{SM} = \mathcal{L}_{QCD} + \mathcal{L}_{EW},$$

which is locally invariant under gauge transformations belonging to the symmetry group

$$SU(3)_C \otimes SU(2)_L \otimes U(1)_Y.$$

The  $SU(3)_C$  group refers to colour, the conserved charge of Quantum Chromodynamics (QCD) – the theory which describes strong interactions between quark and gluons. The  $SU(2)_L \otimes U(1)_Y$  group refers to the electroweak interactions, which conserve the weak hypercharge  $Y$  and isospin  $I$ .

### 1.1.2 Quantum Electrodynamics

A first illustrative example of how symmetries play role in the way the lagrangian density is written is Quantum Electrodynamics (QED). QED is an abelian gauge theory describing an electrically charged particle with spin 1/2 and mass  $m$  (and, eventually, the one of its antiparticle), represented by its field  $\psi$ , and its electromagnetic field, a massless vector boson (the photon), represented by the field  $A^\mu$ . The theory is invariant with respect to the unitary joint transformations

$$\begin{aligned}\psi(x) &\rightarrow U(x)\psi(x) = e^{i\alpha(x)}\psi(x), \\ A_\mu(x) &\rightarrow U(x)A_\mu(x) = A_\mu(x) + \frac{1}{e}\partial_\mu\alpha(x),\end{aligned}$$

where  $\alpha(x)$  is an arbitrary function of the space–time coordinates. The group of these transformations is  $U(1)$ .

The lagrangian density is

$$\mathcal{L}_{QED} = -\frac{1}{4}F^{\mu\nu}F_{\mu\nu} + \bar{\psi}(i\gamma^\mu D_\mu - m)\psi, \quad (1.1)$$

where  $\gamma^\mu$  are the  $4 \times 4$  Dirac matrices<sup>3</sup>  $\bar{\psi} = \psi^\dagger\gamma^0$ ,  $F_{\mu\nu}$  is the electromagnetic field strength tensor<sup>4</sup> and the covariant derivative  $D_\mu$  is defined by

$$D_\mu = \partial_\mu - ieA_\mu.$$

---

<sup>2</sup>An example of conserved charge is the electric charge, which is conserved in electromagnetic interactions. This conservation law follows from, and is represented by, the invariance of the lagrangian density with respect to the unitary global gauge transformation  $U$ :

$$\psi(x) \rightarrow U\psi(x) = e^{i\alpha}\psi,$$

where  $\psi(x)$  is the quantum field evaluated at the space–time point  $x$  and  $\alpha$  is an arbitrary constant.

<sup>3</sup>It holds  $\{\gamma^\mu, \gamma^\nu\} = 2g^{\mu\nu}I_4$ , where  $g^{\mu\nu}$  is the metric tensor and  $I_4$  the  $4 \times 4$  unit matrix.

<sup>4</sup>The electromagnetic field strength tensor is defined by

$$F_{\mu\nu} = \partial_\nu A_\mu - \partial_\mu A_\nu.$$

The coupling constant between the fermion and photon fields is  $e$ , the electric charge of the fermion, which gives the magnitude of the interaction term in Eq. (1.1). A consequence of the invariance of Eq. (1.1) under  $U(1)$  transformations, and in particular of global phase transformations of the Dirac field  $\psi$ , is the conservation of the Noether's current  $J^\mu = \bar{\psi}\gamma^\mu\psi$  and hence of the electric charge.

Precision measures, such as the one of the anomalous magnetic moment of the electron and the Lamb shift of hydrogen energy levels, have shown an impressive agreement between QED predictions and experimental data.

### 1.1.3 Strong Interactions

Strong interactions involve quarks, which are spin 1/2 fermions, and gluons, which are spin 1 bosons (*vector bosons*); colour is the conserved charge of these interactions. Quarks and gluons appear in six different colours (red, green, blue and the corresponding anticolours).

Evidence of colour as a quantum number conserved in strong interactions has been provided both by the decay of the  $\Delta^{++}$  resonance and by the study of  $R = \sigma_{\text{hadrons}}/\sigma_{\text{muons}}$  at increasing  $\sqrt{s}$  in  $e^+e^-$  scattering. Coloured particles are not observed singularly (*colour confinement*), i.e. only colour-neutral states can be observed in Nature.

QCD is a non-abelian gauge theory which aims at describing strong interactions. Its lagrangian density  $\mathcal{L}_{QCD}$  is symmetric under transformations of the  $SU(3)$  group; if we assume only one quark flavour is involved<sup>5</sup>, it can be written as

$$q(x) \rightarrow U(x)q(x) = e^{-ig_S\alpha_a(x)T_a}q(x),$$

where  $g_S = 4\pi\alpha_S$  is the coupling constant of strong interactions,  $\alpha_a$  are arbitrary functions and  $T_a$  are the eight generators of  $SU(3)$ <sup>6</sup>.

In a way analogous to QED, the eight generators of  $SU(3)$  call for the introduction of eight fields, the gluons  $G^a$ , which are mediators of strong interactions and transform as

$$G_\mu^a \rightarrow G_\mu^a - \frac{1}{g_S}\partial_\mu\alpha_a - f_{abc}\alpha_b G_\mu^c.$$

The lagrangian density can then be written in terms of the covariant derivative

$$D_\mu = \partial_\mu + ig_S T_a G_\mu^a$$

as

$$\mathcal{L}_{QCD} = -\frac{1}{4}\sum_a F_{\mu\nu}^a F^{a,\mu\nu} + \bar{q}(\gamma^\mu D_\mu - m)q,$$

where  $F_{\mu\nu}^a$  are tensors defined as

$$F_{\mu\nu}^a = \partial_\mu G_\nu^a - \partial_\nu G_\mu^a - g_S f_{ajk} G_\mu^j G_\nu^k. \quad (1.2)$$

<sup>5</sup>Extension to all flavours can be easily restored replacing  $q$  by  $q_r$ , and summing up over the quark flavour  $r$ .

<sup>6</sup>It holds

$$[T_a, T_b] = if_{abc}T_c,$$

where  $f_{abc}$  are the structure constants of  $SU(3)$  (for an abelian theory  $f_{abc} = 0$ ). Note that  $U$  and  $T_a$  are  $3 \times 3$  matrices; summation is implied on latin indices  $a, b, c = 1 \dots 3$ .

A notable difference between the electromagnetic field strength tensor  $F^{\mu\nu}$  and Eq. (1.2) is that, since QCD is non-abelian, there is the third term which accounts for self-interaction between gauge bosons, i.e. it represents vertices with three or four gluons. A fundamental feature of QCD is *asymptotic freedom*: quarks interact weakly at high energies, hence allowing for perturbative calculations, but strongly at low energies, preventing the unbinding of baryons and mesons.

### 1.1.4 Electroweak Interactions

The roots of electroweak theory fall back to 1934, when Enrico Fermi provided a theoretical description of the  $\beta$  radioactive decay[1]

$$n \rightarrow p + e^- + \bar{\nu}_e,$$

which happens at very low rates due to the involvement of weak interactions rather than electroweak or strong interactions. Fermi's description happens via the contact interaction

$$\mathcal{L} = -G_F(\bar{\psi}_p\gamma^\mu\psi_n)(\bar{\psi}_e\gamma^\mu\psi_\nu) + \text{h.c.},$$

where  $G_F$  is the Fermi constant. This picture is not renormalizable and does violate unitarity; thus, it offers a good effective description of weak interactions only at low energies<sup>7</sup>. Experiments show that weak interactions involve both charged and neutral currents: the first account for transitions between up- and down-type leptons or quarks, the latter conserve flavour.

The electroweak theory aims at unifying the theory of weak interactions and electromagnetic interactions. It is invariant under transformations of the symmetry group

$$SU(2)_L \otimes U(1)_Y.$$

Fermions are grouped according to their chirality eigenstate, i.e. in left-handed and right-handed fields  $\psi_{L,R}$ , where

$$\begin{aligned}\psi_L &= P_L\psi = \frac{1}{2}(1 - \gamma^5)\psi, \\ \psi_R &= P_R\psi = \frac{1}{2}(1 + \gamma^5)\psi,\end{aligned}$$

and  $P_{L,R}$  is the left (right)-handed projection operator, while  $\gamma^5 = i\gamma^0\gamma^1\gamma^2\gamma^3$ . Left-handed fermions are paired in doublets with isospin  $I = 1/2$ , while right-handed ones are  $I = 0$  singlets: there are three families of quarks,

$$\begin{pmatrix} u \\ d \end{pmatrix}_L, \begin{pmatrix} c \\ s \end{pmatrix}_L, \begin{pmatrix} t \\ b \end{pmatrix}_L, \quad (u)_R, (d)_R, (c)_R, (s)_R, (t)_R, (b)_R,$$

and analogously three families of leptons,

$$\begin{pmatrix} \nu_e \\ e \end{pmatrix}_L, \begin{pmatrix} \nu_\mu \\ \mu \end{pmatrix}_L, \begin{pmatrix} \nu_\tau \\ \tau \end{pmatrix}_L, \quad (e)_R, (\mu)_R, (\tau)_R.$$

---

<sup>7</sup>Since the complete theory of weak interaction involves massive mediators, the  $W$  and  $Z$  bosons, this effective theory is valid for energies negligible with respect to the mass of the  $W$  boson,  $E \ll m_W \sim 80$  GeV.

Weak hypercharge and electric charge are linked to the weak isospin by the relation

$$Q = I_3 + \frac{Y}{2},$$

where  $I_3$  is the third component of the weak isospin.

Hypercharge symmetry involves both chiralities, i.e. the lagrangian density is invariant under the transformations of the  $U(1)$  group,

$$\psi_{L,R} \rightarrow e^{i\alpha(x)\frac{Y}{2}} \psi_{L,R},$$

while weak isospin symmetry involves only left-handed doublets, with invariance under transformations of  $SU(2)$ ,

$$\psi_L \rightarrow e^{i\beta_a(x)\frac{\tau^a}{2}} \psi_L,$$

where  $\tau^a/2$  are the generators of  $SU(2)$ <sup>8</sup> and summation over  $a = 1, 2, 3$  is implied.

As a consequence of the local gauge symmetries of the electroweak lagrangian density, four gauge fields are introduced, in a way analogous to QED: one has a triplet of vector bosons,  $W_i^\mu$  ( $i = 1, 2, 3$ ) for  $SU(2)_L$  and a singlet  $B^\mu$  for  $U(1)_Y$ ; while the  $W_i^\mu$  fields couple only to left-handed fermion fields,  $B^\mu$  couples to fermions with either chirality. Physical fields, corresponding to the four observed bosons – two neutral, the photon and the  $Z$  boson, and two charged, the  $W^+$  and  $W^-$  bosons – can be then obtained with the linear combinations

$$A^\mu = \sin \theta_W W_3^\mu + \cos \theta_W B^\mu, \quad (1.3)$$

$$Z^\mu = \cos \theta_W W_3^\mu - \sin \theta_W B^\mu, \quad (1.4)$$

$$W_\pm^\mu = \frac{W_1^\mu \mp iW_2^\mu}{\sqrt{2}}, \quad (1.5)$$

where  $\theta_W$  is the weak mixing angle.

The electroweak lagrangian density can be expressed as the sum of the field strength tensors

$$\mathcal{L}_{EW} = -\frac{1}{4} \sum_V F_V^{\mu\nu} F_{V,\mu\nu} + i \sum_f \bar{f} D_\mu \gamma^\mu f, \quad (1.6)$$

where summations run over all gauge vector bosons,  $V$ , and fermion fields,  $f$ . The covariant derivative  $D_\mu$  is defined as

$$D_\mu = \partial_\mu - ig_V (\lambda^a V_a)_\mu,$$

where  $g_V$  is the generic coupling constant of a fermion to the  $V$  field,  $\lambda^a$  are the generators of the corresponding symmetry group, and  $V_a$  is the field tensor. Explicitly, for a single fermion field  $\psi$  one has

$$\mathcal{L}_{EW} = -\frac{1}{4} W_{\mu\nu}^a W_a^{\mu\nu} - \frac{1}{4} B_{\mu\nu} B^{\mu\nu} + i \bar{\psi} \gamma^\mu D_\mu \psi,$$

---

<sup>8</sup>We denote by  $\tau^a$  ( $a = 1, 2, 3$ ) the Pauli matrices.

with

$$\begin{aligned} W_i^{\mu\nu} &= \partial_\nu W_i^\mu - \partial_\mu W_i^\nu - g\epsilon_{ijk}W_i^\mu W_j^\nu, \\ B^{\mu\nu} &= \partial_\nu B_\mu - \partial_\mu B_\nu, \end{aligned}$$

and

$$D_\mu = \partial_\mu + igW_\mu^a I_a + i\frac{g'}{2}B_\mu Y,$$

where  $g$  and  $g'$  are the  $SU(2)$  and  $U(1)$  coupling constants, respectively, which are linked to  $\theta_W$  via the relations

$$\begin{aligned} \sin \theta_W &= \frac{g'}{\sqrt{g^2 + g'^2}}, \\ \cos \theta_W &= \frac{g}{\sqrt{g^2 + g'^2}}. \end{aligned}$$

Moreover, the electric charge  $e$  can be written as  $e = g \sin \theta_W$ .

What is missing in Eq. (1.6) are terms which give mass to fermions and vector bosons<sup>9</sup>: this prediction is in contrast with the experimental observation, and calls for a technique which allows for non-zero fermion and vector boson masses but at the same times preserves gauge invariance.

## 1.2 Giving Mass to Particles: the Higgs–Brout–Englert Mechanism

### 1.2.1 Electroweak Symmetry Breaking

A way to modify the electroweak lagrangian density to give masses to fermions and vector bosons is the so-called *Higgs–Brout–Englert mechanism*[2]. The idea is to introduce a scalar isospin doublet, eigenstate of weak isospin with  $I = 1/2$ ,  $I_3 = -1/2$  and hypercharge  $Y = 1$ <sup>10</sup>,

$$\phi(x) = \begin{pmatrix} \phi^+(x) \\ \phi^0(x) \end{pmatrix},$$

where  $\phi^+$  and  $\phi^0$  are complex fields. This term yields a corresponding contribution in the lagrangian density,

$$\mathcal{L}_H = (D_\mu \phi)^\dagger (D^\mu \phi) - V(\phi),$$

where the potential term can be expressed as

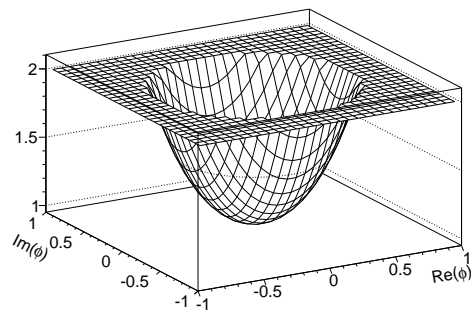
$$V(\phi) = \mu^2 \phi^\dagger \phi + \lambda (\phi^\dagger \phi)^2 = \mu^2 \phi^2 + \lambda \phi^4. \quad (1.7)$$

<sup>9</sup>For example, in the case of the fermion field, one cannot include a mass term proportional to  $\bar{\psi}\psi$  since

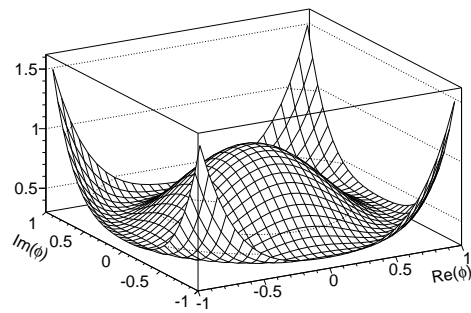
$$\bar{\psi}\psi = \bar{\psi}_L \psi_R + \bar{\psi}_R \psi_L$$

would mix left- and right-handed fields, breaking the invariance of the lagrangian density under transformations of  $SU(2)_L \otimes U(1)_Y$ .

<sup>10</sup>In this way,  $Q = 0$  for the lower component.



(a)  $\mu^2 > 0$



(b)  $\mu^2 < 0$

**Figure 1.1.**  $V(\phi)$ , as defined in Eq. (1.7), for  $\lambda > 0$  and different signs of  $\mu^2$ .

The potential  $V$  defined in Eq. (1.7) has a finite lower bound when  $\lambda > 0$ , which defines a ground state  $|0\rangle$  (the *vacuum state*). According to the sign of  $\mu^2$ , this ground state can be unique ( $\mu^2 > 0$ , with minimum for  $\phi = 0$ ) or degenerate ( $\mu^2 < 0$ ), due to the shape of the potential which has a minimum in  $\phi = 0$  (Fig. 1.1a) or in a set of points (Fig. 1.1b), respectively.

We are interested in the latter case,  $\mu^2 < 0$ . One can solve the degeneracy of the ground states adding a *driving term*

$$\epsilon^* \phi + \epsilon \phi^\dagger,$$

to the lagrangian density of Eq. (1.6), where  $\epsilon$  is in general a complex number. When we let  $\epsilon$  tend to zero, the driving term forces the potential to have a single minimum in

$$\phi = \phi_0 = \begin{pmatrix} 0 \\ \eta \end{pmatrix},$$

with  $\eta = \sqrt{-\mu^2/2\lambda}$ , for which the expectation value of the field  $\phi$  on the vacuum state is non-zero,

$$\langle 0 | \phi | 0 \rangle = \eta \equiv \frac{v}{\sqrt{2}} \neq 0.$$

We introduced in this way a preferential direction in the  $\phi$  complex plane: the minimum energy configuration is no more symmetric, and the symmetry is spontaneously broken by the ground state.

By applying perturbation theory around the vacuum state to the  $\phi$  field, one can see that the two degrees of freedom associated to the complex field  $\phi$  are represented by two particles, one with mass  $4\lambda\eta^2$  and one massless (*Goldstone theorem*). However, there is no experimental evidence of a massless scalar boson (the *Goldstone boson*): in fact, invariance of the electroweak lagrangian density under local phase transformations of the fields always allows us to choose a gauge (*unitary gauge*) in which the Goldstone boson and the massive boson are replaced by two fields, a scalar  $H$  and a vector  $A$ , with masses

$$\begin{aligned} m_H^2 &= -2\mu^2 = 4\lambda\eta^2, \\ m_A^2 &= 2e^2\eta^2. \end{aligned}$$

As a consequence of this gauge choice, Eq. (1.2.1) can be written as

$$\phi(x) = \frac{1}{\sqrt{2}} \begin{pmatrix} 0 \\ v + h(x) \end{pmatrix}. \quad (1.8)$$

We note that the spontaneous symmetry breaking of the electroweak lagrangian density still conserves the gauge symmetry of electromagnetism, i.e.

$$SU(2)_L \otimes U(1)_Y \longrightarrow U(1)_{EM}.$$

### 1.2.2 Gauge Bosons

If we consider the kinetic part of the lagrangian density of Eq. (1.2.1), replacing  $\phi$  with Eq. (1.8), one has

$$(D_\mu \phi)^\dagger (D^\mu \phi) = \frac{1}{2} \partial^\mu h \partial_\mu h + \frac{1}{8} g^2 (v + h)^2 |W_1^\mu + iW_2^\mu|^2 + \frac{1}{8} (v + h)^2 |g'W_3^\mu - gB_\mu|^2.$$

Applying Eq. (1.5), masses for the vector boson fields are identified: we have an intermediate charged boson, the  $W$ , with mass  $m_W = gv/2$ , a massive neutral boson, the  $Z$ , with mass  $m_Z = \sqrt{g^2 + g'^2}v/2$ , and the photon, with  $m_\gamma = 0$ . It holds

$$M_W/M_Z = \cos \theta_W.$$

### 1.2.3 Fermions

We cannot obtain a mass  $m$  for a fermion field  $f$  by adding to the electroweak lagrangian density a term

$$m\bar{f}f = m(\bar{f}_L f_R + \bar{f}_R f_L),$$

since this term has an overall weak isospin  $1/2$ , but we can restore invariance under transformations of  $SU(2)_L \otimes U(1)_Y$  by adding instead a Yukawa term representing the interaction between the Higgs field and fermion fields. For electrons, for example, one can write

$$\mathcal{L}_{e\phi} = g_e (\bar{\ell}\phi e_R + \bar{e}_R \phi^\dagger \ell),$$

where  $\ell = (\nu, e)^T$ . This term becomes, after spontaneous symmetry breaking and after choosing the unitary gauge,

$$\bar{\ell}\phi = \bar{n}u_L\phi^+ + \bar{e}_L\phi^0 = \bar{e}_L \left( \eta + \frac{h}{\sqrt{2}} \right),$$

from which one has

$$\mathcal{L}_{e\phi} = g_e \eta e e + \frac{g_e}{\sqrt{2}} h e e.$$

We can recognize that the first term is a mass term, with

$$m_e = g_e \eta = g_e \frac{v}{\sqrt{2}}.$$

The coupling of the Higgs field to fermions is therefore proportional to their mass. The mass of the Higgs boson itself depends on the two parameters of the potential  $V(\phi)$ , i.e. the vacuum expectation value  $v$  and the coupling parameter  $\lambda$ . It can be shown that

$$v = \frac{2m_W}{g} = (\sqrt{2}G_F)^{-\frac{1}{2}}.$$

Precision measurements of  $G_F$  from muon lifetime measurements yield  $v \approx 247$  GeV. The Higgs mass  $m_H$  is a free parameter of the theory.

### 1.2.4 Theoretical Constraints on $m_H$

There are multiple theoretical constraints which put lower and upper bounds to the value of  $m_H$ , which is a free parameter of the theory<sup>11</sup>[3, 4, 5, 6]. A lower bound on the Higgs mass is given by the stability of the vacuum state (*stability bound*) and upper bounds are given both by the requirement for the Higgs self-coupling not

<sup>11</sup> $\lambda$  can be always expressed as a function of  $m_H$  and  $v$ .

to blow up at high energy (*triviality bound*), and by the requirement of scattering amplitudes of longitudinal bosons not to exceed the *unitarity bound*.

The triviality bound comes as a consequence of the renormalization group equations (RGEs) of the SM. If we assume that the RGEs are in the perturbative regime, first-order radiative corrections predict a running value of the quartic coupling  $\lambda$ , as a function of the involved energy scale  $Q$ . Neglecting the Yukawa contribution for the top quark, valid only for heavy  $m_H$ , one has

$$\lambda(Q) = \frac{\lambda(v)}{1 - \frac{3}{4\pi^2} \log \frac{Q^2}{v^2} \lambda(v)},$$

which is linked to  $m_H$  from the dependence on  $\lambda(v)$  by  $m_H^2 = 2\lambda(v)v^2$ . In order for the perturbative regime to be valid at all energies, the self-coupling  $\lambda(Q)$  has to remain finite for  $Q^2 \rightarrow \infty$ : the consequence is however be that at low energies one would have  $\lambda = 0$ , i.e. the theory would be free in the infrared region (*triviality*). This means that either the theory becomes non-perturbative above a certain energy scale  $\Lambda_c$ , or that the SM is not valid above that scale  $\Lambda_c$ . This results in an upper limit on the Higgs mass.

The stability bound, on the other hand, is related to the fact that symmetry breaking actually occurs only when  $V(v) < V(0)$ , hence the requirement  $\lambda > 0$ . RGEs show that, as a function of the top quark mass  $m_t$ , when  $m_H$  is low enough the electroweak vacuum is only a local minimum of the potential  $V$ , while the global minimum is located at values of the field beyond an energy scale lower than the Planck mass,  $\Lambda < M_P$ , for which  $\lambda < 0$ . The local minimum can potentially become unstable in favour of the global minimum, unless there is new physics at or before the scale  $\Lambda$  that prevents this.

A metastability region can be identified as the regime in which the lifetime of the electroweak vacuum is greater than the age of the universe.

Moreover, one of the reasons of the introduction of the Higgs field is to recover unitarity in the high-energy scattering of longitudinal  $W$  and  $Z$  bosons. The quadratic growth with the energy of the amplitude of these processes is in fact cancelled by the introduction of diagrams involving the Higgs boson, provided that its mass satisfies the relation

$$m_H < \sqrt{\frac{8\pi\sqrt{2}}{3G_F}} \approx 1 \text{ TeV},$$

or that new physics appears at a similar energy scale.

Fig. 1.2 shows, in the  $m_H$  vs  $\Lambda$  plane, the regions allowed and forbidden by these theoretical arguments.

### 1.3 Looking for the Higgs Boson

The fact that  $m_H$  is a free parameter of the theory draws an important experimental challenge in the search of the Higgs boson. Different values of the Higgs mass, in fact, yield different interplay between the possible production mechanisms and the open decay channels, and therefore call for different reconstruction strategies as a function of  $m_H$ .

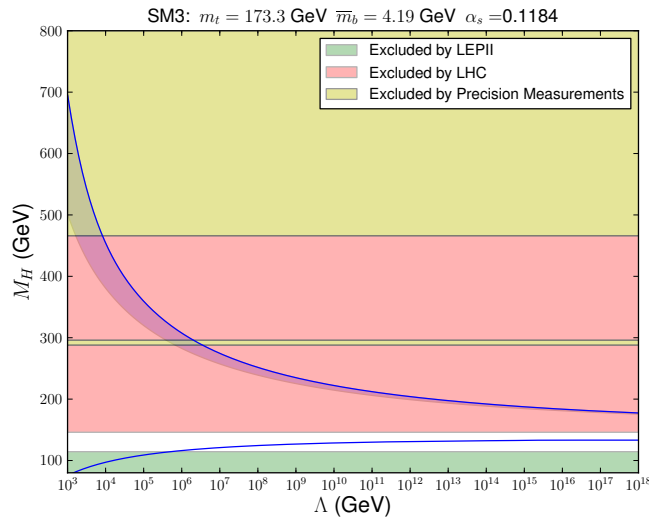


**Figure 1.2.** Stability and triviality bounds for the Standard Model, as a function of the Higgs boson mass  $M_H$  and the scale of new physics  $\Lambda$ [3].

### 1.3.1 Production Mechanisms

The dominant contribution on the production side in  $pp$  collisions is the *gluon fusion* (ggF) mechanism,

$$pp \rightarrow gg \rightarrow H.$$

Its lowest order Feynman diagram is shown in Fig. 1.3a: this process cannot happen at tree level and therefore involves fermion loops. Since the coupling between the Higgs field and fermions is proportional to their mass, the dominant contribution to this vertex in the SM comes from the  $ttH$  coupling. Gluon fusion yields the highest production cross-section in the full Higgs mass range; its value is known at next-to-leading-order (NLO) and next-to-next-to-leading-order (NNLO) in QCD, with an uncertainty of about 10% [8], arising mainly from missing terms in the perturbative expansion, as well as from the imprecise knowledge of parton distribution functions.

Vector boson fusion (VBF)

$$qq \rightarrow qqV^*V^* \rightarrow qqH,$$

which is shown in Fig. 1.3b, involves instead the coupling with intermediate vector bosons radiated from the initial state partons. Experimentally, the hadronization induced from the initial state partons is observed as two high-energy jets almost collinear with the colliding beams: by identifying those jets, one has an handle to effectively tag VBF events. The VBF production cross-section in  $pp$  collisions, as shown in Fig. 1.4, is about one order of magnitude less than the ggF value. It receives small QCD corrections and it is known at NLO with less than 10% uncertainty.

Associated production with a vector boson ( $VH$ )

$$q\bar{q} \rightarrow V^* \rightarrow VH,$$

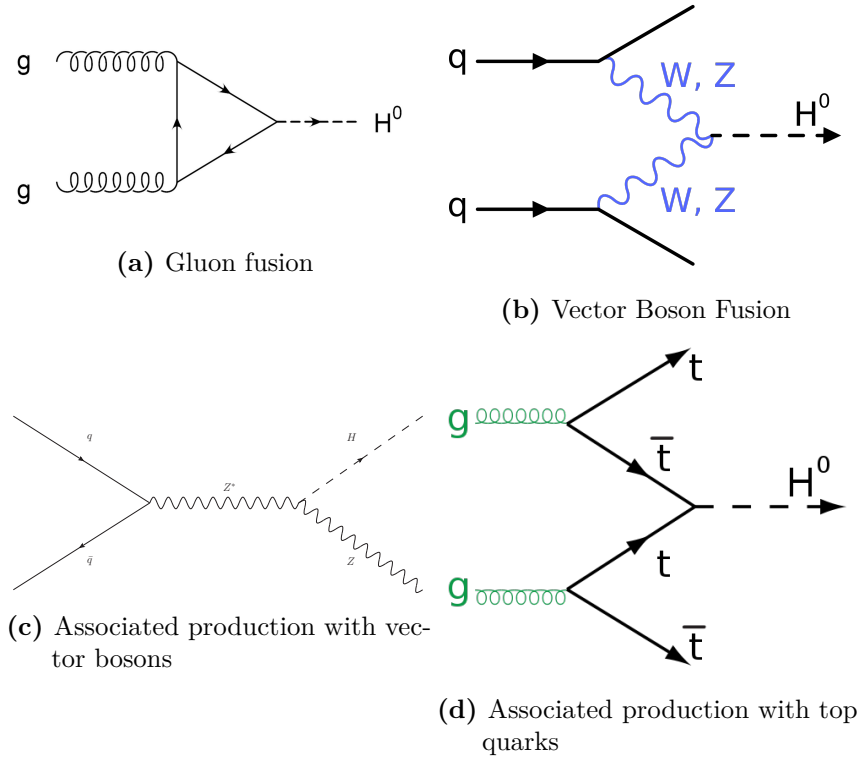


**Figure 1.3.** Lowest order Feynman diagrams for different production mechanisms of the Higgs boson.

which is shown in Fig. 1.3c, happens when a Higgs boson is radiated from an intermediate vector boson (*Higgsstrahlung*). Its experimental signature is clear, due to the possibility to reconstruct the decay of the intermediate boson as well as the Higgs decay products. This production mechanism has lower cross-section than ggF and VBF, has moderate QCD corrections and it is known at NLO and NNLO in QCD, with an uncertainty of less than 5%.

Associated production with a top quark ( $ttH$ ), shown in Fig. 1.3d, involves the production two top quarks together with the Higgs boson. The cross-section of this process is however negligible when compared with the other production mechanisms.

### 1.3.2 Decay Channels

Depending on the value of the Higgs mass, different are the open decay channels and their production cross-section times decay branching ratio (BR), which sets the magnitude between the different processes. Fig. 1.5 shows the cross-section times BR ( $\sigma \times BR$ ) as a function of  $m_H$ , for  $pp$  collisions both at  $\sqrt{s} = 7$  TeV and 8 TeV: we can identify three different mass regions where the sensitivity of the various channels is different.

In the low mass region ( $m_H < 130$  GeV), the dominant branching ratio is the one of  $H \rightarrow b\bar{b}$ . Experimentally, however, this channel can be really challenging at hadron colliders, where one has to discriminate a signal with a cross-section of  $\mathcal{O}(10$  pb) over a background from QCD multi-jet production with a cross-section of

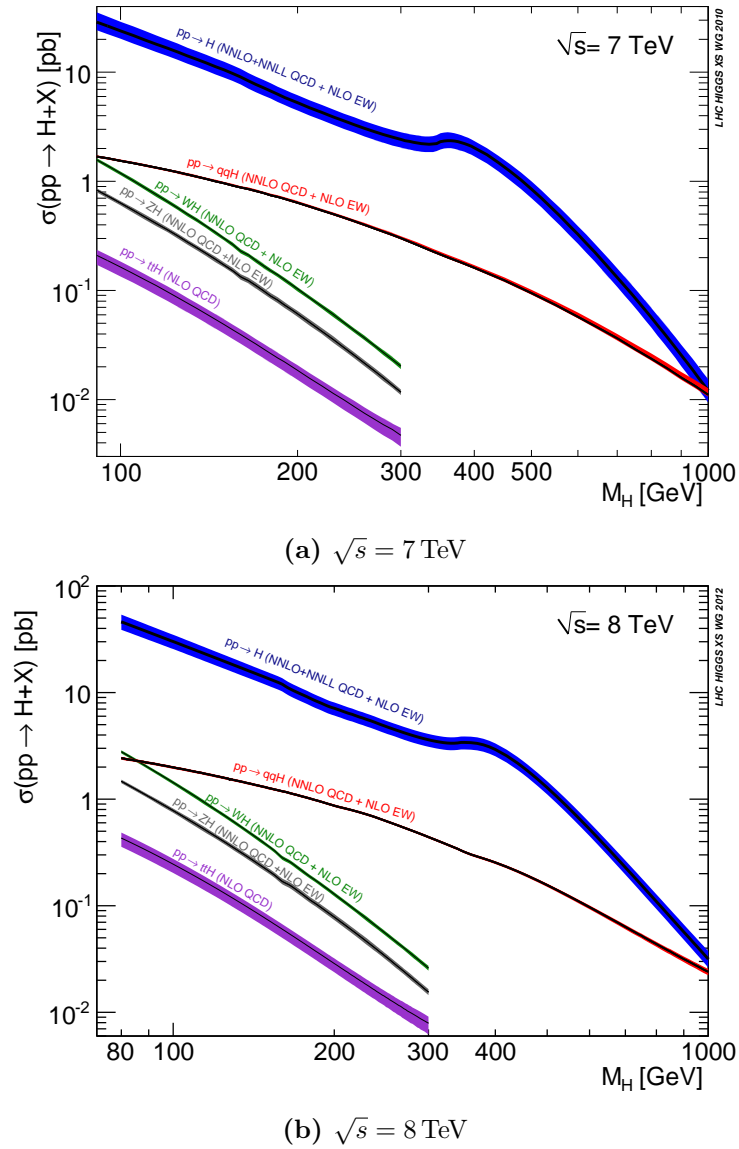


**Figure 1.4.** Cross-section for the  $pp \rightarrow H + X$  process, as a function of the Higgs mass  $m_H$ , for different production mechanisms and different center-of-mass energies.

$\mathcal{O}(100 \mu\text{b})$ . Signal to background ratio  $S/B$  is higher for the  $H \rightarrow \gamma\gamma$  decay channel, with  $S/B = \mathcal{O}(10^{-2})$ . Its signature consists of two high-energy photons whose invariant mass distribution has a narrow peak at  $m_{\gamma\gamma} \approx m_H$ ; main backgrounds, namely direct di-photon production and  $jj/\gamma j$  with at least one jet misidentified as a photon, can be evaluated with data-driven techniques using the sidebands of the  $m_{\gamma\gamma}$  distribution. Moreover the  $H \rightarrow ZZ^* \rightarrow 4\ell$  channel<sup>12</sup>, despite its low  $\sigma \times BR$ , has  $S/B = \mathcal{O}(1)$  due to the presence of four leptons in the final state. Its signature consists of four leptons, the invariant mass of two of which is compatible with an on-shell  $Z$  boson, and a peak in the four-lepton invariant mass  $m_{4\ell}$ . The main background is  $pp \rightarrow ZZ^* \rightarrow 4\ell$ , with minor contributions from  $Z + jj$ ,  $Z + b\bar{b}$  and  $t\bar{t}$ .

In the mass region  $130 \text{ GeV} < m_H < 180 \text{ GeV}$ , the two dominant channels are  $H \rightarrow ZZ^{(*)}$  and  $H \rightarrow W^+W^-$ . With respect to  $H \rightarrow ZZ$ , the cross-section of the process  $p \rightarrow H \rightarrow WW$  is higher, due to the bigger coupling of the Higgs field with  $W$  bosons and to the reaching of the kinematic threshold  $2m_W$ , where the decay to two on-shell  $W$  bosons is open. The most promising final state for this channel is the one with leptonic decays of the intermediate bosons,  $W \rightarrow \ell\bar{\nu}_\ell$ , whose experimental signature consists of an high-energy charged lepton and high missing transverse momentum. Due to the presence of neutrinos in the final state, it is however not possible to reconstruct completely the final state: the Higgs boson is identified from the transverse mass distribution of the  $\ell\nu\ell\nu$  system<sup>13</sup>, and resolution on the Higgs boson mass is poor.

In the high mass region,  $180 \text{ GeV} < m_H < 1 \text{ TeV}$ , the most promising channel for the identification of the Higgs boson is  $H \rightarrow ZZ$ , with subsequent decay in  $\ell\ell q\bar{q}$ ,  $\ell\ell\nu\nu$  and in four leptons. Both  $Z$  bosons are in this case on-shell, which allows to further reduce backgrounds applying a more stringent kinematic selection on the decay leptons.

Fig. 1.6 shows the total decay width  $\Gamma_H$  of the Higgs boson, as a function of its mass[7]. For low values of  $m_H$ , below the threshold for the production of two  $W$  bosons, the decay width is of the order of 1 MeV to 10 MeV. It then increases rapidly with the opening of diboson decays, until – for masses at the level of 1 TeV – the Higgs boson becomes a quite broad resonance. The interplay between  $\Gamma_H$  and the experimental resolution on  $m_H$  becomes important, if we take as an estimate of the mass resolution the resolution on  $m_{4\ell}$  in the  $H \rightarrow ZZ \rightarrow 4\ell$  decay, at about 350 GeV.

### 1.3.3 Where do We Stand?

Various have been the experimental searches for the Higgs boson in the last decades. Collider experiments have been purposely designed to cope with the challenges of a chase which spans over the full mass range allowed by theoretical arguments, while precision measurements in the electroweak sector further allowed to put constraints

<sup>12</sup>To ease the notation, we will indicate with  $H \rightarrow ZZ^{(*)}$  also the process  $H \rightarrow ZZ^*/\gamma^*$ .

<sup>13</sup>Transverse mass is defined as

$$m_T = \sqrt{(E_T^{\ell\ell} + E_T^{\text{miss}})^2 - |\mathbf{p}_T^{\ell\ell} + \mathbf{E}_T^{\text{miss}}|^2},$$

where  $E_T^{\ell\ell} = (|\mathbf{p}_T^{\ell\ell}|^2 + m_{\ell\ell}^2)^{1/2}$ .

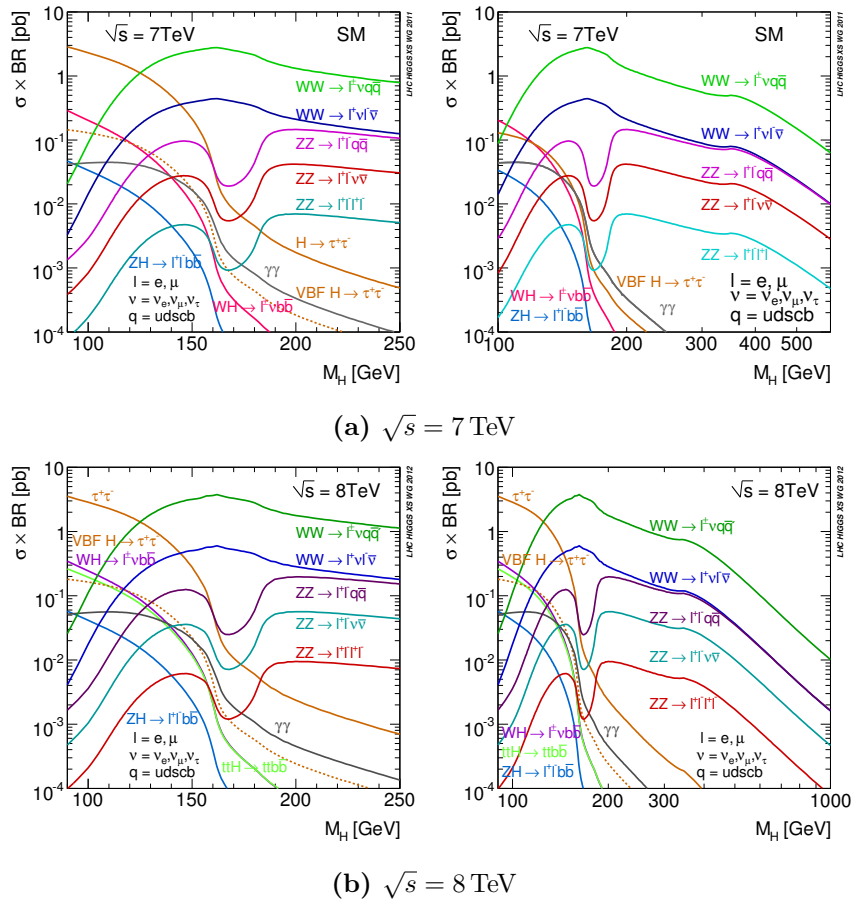


**Figure 1.5.** Cross-section times branching ratio, as a function of the Higgs mass  $m_H$ , for different decay channels and different center-of-mass energies.

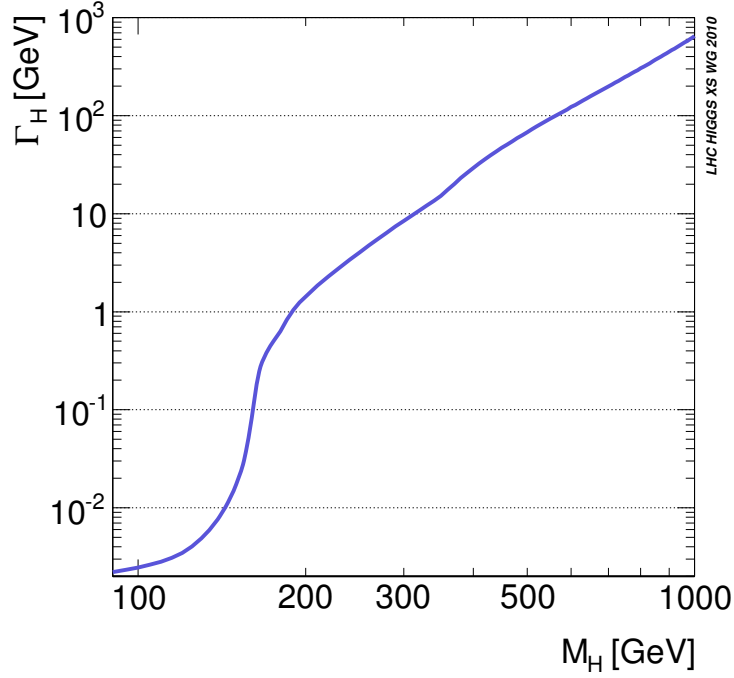


**Figure 1.6.** Total decay width of the Standard Model Higgs boson, as a function of its mass. From Ref. [7].

on its mass  $m_H$ .

LEP, the  $e^+e^-$  collider at the SPS at CERN, provided the first limits on the Higgs mass by direct searches[9], using about  $2.5 \text{ fb}^{-1}$  of data collected by the ALEPH, DELPHI, L3, and OPAL collaborations at a center-of-mass energy  $\sqrt{s} = 189 \text{ GeV}$  to  $209 \text{ GeV}$ . The most sensitive channel was  $H \rightarrow b\bar{b}$ , with the Higgs produced in association with a  $Z$  boson in the process  $e^+e^- \rightarrow Z^* \rightarrow HZ$ . A Higgs boson with a mass  $m_H < 114.4 \text{ GeV}$  was excluded at 95% CL, as shown in Fig. 1.7.

Precision measurements in the electroweak sector also give an indirect information on the Higgs mass, since  $m_H$  enters in the radiative corrections. Best fits including data from LEP and SLD experiments have been performed[10]. Fig. 1.8 shows results obtained without including data from direct searches: the best fit mass is  $m_H = 91_{-23}^{+30} \text{ GeV}$ , where uncertainties include the 68% CL interval around the maximum likelihood estimate (MLE).

Results from the CDF and D0 collaborations at the Tevatron accelerator at Fermilab, based on up to  $10 \text{ fb}^{-1}$  of data collected in  $p\bar{p}$  collisions at  $\sqrt{s} = 1.96 \text{ TeV}$ , are shown in Fig. 1.9[11]. The most important production mechanism is the associate production with  $W$  or  $Z$  bosons, which then decay leptonically; the most sensitive decay channel is  $H \rightarrow b\bar{b}$ , while the center-of-mass energy allows also  $H \rightarrow WW$  and  $H \rightarrow ZZ$  to be kinematically permitted. Results exclude a SM Higgs boson, at the 95% confidence level (CL), from 90 to 109 GeV and from 149 to 182 GeV.

In July 2012, the ATLAS and CMS collaborations at the LHC announced the observation of a new particle within the search of the Higgs boson[12, 13], at a mass of about 125 GeV, using up to  $5.1 \text{ fb}^{-1}$  of data collected in  $pp$  collisions at  $\sqrt{s} = 7 \text{ TeV}$

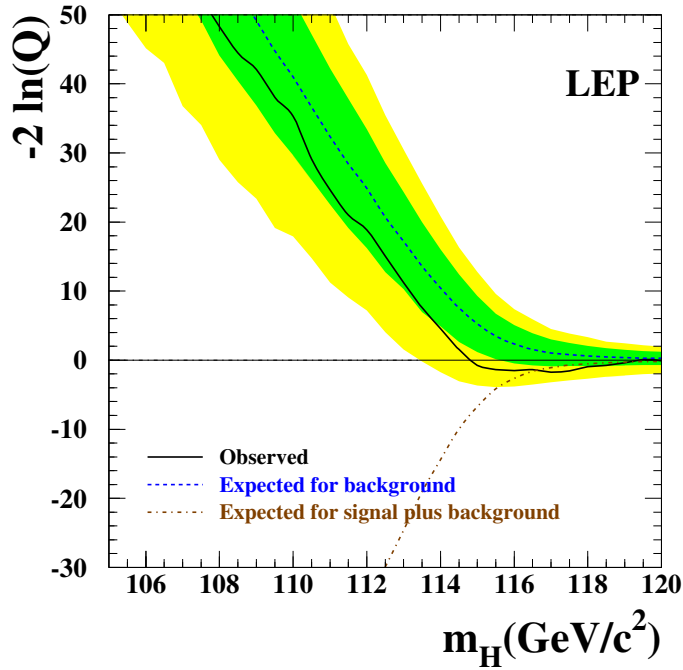


**Figure 1.7.** Observed and expected test statistics  $-2 \ln Q$ , where  $Q = L(s+b)/L(b)$  is expressed in terms of the likelihood of data in the signal plus background and the background-only hypotheses, as a function of the tested Higgs mass  $m_H$ , obtained combining data of the four LEP experiments. From Ref. [9].

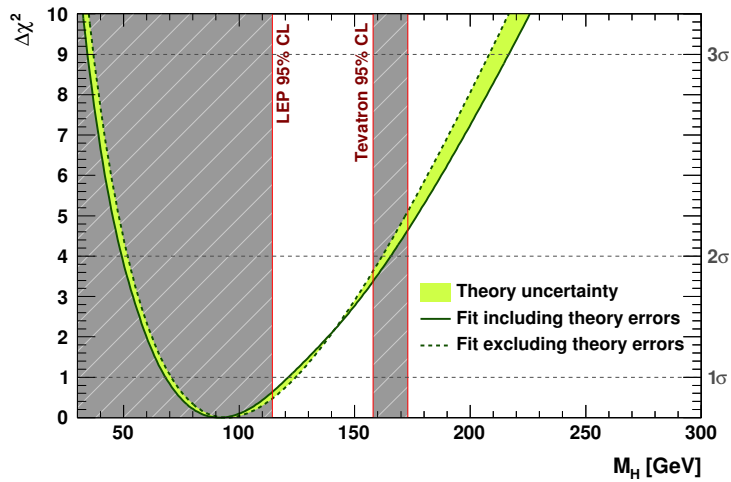


**Figure 1.8.**  $\Delta\chi^2 = \chi^2 - \chi_{\min}^2$  vs  $m_H$  curve for the electroweak global fit; the grey band represents the 95% CL exclusion range from direct searches using LEP data and part of Tevatron data[10].

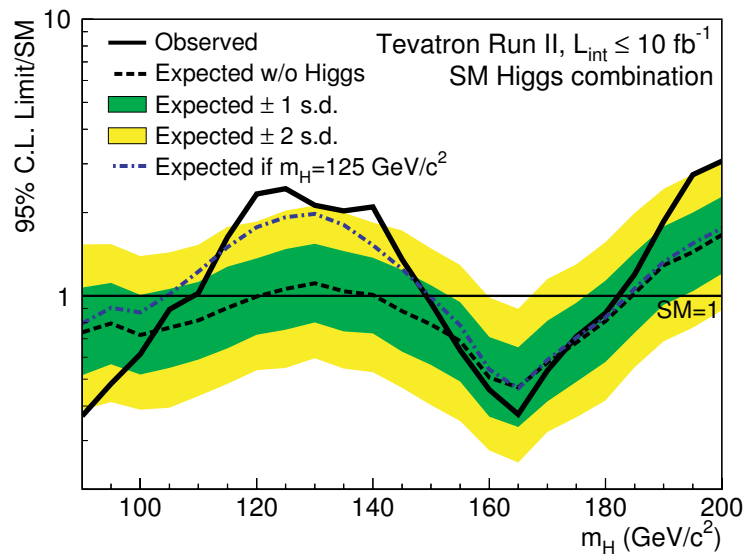
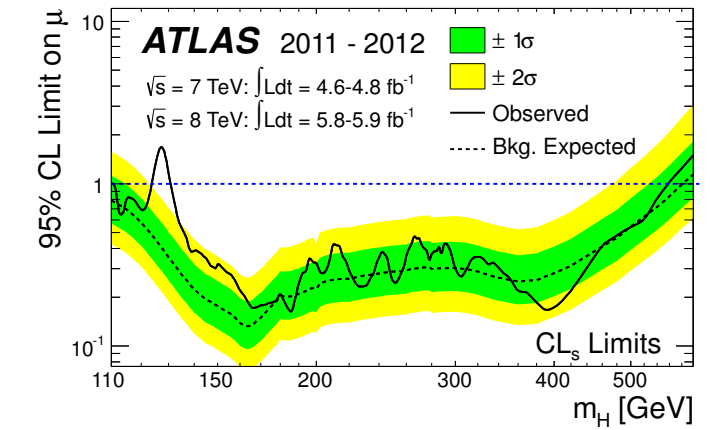


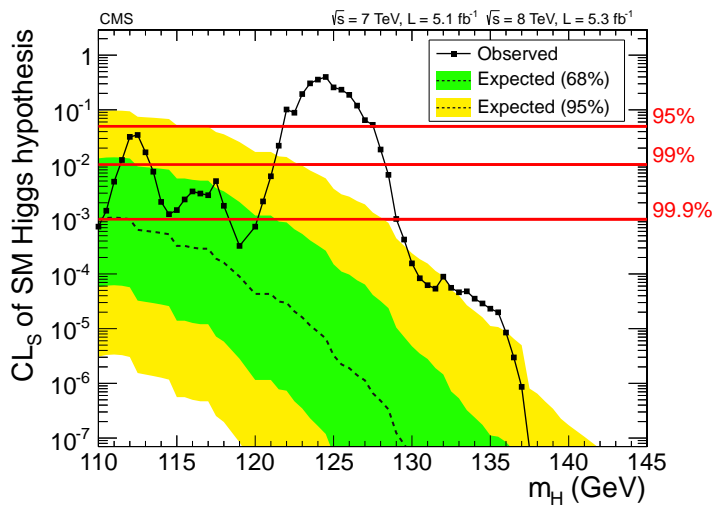
**Figure 1.9.** 95% CL limit on the ratio between the measured cross-section and the cross-section predicted for a SM Higgs boson of mass  $m_H$ , from Ref. [11].

and up to  $5.9 \text{ fb}^{-1}$  at  $\sqrt{s} = 8 \text{ TeV}$ . Fig. 1.10 shows how, already with this statistics, the exclusion limit covers the full mass range probed by LHC experiments, apart from a narrow region around the mass of the observed particle. Recent Tevatron results show that an excess of  $3.0\sigma$  is also observed at the CDF and D0 experiments for  $m_H = 125 \text{ GeV}$ , and recent LHC results using the full 2012 dataset confirm the discovery of the new particle with a significance against the background-only hypothesis of more than  $6\sigma$ [14, 15].

This thesis work focuses both on the discovery of the new particle, using ATLAS data in the  $H \rightarrow ZZ^{(*)} \rightarrow 4\ell$  channel, and on the characterization of its properties. The nature of the new boson is in fact not obvious: is it *the* Standard Model Higgs boson, or just *one* of the Higgs bosons predicted or allowed by theories beyond the Standard Model (BSM)? Does it *behave*, from the point of view of couplings to SM particles and of quantum numbers, in the same way as the Standard Model Higgs boson does? Do current data allow or ask for a more general explanation of particle physics at the current energy scale?



(a) ATLAS[12]



(b) CMS[13]

**Figure 1.10.** **a:** 95% CL limit on the ratio between the measured cross-section and the cross-section predicted for a SM Higgs boson of mass  $m_H$ . **b**  $CL_s$  values for the SM Higgs boson hypothesis as a function of  $m_H$ , together with expectation for the background only hypothesis.



## Chapter 2

# The ATLAS Experiment at the LHC

Looking for the Higgs boson is among the reasons for which the LHC and in particular the ATLAS experiment were designed. Exploiting the energy frontier is both an unprecedented technical and experimental challenge: it requires an excellent design and operation of the accelerator complex, together with a deep understanding of each detector subsystem. In this chapter, a description of the LHC and of the ATLAS experiment is provided.

### 2.1 The Large Hadron Collider

The Large Hadron Collider (LHC)[16] is a proton–proton and heavy ions collider, with design center–of–mass energies of 14 TeV and 5.52 TeV per nucleon, respectively, and a design instantaneous luminosity of  $1 \times 10^{34} \text{ cm}^{-2}\text{s}^{-1}$ . It is a 26.7 km wide ring formed by 1232 superconducting magnets, each 15 m long, which generate a dipole magnetic field of 8.4 T. Eight experimental halls are built, one of which hosts the ATLAS experiment. In the linear section of the ring before each experiment, a system of three magnets with quadrupole field is placed at each side of the detector, in order to focus the two beams in such a way to obtain a RMS width of the beam in the transverse plane of about 16.63  $\mu\text{m}$ . Collisions take place when *bunches* of particles of each beam collide with bunches from the other beam (*bunch crossing*, BC): the design BC period is about 25 ns.

In a scattering process, luminosity is defined as the proportionality factor between the cross–section of the process,  $\sigma$ , and the number of observed events for that process,  $N$ , via the relation  $N = L\sigma$ . The instantaneous luminosity  $\mathcal{L}$ , with  $L = \int dt\mathcal{L}$ , can be expressed as a function of the characteristic parameters of the collider:

$$\mathcal{L} = F \frac{n_b N_b^2 f_{\text{rev}}}{4\pi\sigma^{*2}},$$

where  $n_b$  is the number of bunches which circulate in the accelerator,  $N_b$  is the number of protons per bunch,  $f_{\text{rev}}$  is the revolution frequency of the machine and  $\sigma^*$  is the RMS beam width in the interaction point, while  $F$  is a geometric factor depending on the angle at which the two beams cross each other. If this angle,  $\theta_c$ , is

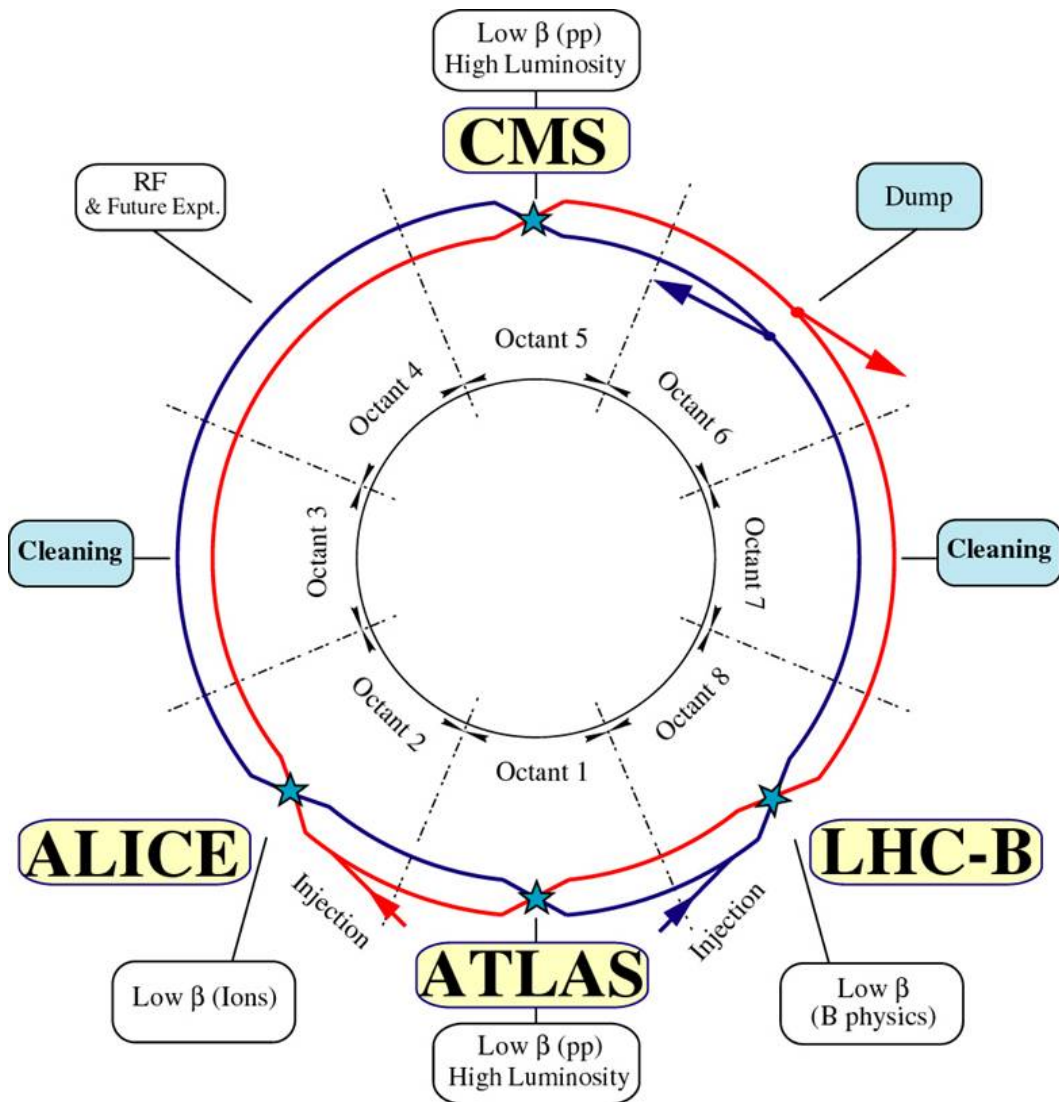


Figure 2.1. Scheme of the Large Hadron Collider at CERN, Geneva.

Parameter	Value
$n_b$	2808 bunch
$N_b$	$1.15 \cdot 10^{11} p/\text{bunch}$
$f_{\text{rev}}$	11 245 kHz
$\sigma^*$	16.7 $\mu\text{m}$
$\theta_c$	285 $\mu\text{rad}$
$\sigma_z$	7.55 cm
$F$	0.84

**Table 2.1.** Design parameters for the LHC[16].

low enough<sup>1</sup>, one can write

$$F \approx \frac{1}{\sqrt{1 + \left(\frac{\theta_c \sigma_z}{2\sigma^*}\right)^2}},$$

where  $\sigma_z$  is the RMS length of each bunch. Table 2.1 shows the design parameters for the LHC[16].

During 2011, the LHC has collided proton beams at  $\sqrt{s} = 7 \text{ TeV}$ , reaching a peak instantaneous luminosity of  $3.65 \times 10^{33} \text{ cm}^{-2} \text{ s}^{-1}$  and delivering an integrated luminosity of  $5.6 \text{ fb}^{-1}$ [18]. In 2012, with a center-of-mass-energy of 8 TeV, the LHC has reached a peak instantaneous luminosity of  $7.73 \times 10^{33} \text{ cm}^{-2} \text{ s}^{-1}$  and delivered a total of  $23.3 \text{ fb}^{-1}$ . Fig. 2.2 and Fig. 2.3 show the behaviour of integrated and (peak) instantaneous luminosity as a function of time, for both years.

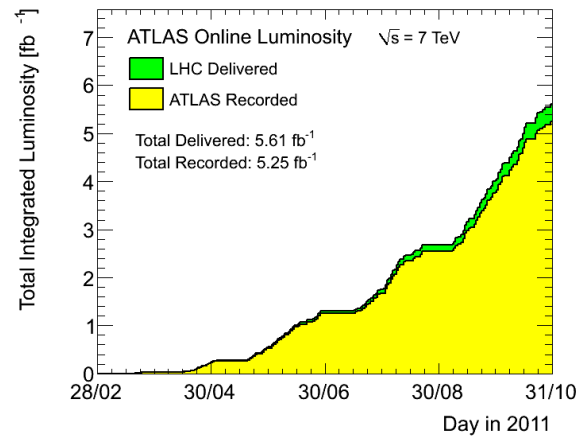
The number of inelastic interactions between partons which take place each time proton beams collide is proportional to the instantaneous luminosity of the single bunch and inversely proportional to  $f_{\text{rev}}$ . Fig. 2.4 shows the distribution of the mean number of interactions per bunch crossing,  $\langle \mu \rangle$ , for 7 TeV and 8 TeV.

### 2.1.1 The High Luminosity LHC

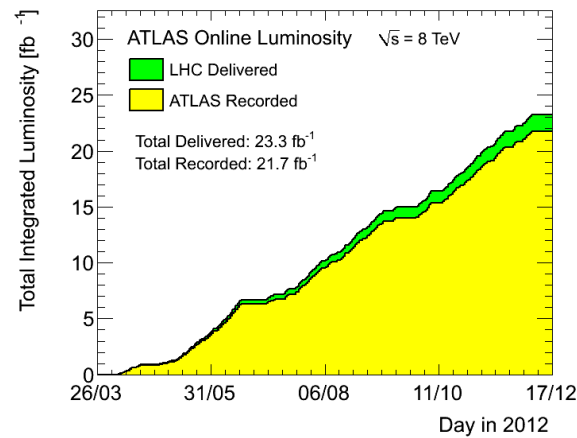
In 2015 the LHC will start taking data at  $\sqrt{s} = 13 \div 14 \text{ TeV}$ , and will reach progressively the design luminosity of  $1 \times 10^{34} \text{ cm}^{-2} \text{ s}^{-1}$ , being able to collect about  $40 \text{ fb}^{-1}$  per year. At this luminosity, however, by 2019 the LHC will need to run for more than ten years to half the statistical uncertainty in physics measurements, which is crucial for the observation of rare processes and the study of new particles.

The *High Luminosity LHC* programme (HL-LHC)[17] is an upgrade project, whose start is foreseen in 2020, which aims at improving by a factor 10 the design instantaneous luminosity of the accelerator, i.e. up to  $1 \times 10^{35} \text{ cm}^{-2} \text{ s}^{-1}$  (for an average number of interactions per bunch crossing up to  $\langle \mu \rangle = 140$ ). The goal of the project, which relies on the replacement of the inner triplet magnets and other hardware changes that will occur in 2022–2023, is to be able to integrate  $300 \text{ fb}^{-1}$  within the first  $10 \div 12$  years of life of the LHC, and to reach the threshold of  $3000 \text{ fb}^{-1}$  in  $10 \div 12$  additional years.

<sup>1</sup>At the LHC,  $\theta_c = 285 \mu\text{rad}$ .

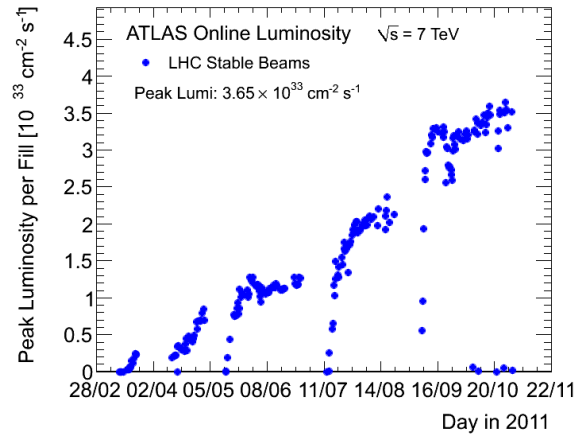


(a) 2011

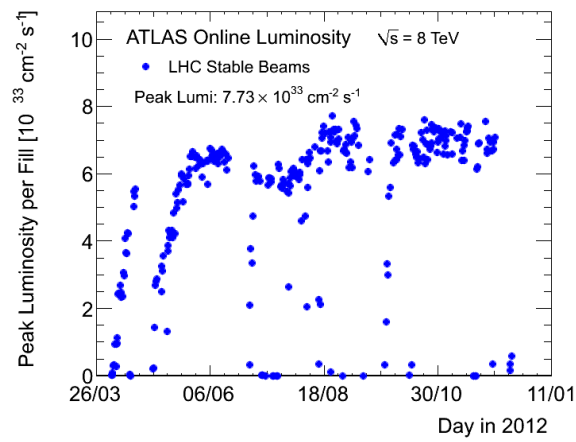


(b) 2012

**Figure 2.2.** Integrated luminosity versus day, for 2011 and 2012 data taking periods. Green histogram is the value delivered by LHC to ATLAS, while the yellow histogram represents the luminosity recorded by ATLAS.



(a) 2011



(b) 2012

**Figure 2.3.** Maximum instantaneous luminosity versus day, for 2011 and 2012 data taking periods.

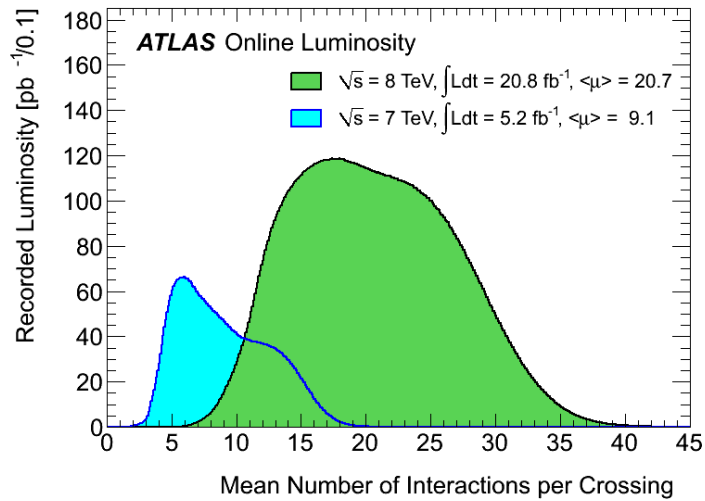


Figure 2.4. Average number of interactions per bunch–crossing[18].

## 2.2 ATLAS, a Particle Physics Experiment

### 2.2.1 Detecting Particles

Various are the reconstruction strategies used by particle physics experiments to identify and reconstruct elementary and composed particles. Fig. 2.5 shows a cross section of the ATLAS detector (described in the next section and in the rest of the chapter), showing the behaviour of different kinds of particles (electrons, photons, muons, neutrinos, neutrons and protons) when interacting with different detectors in a  $pp$  collider.

Electrically charged particles, whether elementary or not, are bent by magnetic fields. Their trajectory is therefore changed, since they obtain an angular momentum which depends on the sign of their charge: positive and negative particles (electrons and positrons, for example) can be discriminated by looking at the curvature of their trajectory. Trajectories, on the other hand, can be reconstructed for example using silicon or straw tubes detectors, identifying the points (*hits*) where there is a signal compatible to a particle interacting with the matter of the detector and fitting them back to a common trajectory. Neutral particles are not bent by magnetic fields, so other detection techniques must be used.

For this reason, a tracking system with excellent spatial resolution is usually placed close to the interaction point where the two beams collide, in order to be able to identify promptly tracks associated to particles produced in the interaction. After reconstructing all tracks in each event, it is also possible to identify the point where the primary interaction has taken place (*primary vertex*) and all other spatial points compatible with a secondary interaction (*secondary vertices*), which can be either associated to the subsequent decay of a short–lived particle into two or more charged particles, or to additional interactions other than the primary one (*pile-up*).

Charged particles also undergo Bremsstrahlung, the magnitude of which varies inversely with the square of their mass: hence, this is an effect that is stronger

for electrons than for other particles. Electrons interact with matter and produce photons, which can in turn produce electron–positron pairs if their energy is above the kinematic threshold  $2m_e$ , thus producing *electromagnetic showers*. Electromagnetic calorimeters are designed to detect electromagnetic showers by ionization of some scintillating material; the quantity of material is designed in such a way to be able to contain (almost) the full cascade, whose length is expressed in terms of radiation lengths  $X_0$ . Electrons and photons behave similarly in the electromagnetic calorimeter, and can be discriminated using the information from the inner tracking system (an electromagnetic cluster associated to a track can be identified as an electron).

Hadrons interact mainly with the strong force, via anelastic nuclear processes: hadronic showers are formed by the cascade production of other hadrons, nuclear deexcitation and decays of pions and muons. Their longitudinal development is characterized by the interaction length  $\lambda$ , which sets the geometrical size scale of hadronic calorimeters. Hadronic showers have also an electromagnetic component: to obtain a linear energy response for hadrons, the ratio between the detection efficiency for electrons and hadrons,  $e/h$ , should be close to 1. Shower shapes can also be investigated to obtain informations on the particle originating them<sup>2</sup>.

The thickness of electromagnetic and hadronic calorimeters, designed in terms of  $X_0$  and  $\lambda$ , is such that only particles weakly interacting with matter survive after passing through them. It is the case of muons, for which dedicated tracking systems are deployed: an external muon spectrometer in magnetic field allows to reconstruct their trajectory and momentum with high precision, which can also profit from the information coming from the inner tracking system (where muons are expected to leave a track since they are electrically charged) and from the calorimetric system (where muons, at least for energies below 100 GeV, have to leave a deposit consistent with their being minimum ionizing particles). Neutrinos, on the other hand, have too low interaction cross–sections with matter for a typical collider experiment: they can be identified assuming the conservation of energy and momentum in the transverse plane (see next section) as non–zero  $p_T(\nu) = -\sum_i p_T$  (*missing transverse momentum*, which is ideally zero when all particles produced in an event are reconstructed).

### 2.2.2 A Toroidal LHC Apparatus

The ATLAS detector (*A Toroidal LHC Apparatus*[19]) is a multi–purpose collider experiment. It is composed by a series of sub–detectors, placed in cilindric symmetry around the beam axis: it consists of a central region, called *barrel*, which is 42 m long and has a radius of about 11 m, closed at the two edges by two *endcaps*, with the purpose of detecting also particles in the forward region. Fig. 2.6 shows a picture of the experiment; from the innermost to the outermost layer, there are:

- a tracking system (*Inner Detector*), for the reconstruction of tracks of electrically charged particles and the reconstruction of primary and secondary interaction vertices;

---

<sup>2</sup>For example, gluons have higher colour charge than quarks, and therefore produce wider hadronic jets.

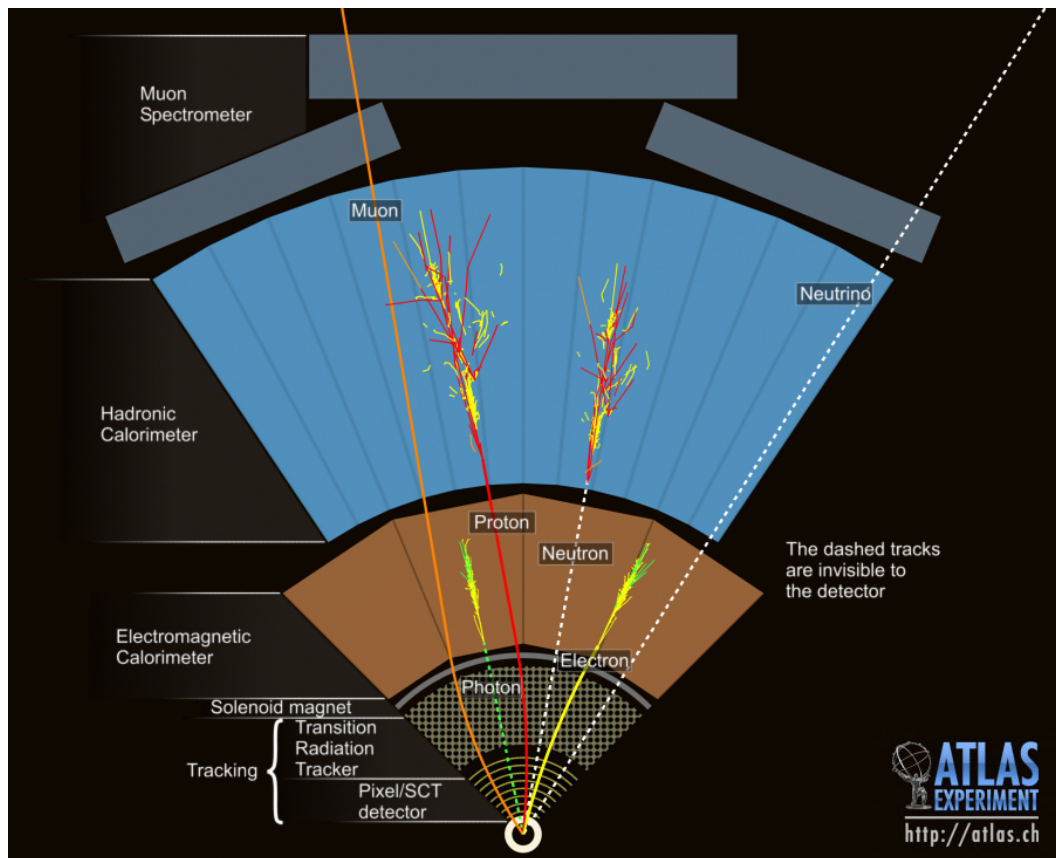
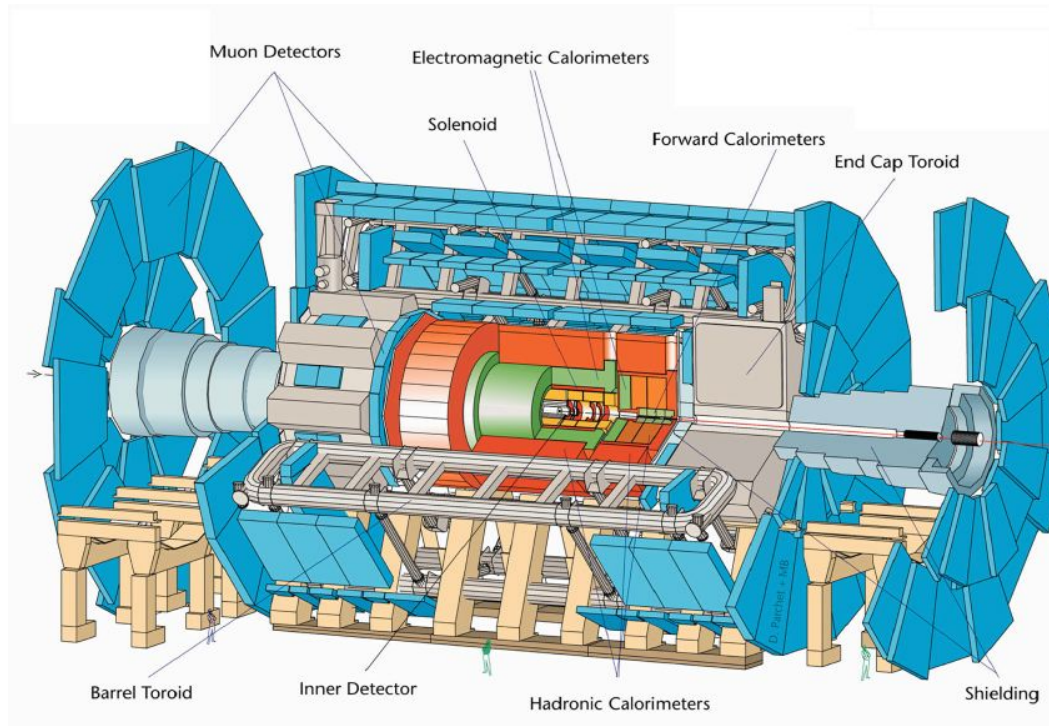


Figure 2.5. Event Cross Section in a computer generated image of the ATLAS detector.



**Figure 2.6.** Scheme of the ATLAS experiment at the LHC.

- a solenoidal magnetic field, the symmetry axis being the beam collision axis;
- an electromagnetic calorimeter (*ECAL*), for the reconstruction of electromagnetic showers induced by electrons and photons;
- an hadronic calorimeter (*HCAL*), for the reconstruction of hadronic showers and the study of jet structures;
- a muon spectrometer, for the high-precision reconstruction of tracks of penetrating electrically charged particles;
- a system of toroidal magnets in air.

ATLAS, as shown in Fig. 2.7, uses a right-handed coordinate system in which the  $x$  axis points towards the center of the LHC ring, the  $z$  axis corresponds to the direction of the beams and the  $y$  axis is vertical. Cylindrical coordinates are often used, defining the azimuthal angle  $\phi \in [\pi, \pi]$ , and the polar angle  $\theta$  which is measured with respect to the  $z > 0$  axis.

For a particle with energy  $E$  and longitudinal ( $z$ ) momentum component  $p_L$ , *rapidity* is defined as

$$y = \frac{1}{2} \ln \left[ \frac{E + p_L}{E - p_L} \right].$$

It can be shown that the rapidity difference  $\Delta y$  is invariant under longitudinal boosts.

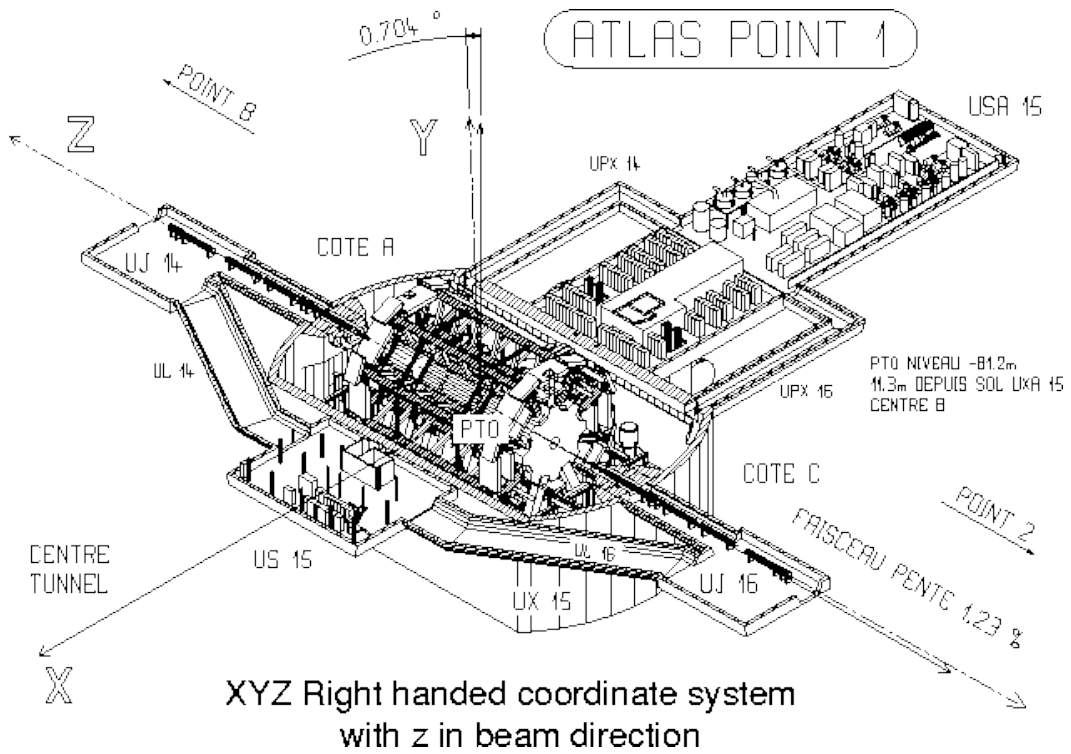


Figure 2.7. ATLAS coordinate system.

In the ultra-relativistic limit one has  $E \approx p_L$ , and the rapidity  $y$  can be approximated by the *pseudorapidity*,

$$\eta = -\ln \left[ \tan \frac{\theta}{2} \right].$$

Fig. 2.8 shows how the pseudorapidity is 0 for  $\theta = 90^\circ$  (barrel region), and grows asymptotically for  $\theta \rightarrow 0$  (endcap region).

The LHC is a hadron collider: this means that the collision itself does not involve elementary particles, but rather composite particles (which contain quarks and gluons). The effective interaction energy in the center-of-mass system depends on the momenta of the partons actually involved in the interaction, and is therefore

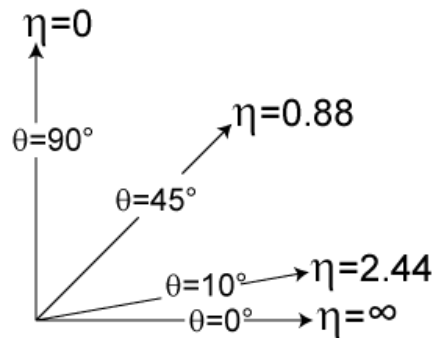
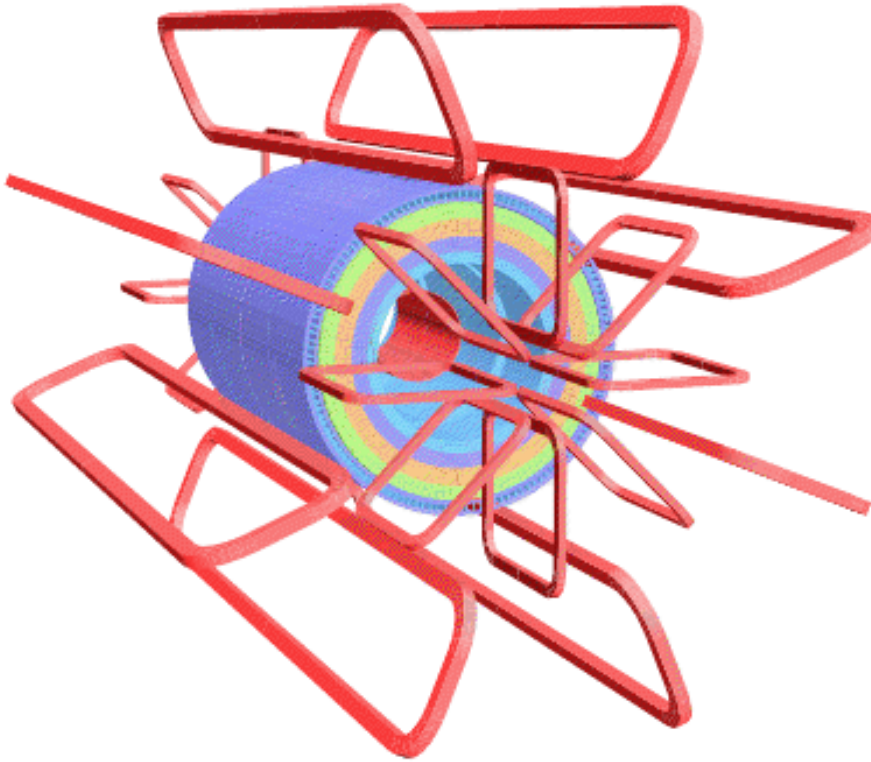


Figure 2.8. Pseudorapidity  $\eta$  for different values of the polar angle  $\theta$ .



**Figure 2.9.** Scheme of the ATLAS superconducting magnet system: solenoid (blue) and toroid (red).

unknown. It is consequently natural to study kinematics in the transverse plane  $xy$ , in which kinematics is closed and energy and momentum conserved if we assume that the longitudinal momentum component of partons is always dominant over their average transverse momentum.

Distance between particles in the  $\eta\phi$  plane is usually expressed as a function of  $\Delta R = \sqrt{\Delta\eta^2 + \Delta\phi^2}$ .

### 2.2.3 The Magnet System

ATLAS superconducting magnet system[22] is shown in Fig. 2.9; it is composed by

- a solenoid, its symmetry axis being the  $z$  axis, placed within the Inner Detector in the barrel region: the trajectories of charged particles are bent by its axial magnetic field of 2 T, allowing the measurement of their momentum;
- a toroid for the barrel and two toroids for the two endcaps: all of them are air-core, in order to minimize multiple scattering, and produce a radial magnetic field used to measure momenta of charged penetrating particles.

The central solenoid is 5.3 m long, with a diameter of 2.4 m, and has been designed in order to reduce the amount of energy lost by particles before reaching

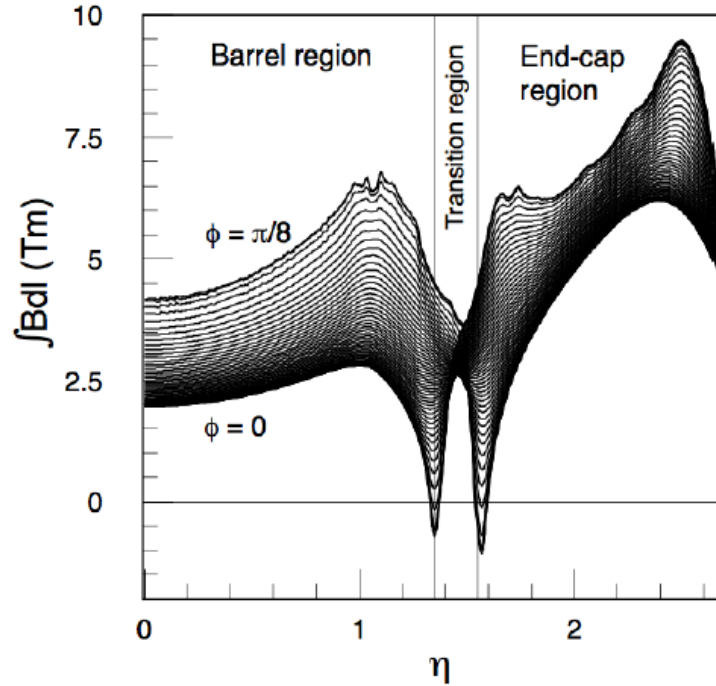


**Figure 2.10.** Behaviour of the bending power  $\int d\ell B$  as a function of pseudorapidity  $\eta$ , for different values of the azimuthal angle  $\phi$ .

the calorimetric system. It produces a magnetic field of 2 T in the central tracking region and a 2.6 T peak field.

The toroidal magnet system consists of eight barrel coils, built on different cryostats, and two endcap cryostats which host eight coils each, rotated by  $22.5^\circ$  with respect to the barrel coils in order to obtain radial superposition and optimize the bending power  $\int d\ell B$  in the superimposing region. The choice of toroidal magnets is motivated by the fact that in this way the magnetic field is confined without need for additional material, thus reducing the effect of multiple scattering on momentum resolution.

The toroidal field has a complex behaviour, shown in Fig. 2.10 in terms of its bending power, which goes from 2 T to 6 T in the barrel and from 4 T to 8 T in the endcaps. In the region  $1.3 < |\eta| < 1.6$  (*transition region*) one can see the effect of the superposition of the barrel and endcap fields, which yields lower values of  $\int d\ell B$  less homogenous in  $\eta$ .

#### 2.2.4 The Inner Detector

The purpose of the Inner Detector (ID)[23] is the reconstruction of tracks of charged particles, the precision measurement of their momenta and the reconstruction of primary and secondary interaction vertex. The momentum  $\mathbf{p}$  of a particle (with charge  $q$  and speed  $\mathbf{v}$ ) in an axial magnet field  $\mathbf{B}$  is bound to the curvature of its

trajectory by the Lorentz force

$$\mathbf{F} = q\mathbf{v} \times \mathbf{B}.$$

The field  $\mathbf{B}$  is longitudinal, hence trajectories are bent in the transverse plane  $xy$ .

In uniform magnetic field, the trajectory of a particle can be represented by an helix. Five are the measured parameters:

$1/p_{\mathbf{T}}$  inverse of the transverse momentum of the particle;

$\phi$  azimuthal angle of the track, defined in terms of momentum components by  
 $\tan \phi \equiv p_y/p_x$ ;

$d_0$  transverse impact parameter, defined as the distance in the  $xy$  plane between the  $z$  axis and the maximum approach point of the helix (MAP) to the  $z$  axis itself; its sign is given by the angular momentum of the track with respect to the  $z$  axis;

$\cot \theta$  cotangent of the polar angle  $\theta$ , defined in terms of momentum components by  
 $\cot \theta \equiv p_z/p_{\mathbf{T}}$ ;

$z_0$  longitudinal impact parameter, defined as the  $z$  coordinate of the MAP.

Momentum resolution can be expressed as a function of the resolution on the single point,  $\epsilon$ , of the number of points used for reconstructing the track,  $N$ , and of the momentum itself  $p$ ; it holds

$$\frac{\Delta p}{p^2} = \frac{8}{0.3Bl^2} \Delta s,$$

where  $B$  is in T,  $l$  is the length of the reconstructed track, in m and [20]

$$\Delta s = \frac{\epsilon}{8} \sqrt{\frac{720}{N+4}}.$$

The Inner Detector has cylindrical symmetry around the beam axis. It extends over  $z = \pm 345$  cm (the barrel region corresponds to  $\pm 80$  cm), with a diameter of 115 cm. Fig. 2.11) shows the three different subdetectors:

- a *Silicon Pixel Detector*, with high precision and granularity, placed close to the interaction point; it contributes significantly to the resolution over the impact parameter  $d_0$  and to the reconstruction of primary and secondary interaction vertices;
- a *Semiconductor Tracker* (SCT), with high granularity, which contributes to the momentum and  $d_0$  measurements and to vertex reconstruction;
- a *Transition Radiation Tracker* (TRT), with lower  $\epsilon$  with respect to the other two subdetectors, but with less quantity of material per reconstructed point.

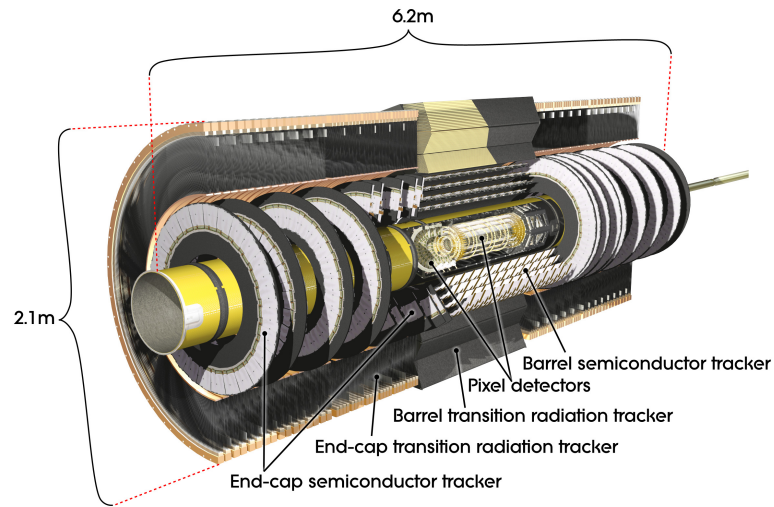
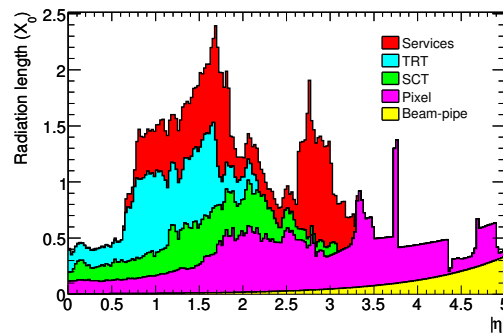
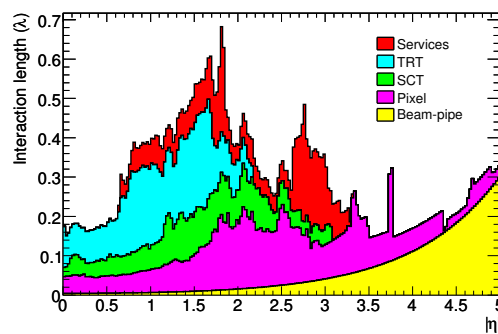


Figure 2.11. Scheme of the ATLAS Inner Detector.



(a) Radiation length  $X_0$ .



(b) Interaction length  $\lambda$ .

Figure 2.12. Radiation and interaction lengths, averaged over  $\phi$ , as a function of the absolute value of the pseudorapidity  $|\eta|$ . Different contributions from external services and subdetector systems are shown.

Contributions to the radiation and interaction lengths,  $X_0$  and  $\lambda$ , as a function of pseudorapidity, are shown in Fig. 2.12.

The Silicon Pixel Detector is the closest to the collision axis and consists of three cylindrical layers placed at 4 (barrel layer, or *B-layer*, covering  $|\eta| < 2.5$ ), 10 and 13 cm (covering  $|\eta| \leq 1.7$ ) from the interaction point, plus five endcap disks with radii between 11 and 20 cm (covering  $1.7 < |\eta| < 2.5$ ). Resolution on the single point for the three cylindrical layers is  $12\ \mu\text{m}$  in the  $r\phi$  plane and  $66\ \mu\text{m}$  in  $z$ , while the five disks have a resolution on  $r$  of  $77\ \mu\text{m}$ [21]. On average, a track crosses three pixel layers.

The Semiconductor Tracker consists of eight silicon micro-strip detectors, with a single point resolution of  $16\ \mu\text{m}$  in the  $r\phi$  plane and of  $580\ \mu\text{m}$  on  $z$ . It allows to discriminate tracks originating from different particles, if they have a spatial separation of more than  $200\ \mu\text{m}$ . On average, the SCT provides eight precision position measurements for a track crossing it in the barrel region.

The Transition Radiation Tracker consists of straw tubes, with a 4 mm diameter each, and can provide on average 30 and up to 36 hits per track in the region  $|\eta| < 2.0$ . Single point resolution is of the order of  $170\ \mu\text{m}$ : this is compensated by the fact that the outermost TRT hits contribute more to the momentum measurement of the particle, due to the higher lever arm. Transition radiation foils and fibers allow also to discriminate between pions and electrons.

Overall, the combined momentum measurement of the inner detector system has a resolution of

$$\frac{\sigma_{p_T}}{p_T} = 0.05\% \cdot p_T \oplus 1\%,$$

where  $\oplus$  indicates that the two contributions are summed in quadrature.

### 2.2.5 Calorimeters

ATLAS calorimetric system[24] (shown in Fig. 2.13) consists of an electromagnetic calorimeter (ECAL) for the identification of electromagnetic showers induced by electrons and photons, and of an hadronic calorimeter (HCAL) for the reconstruction of hadronic jets.

#### Electromagnetic Calorimeter

The electromagnetic calorimeter is a lead-liquid argon (LAr) sampling calorimeter, with accordion geometry (shown in Fig. 2.14) which provides complete coverage and symmetry in  $\phi$ . Thickness of active material layers is of about 2.1 mm, while the thickness of the lead absorbers varies with  $\eta$  in order to optimize energy resolution. ECAL covers the pseudorapidity region  $|\eta| < 3.2$ : the barrel calorimeter covers  $|\eta| < 1.475$ , while the endcap calorimeter covers the rest of the  $|\eta|$  range. A presampler detector is present for  $|\eta| < 1.8$ , to estimate particle energy loss before the calorimeter itself.

The barrel region has cylindrical symmetry around the beam axis, and is composed by three sampling calorimeters formed by tiles of plastic scintillators alternated with layers of absorbing material (iron):

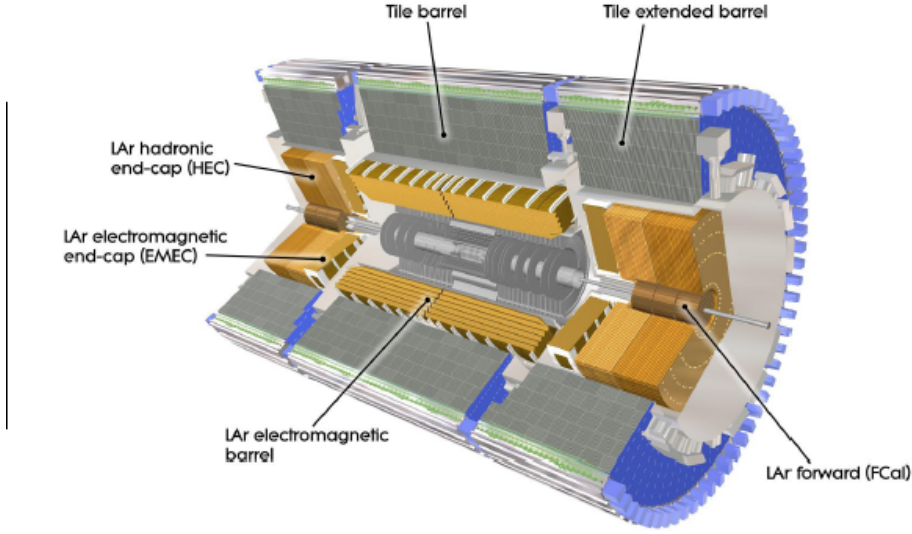


**Figure 2.13.** Scheme of the ATLAS calorimetric system.

- the first sampling is  $4.3X_0$  thick and consists of small strips with  $\Delta\eta = 0.0031$ ; its purpose is to separate electrons and positrons from charged pions and photons from  $\pi^0$ ;
- the second sampling is  $16X_0$  thick, and is segmented in square towers of size  $\Delta\eta \times \Delta\phi = 0.025 \times 0.025$ ;
- the third sampling is designated for high energy electrons and photons ( $E > 50 \text{ GeV}$ ): since they can produce larger clusters, the  $\eta$  size is doubled without loss in resolution.

The endcap region uses copper and LAr, with parallel plates; for  $|\eta| > 3.1$  a forward LAr calorimeter is present.

The total thickness of ECAL is of more than  $24X_0$  in the barrel and  $26X_0$  in the endcaps. Energy resolution is given by

$$\frac{\Delta E}{E} = \frac{10\%}{\sqrt{E[\text{GeV}]}} \oplus 0.3\%,$$

while the pseudorapidity resolution is

$$\Delta\eta = \frac{40 \text{ mrad}}{\sqrt{E[\text{GeV}]}}.$$

### Hadronic Calorimeter

The hadronic calorimeter covers the pseudorapidity region  $|\eta| < 4.9$ . It has been built with the purpose of containing hadronic showers reducing the effect of *punch-through* (particles, other than muons, which manage to pass through calorimeters and reach

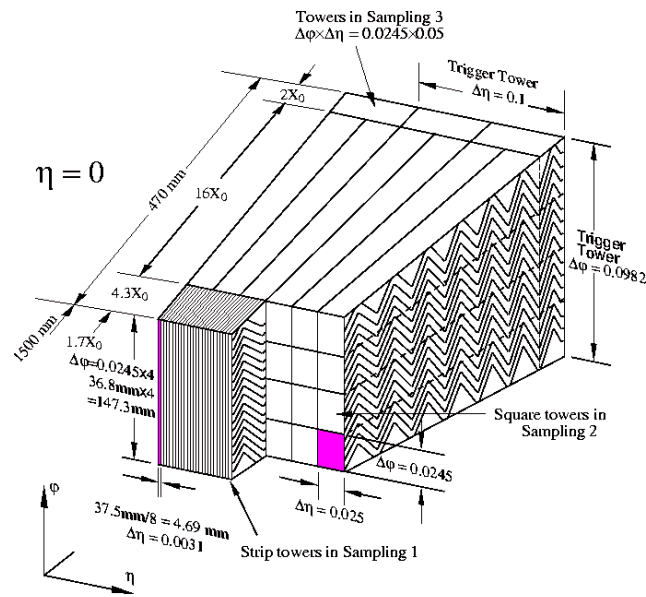


**Figure 2.14.** Accordion structure of the LAr and Pb layers of ATLAS electromagnetic calorimeter.

the muon spectrometer). Its thickness at  $\eta = 0$  in terms of interaction lengths is  $11\lambda$ .

The barrel region ( $|\eta| < 1.0$ ) and the extended barrel region ( $0.8 < |\eta| < 1.7$ ) consist of a tile detector. It is a sampling calorimeter, composed by iron plates (absorber) and scintillating tiles (active material). Granularity is  $\Delta\eta \times \Delta\phi = 0.1 \times 0.1$ ; the ratio  $e/h$  between the calorimeter response for an electron and for a hadron is close to 1.3.

In the endcap region ( $1.5 < |\eta| < 3.2$ ), where radiation hardness is crucial, the calorimeter uses liquid argon as active material and copper plates as absorber. Granularity is  $\Delta\eta \times \Delta\phi = 0.1 \times 0.1$  for  $1.5 < |\eta| < 2.5$  and  $\Delta\eta \times \Delta\phi = 0.2 \times 0.2$  for  $2.5 < |\eta| < 3.2$ .

A third subdetector system is the forward calorimeter, which covers  $3.1 < |\eta| < 4.9$  and has a granularity of  $\Delta\eta \times \Delta\phi = 0.2 \times 0.2$ . It is composed by three regions: the one closest to the interaction point has LAr as active material and copper as absorber, while the other two use tungsten instead of copper to cope with the more demanding radiation hardness requirements in the high pseudorapidity region.

The overall energy resolution of the barrel/endcap system is

$$\frac{\Delta E}{E} = \frac{50\%}{\sqrt{E[\text{GeV}]}} \oplus 3\%,$$

while for the forward calorimeter it is

$$\frac{\Delta E}{E} = \frac{100\%}{\sqrt{E[\text{GeV}]}} \oplus 10\%.$$

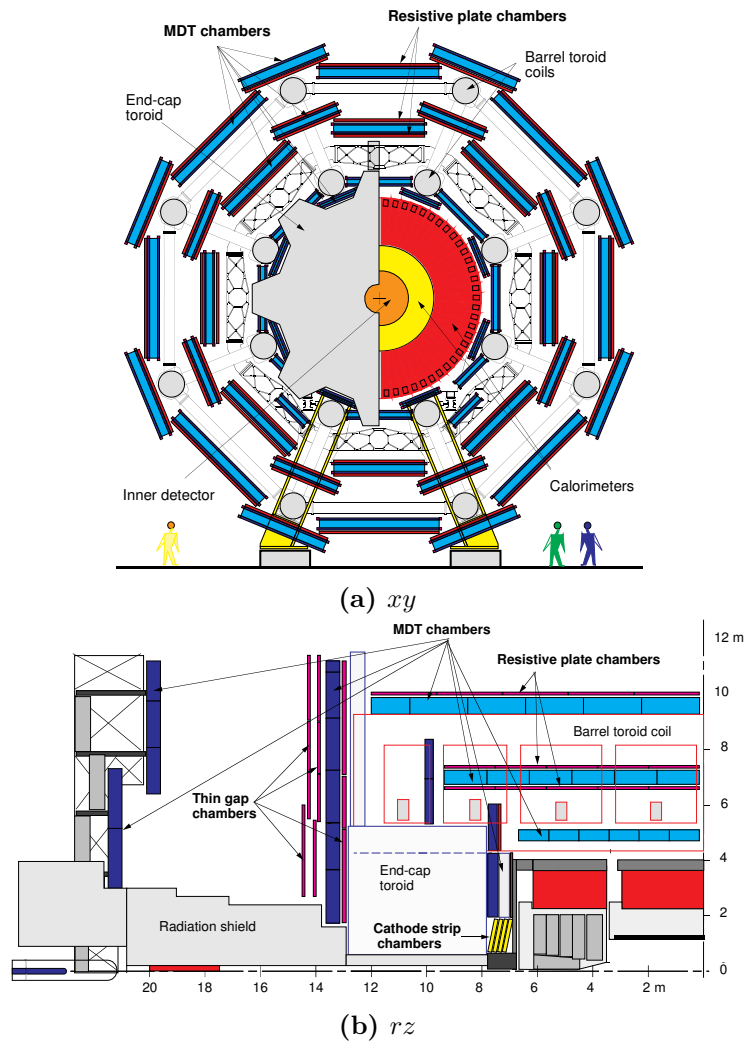


**Figure 2.15.** Cross section of the ATLAS muon spectrometer, in the  $xy$  and  $rz$  planes.

### 2.2.6 The Muon Spectrometer

The aim of the muon spectrometer[25] (shown in Fig. 2.15), is to provide a precision measurement of the momentum of those particles which manage to survive after passing through the calorimetric system. It exploits the high intensity of the toroidal magnetic field and the high lever arm of the momentum measurement for particles originating in the interaction point. The magnetic field is almost orthogonal to particle trajectories: momentum measurement happens in the  $rz$  plane.

The barrel region of the muon spectrometer ( $|\eta| < 1.05$ ) is composed by three cylindrical layers around the beam axis, called *stations*, placed at  $r = 5, 7.5$  and  $10$  m. The endcap region and the transition region between barrel and endcaps are composed by four vertical disks, concentric to the beam axis, placed at  $|z| = 7.4, 10.8, 14$  and  $21.5$  m.

Tracks are measured using three layers of Monitored Drift Tubes (MDTs), in the region  $|\eta| < 2$ , and by a layer of Cathode Strip Chambers (CSCs) and three

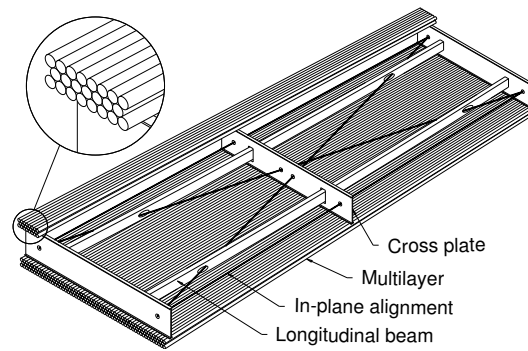


Figure 2.16. Scheme of MDT chambers.

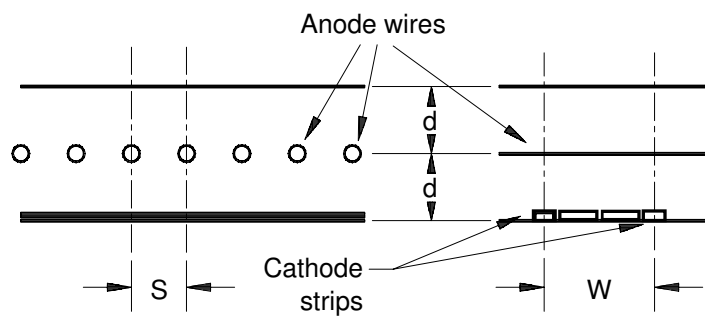


Figure 2.17. Scheme of CSC chambers.

layers of MDTs for  $2 < |\eta| < 2.7$ . Chambers are placed in such a way that every track originating in the interaction point crosses three stations. Precision momentum measurement happens in the principal bending direction of the magnetic field.

MDTs (shown in Fig. 2.16) are aluminium drift tubes with a diameter of 30 mm, filled with a mixture of argon and carbon dioxide at a pressure of 3 bar, for a total volume of  $800 \text{ m}^3$ . In the middle of each of these tubes, a tungsten–rhenium wire with a diameter of  $50 \mu\text{m}$  is used as an anode, placed at 3080 V to create avalanches from the ionization electrons. Spatial resolution for each tube is about  $80 \mu\text{m}$ .

In the high pseudorapidity region ( $|\eta| > 2$ ), the rate of forward interactions is higher than  $1150 \text{ Hz/cm}^2$ . The first layer of MDTs is therefore replaced by CSCs, which have lower neutron sensitivity. CSCs (shown in Fig. 2.17) are multiwire proportional chambers filled with an argon–carbon dioxide mixture, with cathode strip readout. Anode wires are kept at 1800 V: once an avalanche is formed by a ionizing particle, a charge is induced on the cathode, which consists of strips orthogonal to the anode wires. The precision coordinate is obtained measuring this charge; the transverse coordinate is instead obtained using orthogonal strips, parallel to the anode wires, which form the second cathode of the chamber. Spatial resolution for the precision coordinate is of the order of  $60 \mu\text{m}$ .

A system of trigger detectors is present for  $|\eta| < 2.4$ : it consists of Resistive Plate Chambers (RPCs) in the barrel, located on both sides of the middle MDT station and either directly above or below the outer MDT station, and Thin Gap Chambers

(TGCs) in the endcap region, located near the middle MDT station. They also provide a second-coordinate measurement of track parameters in the non-bending projections, in a direction approximately parallel to the magnetic field lines.

RPCs are gas detectors formed by two resistive Bakelite plates. The gap between the plates, which is 2 mm wide, is filled by a mixture of gases (97%  $C_2H_2F_4$ , 3%  $C_4H_1O$ ) under an electric field of typically 4.5 kV/mm. Ionization electrons are multiplied into avalanches, and the signal is read out using metal strips on both sides of the detector, along directions both parallel ( $\eta$ ) and orthogonal ( $\phi$ ) to the MDT wires. RPCs provide a typical space-time resolution of  $1\text{ cm} \times 1\text{ ns}$ .

TGCs are multi-wire proportional chambers where the anode wire pitch is larger than the distance between the cathode and the anode. They use a gas mixture of 55%  $CO_2$  and 45%  $n$ -pentane ( $n - C_5H_{12}$ ), and operate in saturated mode. Anodes are parallel to the MDT wires, and together with readout strips orthogonal to the wires they provide the trigger information. Second coordinate measurement is obtained using the readout strips. Typical time resolution is 5 ns.

Momentum resolution  $\sigma(p_T)/p_T$  of the ATLAS muon spectrometer system is of about  $2 \div 3\%$  over most of the kinematic range, while it reaches 10% for momenta of the order of 1 TeV.

### 2.2.7 Taking Data: the Trigger System

At the design value of LHC instantaneous luminosity,  $1 \times 10^{34}\text{ cm}^{-2}\text{ s}^{-1}$ , the average number of interactions per bunch crossing is of about 40 MHz, corresponding to an interaction rate of the order of 1 GHz. ATLAS records an amount of data per event which is at the level of 1.5 Mbyte: this, given the current maximum data transfer rate on disk, means that the maximum rate of events which can be saved on disk is of about 200 Hz. Real-time (*online*) hardware and software systems (*trigger systems*) are therefore necessary to reduce the output event rate by a factor  $10^6$ , keeping at the same time an high efficiency over interesting events.

The ATLAS trigger system[26] is organised in three different levels of event selection, first level (LVL1), second level (LVL2) and *event filter* (EF), as shown in Fig. 2.18. The amount of detector data needed to take a decision, or equivalently the number of detector channels involved, increases from LVL1 (which is entirely hardware) to LVL2 and EF (which are software-based), in such a way to be able to apply more and more stringent selection criteria and to reduce dead time.

Since the LVL1 trigger has about  $2\text{ }\mu\text{s}$  to take a decision, only fast detector systems are used: calorimeters for electrons, jets,  $\tau$ -leptons and missing transverse energy, muon trigger chambers for muons. As for calorimeters[27], reduced granularity signals which cover  $\Delta\eta \times \Delta\phi \approx 0.1 \times 0.1$  (*trigger towers*) are used to build clusters and compute their transverse energy  $E_T$ , summing up signals from ECAL and HCAL cells, with a precision of about 1 GeV. As for the muon system[28], only RPCs and TGCs are used: muon  $p_T$  thresholds, as shown in Fig. 2.20, are applied looking for hits within defined *coincidence windows* around the extrapolation to the interaction point of the first hit. LVL1 can reduce in this way the event rate to about 75 kHz.

The LVL2 trigger uses information from all the detector systems, restricted around a *region of interest* (RoI) identified by LVL1. The available processing time, of the order of 10 ms, allows a first reconstruction of physics objects using various

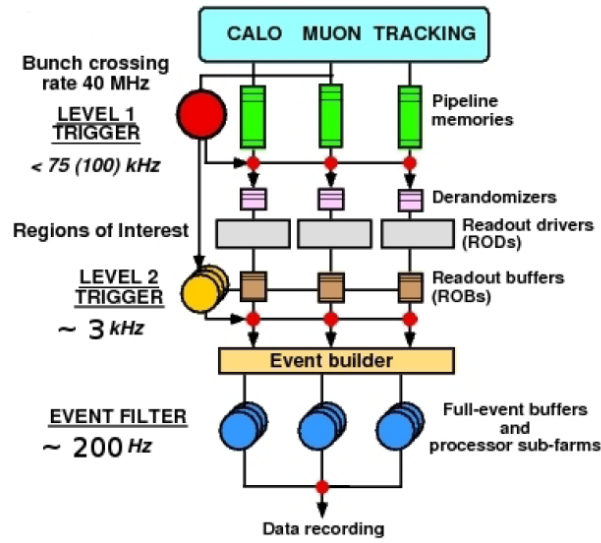


Figure 2.18. Flow chart of the ATLAS trigger system.

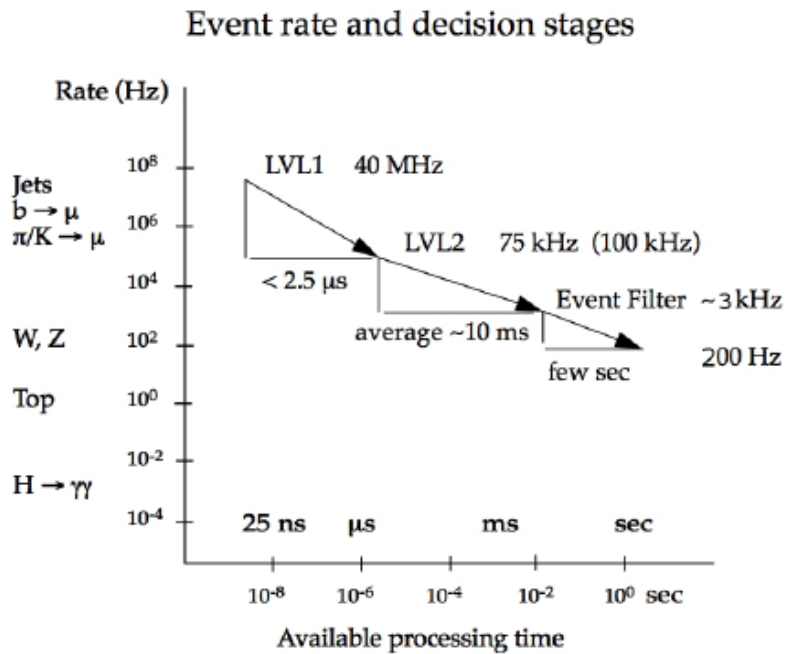
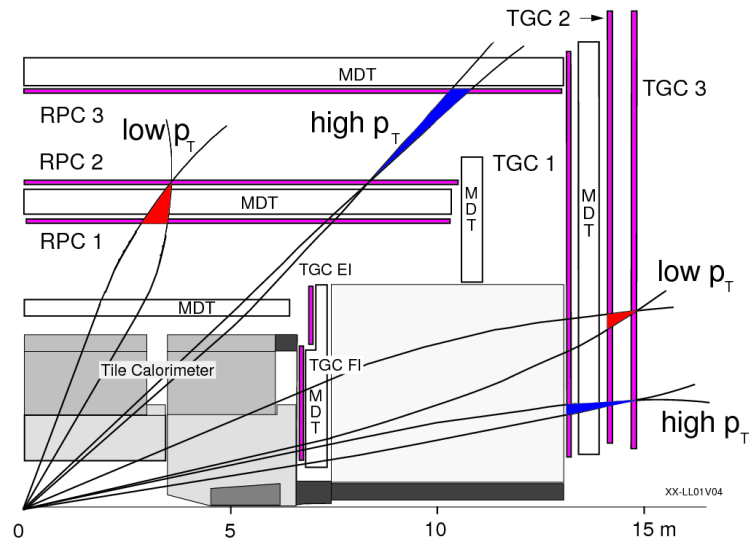


Figure 2.19. Event rate at different trigger levels.



**Figure 2.20.** Quarter section of the muon system in the  $rz$  plane: coincidence windows (red and blue) are shown for low and high- $p_T$  muons.

detector systems and fast, optimized software algorithms. For example, muons are identified matching a track reconstructed in the muon spectrometer to a track reconstructed in the inner detector; information from ID and calorimeters is also used to require muons to be produced isolated. The output event rate of LVL2 is of about 1 kHz.

At event filter, decisions are taken using the full granularity available from each subdetector. Optimized algorithms similar to the offline reconstruction and identification algorithms can be used, as the processing time available is of about 1 s.

## Chapter 3

# Lepton Reconstruction

Charged leptons give, at a hadron collider, the cleanest and clearest detector signatures. Excellent electron and muon reconstruction performance is crucial for the  $H \rightarrow ZZ^{(*)} \rightarrow 4\ell$  search, both in terms of Higgs mass resolution and of acceptance in the low  $m_H$  region. This can be achieved with the contribution of all ATLAS detector systems, which have been designed to provide high efficiency and resolution in a wide momentum range, from some GeV to the TeV scale. In this chapter, reconstruction techniques for electrons and muons are reviewed.

### 3.1 Tracking Charged Particles

The track reconstruction strategies in the inner detector are different for primary and secondary particles[29]. A particle is considered as primary if it has a mean lifetime longer than  $3 \times 10^{-11}$  s and has been produced either at the interaction point or by the decay of a particle with a lifetime shorter than the same value. In this case, track reconstruction happens with an inside-out algorithm, which starts the iterative track building procedure from the innermost subdetector layers. On the other hand, an outside-in strategy is designed for the reconstruction of secondary particles. Inside-out and outside-in sequences are consecutive.

#### 3.1.1 Inside-out Algorithm

For primary particles, reconstruction starts from seeds composed by at least 3 hits in the silicon detectors (B-layer, SCT). Each track seed identifies a set of detector elements, the *road*, in which further hits to be associated to the same track candidate are searched. A combinatorial Kalman filter algorithm, which takes into account energy loss and multiple scattering in the detector material, is used to predict the position of the track in each point of the detector, thus including successive hits into the track candidate.

Track candidates are then refitted, minimizing a  $\chi^2$  which takes into account the distance of each hit from the most likely trajectory. Since many track candidates either share hits or are incomplete, an ambiguity solving procedure is applied, which scores morphologic parameters of each track. A track for which a B-layer hit is

expected by extrapolation but not found (*hole*<sup>1</sup>) will for example receive a penalty score. Hits shared between different tracks are assigned to the track with highest score and removed from the fit of the other, with an iterative procedure after which track candidates beyond a certain quality cut are rejected.

Tracks are then extended to the TRT. First, an extended track is formed simply adding hits compatible with the extension of the silicon track candidate to the TRT. Tracks are then refitted using the combined information from silicon detectors and TRT, and a track scoring procedure is applied. At this stage, either silicon or TRT hits which lower the fit quality can be flagged as *outliers* and discarded from the track fit.

The inside-out reconstruction applies a track transverse momentum cut  $p_T > 400$  MeV. Reconstruction efficiency, defined as the fraction of primary particles with  $p_T > 400$  MeV and  $|\eta| < 2.5$  which are matched to a reconstructed track<sup>2</sup>, is shown in Fig. 3.1. Reconstruction efficiency is stable within 1% against increasing pile-up conditions, with values above 90% for transverse momenta above 10 GeV.

### 3.1.2 Outside-in Algorithm

Secondary particles coming from secondary decay vertices or from photon conversions can produce tracks which do not have enough silicon hits to be selected by the inside-out algorithm. Electrons with high energy loss might as well result in a failed attempt by the inside-out algorithm to find a TRT extension of the silicon track candidate. A dedicated outside-in procedure (*back-tracking*) is therefore applied after the reconstruction of primary tracks has taken place: track segments reconstructed in the TRT are extended inwards by adding silicon hits, to form track candidates in a way analogous to the inside-out algorithm. Reconstruction efficiency is shown in Fig. 3.2.

### 3.1.3 Primary Vertices

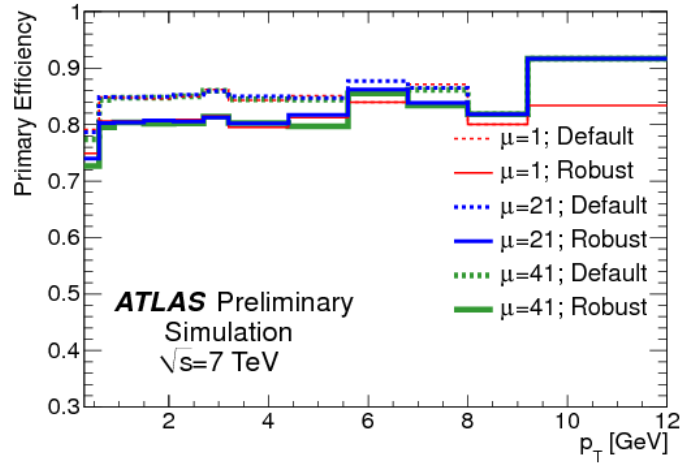
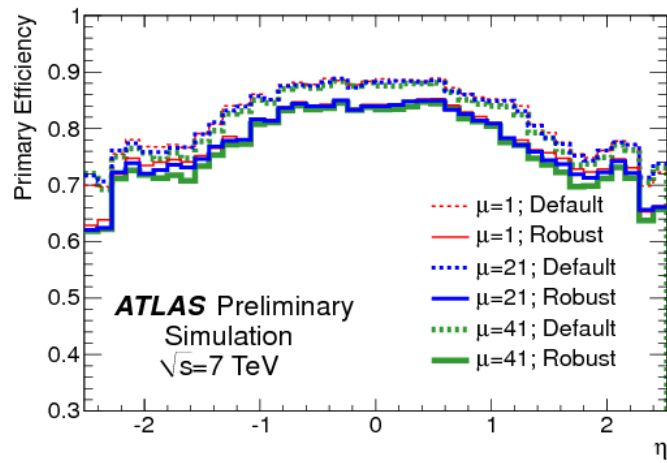
Reconstructed tracks are used to reconstruct primary vertices, by means of an iterative vertex finding algorithm[30]. First, the maximum of the distribution of the  $z$  position of closest approach point of reconstructed tracks to the beam interaction point is used to obtain vertex seeds. An iterative procedure progressively downgrades the contribution from tracks close to the vertex seed to the global vertex fit  $\chi^2$ ; tracks incompatible with the vertex by more than  $7\sigma$ <sup>3</sup> are used to seed a new vertex. The procedure stops when all tracks are associated to a vertex candidate, or when no additional vertex can be found. The position of the beam spot, i.e. of the point at which proton beams collide, is used as a three-dimensional constraint in the procedure.

Resolution on vertex position is of about  $30\ \mu\text{m}$  in the  $xy$  plane and  $50\ \mu\text{m}$  in the  $z$  direction. A single primary vertex is usually selected choosing, among primary

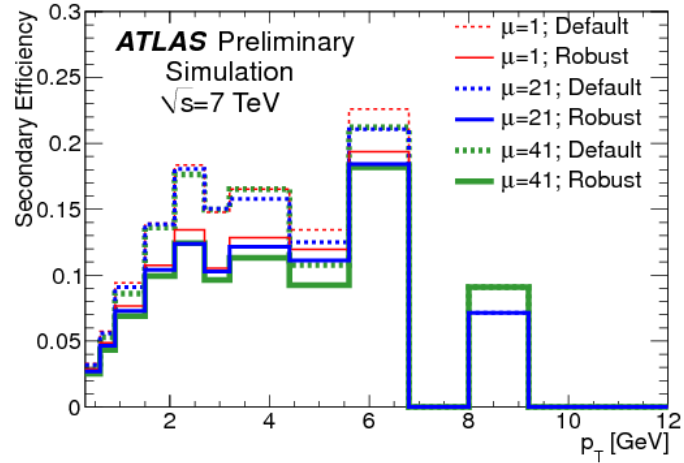
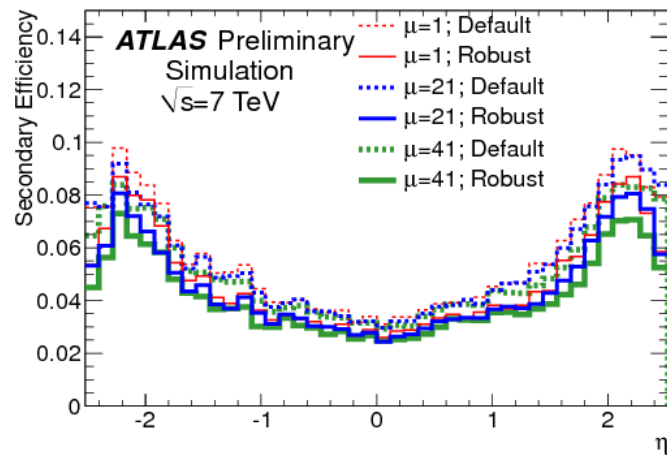
<sup>1</sup>Inactive detector modules are excluded from the definition of holes.

<sup>2</sup>Particle-track matching is based on the fraction of hits of the track which are actually produced by the simulated primary particle.

<sup>3</sup>Compatibility is in terms of a  $\chi^2$  with 2 degrees of freedom.

(a)  $p_T$ (b)  $\eta$ 

**Figure 3.1.** Track reconstruction efficiency for primary particles by the standard inside-out algorithm (dashed lines), as a function of  $p_T$  and  $\eta$ . Distributions are shown for different average number of interactions per bunch crossing ( $\mu = 1$  or  $|\mu| = 21, 41$ ).

(a)  $p_T$ (b)  $\eta$ 

**Figure 3.2.** Track reconstruction efficiency for secondary particles by the standard outside-in algorithm (dashed lines), as a function of  $p_T$  and  $\eta$ . Distributions are shown for different average number of interactions per bunch crossing ( $\mu = 1$  or  $|\mu| = 21, 41$ ).

vertex candidates, the one which maximizes the scalar sum of the square of the transverse momenta of the associated tracks,  $\sum p_{\text{T}}^2$ .

## 3.2 Muons

Muon reconstruction strategies[31] exploit the fact that muons, in principle, leave a signal in all detector systems. Muons are charged, minimum ionizing and penetrating particles, which means one can expect a inner detector track to be reconstructed, associated with low calorimetric deposit and a track in the muon spectrometer. Different reconstruction techniques take into account the different acceptance of the subdetector systems in terms of geometrical coverage  $(\eta, \phi)$  and transverse momentum.

ATLAS muon reconstruction and identification techniques are influenced by considerations on muon acceptance:

- the acceptance of the ID is  $|\eta| < 2.5$ : inner tracker information is therefore not available in the forward region of the detector;
- the overall quantity of material of the ID, ECAL and HCAL systems is such that muons are expected to lose 3 GeV before being able to reach the muon spectrometer;
- uninstrumented regions are present in the MS for  $|\eta| < 0.1$ , due to the presence of detector services, and for  $1.1 < \eta < 1.3$ .

The muon spectrometer has been designed to be able to provide an high resolution standalone reconstruction of muon tracks, *standalone muons*. A combination of measurements from the inner detector and the muon spectrometer allows of course to obtain better momentum resolution than using the ID or MS measurements alone, and leads to the definition of *combined muons*. When an accurate MS measurement is not available, the association of an ID track to a track segment in the muon system (*segment-tagged muons*) or to an energy deposit in the calorimeter consistent with a minimum ionizing particle (*calorimeter-tagged muons*) helps to recover reconstruction efficiency.

### 3.2.1 Muon Spectrometer

Stand-alone reconstruction[32] starts from a *Region of Activity* (ROA), with size  $\Delta\eta \times \Delta\phi \approx 0.4 \times 0.4$ , identified by the trigger chambers. ROAs are cones pointing to the interaction point and centered where there exists at least one RPC or TGC hit in both coordinates. Chambers crossing the ROA are used for the muon reconstruction.

Straight line track segments are reconstructed in two steps. First, a *strict search* is performed both in the transverse plane, using stations where the second coordinate chambers are available<sup>4</sup>, and using 3D input from the CSCs. Efficiency in regions where trigger chambers are not available is recovered using, on a second pass of the segment finding algorithm, MDT-based ROAs defined by accumulation of hits in  $\eta$

<sup>4</sup>Outer and middle stations in the barrel, middle MDT stations in the endcaps.

in the MDT stations. An independent *loose search* then follows, without requiring a matching with a second coordinate hit<sup>5</sup>.

After a first estimate of the transverse momentum using their position and direction, strict segments are extrapolated to the first station found using tracking in magnetic field, performing several trials for different  $p_T$  hypotheses around the initial rough estimate (*momentum scan*). The best matching loose segment, if present, is used to build a track candidate with a full track fitting procedure. A second momentum scan after the fit is performed, in order to include also segments coming from other stations: if the track is associated to at least two segments, another global fit takes place.

A more accurate estimate of the parameters of the track is obtained refitting it again, this time using full raw detector information instead of track segments and taking into account holes and outlier hits. Detector material is finally included in the last  $\chi^2$  fit, in which chambers and dead material around the track are discretized into a finite number of scattering centers<sup>6</sup>.

Each muon track is represented by a five-dimensional vector, corresponding to the helix parameters, and a  $5 \times 5$  covariance matrix, which is obtained varying helix parameters (taking into account correlations) in such a way to obtain a  $\Delta\chi^2$  of unity. Extrapolation of MS tracks to the interaction point is then performed: energy loss and multiple scattering in the calorimeters are taken into account and propagated to track parameters and covariance matrix.

### 3.2.2 Combining Inner Detector and Muon Spectrometer Measurements

#### Combined Muons

The inner detector and muon spectrometer measurements can be combined, using a statistical procedure which takes into account the covariance matrices of the two tracks, and hence the different uncertainty over the measurement of track parameters. If we denote as  $\mathbf{v} = (d_0, z_0, p_T, \eta, \phi)^T$  the vector of helix parameters, as  $C$  the associated covariance matrix and if we use *MS* and *ID* to label muon spectrometer and inner detector measurements, for a given MS track the ID track which minimizes<sup>7</sup>

$$\chi^2 = (\mathbf{v}_{\text{MS}} - \mathbf{v}_{\text{ID}})^T (C_{\text{ID}} + C_{\text{MS}})^{-1} (\mathbf{v}_{\text{MS}} - \mathbf{v}_{\text{ID}})$$

is used for the combination.

<sup>5</sup>When no trigger hit in  $\phi$  is available, the second coordinate is determined trying five different positions along the tube. Hit pairs are required to point loosely to the interaction point, in order to suppress background and combinatorial tracks.

<sup>6</sup>Energy loss is taken into account, while scattering angles are constrained fit parameters of the overall  $\chi^2$  minimization.

<sup>7</sup>This is a consequence of the fact that the  $\chi^2$  of a generic track fit can be expanded around its minimum  $\chi^2(\mathbf{v}_0) = \chi_0^2$  as

$$\chi^2(\mathbf{v}) = \chi_0^2 + (\mathbf{v} - \mathbf{v}_0)^T C^{-1} (\mathbf{v} - \mathbf{v}_0). \quad (3.1)$$

Writing the  $\chi^2$  of the combined measurement in the form of Eq. (3.1) and in terms of the analogous expansions for ID and MS measurements, one gets the final relations presented in this section.

The combined helix parameters can then be expressed as

$$\mathbf{v} = (C_{ID}^{-1} + C_{MS}^{-1})(C_{ID}^{-1}\mathbf{v}_{ID} + C_{MS}^{-1}\mathbf{v}_{MS}),$$

while the associated covariance matrix is

$$C = (C_{ID}^{-1} + C_{MS}^{-1})^{-1}.$$

### Segment-tagged Muons

Segment-tagged muons are composed by a inner detector track, with sufficient momentum, which is geometrically compatible with at least a track segment in the MDTs or CSCs. ID tracks and MS track segments are used only if they have not been used by the previous algorithm to build any combined muon. Matching between the ID track and the MS segment(s) is done in terms of a compatibility  $\chi^2$  between the extrapolation of the ID track and the reconstructed MS segments. Helix parameters of segment-tagged muons are those of the associated ID track.

### 3.2.3 Combining Calorimeter and Muon Spectrometer Measurements

Calo-tagged muons are composed by a inner detector track associated to an energy deposit in the calorimeters compatible with the expectation for a minimum ionizing particle. In this way, despite the resulting low muon purity, it is possible to recover reconstruction efficiency in those detector regions where MS instrumentation is not available. Identification criteria for calo-tagged muons are optimized for  $|\eta| < 0.1$  and  $25 \lesssim p_T \lesssim 100$  GeV.

### 3.2.4 Performance

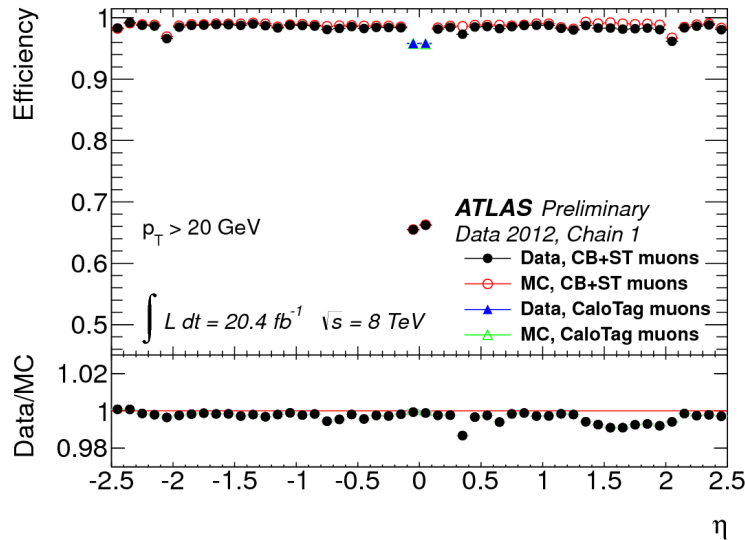
#### Reconstruction Efficiency

Fig. 3.3 shows the muon reconstruction efficiency[31], measured with a sample of muons with  $p_T > 20$  GeV coming from  $Z$  decays, as a function of  $\eta$ . Reconstruction efficiency is almost uniform in the whole pseudorapidity range, with a value of about 98%. The efficiency recovery due to the use of calo-tagged muons for  $\eta \approx 0$  is also visible. Reconstruction efficiencies are expected to be almost independent on the muon transverse momentum, as it is shown in Fig. 3.4.

Comparison with Monte-Carlo (MC) simulation is also shown on the lower panel of each efficiency plot, in terms of the efficiency scale factor

$$SF = \frac{\epsilon(\text{data})}{\epsilon(\text{MC})},$$

which is used in physics analyses as a weight correction of simulated events to match observed data distributions. Uncertainties on muon reconstruction scale factors arise mainly from the estimation of backgrounds to the pure muon sample selected for efficiency studies (0.2%) and to extrapolation of  $Z \rightarrow \mu\mu$  data either to the low  $p_T$  region<sup>8</sup> or in the very high  $p_T$  region<sup>9</sup>.



**Figure 3.3.** Muon reconstruction efficiency as a function of  $\eta$  for muons with  $p_T > 20$  GeV, for different muon reconstruction types. Calo-tagged muons are used only in the region  $|\eta| < 0.1$ . Ratio between data and MC efficiencies is also shown; the deviation from unity for  $1.5 \lesssim \eta \lesssim 2.2$  is due to mismodeling of pixel subdetectors in MC simulation.

Fig. 3.5 shows the muon reconstruction efficiency for combined and segment-tagged muons as a function of the average number of interactions per bunch crossing. Efficiency, which on average is above 97%, is almost stable against event pile-up.

### Momentum Scale and Resolution

Monte Carlo simulation is corrected for residual mismodeling of detector material, geometric alignment of subdetector systems and intrinsic detector resolution, by comparison with data. A parametrization of momentum correction is used, analogous to the one for momentum resolution,

$$\frac{\sigma(p_T)}{p_T} = a \oplus b \cdot p_T,$$

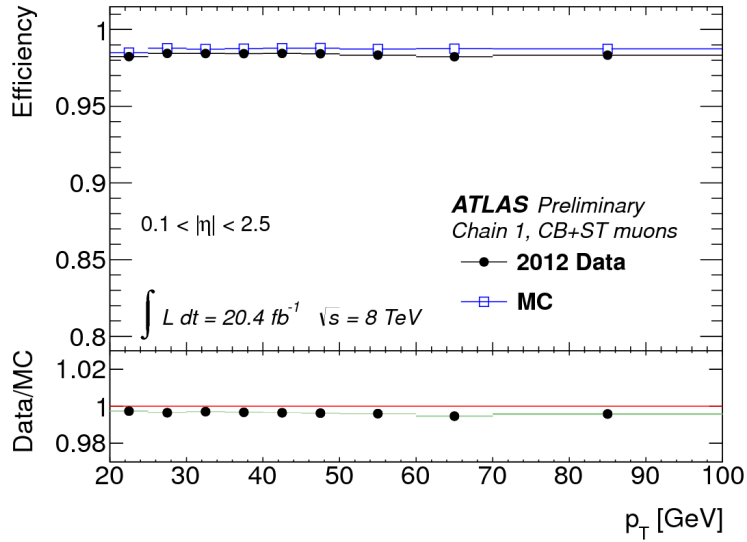
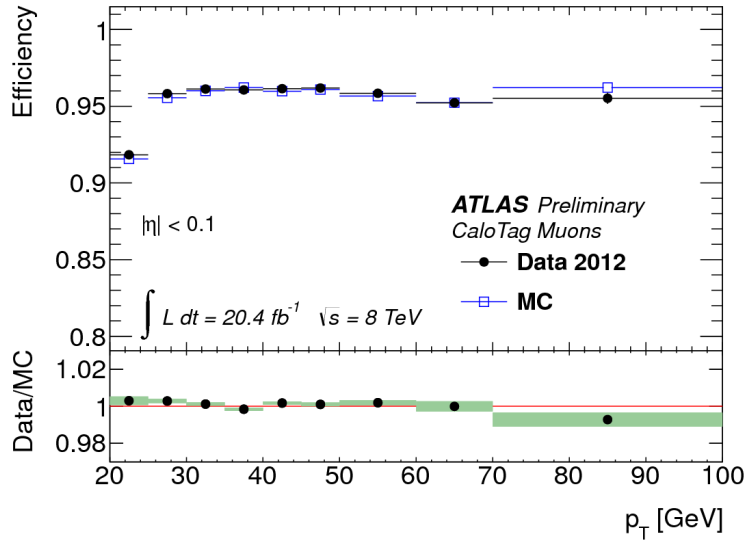
where the first term takes into account contributions from multiple scattering, while the second term describes both the intrinsic resolution of each detector component and residual misalignments. In this way, the momentum measured in the simulation (either in the ID or MS<sup>10</sup>),  $p_T^{(\text{MC})}$ , is corrected on an event-by-event basis as

$$p_T^{(\text{MC,corr})} = p_T^{(\text{MC})} \cdot s(\eta) \left[ 1 + \Delta a(\eta)G(0, 1) + \Delta b(\eta)G(0, 1)p_T^{(\text{MC})} \right]$$

<sup>8</sup>In the region  $7 < p_T < 10$  GeV differences with respect to SFs computed with  $J/\psi \rightarrow \mu\mu$  events are below 1%, while for  $p_T < 7$  GeV they are below 2%.

<sup>9</sup>Above 100 GeV a systematic uncertainty of  $1\% \times p$ , with  $p$  in TeV, is assigned, from Monte Carlo studies where conservative residual misalignments and a 10% variation of muon energy loss are simulated.

<sup>10</sup>The correction applied to combined muons is the average of the ID and MS corrections, where each of the two components is weighted with the corresponding momentum resolution.

(a) Combined and segment-tagged muons ( $0.1 < |\eta| < 2.5$ )(b) Calo-tagged muons ( $|\eta| < 0.1$ )

**Figure 3.4.** Muon reconstruction efficiency as a function of muon  $p_T$ , for different muon types and pseudorapidity regions. Ratio between data and MC efficiencies is also shown.

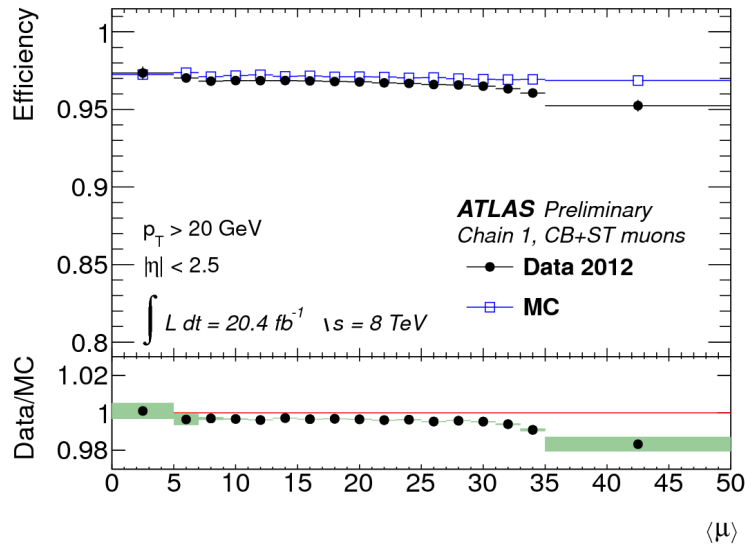


**Figure 3.5.** Muon reconstruction efficiency as a function of  $\langle \mu \rangle$  for muons with  $p_T > 20 \text{ GeV}$ , for combined or segment-tagged muons. Ratio between data and MC efficiencies is also shown.

where  $s$  corrects the momentum scale, and  $\Delta a, \Delta b$  are correction factors analogous to  $a, b$  and multiplied by  $G(0, 1)$ , a random variable which follows a Gaussian distribution with mean 0 and variance 1 (*momentum smearing*).

The correction factors  $s, a, b$ , which are computed for each detector system (ID, MS<sup>11</sup>) in 16 bins in pseudorapidity, are estimated by fitting the  $Z \rightarrow \mu\mu$  data mass spectrum with Monte Carlo templates. Different templates are obtained from simulation varying the correction parameters, and the fitting procedure selects the best match to the data mass spectrum. Systematic uncertainties on the  $a, b$  parameters are obtained varying the mass region used to derive the dimuon mass templates. Systematic uncertainties on  $s$  of 1% in the central and 2% in the forward region are introduced to cover possible dependence of the scale corrections on muon momentum.

Fig. 3.6 shows the  $Z \rightarrow \mu\mu$  mass shape, in data and Monte Carlo simulation, before (top) and after (bottom) applying the correction factors estimated as above: better agreement is obtained when smearing and scale corrections are applied.

Mass scale is shown in Fig. 3.7, as a function of pseudorapidity, and compared with results obtained using  $\Upsilon$  and  $J/\psi$  decays, selected with  $p_T > 6.5 \text{ GeV}$  and  $6 \text{ GeV}$ , respectively. Negligible dependence of the mass scale on muon momentum is observed, with an effect visible only at low momenta and covered by the assigned systematic uncertainties.

Mass resolution, obtained fitting the dimuon mass distribution in data using a convolution of the mass shape of generated Monte Carlo events<sup>12</sup> with a gaussian

<sup>11</sup>Independent measurements from the study of multiple scattering in the ID using secondary interaction vertices, and from the study of residual misalignments in the MS, constrain  $a_{\text{ID}}$  and  $b_{\text{MS}}$  to be small.

<sup>12</sup>*Generated* means that the simulated particles, after final state radiation but before passing through detector simulation, are used.

resolution model using per-event uncertainties on  $m_{\mu\mu}$  as estimated from the muon track fit, is shown in Fig. 3.8, as a function of pseudorapidity. Dimuon mass resolution, which ranges from 1.5 GeV to 3 GeV depending on the detector region, is again shown before (left) and after (right) applying muon smearing and scale corrections.

### 3.3 Electrons

Three are the electron reconstruction strategies followed in ATLAS:

- the standard reconstruction is seeded from electromagnetic (EM) clusters and looks for a compatible ID track;
- the standard reconstruction extends also outside  $|\eta| > 2.5$ , where ID information is not available and hence the measurement relies only on the EM cluster;
- a reconstruction optimized for low- $p_T$  (some GeV) non-isolated electrons, which starts from an ID track and looks for a match with a relatively isolated energy deposit in the calorimeter.

The standard algorithm for electrons in the central calorimeter region ( $|\eta| < 2.47$ ), which are the ones relevant to the  $H \rightarrow ZZ^{(*)} \rightarrow 4\ell$  analysis, is the one described in this section.

#### 3.3.1 The Gaussian Sum Filter

The inner detector track fitting, described in Sec. 3.1, is based upon a regressive least squares estimator, the Kalman filter. The Kalman filter performs the measurement of track parameters in steps, incorporating measurement from each detector component sequentially<sup>13</sup>. It relies on the assumption that all measurement uncertainties (such as those arising from energy loss) can be described by gaussian probability density functions.

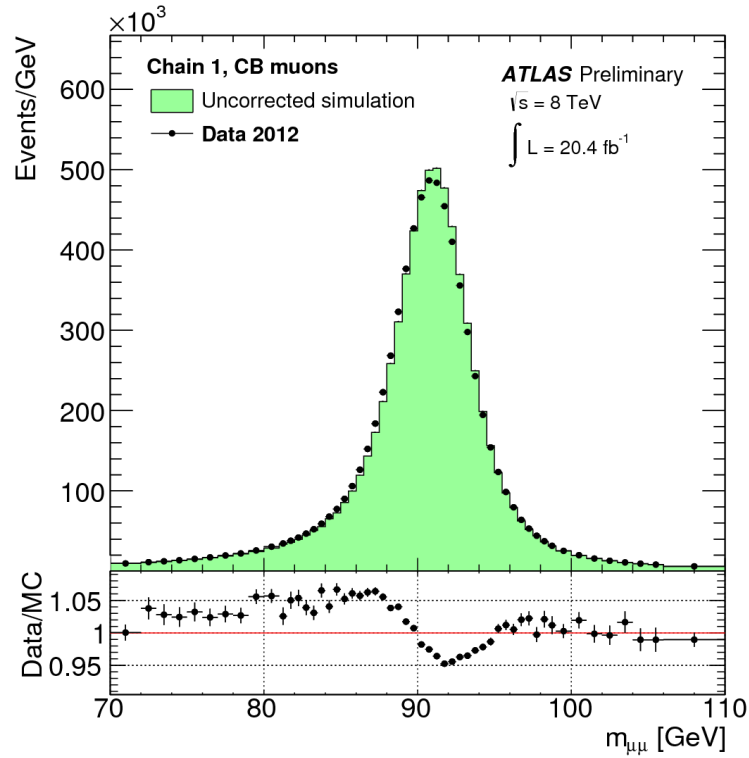
ATLAS track reconstruction applies the pion mass hypothesis when estimating the effect of energy loss for ionization, bremsstrahlung and multiple scattering. Electrons, on the other hand, lose energy mainly by bremsstrahlung, well described by the Bethe-Heitler distribution, which expresses the probability for an electron to retain a fraction  $z$  of its initial energy after passing through a material thick  $t$  radiation lengths ( $X_0$ ) as<sup>[33]</sup>

$$f(z) = \frac{(-\ln(z))^{a-1}}{\Gamma(a)},$$

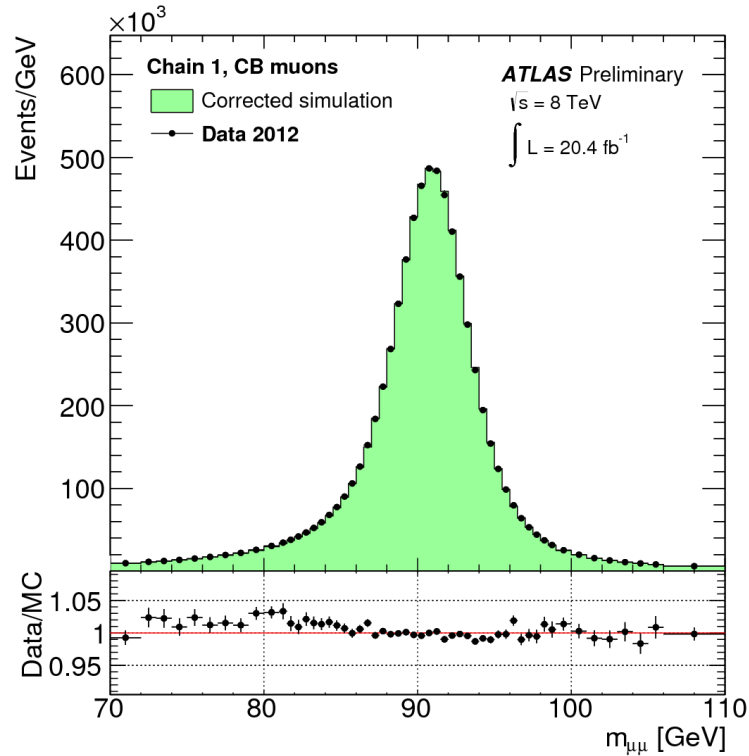
where  $a = t \ln(2)$ . Moreover, for electrons above the GeV scale additional effects<sup>14</sup> lead to a  $f(z)$  which can be calculated only numerically. This probability density

<sup>13</sup>This approximation aims at reducing the CPU time needed to obtain the best estimate of track parameters using all available measurements.

<sup>14</sup>For example, corrections due to interference effects in the scattering processes for ultrarelativistic electrons (Landau-Pomeranchuk-Migdal effect) and to longitudinal density of the matter, the Ter-Mikaelian effect.



(a) MC with no corrections



(b) MC with smearing and scale corrections

**Figure 3.6.** Distribution of the dimuon invariant mass for combined, isolated muons with  $p_T > 25 \text{ GeV}$ , as obtained from 8 TeV data, compared with Monte Carlo simulation for  $Z \rightarrow \mu\mu$  and backgrounds. The effect of applying smearing and scale corrections defined in the text is shown on the right plot.

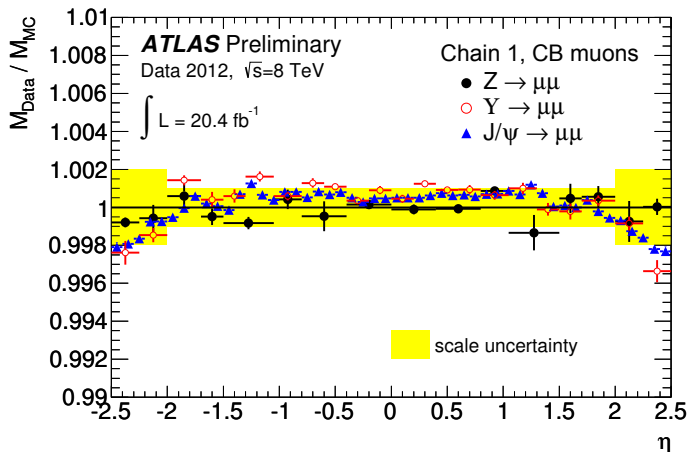


**Figure 3.7.** Ratio between the data and MC mass scales, obtained from  $J/\psi$ ,  $\Upsilon$  and  $Z \rightarrow \mu\mu$  decays, as a function of the pseudorapidity of the pair of muons ( $\Upsilon$ ,  $Z$  or of the muon with highest  $p_T$  ( $J/\psi$ )).

function (p.d.f.) is manifestly non gaussian, and hence the Kalman filter is no more an optimal approximation.

Electron inner detector tracks are therefore reconstructed using a generalization of the Kalman filter, the *Gaussian Sum Filter* (GSF)[34]. The GSF approximates the uncertainties p.d.f. as a sum of gaussian components, and uses a Kalman filter for each of these. In this way, many Kalman filters process in parallel, each one representing a different contribution to the Bethe–Heitler spectrum.

ATLAS electron reconstruction uses the GSF to account for the energy loss by bremsstrahlung in the silicon detectors<sup>15</sup>. The GSF algorithm is applied to refit inner detector tracks already assigned to electrons (as explained in the next section), and reduces the dependence of the momentum measurement on the amount of material at given pseudorapidity. This is shown in Fig. 3.9, where the average of the distribution of the ratio of the reconstructed versus true  $q/p$ , for simulated electrons with  $p_T$ , from 7 GeV to 80 GeV is compared between electrons with low or high bremsstrahlung, as a function of  $\eta$ , before and after GSF is applied.

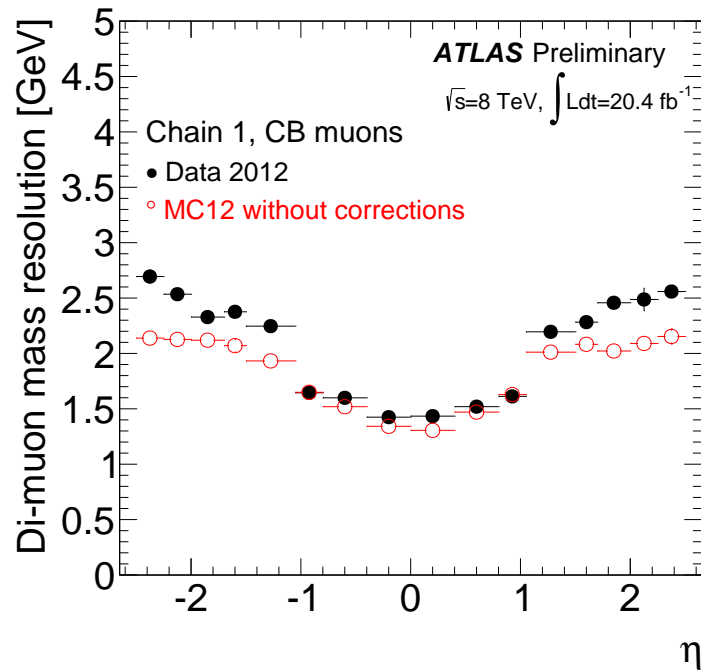
### 3.3.2 Electron Reconstruction

Standard electron reconstruction is seeded from an electromagnetic cluster. Clusters are reconstructed with a *sliding window algorithm*, following a three–steps procedure[35]:

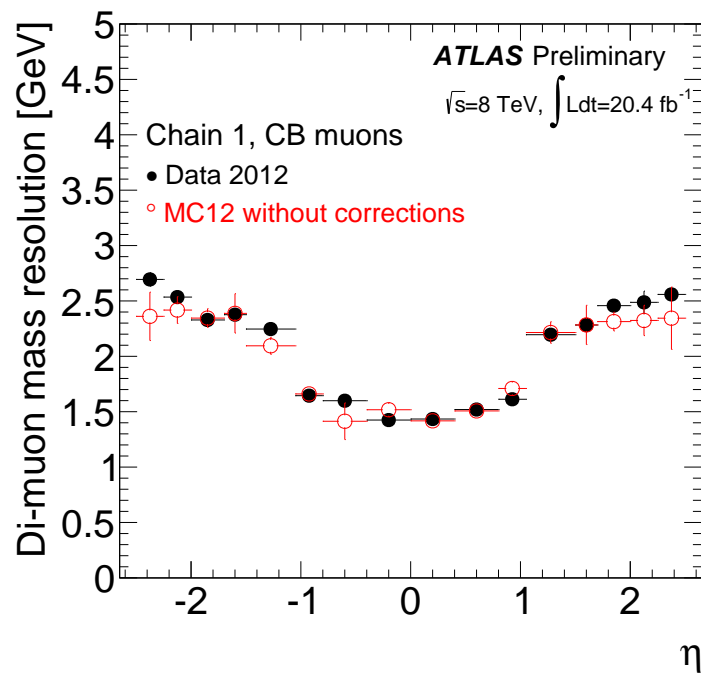
**Tower Building** The middle layer of ECAL is divided in a grid of towers of size  $\Delta\eta \times \Delta\phi = 0.025 \times 0.025$ , to which an energy  $E$  is assigned by the sum of all cluster cells crossing this geometrical region<sup>16</sup>.

<sup>15</sup>The GSF does not bring any substantial improvement in the case of the TRT, due to the more homogeneous distribution of detector material and the lower measurement precision.

<sup>16</sup>The contribution of cells crossing more than one tower is proportionally shared among each of them.

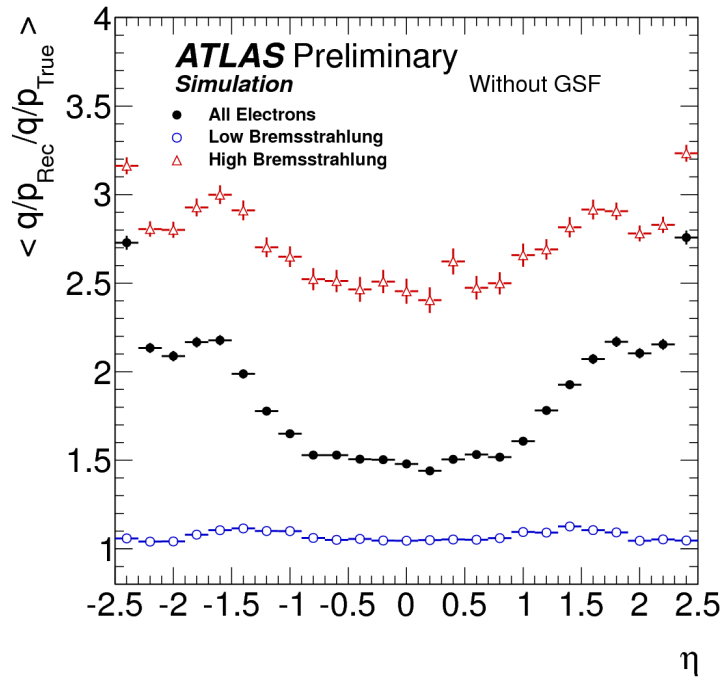


(a) MC with no corrections

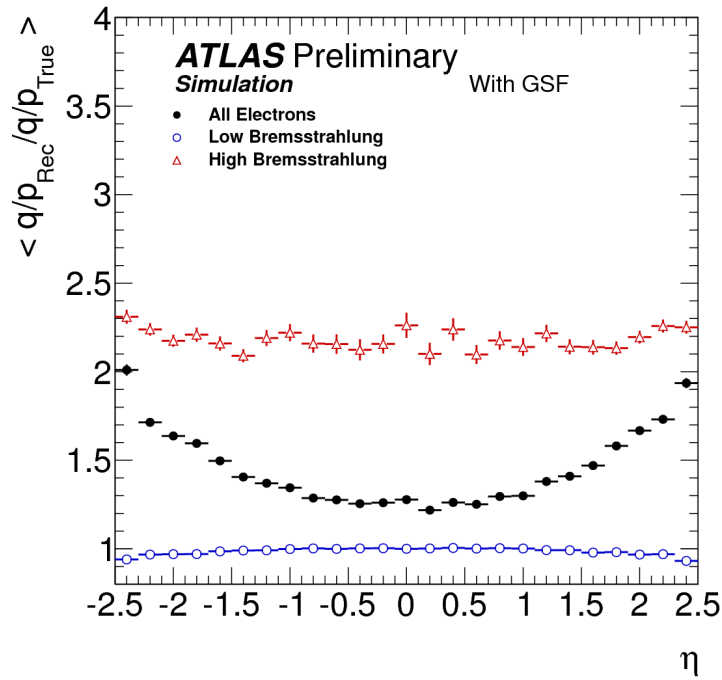


(b) MC with smearing and scale corrections

**Figure 3.8.** Dimuon invariant mass resolution in data, compared with Monte Carlo simulation before and after corrections.



(a) Before GSF refit



(b) After GSF refit

**Figure 3.9.** Average of the distribution of the ratio of reconstructed and true electron  $q/p$ , as a function of  $\eta$ , for simulated electrons between 7 GeV and 80 GeV (black), before and after GSF refit is applied. Electrons which lose more (red) or less (blue) than 20% of energy by bremsstrahlung are also shown. High-bremsstrahlung events are dominant at high  $|\eta|$ , as expected from Fig. 2.12a.

**Seed Finding** A sliding window (with a fixed width of  $5 \times 5$  in tower units  $\Delta\eta \times \Delta\phi$ ) is moved around the grid of towers: a seed (*pre-cluster*) is formed if the transverse energy of the window, defined as the sum of transverse energies of the included towers, is a local maximum and is above 3 GeV. The position of the pre-cluster is computed with an energy-weighted average of  $\eta$  and  $\phi$  baricenters of all cells within a window spreading by  $3 \times 3$  towers around the central tower<sup>17</sup>. Duplicate pre-clusters within a  $\Delta\eta \times \Delta\phi = 2 \times 2$  region are removed selecting the highest energy pre-cluster.

**Cluster Filling** Clusters are built selecting all barrel (endcap) cells within a  $3 \times 7$  ( $5 \times 5$ )  $\Delta\eta \times \Delta\phi$  region<sup>18</sup> around the position of the seed. This is done in different steps: one starts from the ECAL middle layer, using as seed position the baricenter of the pre-cluster, adds the middle layer cells and then uses their baricenter as seed for the search in the strip layer and in the back layer, while for the pre-sampler the baricenter of the cells in the strip layer is used.

The cluster building efficiency is measured on electrons from  $Z \rightarrow ee$  decays to be  $\approx 100\%$ .

Electrons are then reconstructed matching the calorimeter cluster to a track selected by the GSF algorithm. If more than one match is possible, the ones with hits in the silicon detectors are preferred, and the one with lower distance in  $\Delta R$  with respect to the cluster is chosen. Electron momentum is then obtained using

- the inner detector information for the measurement of  $d_0, z_0, \eta$  and  $\phi$ , and for the charge determination;
- the cluster information for the determination of  $E$ .

Fig. 3.10 shows, in blue, the electron reconstruction efficiency for  $Z \rightarrow ee$  events in 8 TeV  $pp$  collision data and Monte Carlo, when a requirement of at least 1 pixel hit and 7 SCT hits is applied on the associated ID track. The effect of applying GSF refit to reconstruction efficiencies, expressed as a function of cluster  $\eta$  and  $E_T$ , is shown: average reconstruction efficiency is above 97%.

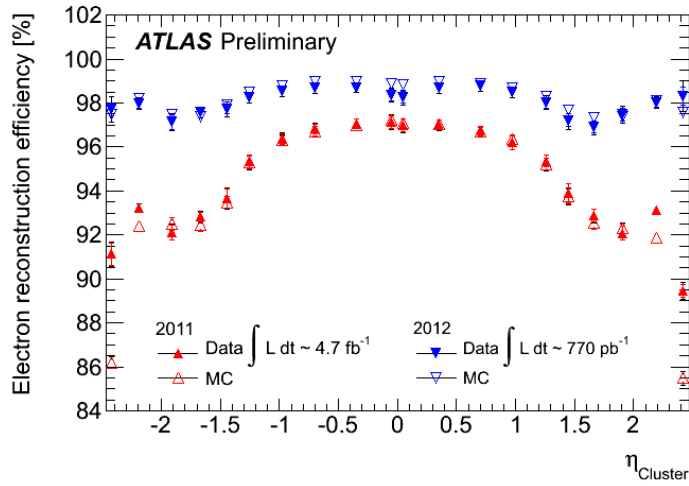
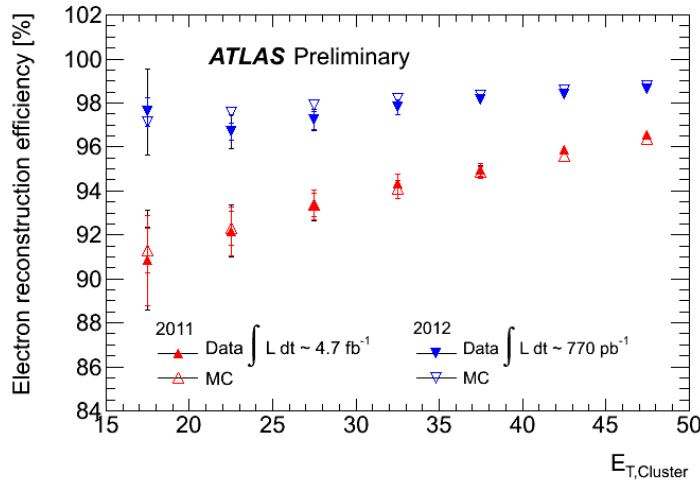
### 3.3.3 Electron Identification

The aim of electron identification is to provide a set of selection requirements, based on variables associated to the reconstructed object, which allow to discriminate true isolated electrons from hadronic jets faking electrons. Different identification criteria have been developed in ATLAS, optimized for different working points in the plane of the efficiency on isolated electrons versus the rejection against non-isolated electrons[35]. We will describe in this section a set of requirements optimized for the  $H \rightarrow ZZ^{(*)} \rightarrow 4\ell$  analysis at 8 TeV, the so-called *MultiLepton menu*, and the *loose++* requirements used for processing 7 TeV data.

Electron identification in the MultiLepton menu is based on:

<sup>17</sup>At the calorimeter edges, this second window may be instead centered on the highest energy tower.

<sup>18</sup>In the barrel  $\Delta\phi$  is large, due to the fact that the magnetic field curvature is in this direction. In the endcap, on the other hand,  $\Delta\phi$  is lower because the bending effect is lower, and  $\Delta\eta$  is higher due to the fact that the physical size of the calorimeter cells is smaller than in the barrel.

(a) Efficiency vs  $\eta^{\text{cluster}}$ (b) Efficiency vs  $E_T^{\text{cluster}}$ 

**Figure 3.10.** Electron reconstruction efficiency, for 2011 (red) and 2012 (blue) data and MC simulation, as a function of  $\eta$  and  $E_T$  of the associated cluster, from  $Z \rightarrow ee$  events. Unlike the 2012 data/MC sample, the 2011 reconstruction used here did not include the GSF refit: for the analyses presented in this thesis, however, GSF was applied in electron reconstruction also for 7 TeV data and MC.

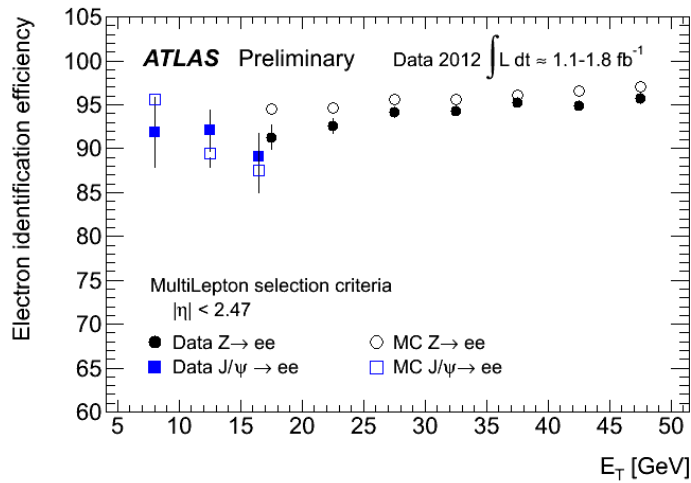
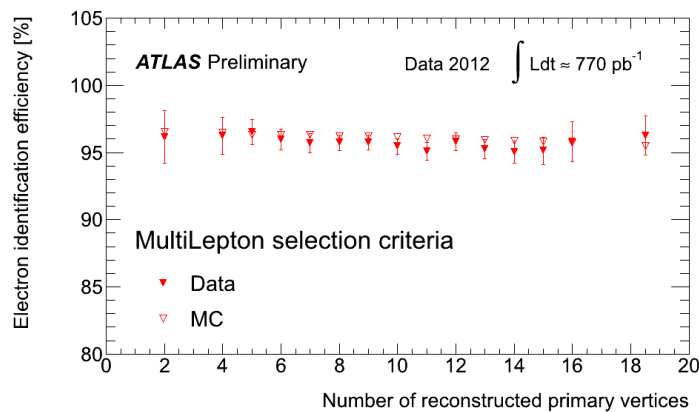
- the number of silicon hits (one hit in the B-layer and at least 2 pixel hits are required);
- the *hadronic leakage*  $R_{\text{had}}$ , i.e. the ratio between the transverse energy deposit in ECAL and HCAL (electrons are expected to release most of their energy in the electromagnetic calorimeter);
- the fraction of electron energy deposited on the third and outermost ECAL layer;
- the energy deposit on the second sampling of ECAL (electrons are expected to deposit there most of their energy);
- the cluster isolation in pseudorapidity, defined in terms of the ratio of energy deposited in a  $3 \times 7$  towers window divided by the energy deposit in a  $7 \times 7$  window,  $R_\eta$ ;
- the shower width in  $\eta$  measured using the strips of the first layer of the calorimeter,  $w_{\text{stot}}$ , and in the second layer,  $w_{\eta 2}$  (average over detector cells, weighted with their associated energy);
- the energy deposit in the hadronic calorimeter and the second ECAL sampling (to reject jets containing pions and wide showers);
- the  $\eta, \phi$  matching between cluster and ID track (which is expected to be poor for jets faking electrons);

After these selections, jets with one or more neutral particle (like the  $\pi^0$ ), which give rise to significant electromagnetic showers, become an important contribution to electron background. Rejection of this kind of jets can be achieved using the first ECAL layer: its fine granularity allows to discriminate between electrons, which leave an energy deposit with a single maximum  $E_1$ , and these jets, which can cause a significant second maximum  $E_2$ . Selection criteria are applied on  $E_{\text{ratio}} = (E_1 - E_2)/(E_1 + E_2)$

Jets with low particle multiplicity containing mainly  $\pi^0$ s, photon conversions and non-isolated electrons from decay of heavy flavours remain as main backgrounds. In order to further reject them, in the transition region between ECAL barrel and endcap cuts are applied on the fraction of high-threshold hits in the TRT (which helps to identify electrons, which are in the ultra-relativistic regime).

The electron identification efficiency is shown in Fig. 3.11. Efficiency as a function of electron  $E_T$  is estimated using decay electrons from  $J/\psi$ s produced promptly and  $Z$  bosons. Identification efficiency is shown to be flat as a function of transverse energy within 5%; the agreement between efficiency estimated in data and Monte Carlo simulation is better than 4% for low  $E_T$  and better than  $0.5 \div 1\%$  at high  $E_T$ . As estimated from  $Z \rightarrow ee$  events, identification efficiency is also flat – within 2% – with respect to the average number of interactions per bunch crossing, and is well described by the Monte Carlo simulation within 0.5%.

In the case of the 2011 data taking, electron identification is based on the *loose++* menu. Electron identification is in this case based on  $R_{\text{had}}$ ,  $R_\eta$ ,  $w_{\eta 2}$ ,  $w_{\text{stot}}$ ,  $E_{\text{ratio}}$ ,

(a) Efficiency vs  $E_T$ (b) Efficiency vs  $\langle \mu \rangle$ 

**Figure 3.11.** Electron identification efficiency, for 2012 data (filled markers) and MC simulation (open markers), as a function of electron  $E_T$  (measured from  $J/\psi \rightarrow ee$  and  $Z \rightarrow ee$  events), and of the average number of interactions per bunch crossing (measured from  $Z \rightarrow ee$  events).

on the number of pixel and silicon hits and on the  $\Delta\eta$  match between the inner detector track and the electromagnetic cluster.

## Chapter 4

# $H \rightarrow ZZ \rightarrow 4\ell$ : the Golden Channel

Various are the reasons for which the  $H \rightarrow ZZ^{(*)} \rightarrow 4\ell$  channel is universally known as the *golden channel* in the search for the Higgs boson. Despite its lower cross-section with respect to  $H \rightarrow \gamma\gamma$  and  $H \rightarrow WW$  at low  $m_H$ , it offers a clear, clean signature with a good signal to background ratio, which extends to a wide Higgs mass range. The presence of charged leptons in the final state allows for a complete reconstruction of the decay chain: kinematical variables of the final state can be measured with excellent precision, allowing to study the properties of the Higgs boson and to determine the quantum number of the observed, new particle. In this chapter, the main features of the  $H \rightarrow ZZ^{(*)} \rightarrow 4\ell$  channel are reviewed, both in the context of the Higgs boson search and of the spin-parity studies of a generic particle decaying via  $X \rightarrow ZZ \rightarrow 4\ell$ .

### 4.1 The Standard Model Signature

The tree-level Feynman diagram for the  $H \rightarrow ZZ^{(*)} \rightarrow 4\ell$  decay is shown in Fig. 4.1. The Higgs boson interacts with two  $Z$  bosons, which can possibly be off mass shell (virtual), which then decay into pairs of opposite-sign leptons<sup>1</sup>. For  $m_H \lesssim 2m_Z$ , interference effects between final state leptons are present for the decay channels with identical leptons, e.g.  $H \rightarrow ZZ^{(*)} \rightarrow \mu^+\mu^-\mu^+\mu^-$  and  $H \rightarrow ZZ^{(*)} \rightarrow e^+e^-e^+e^-$ , which lead to an enhancement of the branching ratio in final states with same flavour leptons of about 10% ( $m_H = 120$  GeV), while the one for opposite flavour leptons is proportionally reduced.

The  $H \rightarrow ZZ^{(*)} \rightarrow 4\ell$  process can be simulated either at leading order (using the PYTHIA event generator[37]) or next-to-leading order (using the POWHEG event generator<sup>2</sup>[38]). The perturbative order of the calculation influences the transverse momentum distributions of the Higgs boson: Fig. 4.2 shows different predictions for the Higgs  $p_T$  between the two generators, especially visible in the case of VBF production. In the case of the ggF production mechanism, further  $p_T$  corrections

<sup>1</sup>The branching ratio for  $Z \rightarrow \ell\ell$ , with  $\ell = e, \mu$ , is 6.7% (10.1% if we consider also  $\tau$  leptons)[36]

<sup>2</sup>The POWHEG event generator is interfaced to PYTHIA for parton shower, hadronization and underlying event simulation.

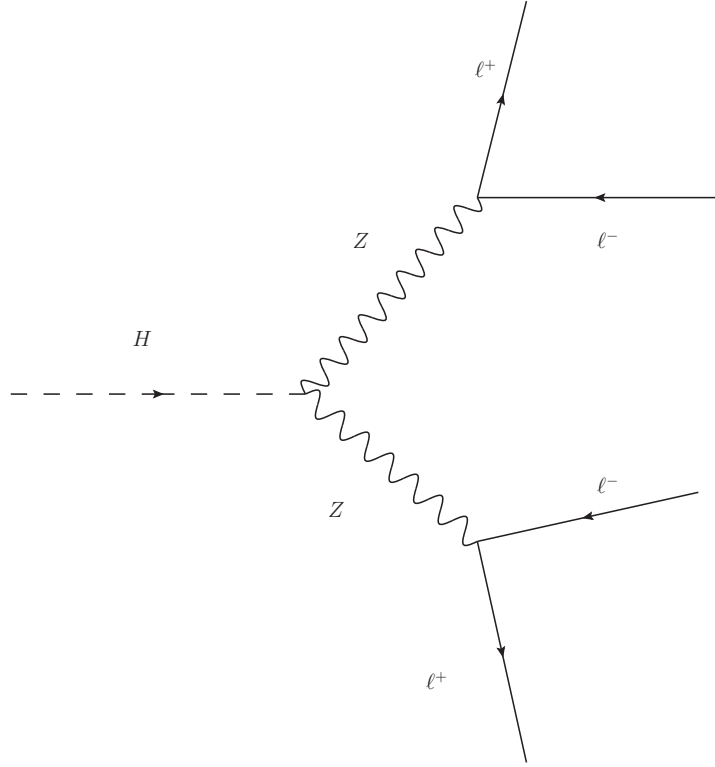


**Figure 4.1.** Lowest order Feynman diagram for the  $H \rightarrow ZZ^{(*)} \rightarrow 4\ell$  decay.

to the NNLO spectrum arise from calculations at NLO in QCD corrections and next-to-next-to-leading-logarithm (NNLL) in QCD soft-gluon resummations[39] and are shown in Fig. 4.3. The choice of the set of parton density functions and of the  $\alpha_s$  scale has an impact of less than 2% on the signal acceptance, independent on  $m_H$ .

The signature of  $H \rightarrow ZZ^{(*)} \rightarrow 4\ell$  is the presence of four final state leptons, which are produced isolated and which come from the decay of two intermediate bosons. Selection criteria are based on requirements on the kinematic variables of the event — momentum, invariant mass of the dilepton pairs, lepton isolation measured with the tracking system and calorimeters, lepton impact parameter — and aim at selecting a pure signal sample, thus reducing the contribution from backgrounds. Different is the impact on purity coming from different background sources, as a function of the Higgs mass value.

#### 4.1.1 Low and High Mass Searches

The kinematic production threshold of two  $Z$  bosons,  $\approx 2m_Z$ , defines two Higgs mass regions, in which experimental event selection strategies are different.

The main background over the full mass range is  $pp \rightarrow ZZ^{(*)} \rightarrow 4\ell$ , which is called *irreducible background* since presents the same final state as the signal; it is described in Sec. 4.1.2. For  $m_H \gtrsim 2m_Z$ , where both  $Z$  bosons are on the mass shell and hence give rise to high- $p_T$  leptons, it is by far the dominant background source.

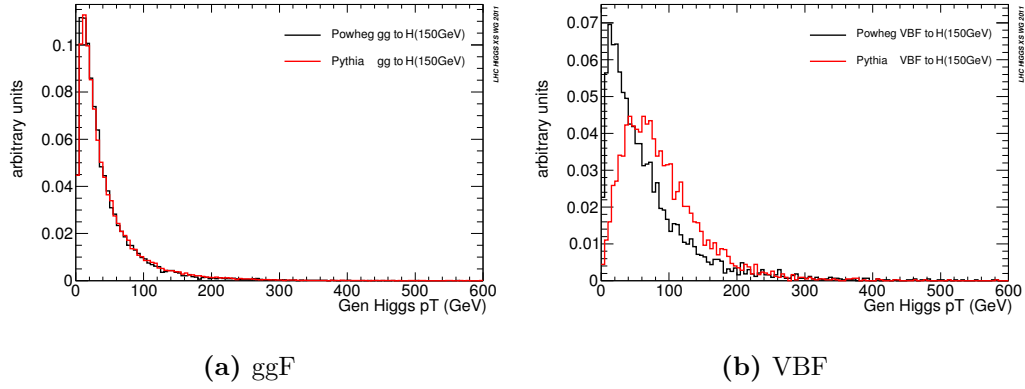


**Figure 4.2.** Generated Higgs transverse momentum for ggF and VBF production, compared between LO and NLO generators[7].

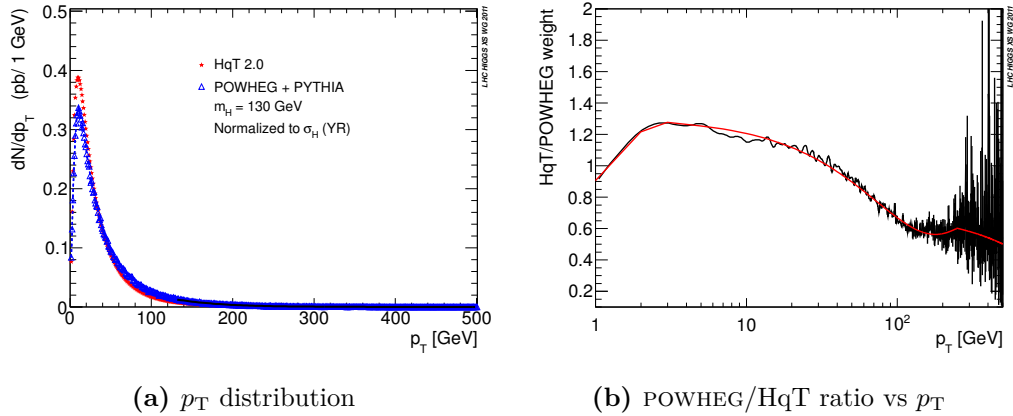


**Figure 4.3.** Higgs transverse momentum distribution, for  $m_H = 130$  GeV, compared between POWHEG (NNLO) and HqT (NNLO+NNLL). The ratio between the two distributions is also shown as a function of Higgs  $p_T$ . From Ref. [7].

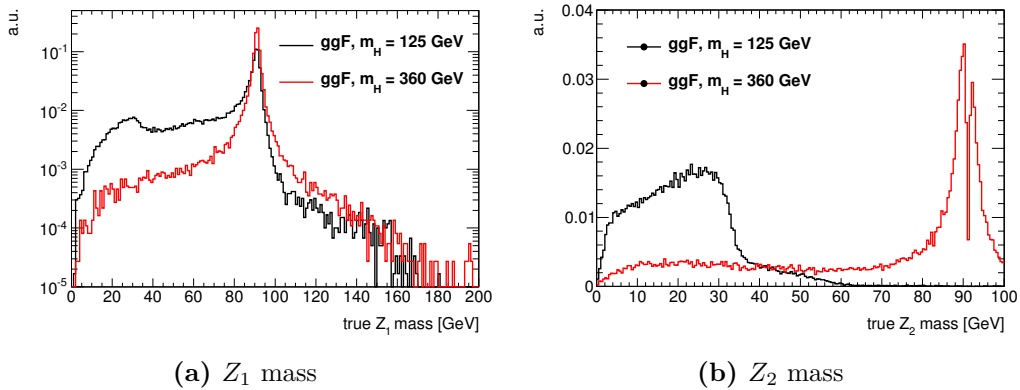


**Figure 4.4.** Generated invariant mass of  $Z_1$  and  $Z_2$ , defined respectively as the dilepton pair with invariant mass closest and farthest from the  $Z$  pole, for Higgs masses of 125 GeV and 360 GeV and ggF production. The double peak structure in the  $Z_2$  mass distribution for  $m_H = 360$  GeV is due to the definition criteria of  $Z_1$  and  $Z_2$ .

For  $m_H \lesssim 2m_Z$ , at least one of the two  $Z$  bosons is off the mass shell. This means that the pair of opposite charged leptons in the final state with lower invariant mass will determine the purity of the selected data sample. Indeed, if we denote by  $Z_1$  the four-momentum of the dilepton pair  $ff$  with invariant mass closest to the  $Z$  mass, and by  $Z_2$  the one of the pair  $f'f'$ , it is the lepton pair  $f'f'$  which will have a softer single lepton  $p_T$  spectrum. Let us restrict to  $\ell = e, \mu$ : since reconstruction and electron performance are very different between electrons and muons, one expects different signal efficiency and background rejection between final states with  $Z_2 \rightarrow \mu\mu$ , which are expected to be cleaner, and those with  $Z_2 \rightarrow ee$ , where backgrounds from jets and non-isolated electrons become relevant. This usually gives rise to contributions from the so-called *reducible backgrounds*, described in Sec. 4.1.3, which are more relevant in  $4e, 2\mu 2e$  final states than in  $4\mu, 2e2\mu$  (here and in the following we denote as  $2f2f'$  the final state with  $Z_1 \rightarrow ff$  and  $Z_2 \rightarrow f'f'$ ).

Fig. 4.4 shows the behaviour of the invariant masses of the two  $Z$  bosons for  $m_H = 125$  and 360 GeV, at generator level. One can see that, for low Higgs mass, the distribution of the mass of the on-shell  $Z$  boson does not follow a Breit-Wigner distribution as in the case of inclusive  $Z$  production. This effect is reduced at high  $m_H$ . Fig. 4.5 shows, for  $m_H = 125$  GeV, the correlation between the two invariant masses; there is a relevant fraction of events in the region where both  $Z_1$  and  $Z_2$  are far from the  $Z$  pole. The kinematic threshold imposed by the energy conservation  $m_{Z_1} + m_{Z_2} \lesssim m_H$  is also evident.

### 4.1.2 The Irreducible Background

The production mechanisms for the irreducible background  $pp \rightarrow ZZ^{(*)} \rightarrow 4\ell$  are shown in Fig. 4.6. The main process is  $qq \rightarrow ZZ$ : as it can be seen from 4.8b in the case of the  $2e2\mu$  final state, the NLO cross-section (computed with MCFM[40]) of the  $gg \rightarrow ZZ$  production mechanisms is less than 10% of the cross-section of  $qq \rightarrow ZZ$ .

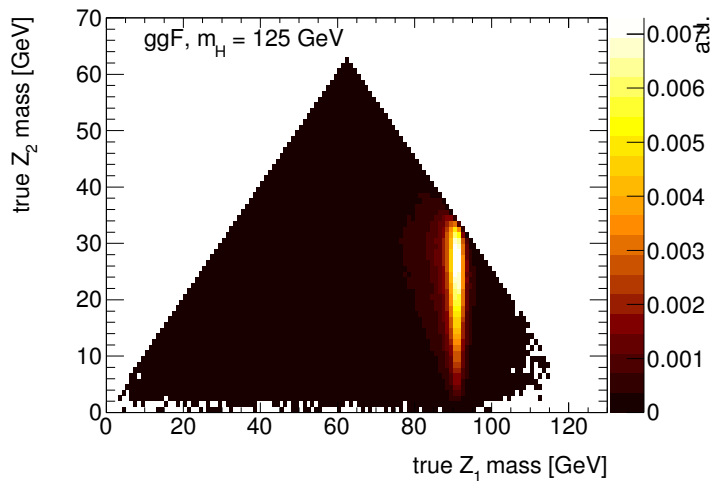


**Figure 4.5.** Correlation between the generated invariant masses of  $Z_1$  and  $Z_2$ , defined respectively as the dilepton pair with invariant mass closest and farthest from the  $Z$  pole, for  $m_H = 125$  GeV and ggF production.

The peak shown in the production cross-section at  $m_{4\ell} \approx m_Z$  is due to the *single resonant* production of a  $Z$  boson, whose Feynman diagram is shown in Fig. 4.7. The effect of the inclusion of this term in the calculation, as shown in Fig. 4.8a, is relevant for  $m_{4\ell} \lesssim 100$  GeV.

The four-lepton mass spectrum of the irreducible background can be therefore divided in three regions:

- single-resonant mass region (below 100 GeV), where the peak at  $m_{4\ell} \approx m_Z$  from single resonant production is present;
- low mass region (below  $2m_Z$ ), which shows a rising shoulder whose shape is influenced by the kinematic cuts applied by the selection;
- high mass region (above  $2m_Z$ ), where the spectrum shows the fall of the kinematic shoulder due to the opening of the decay to real bosons.

Discrimination between signal and background is done mainly in terms of the  $m_{4\ell}$  distribution, since the signature of an Higgs boson decay is a narrow peak in the four-lepton invariant mass, while the  $ZZ$  background is locally flat (apart from  $m_H \approx m_Z, 2m_Z$ ). Further discrimination power is provided, as it can be seen from Fig. 4.9, by the invariant mass of  $Z_2$ <sup>3</sup>.

### 4.1.3 Reducible Backgrounds

Reducible background contributions come from

- production of  $Z$  bosons in association with jets;
- production of  $Z$  bosons in association with heavy flavours;

<sup>3</sup>In Sec. 4.2 a full account of kinematic variables which can be used to discriminate signal and background is presented.

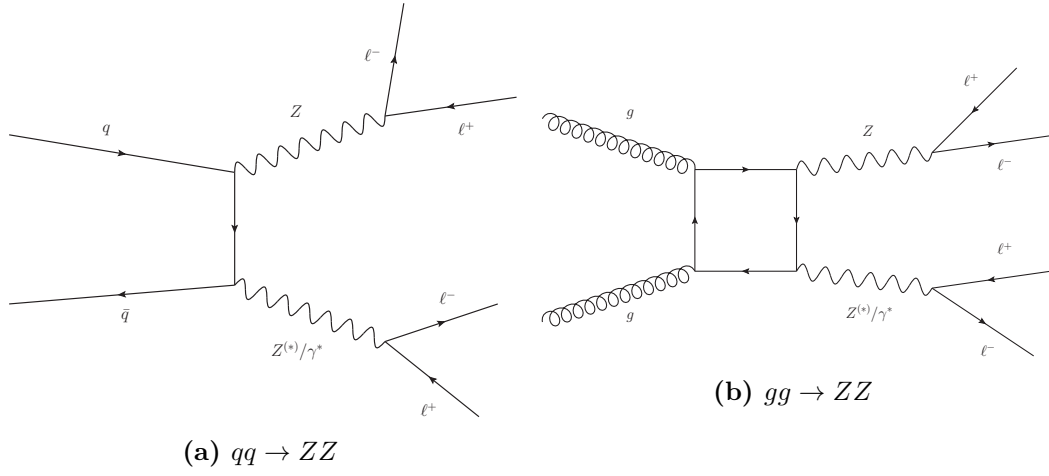


**Figure 4.6.** Lowest order Feynman diagrams for  $qq \rightarrow ZZ$  and  $gg \rightarrow ZZ$  production.

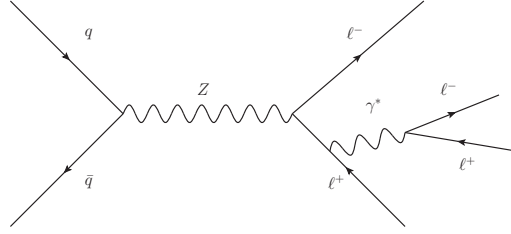


**Figure 4.7.** Lowest order Feynman diagram for the single resonant production mechanism.

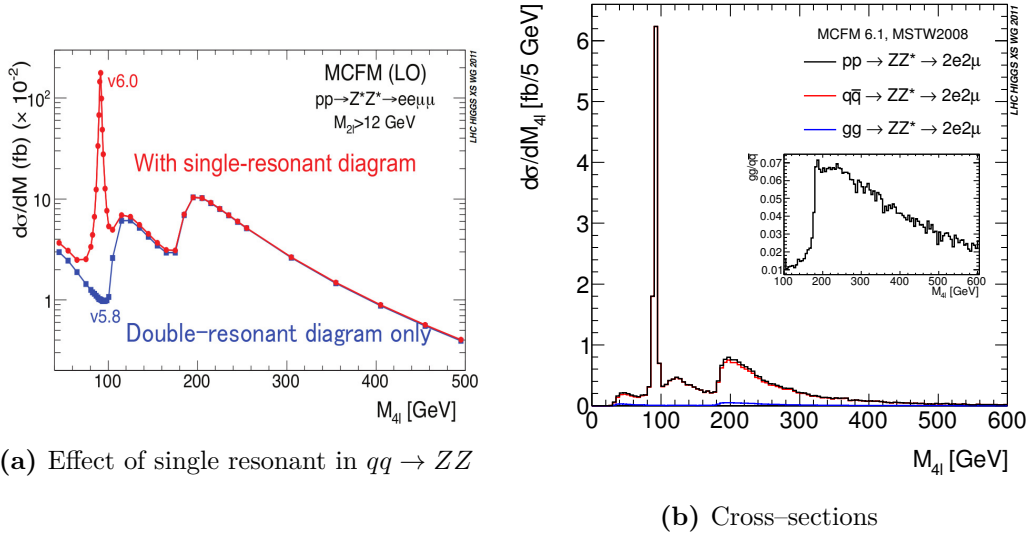


**Figure 4.8.** **a:** effect of the inclusion of the single resonant diagram (Fig. 4.7) in the LO  $qq \rightarrow ZZ \rightarrow 2e2\mu$  cross-section calculation as a function of  $m_{4\ell}$ , where a cut on dilepton mass  $m_{2\ell} > 12$  GeV is applied. **b:** NLO  $pp \rightarrow ZZ \rightarrow 2e2\mu$  cross-section as a function of  $m_{4\ell}$ ; the inset shows the ratio, as a function of  $m_{4\ell}$ , between  $gg \rightarrow ZZ$  and  $qq \rightarrow ZZ$  cross-sections. From Ref. [7].

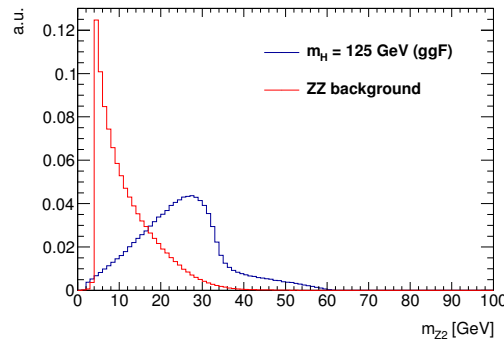


**Figure 4.9.** Generator-level distribution of the invariant mass of the off-shell dilepton pair,  $Z_2$ , for  $ZZ$  background and ggF signal at  $m_H = 125$  GeV (POWHEG NLO).

- production of  $t\bar{t}$  pairs.

Fig. 4.10 and 4.11 show some of the relevant lowest order Feynman diagrams for these processes. In the case of  $Z + jj$  production<sup>4</sup>, the  $Z$  boson decays leptonically, while two jets of the final state are mistakenly reconstructed as leptons, mainly as fake electrons. In the case of  $Z + bb$  production<sup>5</sup>, a real lepton coming from the decay of heavy flavours can be reconstructed; this lepton will be not isolated, since it's produced in the vicinity of a particle jet. In the case of  $t\bar{t}$  production, top quarks decay to  $Wb$  and a four-lepton signature is obtained when the two  $W$ s decay to  $\ell\nu$ <sup>6</sup> and another lepton is produced in the decay of hadrons produced in the hadronization of each of the two  $b$  quarks.

Reducible backgrounds are characterized by the presence of a lepton pair which has a softer  $p_T$  spectrum than leptons from decay of on-shell  $Z$  bosons, hence reducible backgrounds are more relevant in the low  $m_H$  region where one does not place stringent cuts on lepton momenta in order to keep signal acceptance high.

These leptons, unlike signal leptons which are produced isolated, are usually surrounded by other particles, which result in an energy or momentum deposit in the detector. Selection criteria based on the sum of the transverse energy deposits in a cone of size  $\Delta\hat{R}$  around the reconstructed lepton (which has transverse energy  $E_T$  and transverse momentum  $p_T$ ), i.e.

$$\sum_{\Delta R_i < \Delta\hat{R}} E_T^{(i)} / E_T,$$

and on the sum of the transverse momenta of the charged particles within a cone of size  $\Delta\tilde{R}$ ,

$$\sum_{\Delta R_i < \Delta\tilde{R}} p_T^{(i)} / p_T,$$

<sup>4</sup>We denote as  $Z + jj$  the production of a  $Z$  boson in association with light-flavour jets, which are mistakenly reconstructed as leptons.

<sup>5</sup>We will usually denote by  $Z + bb$  the more general production of  $Z$  bosons in association with hadrons with  $b$  or  $c$  quark content.

<sup>6</sup>The branching ratio for  $W \rightarrow \ell\nu$  is 32.4%[36].

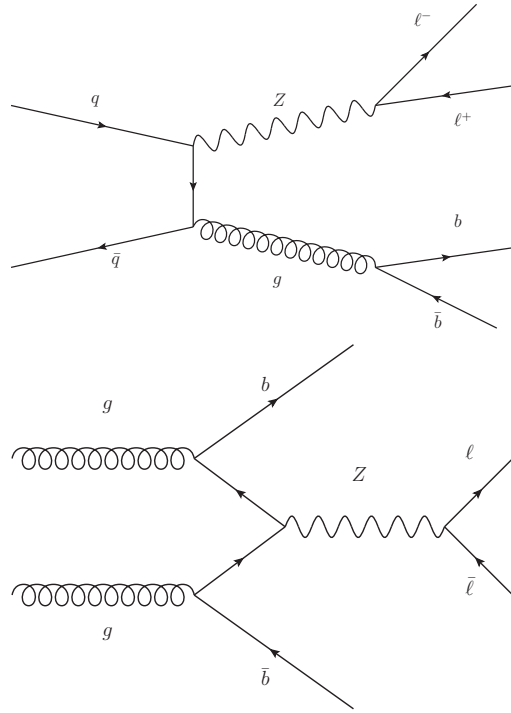


**Figure 4.10.** Lowest order Feynman diagrams for  $pp \rightarrow Z + b\bar{b}$ .

are usually applied to reject non-isolated leptons.

Further rejection power for leptons produced from the decay of heavy flavours, i.e. from displaced secondary vertices, is obtained with selection criteria based on the significance of their impact parameter measurement,

$$\frac{d_0}{\sigma(d_0)},$$

where  $\sigma(d_0)$  is the uncertainty on the  $d_0$  measurement.

## 4.2 Probing the $HZZ$ Vertex

The most interesting feature of the  $H \rightarrow ZZ^{(*)} \rightarrow 4\ell$  channel, apart from the high signal to background ratio which allows for good sensitivity over the full Higgs mass range, is the possibility to fully reconstruct the decay chain of the boson. This is an unique handle to understand the features of the  $H \rightarrow ZZ$  decay, in terms of the tensor structure of the  $HZZ$  vertex and of the intrinsic properties of the new particle.

The topology of the final state is deeply influenced by the spin-parity state of the decaying particle. Techniques have been developed in 1950s[41], to measure the  $\pi^0$  parity in  $\pi^0 \rightarrow \gamma\gamma$  and  $\pi^0 \rightarrow \gamma^*\gamma^* \rightarrow e^+e^-e^+e^-$  decays by studying the photon polarization and the orientation of the planes of the Dalitz pairs, and were later applied in  $B$ -physics for the study of  $CP$  violation with  $B \rightarrow V_1V_2$  decays<sup>7</sup>. The

<sup>7</sup>For example,  $B_s^0 \rightarrow J/\psi\phi$  and  $B_s^0 \rightarrow \phi\phi$  decays.

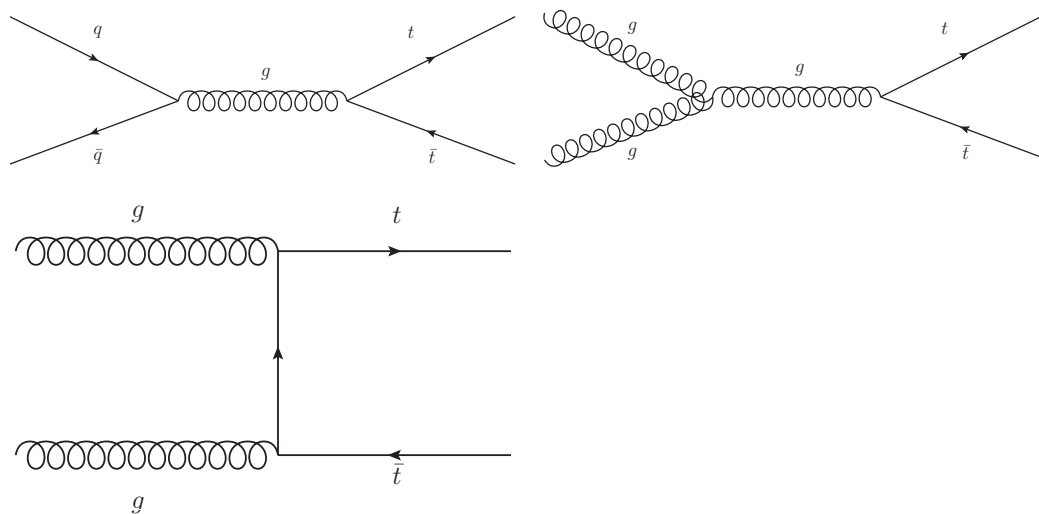


**Figure 4.11.** Lowest order Feynman diagrams for  $pp \rightarrow t\bar{t}$ .

amount of information on the nature of the decay which is available in the study of subsequent decay of a generic particle,  $X$ , into vector bosons that decay then to leptons, is higher than in the case of direct decays to pairs of particles, like  $H \rightarrow \gamma\gamma$ . The  $H \rightarrow ZZ^{(*)} \rightarrow 4\ell$  channel plays therefore an optimal role in probing the  $HZZ$  vertex.

In this section we will introduce the more general description of the decay of a particle  $X$  via  $X \rightarrow ZZ \rightarrow 4\ell$ , where either of the two  $Z$  bosons can be off the mass shell. The decay amplitude into four leptons will be expressed in terms of the kinematic variables which describe the full decay chain, and distributions of the observables for different spin–parity states and production scenarios will be given[42].

### 4.2.1 Kinematic Observables

In the assumption of massless leptons, the final state of the decay

$$X \rightarrow Z_1 Z_2 \rightarrow 4\ell$$

is described with  $4 \times 3 = 12$  degrees of freedom, one per lepton momentum component: they are assigned as follows. Four degrees of freedom come from the four–momentum of  $X$ ,  $(p_T, \eta, \phi, m_X)$  (where  $m_X$  has the same meaning of  $m_H$ <sup>8</sup>), which describes the Lorentz boost into the  $X$  center–of–mass frame. Two additional degrees of freedom are chosen to be the masses of the two  $Z$  bosons,  $m_1$  and  $m_2$ ; we will assume in the following that  $m_1 > m_2$ <sup>9</sup>.

The six remaining degrees of freedom are defined in the  $X$  rest frame, where  $\hat{\mathbf{n}}_z = (0, 0, 1)$  represents the parton collision axis:

<sup>8</sup>We emphasize that  $m_X$  differs from  $m_{4\ell}$  in the fact that the former is the mass pole of the particle  $X$ , while the latter is the reconstructed invariant mass of the four–lepton system.

<sup>9</sup>For  $m_X \ll 2m_Z$ , which is the relevant case for the characterization of the new boson at 126 GeV,  $m_i$  corresponds to the invariant mass of  $Z_i$  defined with the criteria explained in Sec. 4.1.1.

- $\theta^* \in [0, \pi]$  and  $\phi^* \in [-\pi, \pi]$  are defined in terms of the unit vector of the  $Z_1$  flight direction,  $\hat{\mathbf{q}}_1 = (\sin \theta^* \cos \phi^*, \sin \theta^* \sin \phi^*, \cos \theta^*)$ ;
- $\phi, \phi_1 \in [-\pi, \pi]$  are the two azimuthal angles between the three planes, in the  $X$  rest frame, defined by  $X, Z_1, Z_2$  and by each  $Z$  and its decay leptons:

$$\phi = \frac{\mathbf{q}_1 \cdot (\hat{\mathbf{n}}_1 \times \hat{\mathbf{n}}_2)}{|q_1 \cdot (\hat{\mathbf{n}}_1 \times \hat{\mathbf{n}}_2)|} \arccos(-\hat{\mathbf{n}}_1 \cdot \hat{\mathbf{n}}_2),$$

$$\phi_1 = \frac{\mathbf{q}_1 \cdot (\hat{\mathbf{n}}_1 \times \hat{\mathbf{n}}_{\text{sc}})}{|q_1 \cdot (\hat{\mathbf{n}}_1 \times \hat{\mathbf{n}}_{\text{sc}})|} \arccos(-\hat{\mathbf{n}}_1 \cdot \hat{\mathbf{n}}_{\text{sc}}),$$

where if we denote by  $q_i = q_{i1} + q_{i2}$  the three-momentum, in the  $X$  rest frame, of  $Z_i$  (the first term in the sum being the three-momentum of the negatively charged decay lepton, the second being the positively charged one), the normal vectors to the three planes are defined as

$$\hat{\mathbf{n}}_1 = \frac{q_{11} \times q_{12}}{|q_{11} \times q_{12}|},$$

$$\hat{\mathbf{n}}_2 = \frac{q_{21} \times q_{22}}{|q_{21} \times q_{22}|},$$

$$\hat{\mathbf{n}}_{\text{sc}} = \frac{\hat{\mathbf{n}}_z \times q_1}{|\hat{\mathbf{n}}_z \times q_1|}.$$

- the angles  $\theta_1, \theta_2$  are defined as

$$\theta_1 = \arccos\left(-\frac{\hat{\mathbf{q}}_2 \cdot q_{11}}{|\hat{\mathbf{q}}_2||\hat{\mathbf{q}}_{11}|}\right),$$

$$\theta_2 = \arccos\left(-\frac{\hat{\mathbf{q}}_1 \cdot q_{21}}{|\hat{\mathbf{q}}_1||\hat{\mathbf{q}}_{21}|}\right),$$

where this time all three-momenta are in the  $Z_i$  rest frame.

In the following (especially in Sec. A.3) we will sometimes use the convenient substitution  $\psi = \phi_1 + \phi/2$ ,  $\psi \in [-\pi, \pi]$ , and define the set

$$\Omega = \{\cos \theta^*, \phi_1, \cos \theta_1, \cos \theta_2, \phi\}.$$

It has to be noted that the angle  $\phi^*$  offset is arbitrary and is therefore not used in the subsequent analysis. The definition of the five relevant angles is sketched in Fig. 4.12.

## 4.2.2 Angular Distributions

The differential angular and mass final state distribution in the spin  $J$  hypothesis can be written as<sup>10</sup>

$$\frac{d\Gamma_J(m_1, m_2, \Omega)}{dm_1 dm_2 d\Omega} \propto P(m_1, m_2) \cdot \frac{d\Gamma_J(\Omega)}{d\Omega}, \quad (4.1)$$

<sup>10</sup>We will not use momentum and rapidity of the  $X$  boson in the following, despite the fact that they depend on the production process, since the QCD uncertainties on their determination are high.

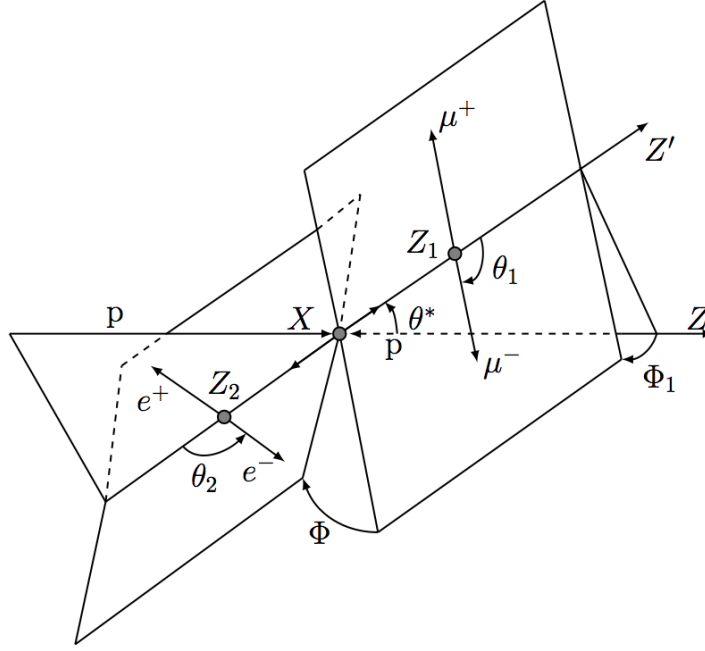


**Figure 4.12.** Definition of the five production and decay angles in the  $X \rightarrow ZZ^{(*)} \rightarrow 4\ell$  decay.

where the term  $P(m_1, m_2)$  is

$$P(m_1, m_2) = \left[ 1 - \frac{(m_1 + m_2)^2}{m_X^2} \right] \cdot \left[ 1 - \frac{(m_1 - m_2)^2}{m_X^2} \right] \cdot \frac{m_1^3}{(m_1^2 - m_Z^2)^2 + m_Z^2 \Gamma_Z^2} \cdot \frac{m_2^3}{(m_2^2 - m_Z^2)^2 + m_Z^2 \Gamma_Z^2}, \quad (4.2)$$

where  $\Gamma_Z$  is the total decay width of the  $Z$  boson, and  $m_Z$  its mass.

After integrating over the five angular variables, one gets

$$\frac{d\Gamma_J}{dm_1 dm_2} \propto \sum_{\alpha, \beta=0, -, +} |A_{\alpha\beta}(m_1, m_2)|^2 \cdot P(m_1, m_2), \quad (4.3)$$

where  $A_{\alpha\beta}$  are decay amplitudes, which are characteristic of the spin and coupling hypothesis.

In the following we will review the main features of the decay amplitudes for spin states  $J = 0, 1, 2$ . Full details on the parametrization of the angular part of Eq. (4.1) are given in Sec. A.3.

### 4.2.3 Decay Amplitudes

In this section we will show the general scattering amplitudes that describe the interaction  $X \rightarrow Z_1 Z_2$ . We will assume each of the  $Z$  bosons has a transverse polarization vector  $\epsilon_i$ , so that  $q_i \epsilon_i = 0$ , and a field strength tensor  $f^{(i), \mu\nu} = \epsilon_i^\mu q_i^\nu - \epsilon_i^\nu q_i^\mu$  whose conjugate is  $\tilde{f}_{\mu\nu}^{(i)} = 1/2 \epsilon_{\mu\nu\alpha\beta} f^{(i), \alpha\beta}$ ; the  $X$  boson will have a polarization vector

$\epsilon_X$ . We will also denote by  $\tilde{q} = q_1 - q_2$  the difference between the momenta of the two  $Z$  bosons, and in the case of spin 2 we will use the symmetric traceless tensor  $t_{\mu\nu}$  which is transverse to the momentum of the particle  $X$ ,  $t_{\mu\nu}q^\nu = 0$ , and is reported on Ref. [42]. We will use  $\Lambda$  to denote the scale at which new physics could appear, and  $v$  to denote the vacuum expectation value of the field associated to  $X$ .

### Spin Zero

If the spin  $J$  of the boson  $X$  is zero, one can write the more general  $X \rightarrow Z_1 Z_2$  scattering amplitude as

$$A(X \rightarrow Z_1 Z_2) = v^{-1} \left( g_1 m_Z^2 \epsilon_1^* \epsilon_2^* + g_2 f_{\mu\nu}^{*(1)} f^{*(2),\mu\nu} + g_3 f^{*(1),\mu\nu} f_{\mu\alpha}^{*(2)} \frac{q_\nu q^\alpha}{\Lambda^2} + g_4 f_{\mu\nu}^{*(1)} \tilde{f}^{*(2),\mu\nu} \right), \quad (4.4)$$

where the couplings  $g_i$  are in general complex momentum-dependent form factors. If we make the assumption they are constants<sup>11</sup>, Eq. 4.4 can be written as

$$A(X \rightarrow Z_1 Z_2) = v^{-1} \epsilon_1^{*\mu} \epsilon_2^{*\nu} \left( a_1 g_{\mu\nu} m_X^2 + a_2 q_\mu q_\nu + a_3 \epsilon_{\mu\nu\alpha\beta} q_1^\alpha q_2^\beta \right), \quad (4.5)$$

where the coefficients  $a_i$  are related to the couplings  $g_i$  by

$$\begin{aligned} a_1 &= g_1 \frac{m_Z^2}{m_X^2} + \frac{s}{m_X^2} \left( 2g_2 + g_3 \frac{s}{\Lambda^2} \right), \\ a_2 &= - \left( 2g_2 + g_3 \frac{s}{\Lambda^2} \right), \\ a_3 &= -2g_4. \end{aligned}$$

with

$$s = q_1 q_2 = \frac{m_X^2 - m_1^2 - m_2^2}{2}.$$

The explicit form of the decay amplitudes in the spin zero case is, in the helicity base<sup>12</sup>,

$$\begin{aligned} A_{00} &= -\frac{m_X^2}{v} \left( a_1 \sqrt{1+x} + a_2 \frac{m_1 m_2}{m_X^2} x \right), \\ A_{++} &= \frac{m_X^2}{v} \left( a_1 + i a_3 \frac{m_1 m_2}{m_X^2} \sqrt{x} \right), \\ A_{--} &= \frac{m_X^2}{v} \left( a_1 - i a_3 \frac{m_1 m_2}{m_X^2} \sqrt{x} \right), \end{aligned}$$

where  $x$  is defined as

$$x = \left( \frac{m_X^2 - m_1^2 - m_2^2}{2m_1 m_2} \right)^2 - 1.$$

<sup>11</sup>Under this assumption, an effective Lagrangian density can be written, where terms with  $g_1$  are associated with operators of dimension 3, those with  $g_2, g_4$  with operators of dimension 5 and terms with  $g_3$  to operators with dimension 7.

<sup>12</sup>See Sec. 4.2.4 for details

The Standard Model Higgs boson has, at tree level,

$$g_1 = 2v, \quad g_2 = g_3 = g_4 = 0,$$

while small values for  $g_2$  are generated by electroweak radiative corrections<sup>13</sup>, and  $g_4$  is zero up to three-loop corrections.

### Spin One

The general scattering amplitude for a spin 1 boson<sup>14</sup> can be written as

$$A(X \rightarrow Z_1 Z_2) = b_1 [(\epsilon_1^* q)(\epsilon_2^* \epsilon_X) + (\epsilon_2^* q)(\epsilon_1^* \epsilon_X)] + b_2 \epsilon_{\alpha\mu\nu\beta} \epsilon_X^\alpha \epsilon_1^{*\mu} \epsilon_2^{*\nu} \tilde{q}^\beta. \quad (4.7)$$

The two coupling constants  $b_1, b_2$  are such that, if we assume parity-conserving interactions, a vector resonance corresponds to  $b_1 \neq 0$ , while a pseudo-vector resonance to  $b_2 \neq 0$ .

Full expressions of the decay amplitudes are shown in Sec. A.1.

### Spin Two

The general scattering amplitude for a spin 2 boson can be written as

$$\begin{aligned} A(X \rightarrow Z_1 Z_2) = \Lambda^{-1} & \left[ 2g_1 t_{\mu\nu} f^{*(1)\mu\alpha} f^{*(2)\nu\alpha} + 2g_2 t_{\mu\nu} \frac{q_\alpha q_\beta}{\Lambda^2} f^{*(1)\mu\alpha} f^{*(2)\nu\beta} \right. \\ & + g_3 \frac{\tilde{q}^\beta \tilde{q}^\alpha}{\Lambda^2} t_{\beta\nu} \left( f^{*(1)\mu\nu} f_{\mu\alpha}^{*(2)} + f^{*(2)\mu\nu} f_{\mu\alpha}^{*(1)} \right) + g_4 \frac{\tilde{q}^\nu \tilde{q}^\mu}{\Lambda^2} t_{\mu\nu} f^{*(1)\alpha\beta} f_{\alpha\beta}^{*(2)} \\ & + m_Z^2 \left( 2g_5 t_{\mu\nu} \epsilon_1^{*\mu} \epsilon_2^{*\nu} + 2g_6 \frac{\tilde{q}^\mu q_\alpha}{\Lambda^2} t_{\mu\nu} (\epsilon_1^{*\nu} \epsilon_2^{*\alpha} - \epsilon_1^{*\alpha} \epsilon_2^{*\nu}) \right. \\ & + g_7 \frac{\tilde{q}^\mu \tilde{q}^\nu}{\Lambda^2} t_{\mu\nu} \epsilon_1^* \epsilon_2^* \left. \right) + g_8 \frac{\tilde{q}_\mu \tilde{q}_\nu}{\Lambda^2} t_{\mu\nu} f^{*(1)\alpha\beta} \tilde{f}_{\alpha\beta}^{*(2)} \\ & \left. + m_Z^2 \left( g_9 \frac{t_{\mu\alpha} \tilde{q}^\alpha}{\Lambda^2} \epsilon_{\mu\nu\rho\sigma} \epsilon_1^{*\nu} \epsilon_2^{*\rho} q^\sigma + g_{10} \frac{t_{\mu\alpha} \tilde{q}^\alpha}{\Lambda^4} \epsilon_{\mu\nu\rho\sigma} q^\rho \tilde{q}^\sigma (\epsilon_1^{*\nu} (q \epsilon_2^*) + \epsilon_2^{*\nu} (q \epsilon_1^*)) \right) \right], \quad (4.8) \end{aligned}$$

which is a function of the 10 couplings  $g_i$ . The first seven coupling factors,  $g_1 \dots g_7$ , correspond to a particle with spin-parity state  $J^P = 2^+$ , while the other three,  $g_8, g_9, g_{10}$ , correspond to a  $2^-$  particle. A minimal coupling scenario, where only lowest-order operators are involved, corresponds to the case  $g_1 = g_5 \neq 0$ .

Full expressions of the decay amplitudes are shown in Sec. A.2.

<sup>13</sup>One has  $g_2 = \mathcal{O}(\alpha^2) \approx 10^{-2}$ .

<sup>14</sup>The observation of the 126 GeV resonance also in the  $H \rightarrow \gamma\gamma$  decay channel implies, by the Landau–Yang theorem[43], that spin one states are studied in  $H \rightarrow ZZ^{(*)} \rightarrow 4\ell$  under the assumption that the observed resonances are actually more than one. This is for example true for the model in Ref. [44], hence it is interesting to investigate also the possible  $J = 1$  nature of the new boson.

#### 4.2.4 $CP$ Admixtures

In Eq. (4.6) we have expressed the scattering amplitude for a spin zero  $X$  boson in the *helicity basis*<sup>15</sup>. Helicity  $\lambda$ , i.e. the projection of the spin of a particle along its momentum, is invariant under rotations and is a pseudoscalar, since it changes sign under the parity transformation. Amplitudes expressed in the helicity base are therefore not eigenstates of the charge–conjugation–parity operator,  $CP$ .

To reveal the  $CP$  nature of the spin zero scattering amplitudes we have to use the *transversity base*. Transversity is defined as the projection of the spin of a particle over a plane orthogonal to the momentum of that particle. The amplitudes

$$A_0 = A_{00}, \quad (4.9)$$

$$A_{\parallel} = \frac{1}{\sqrt{2}}(A_{++} + A_{--}), \quad (4.10)$$

$$A_{\perp} = \frac{1}{\sqrt{2}}(A_{++} - A_{--}), \quad (4.11)$$

which are expressed in terms of helicity amplitudes, are eigenstates of  $CP$ :  $A_0$  and  $A_{\parallel}$  correspond to  $CP$ -even states (orbital angular momentum of the two  $Z$  system  $L = 0, 2$ ), while  $A_{\perp}$  corresponds to a  $CP$ -odd state ( $L = 1$ )<sup>16</sup>. Explicitly,

$$\begin{aligned} A_0 &= -\frac{m_X^2}{v} \left( a_1 \sqrt{1+x} + a_2 \frac{m_1 m_2}{m_X} x \right), \\ A_{\parallel} &= \sqrt{2} \frac{m_X^2}{v} a_1, \\ A_{\perp} &= i\sqrt{2} \frac{m_1 m_2}{v} \sqrt{x} a_3. \end{aligned}$$

The  $CP$ -odd term is therefore a function of  $a_3 \propto g_4$ . For a generic boson  $X$  with no definite  $CP$  state, i.e. an *admixture* of  $CP$ -even and  $CP$ -odd components ( $CP$  mixing), we can define a  $CP$ -odd fraction,

$$f_{CP} = \frac{|A_{\perp}|^2}{|A_0|^2 + |A_{\parallel}|^2 + |A_{\perp}|^2}, \quad (4.12)$$

which measures the magnitude of the  $CP$ -odd amplitude with respect to the total decay amplitude. This fraction is in general a function of the event-by-event masses of the two  $Z$  bosons,  $m_1, m_2$ . As it will be shown in Chapter 7, integrating Eq. (4.12) over  $m_1, m_2$  one can obtain an effective fraction of  $CP$ -odd component for the boson  $X$ .

<sup>15</sup>Total angular momentum conservation requires the helicity  $\lambda_i$  of the two decay vector bosons to be the same, i.e.  $\lambda_1 = \lambda_2 = \lambda$ . This explains why  $A_{00}, A_{++}$  and  $A_{--}$  are sufficient to describe the spin zero decay.

<sup>16</sup>The system of two vector bosons transforms under  $CP$  as  $CP |Z_1 Z_2\rangle = (-1)^L |Z_1 Z_2\rangle$ .

## Chapter 5

# Signal Extraction

The first goal of this thesis work was to search for the Higgs boson in the  $H \rightarrow ZZ^{(*)} \rightarrow 4\ell$  decay channel. Event selection criteria – such as kinematic cuts, isolation and impact parameter requirements – have been optimized on Monte Carlo simulation to improve the sensitivity in the low Higgs mass region. Tools have been deployed and validated to improve mass resolution and sensitivity using full information from the final state leptons. In this chapter, the analysis of the full 2011 and 2012 data samples collected by the ATLAS experiment is presented, and results on the search of the Higgs boson are discussed.

### 5.1 Data Samples

#### 5.1.1 Collision Data

Proton–proton collision data from the 2011 and 2012 ATLAS data taking are used, provided that each detector component relevant for the event reconstruction was operating normally during the data taking (*data quality requirements*). The resulting integrated luminosities corresponding to each of the four final states ( $4\mu, 2\mu 2e + 2e 2\mu, 4e$ ) are  $4.6 \text{ fb}^{-1}$  for  $\sqrt{s} = 7 \text{ TeV}$  and  $20.7 \text{ fb}^{-1}$  for  $\sqrt{s} = 8 \text{ TeV}$ .

#### 5.1.2 Monte Carlo Simulation

Events for signal and background processes are generated using the Monte Carlo simulators presented below. Full simulation of each event is performed using the ATLAS detector simulation[61] within the GEANT4 framework[62]. Pile-up interactions, i.e. additional  $pp$  interactions in the same and in nearby bunch crossings, are included in the simulation. Simulated events are re-weighted to reproduce the observed distribution of the mean number of interactions per bunch crossing in data (shown in Fig. 2.4).

#### Signal

Signal processes are modelled using the POWHEG Monte Carlo event generator[38], where gluon fusion (ggF) and vector boson fusion (VBF) production mechanisms are calculated separately, using matrix elements up to the next-to-leading-order. As

discussed in Sec. 4.1, Higgs transverse momentum is reweighted to the HqT spectrum to NLO+NNLL. POWHEG is interfaced to PYTHIA for showering and hadronization, which in turn is interfaced to PHOTOS[45] for final state QED radiative corrections and to TAUOLA[46] for the simulation of the decays of  $\tau$ -leptons. PYTHIA is used to simulate the production of a Higgs boson in association with vector bosons,  $W$  or  $H$ .

Production cross-sections and decay branching ratios, and the relative uncertainties, are taken from Ref. [7]. Cross-sections for the ggF process have been calculated at NLO[8, 47] and NNLO[50] in QCD, and NNLL QCD soft-gluon resummations[51] and NLO electroweak radiative corrections[52] are applied. Cross-sections for the VBF process are calculated with full NLO QCD and EW corrections[53] and approximate NNLO QCD corrections[54]. For the associated production  $WH/ZH$ , cross-sections are calculated at NLO[55] and NNLO[56] in QCD and NLO electroweak radiative corrections[57] are applied. Branching ratios are predicted by PROPHECY4F[58], which includes the complete NLO QCD and electroweak corrections, the interference effects between identical final-state fermions described in Sec. 4.1 and the leading two-loop heavy Higgs boson corrections to the four-fermion decay width.

Cross-section uncertainties arise from:

- QCD scale uncertainties, which for  $m_H = 125$  GeV amount to  ${}^{+7}_{-8}\%$  for ggF and  $\pm 1\%$  for VBF and VH production mechanisms;
- uncertainties in the parton distribution functions (PDF) and  $\alpha_s$ , which yield an uncertainty of  $\pm 8\%$  for gluon-initiated processes and  $\pm 4\%$  for quark-initiated processes;
- the fact that cross-section calculations do not take into account the Higgs width<sup>1</sup>: above  $m_H = 300$  GeV, an uncertainty of  $150\% \times m_H^3$ , with  $m_H$  in TeV, is applied.

Table 5.1 shows the production cross-section and decay branching ratios for  $H \rightarrow ZZ^{(*)} \rightarrow 4\ell$ , for various Higgs mass hypotheses  $m_H$ . These values are used to normalize the signal MC samples to the data luminosity.

### Irreducible Background

The  $ZZ^{(*)}$  continuum background is simulated using POWHEG[59] for  $qq$  production and GG2ZZ[60] for  $gg$  production. Inclusive cross-section and invariant mass ( $m_{4\ell}$ ) shape are taken from MCFM[40], which includes both processes at NLO in QCD.

Uncertainties on the irreducible background cross-section arise from QCD scale uncertainty ( $\pm 5\%$ ) and PDF and  $\alpha_s$  uncertainties ( $\pm 4\%$  for quark-initiated processes and  $\pm 8\%$  for gluon-initiated processes).

### Reducible Backgrounds

The  $Z + jj$  background is simulated using ALPGEN[63] and is divided into two sources:  $Z +$  light jets — which includes  $Z + c\bar{c}$  in the massless  $c$ -quark approximation and

<sup>1</sup>A Breit-Wigner line shape is nevertheless applied at generator level.

$m_H$ [GeV]	$\sigma(gg \rightarrow H)$ [pb]	$\sigma(qq' \rightarrow Hqq')$ [pb]	$\sigma(q\bar{q} \rightarrow WH)$ [pb]	$\sigma(q\bar{q} \rightarrow ZH)$ [pb]	BR( $H \rightarrow ZZ^{(*)} \rightarrow 4\ell$ ) [ $10^{-3}$ ]
$\sqrt{s} = 7\text{TeV}$					
123	$15.8^{+2.3}_{-2.4}$	$1.25 \pm 0.03$	$0.60^{+0.02}_{-0.03}$	$0.33 \pm 0.02$	0.103
125	$15.3 \pm 2.3$	$1.22 \pm 0.03$	$0.57 \pm 0.02$	$0.32 \pm 0.02$	0.125
127	$14.9 \pm 2.2$	$1.20 \pm 0.03$	$0.54 \pm 0.02$	$0.30 \pm 0.02$	0.148
400	$2.05^{+0.30}_{-0.29}$	$0.18 \pm 0.01$	—	—	1.21
600	$0.34^{+0.06}_{-0.05}$	$0.062^{+0.005}_{-0.002}$	—	—	1.23
$\sqrt{s} = 8\text{TeV}$					
123	$20.2 \pm 3.0$	$1.61 \pm 0.05$	$0.73 \pm 0.03$	$0.42 \pm 0.02$	0.103
125	$19.5 \pm 2.9$	$1.58^{+0.04}_{-0.05}$	$0.70 \pm 0.03$	$0.39 \pm 0.02$	0.125
127	$18.9 \pm 2.8$	$1.55 \pm 0.05$	$0.66^{+0.02}_{-0.03}$	$0.37 \pm 0.02$	0.148
400	$2.92^{+0.41}_{-0.40}$	$0.25 \pm 0.01$	—	—	1.21
600	$0.52^{+0.08}_{-0.07}$	$0.097 \pm 0.004$	—	—	1.23

**Table 5.1.** Production cross-sections of an Higgs boson via ggF, VBF and VH production mechanisms in  $pp$  collisions at  $\sqrt{s} = 7$  and 8 TeV. The decay branching ratio for  $H \rightarrow ZZ^{(*)} \rightarrow 4\ell$ , with  $\ell = e, \mu$  is also reported. Uncertainties consist of the linear sum of QCD scale and PDF+ $\alpha_s$  uncertainties described in the text. Above 300 GeV the production cross-section for associated production is negligible.

$Z + b\bar{b}$  from parton showers — and  $Z + b\bar{b}$  which uses matrix element calculations that take into account the  $b$ -quark mass. Normalization is taken from data control regions; for comparisons with simulation, QCD NNLO cross-section calculations are used[48].

The  $t\bar{t}$  background is simulated using MC@NLO[64] and normalized to approximate NNLO cross-section calculations[49]. Uncertainties on the  $t\bar{t}$  cross-section arise from QCD scale uncertainty ( $^{+4}_{-9}\%$ ) and PDF and  $\alpha_s$  uncertainties ( $\pm 7\%$ ).

Both ALPGEN and MC@NLO are interfaced to HERWIG[65] for parton shower hadronization and to JIMMY[66] for the underlying event simulation.

## 5.2 Event Selection

### 5.2.1 Trigger

Events are accepted for analysis if they pass online selection requirements which depend on the final state being looked for ( $4\mu, 2\mu 2e + 2e 2\mu, 4e$ ). Single and di-lepton triggers are used: an event must pass either a single lepton or a di-lepton trigger (logic OR). The set of selection requirements is shown in Table 5.2 for the 2012 data taking and Table 5.3 for the 2011 data taking. Isolation requirements, if present, are applied at Event Filter level, by requiring the scalar sum of the  $p_T$  of the inner detector tracks within a cone  $\Delta R < 0.2$  to be less than 10% of the lepton  $p_T$ . Trigger  $p_T/E_T$  thresholds (and the inclusion or not of isolation requirements in the trigger algorithms) have been chosen in order to keep the trigger output rate within the maximum design rate during the data taking. Reconstructed leptons are requested,

Channel	Single-lepton	Di-lepton
4 $\mu$	isolated, $p_T > 24$ GeV	$(p_T^{(1)}, p_T^{(2)}) > (18, 8)$ GeV $(p_T^{(1)}, p_T^{(2)}) > (13, 13)$ GeV
2e2 $\mu$	4 $\mu \vee 4e$	4 $\mu \vee 4e$ $(E_T^{(e)}, p_T^{(\mu)}) > (12, 10)$ GeV $(E_T^{(e)}, p_T^{(\mu)}) > (24, 8)$ GeV
4e	isolated, $E_T > 24$ GeV	$(E_T^{(1)}, E_T^{(2)}) > (12, 12)$ GeV

**Table 5.2.** Summary of the triggers used during the 2012 data taking for the final states. When multiple triggers are indicated (rows), the logic OR among them,  $\vee$ , is requested.

Channel	Single-lepton	Di-lepton
4 $\mu$	$p_T > 18$ GeV	$(p_T^{(1)}, p_T^{(2)}) > (10, 10)$ GeV
2e2 $\mu$	4 $\mu \vee 4e$	4 $\mu \vee 4e$
4e	$E_T > 20 \div 22$ GeV	$(E_T^{(1)}, E_T^{(2)}) > (12, 12)$ GeV

**Table 5.3.** Summary of the triggers used during the 2011 data taking for the final states. The  $E_T$  threshold of the single electron trigger varied during the data taking, corresponding to different detector conditions (increasing interaction rate).

at analysis level, to match the trigger which selected the event<sup>2</sup>.

The trigger efficiency, i.e. the efficiency of the trigger requirements described above with respect to the full analysis selection criteria, computed on a signal sample with gluon–fusion production of an Higgs boson of mass  $m_H = 130$  GeV is 97.6% for the 4 $\mu$  channel, 97.3% for the 2e2 $\mu$  channel and 99.7% for the 4e channel. Trigger efficiency is measured, as a function of electron  $\eta$  or muon  $\eta, \phi$ , in data and MC using events from  $Z \rightarrow ee$  and  $Z \rightarrow \mu\mu$  decays: simulated events are weighted with a scale factor which accounts for residual differences between data and MC efficiencies<sup>3</sup>.

## 5.2.2 Leptons

### Electrons

Electrons with pseudorapidity of the associated cluster  $|\eta| < 2.47$  and  $E_T > 7$  GeV are used. They are reconstructed as explained in Sec. 3.3. Electrons used for the analysis of 8 TeV (7 TeV) data and Monte Carlo are required to pass the MultiLepton (loose++) identification criteria described in Sec. 3.3.3.

<sup>2</sup>In other words, the reconstructed lepton(s) must be compatible in  $\Delta R$  with the corresponding lepton(s) reconstructed by the Event Filter algorithms.

<sup>3</sup>In the single lepton trigger case, this scale factor  $SF$  can be written as

$$SF = \frac{1 - \prod_i (1 - \epsilon_{\text{data}}(\mathbf{v}_i))}{1 - \prod_i (1 - \epsilon_{\text{MC}}(\mathbf{v}_i))},$$

where  $\epsilon$  is the trigger efficiency in data or MC and  $\mathbf{v}_i$  is the three–momentum of the  $i$ -th lepton forming the Higgs candidate.

Electrons must be compatible with the primary vertex<sup>4</sup> in terms of their longitudinal impact parameter,  $|z_0| < 10$  mm.

### Muons

Combined muons (CB) are used in the pseudorapidity region  $|\eta| < 2.5$ , while stand-alone muons (SA) are used for  $2.5 < |\eta| < 2.7$ . In both cases, a lower  $p_T$  cut at 6 GeV is applied. Acceptance is recovered in the central region of the detector by using calorimeter-tagged muons (CT) for  $|\eta| < 0.1$  if they satisfy the requirement  $p_T > 15$  GeV and if they do not share the same ID track of any reconstructed electron.

The same selection cut as for electrons,  $|z_0| < 10$  mm, is applied to reject muons displaced with respect to the primary vertex. Muons coming from cosmic rays are rejected by a requirement on their transverse impact parameter,  $d_0 < 1$  mm.

### 5.2.3 Candidates

Among all selected leptons, Higgs candidates are formed using all possible pairs of two leptons with same flavour and opposite charge. The highest- $p_T$  lepton of each quadruplet must have  $p_T > 20$  GeV, the second lepton  $p_T > 15$  GeV and the third one  $p_T > 10$  GeV.

Within each quadruplet, dileptons are ordered according to the distance between their invariant mass and  $m_Z$ : the closest one has mass  $m_1$  and is called  $Z_1$ , the other one (which is possibly off-shell) has mass  $m_2$  and is called  $Z_2$ . If at this stage there is more than one selected quadruplet, the one with lower  $\delta_Z = |m_1 - m_Z|$  is selected; if two candidates share the same  $\delta_Z$ , the one with highest  $m_2$  is taken.

The following selection criteria are then applied to the selected quadruplet:

1. leptons must be separated in  $\Delta R$ , with a lower threshold of 0.1 for leptons of the same flavour and — to reject photons coming from muon bremsstrahlung and misidentified as electrons — 0.2 for opposite flavour leptons;
2. in order to remove contamination from  $J\psi$  decays, none of the possible dilepton pairs within the quadruplet can have an invariant mass  $m_{2\ell} < 5$  GeV;
3. the mass of the first dilepton must satisfy the relation  $50 < m_1 < 106$  GeV;
4. the invariant mass of the other dilepton object,  $Z_2$ , must satisfy  $m_{\text{thr}} < m_2 < 115$  GeV, where  $m_{\text{thr}}$  depends on  $m_{4\ell}$  as

$$m_{\text{thr}} = \begin{cases} 12 \text{ GeV} & \text{if } m_{4\ell} < 140 \text{ GeV}, \\ 12 \text{ GeV} + \frac{m_{4\ell} - 140 \text{ GeV}}{190 \text{ GeV} - 140 \text{ GeV}} \cdot (38 \text{ GeV}) & \text{if } 140 < m_{4\ell} < 190 \text{ GeV}, \\ 50 \text{ GeV} & \text{if } m_{4\ell} > 190 \text{ GeV}; \end{cases}$$

<sup>4</sup>A primary vertex must have been reconstructed (see Sec. 3.1.3) by at least 3 inner detector tracks.

5. track isolation criteria are applied on the four decay leptons (electrons and combined, segment-tagged and calorimeter-tagged muons<sup>5</sup>), requiring

$$\sum_{\Delta R < 0.2} p_{\text{T}}^{(i)} / p_{\text{T}} < 15\% \text{ (CB, ST, CT muons),}$$

$$\sum_{\Delta R < 0.2} p_{\text{T}}^{(i)} / E_{\text{T}} < 15\% \text{ (electrons),}$$

where the sum runs over all tracks reconstructed in the inner detector, without any contribution from the leptons within the quadruplet;

6. calorimetric isolation criteria<sup>6</sup> are applied: for electrons,

$$\sum_{\Delta R < 0.2} E_{\text{T}}^{(i)} / p_{\text{T}} < 30\% \text{ (CB, ST, CT muons),}$$

$$\sum_{\Delta R < 0.2} E_{\text{T}}^{(i)} / p_{\text{T}} < 15\% \text{ (SA muons),}$$

$$\sum_{\Delta R < 0.2} E_{\text{T}}^{(i)} / E_{\text{T}} < 20(30)\% \text{ (electrons),}$$

where two values are indicated for electrons referring to 8(7) TeV analyses<sup>7</sup>, and contribution from leptons within the quadruplet which are in the cone  $\Delta R < 0.18$  around the considered lepton is removed;

7. impact parameter significance of the leptons should satisfy the requirements<sup>8</sup>

$$|d_0| / \sigma(d_0) < 3.5 \text{ (muons),}$$

$$|d_0| / \sigma(d_0) < 6.5 \text{ (electrons).}$$

### 5.3 Mass Resolution

The mass of the four lepton system,  $m_{4\ell}$ , is the discriminating variable between signal and backgrounds. The true mass of the Higgs boson,  $m_H$ , is inferred from the  $m_{4\ell}$  distribution: it is therefore crucial to obtain a high four lepton mass resolution. Fig. 5.1 shows the resolution on  $m_{4\ell}$  and the intrinsic width of the Higgs boson,  $\Gamma_H$ , as a function of  $m_H$ : resolution effects are dominant up to about 350 GeV, hence in the low mass region improvements in mass resolution yield significant improvements in the signal sensitivity.

Two are the corrections applied to improve mass resolution: recovery of photons from final state radiation, and the  $Z$  mass constraint fit.

<sup>5</sup>Stand-alone muons do not have an associated inner detector track.

<sup>6</sup>Calorimetric isolation, which is in principle pile-up sensitive (lower selection efficiency at higher  $\mu$ ), is corrected subtracting the average amount of energy deposit in the calorimeter as a function of the average number of interactions per bunch crossing. Track isolation is less pile-up sensitive, since selection cuts, which sensibly reduce the fraction of tracks not coming from the primary vertex, are applied on tracks used in the isolation computation.

<sup>7</sup>The 8 TeV cut is stricter due to the higher average number of interactions per bunch crossing in the 2012 data taking.

<sup>8</sup>The impact parameter selection requirement on electrons is less stringent than for muons, since for electrons impact parameter resolution is affected by bremsstrahlung.

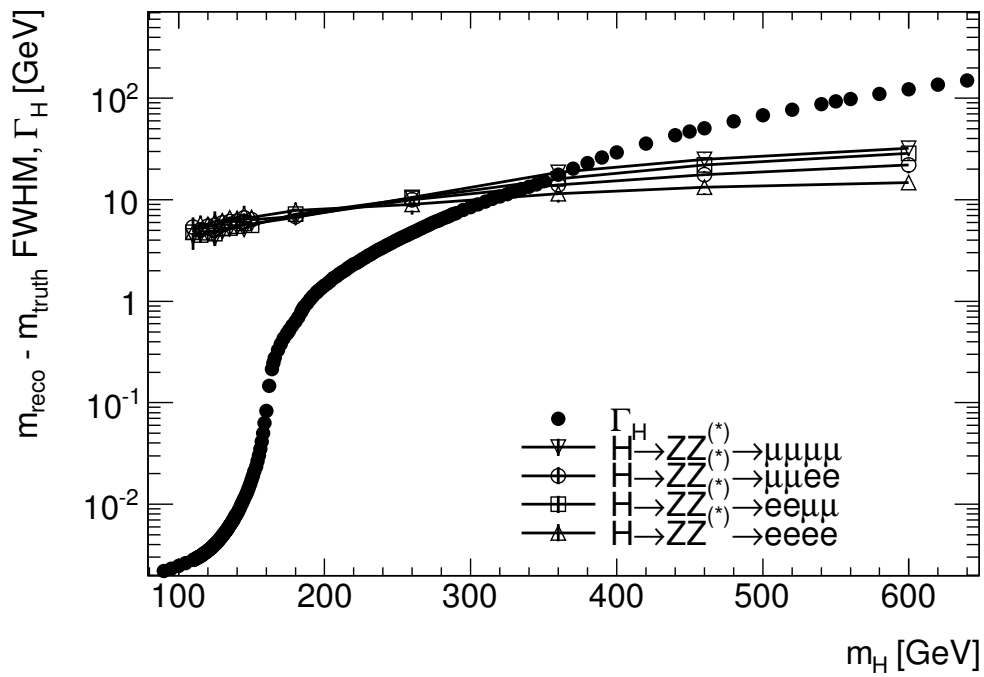


**Figure 5.1.** Intrinsic width of the Higgs boson,  $\Gamma_H$ , and mass resolution for the four final states, as a function of  $m_H$ . Mass resolution is estimated from signal MC as the full width at half maximum (FWHM) of the resolution  $m_{4\ell} - m_{4\ell}^{\text{true}}$ , where  $m_{4\ell}^{\text{true}}$  is the true mass of the Higgs boson in the generated event.

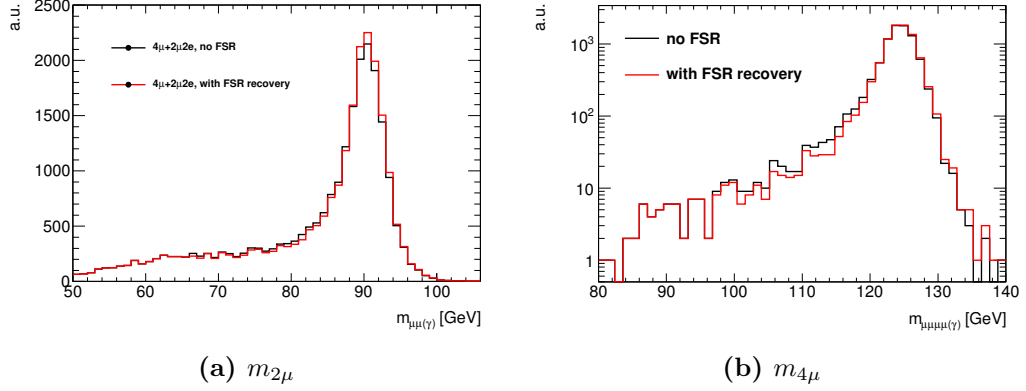


**Figure 5.2.** Effect of FSR recovery on  $Z_1$  in  $4\mu$  and  $2\mu 2e$  final states and  $H \rightarrow 4\mu$  mass distribution for a simulated Higgs signal at 125 GeV. The standard deviation obtained from a gaussian fit to the  $m_{\mu\mu(\gamma)}$  distribution is  $2.77 \pm 0.03$  ( $2.90 \pm 0.03$ ) GeV with (without) FSR recovery.

### 5.3.1 Final State Radiation Recovery

Final state radiation (FSR) of photons from the decay muons of  $Z_1$  is taken into account[67] by summing up to the lepton momenta photons with an energy above 1 GeV and within  $\Delta R < 0.09$  to 0.15 (with a threshold depending on photon  $E_T$ ). Photons between 1 GeV and 3.5 GeV are reconstructed using the topological algorithm[35], which builds clusters of variable size collecting cells around a seeding cell with an energy above a certain signal to noise threshold. Photons above 3.5 GeV are reconstructed using the same sliding window algorithm used for electrons (described in Sec. 3.3.2).

This correction is applied when  $66 < m_1 < 89$  GeV and the corrected  $Z_1$  invariant mass satisfies  $m_{\mu\mu\gamma} < 100$  GeV. It affects about 4% of all selected signal events, as estimated from Monte Carlo simulation. Fig. 5.2 shows the effect of the inclusion of FSR photons both on  $Z_1$  mass distribution and on  $m_{4\ell}$ , for a simulated Higgs signal with  $m_H = 125$  GeV.

### 5.3.2 The $Z$ Mass Constraint Fit

Mass resolution can be further improved by using the fact that the invariant mass of pairs of leptons coming from an on-shell  $Z$  boson is constrained by its intrinsic width  $\Gamma_Z$ . Indeed, the probability distribution of the mass of the  $Z$  boson generated in that single event,  $m_Z^{\text{true}}$ , given the measured dilepton mass  $m_{2\ell}$ , can be written using Bayes' theorem as

$$p(m_Z^{\text{true}}|m_{2\ell}) \propto p(m_{2\ell}|\sigma_{m_{2\ell}}, m_Z^{\text{true}}) \cdot p(m_Z^{\text{true}}|m_Z, \Gamma_Z), \quad (5.1)$$

where we recognize on the RHS:

- a resolution function, which describes the smearing of the reconstructed dilepton mass — due to lepton momentum resolution, which yields an uncertainty<sup>9</sup>  $\sigma_{m_{2\ell}}$  on  $m_{2\ell}$  — around  $m_Z^{\text{true}}$ ;

<sup>9</sup>The dilepton mass uncertainty is computed using the covariance matrix associated to muons,

- the a-priori probability of producing a  $Z$  boson with mass  $m_Z^{\text{true}}$ , given its mass pole  $m_Z$  and its intrinsic width.

The aim of the  $Z$  mass constraint fit is to first obtain in each event the maximum likelihood estimate of  $m_Z^{\text{true}}$  by maximizing Eq. (5.1), and to change the momenta (and covariance matrices) of the  $n$  decay particles (two electrons, two muons or two muons and a FSR photon) under the constraint

$$m_{2\ell} = m_Z^{\text{true}}. \quad (5.2)$$

Mathematically, the problem consists of a  $\chi^2$  fit of the particle momenta (a vector  $\mathbf{x}$  of  $3n$  parameters, i.e. 3 momentum components for each of the  $n$  particles, and the corresponding  $n$   $3 \times 3$  covariance matrices  $V$ ) subject to a single non-linear constraint (Eq. (5.2)). It is solved using the formalism of Lagrange multipliers, in which the constraint is written as

$$\begin{aligned} g(\mathbf{x}) &= [E_{\text{tot}}^2 - p_{\text{tot}}^2] - (m_Z^{\text{true}})^2 \\ &= g(\mathbf{x}_0) + \left. \frac{\partial g(\mathbf{x})}{\partial \mathbf{x}} \right|_{\mathbf{x}=\mathbf{x}_0} (\mathbf{x} - \mathbf{x}_0) + \mathcal{O}((\mathbf{x} - \mathbf{x}_0)^2) \\ &\equiv \mathbf{d} + D\Delta\mathbf{x} + \mathcal{O}(\Delta\mathbf{x}^2) = 0, \end{aligned} \quad (5.3)$$

where we have expanded  $g$  around the initial parameters  $\mathbf{x}_0$ . Here  $d, \Delta x$  are vectors with dimension 1 (number of constraints) and  $D$  a matrix with dimension  $1 \times 3n$ . Applying the constraint of Eq. (5.2) is equivalent to the minimization of

$$\chi^2 = (\mathbf{x} - \mathbf{x}_0)^T V_{\mathbf{x}_0}^{-1} (\mathbf{x} - \mathbf{x}_0) + 2\lambda(D\Delta\mathbf{x} + d),$$

where  $\mathbf{x}_0$  are the solutions of the unconstrained problem ( $\lambda = 0$ ).

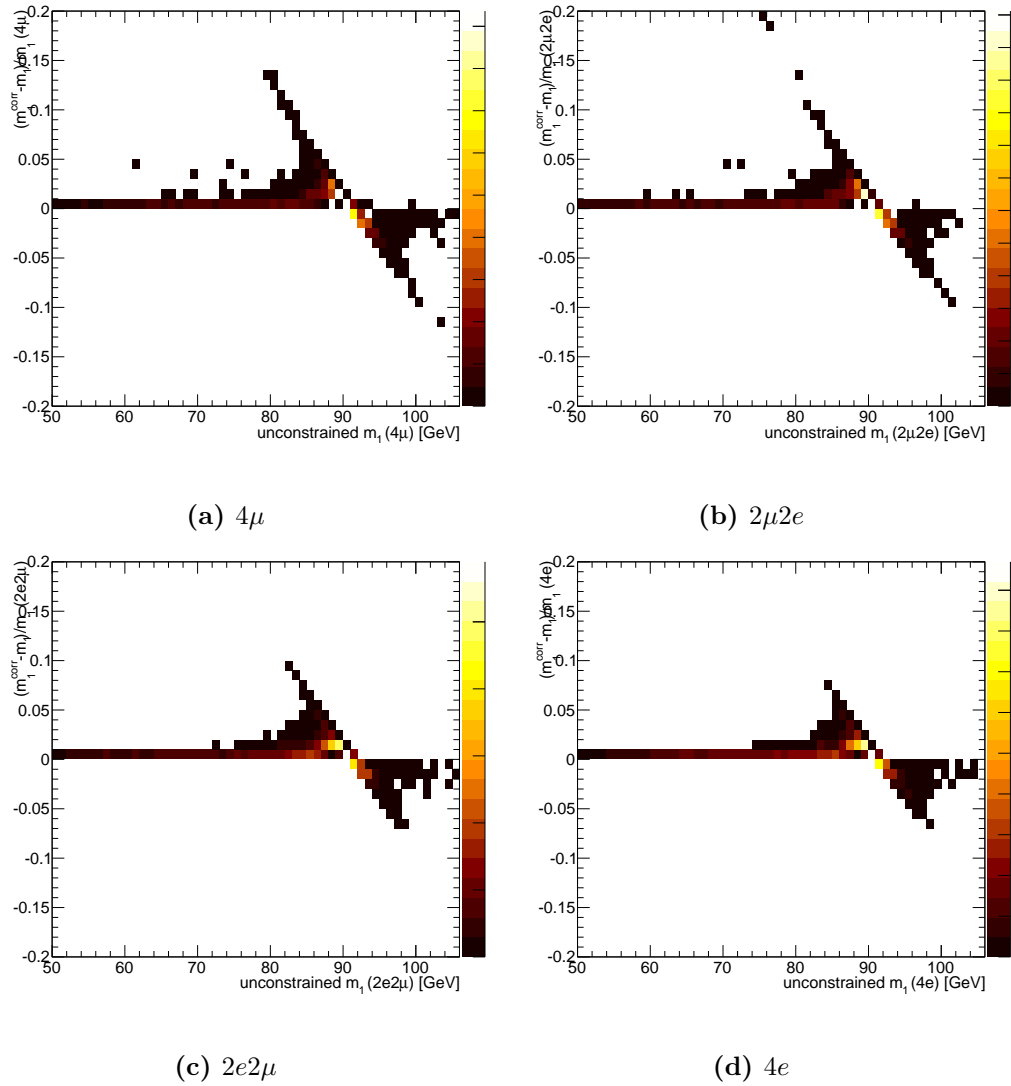
In this way, particle momenta are constrained to the most likely true  $Z$  mass in that event. The higher is the uncertainty on the momentum of a particle, the higher the ‘‘fraction’’ of the correction it is going to take. The estimate of the true  $Z$  mass takes nevertheless into account both (reconstructed) mass resolution and  $Z$  intrinsic width, with the result that when  $|m_{2\ell} - m_Z| \gg 0$  the correction will be minimal, unless momentum uncertainty is high.

The implementation of the  $Z$  mass constraint fit uses a gaussian resolution model and a Breit–Wigner distribution for the prior on  $m_Z$ <sup>10</sup>. Its effect is shown in Fig. 5.3, in terms of the pull between the fitted and the original dilepton mass,  $(m_1^{\text{corr}} - m_1)/m_1$ , as a function of  $m_1 = m_{2\ell}$ . As it can be seen, the effect on the  $m_{2\ell}$  distribution is relevant in the mass region around the  $Z$  mass pole, and is a consequence of the balance between the Breit–Wigner p.d.f. and the mass resolution. Fig. 5.4, 5.5 and 5.6 show the effect on the  $m_{4\ell}$  distribution on a 125 GeV and 360 GeV Higgs boson. The effect on the  $ZZ$  continuum background, as shown in Fig. 5.7, is found to be negligible.

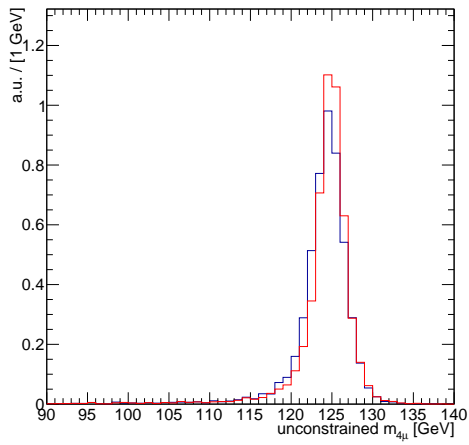
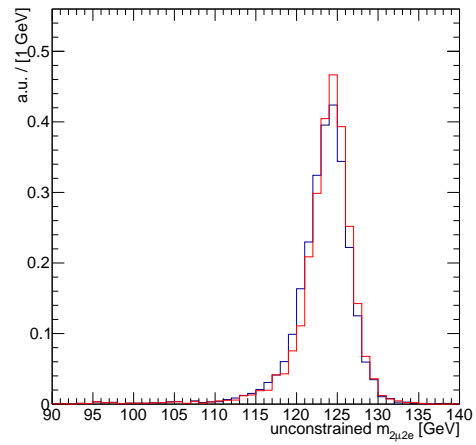
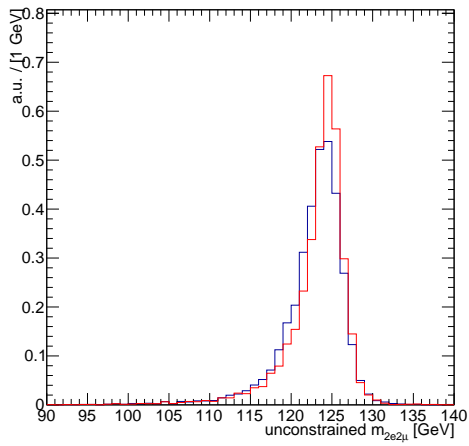
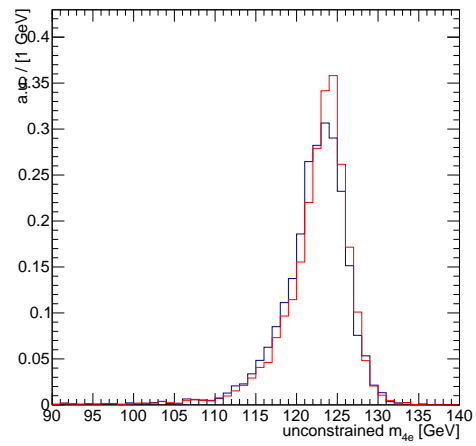
---

electrons and photons, corrected for residual differences in momentum/energy response between data and MC simulation. In the case of electrons, the covariance matrix is built including inner detector uncertainties on the electron direction ( $\eta, \phi$ ) and energy resolution of the calorimeter, while correlations between the ID and ECAL measurements are neglected. In the case of photons, only the energy resolution is used.

<sup>10</sup>The effect of a different choice of the mass resolution model, for example using a Crystal Ball p.d.f. whose parameters are estimated from Monte Carlo, has been found to be negligible within systematic uncertainties on  $m_{2\ell}$ .



**Figure 5.3.** Effect of  $Z$  mass constraint fit, expressed in terms of fractional change  $m_1$  after the constraint, as a function of unconstrained  $m_1$ , for a simulated Higgs boson of 125 GeV.

(a)  $4\mu$ (b)  $2\mu 2e$ (c)  $2e 2\mu$ (d)  $4e$ 

**Figure 5.4.** Comparison between the constrained (red) and unconstrained (black) four-lepton mass, for a simulated Higgs boson of 125 GeV.

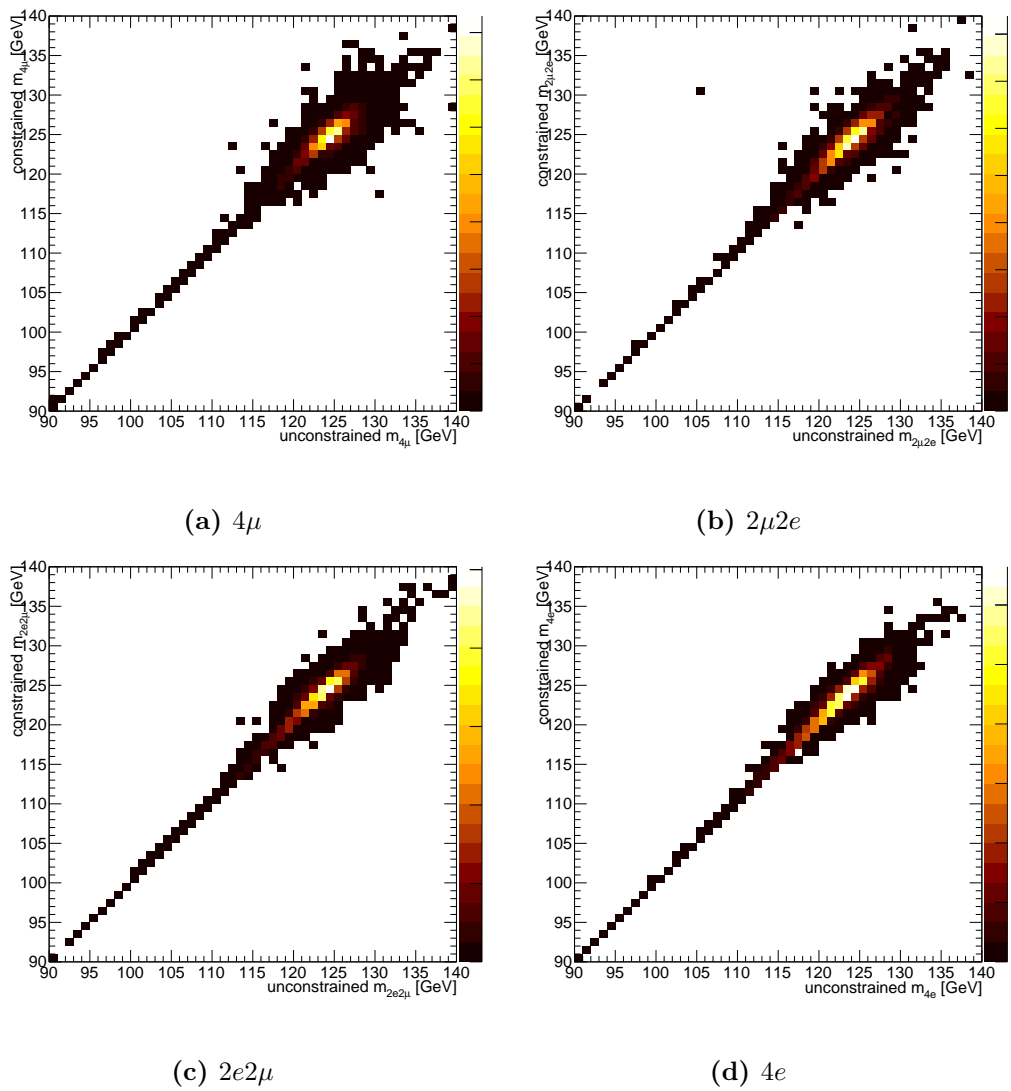


**Figure 5.5.** Correlation between the constrained and unconstrained four-lepton mass, for a simulated Higgs boson of 125 GeV.

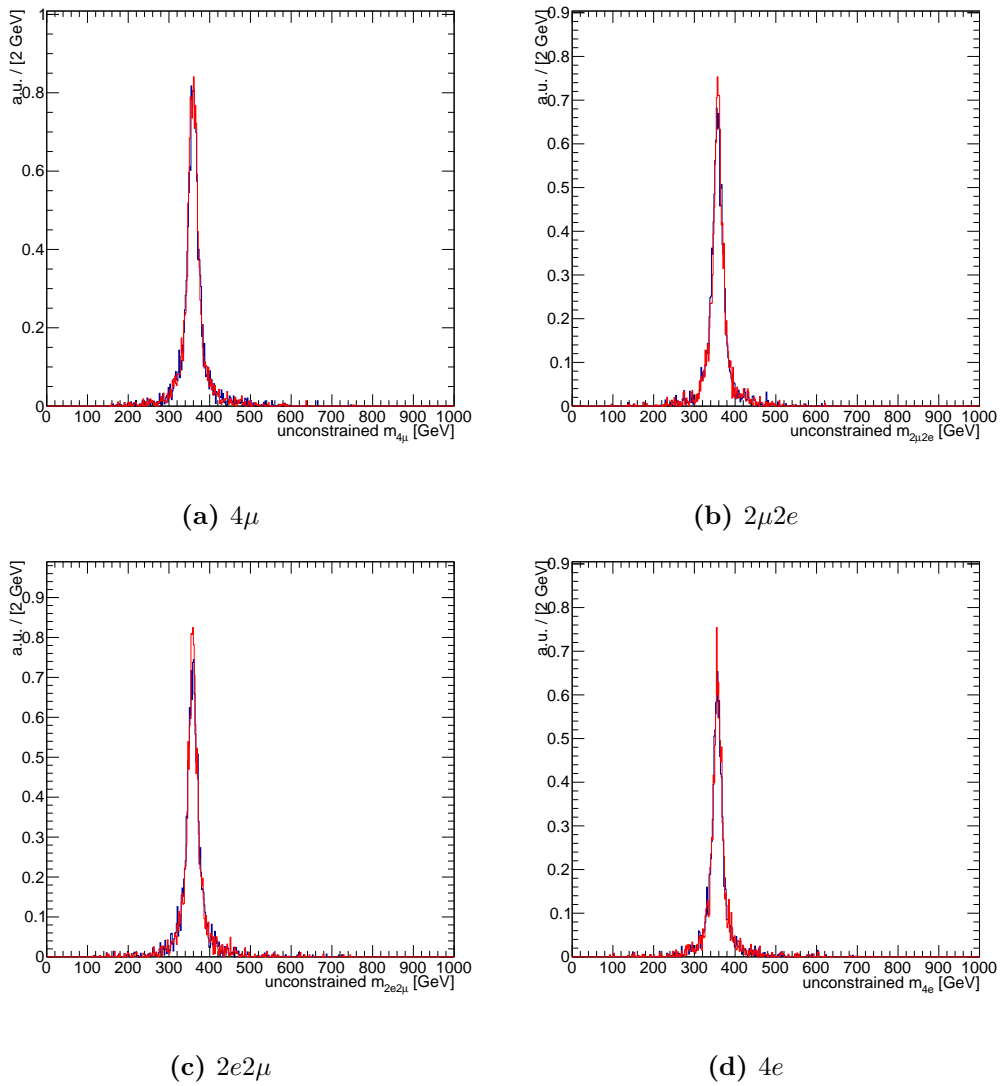


**Figure 5.6.** Correlation between the constrained and unconstrained four-lepton mass, for a simulated Higgs boson of 360 GeV.

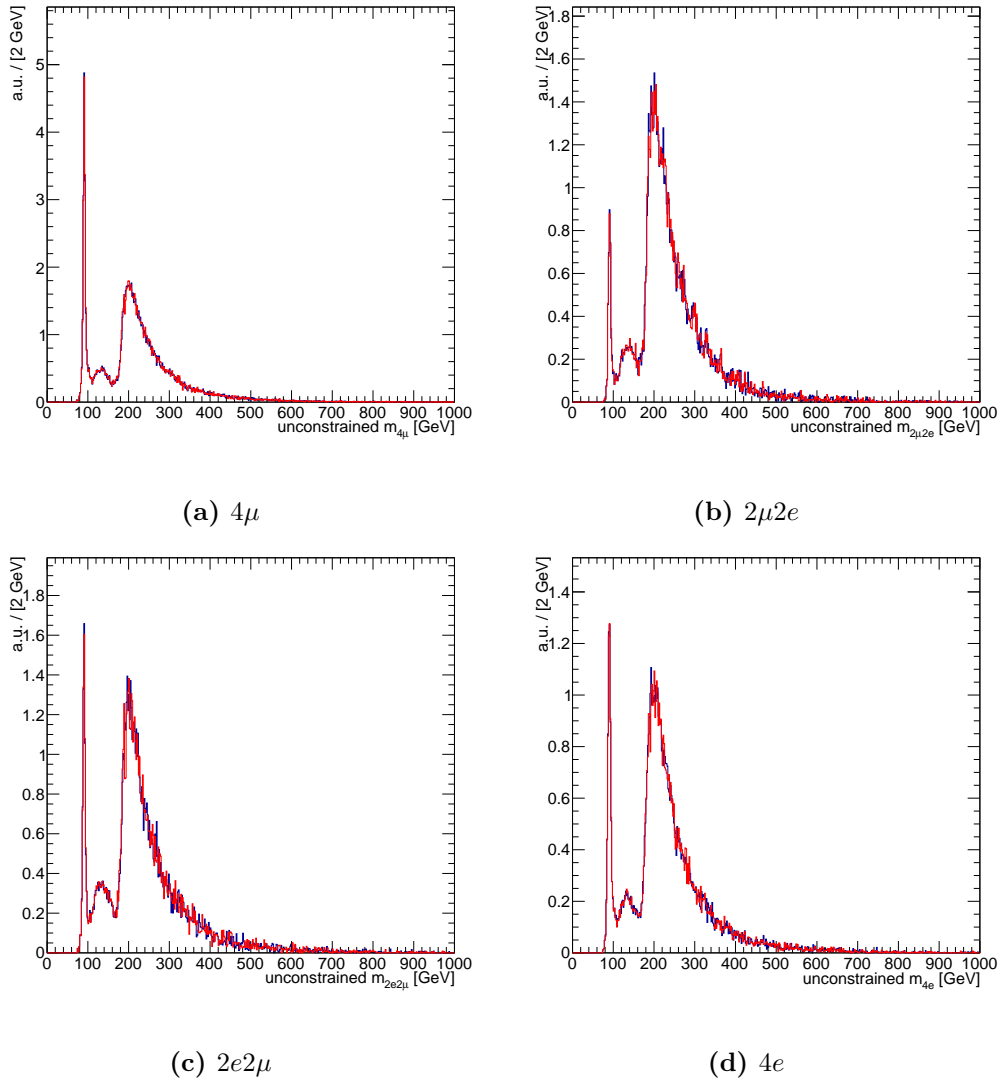


**Figure 5.7.** Comparison between the constrained (red) and unconstrained (blue) four-lepton mass, for the simulated  $ZZ$  background.

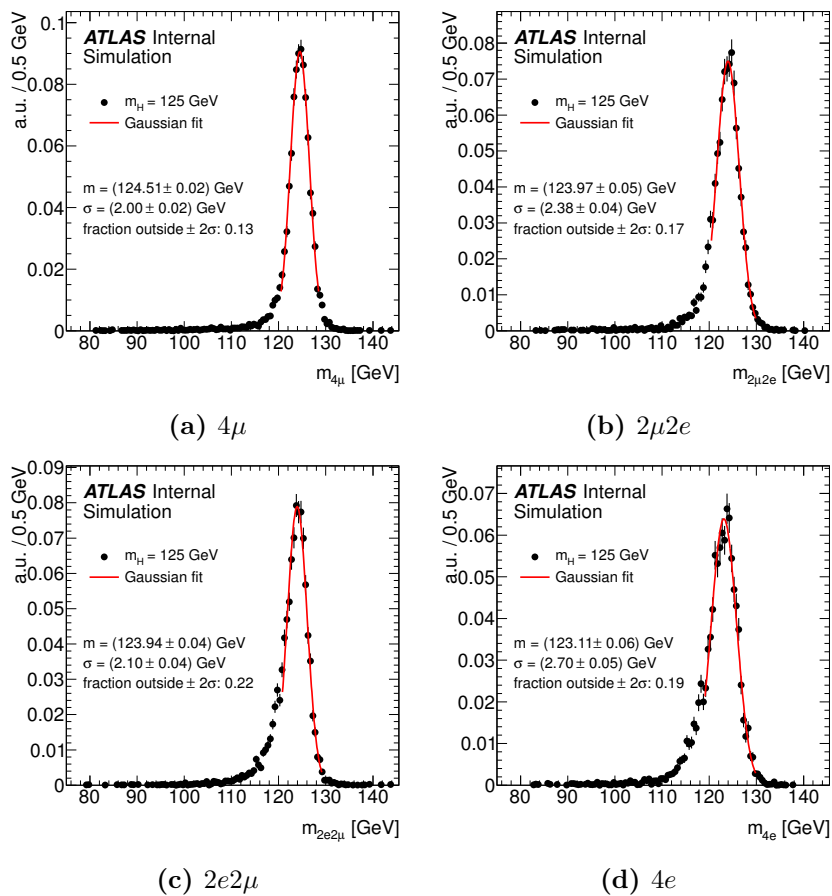


**Figure 5.8.** Four-lepton mass distribution after FSR recovery, for a simulated signal sample with  $m_H = 125$  GeV. A gaussian fit to the  $m_{4\ell}$  peak is superimposed.

### 5.3.3 Results

Mass resolution as a function of pseudorapidity has been studied for a Higgs signal sample with  $m_H = 125$  GeV. Mass resolution is determined by the standard deviation obtained from a fit of the peak of the invariant mass distribution in the four decay channels with a gaussian function<sup>11</sup>.

Fig. 5.8 shows the four-lepton mass distribution without the  $Z$  mass constraint fit, while Fig. 5.9 shows the same distribution after applying the  $Z$  mass constraint fit. Mass resolution after (before) the  $Z$  mass constraint is  $1.64 \pm 0.02$  ( $2.00 \pm 0.02$ ) GeV for the  $4\mu$  final state,  $1.95 \pm 0.03$  ( $2.25 \pm 0.03$ ) GeV for  $2\mu 2e + 2e 2\mu$  and  $2.54 \pm 0.05$  ( $2.70 \pm 0.05$ ) GeV for  $4e$ . Tables 5.4 and 5.5 show the different  $m_{4\ell}$  resolution obtained from gaussian fits to events reconstructed in different detector regions, together with the full-width-at-half-maximum (FWHM) of the fitted distribution, which is an estimate of the overall effect of tails.

<sup>11</sup>The mass fit region is determined iteratively until fit parameters are stable: the mass regions  $\pm 2\sigma$  from the fitted mean  $m_0$  for  $4\mu$  and  $[m_0 - 1.5\sigma, m_0 + 2.5\sigma]$  for the other channels are used, to avoid the tail from FSR and electron bremsstrahlung.

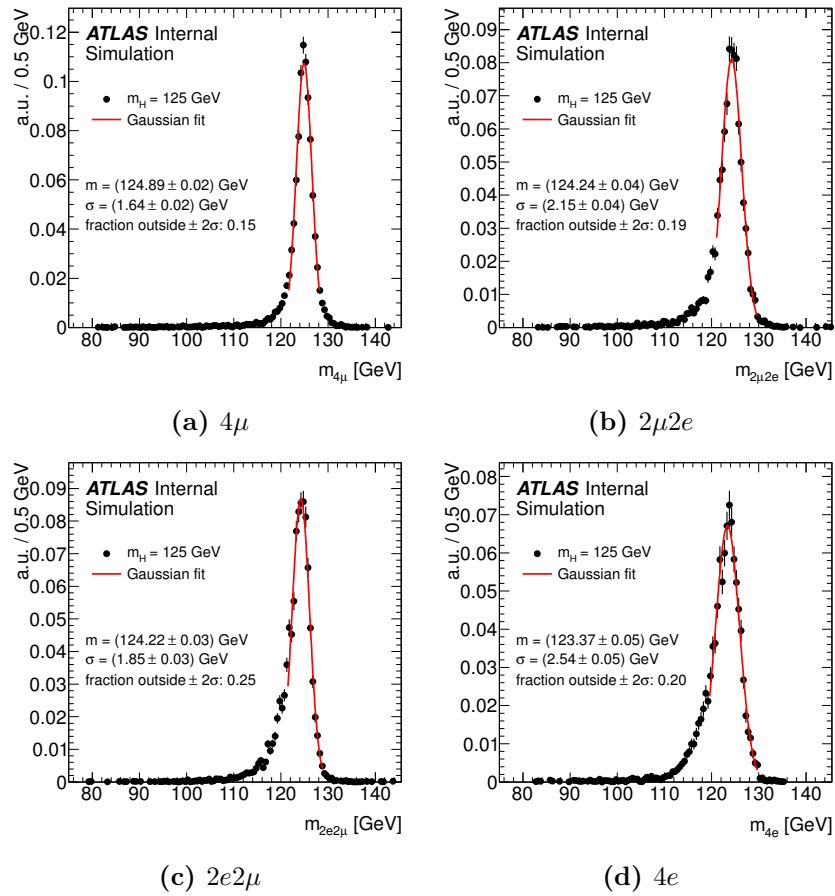


**Figure 5.9.** Four-lepton mass distribution after FSR recovery and the  $Z$  mass constraint fit, for a simulated signal sample with  $m_H = 125$  GeV. A gaussian fit to the  $m_{4\ell}$  peak is superimposed.

**Table 5.4.** Resolution on the four lepton invariant mass, estimated from a signal MC sample ( $m_H = 125\text{GeV}$ ), in different detector reconstruction regions. Barrel for muons is defined as  $|\eta| < 1.05$ ; for electrons, barrel is defined as  $|\eta| < 1.37$ , crack region as  $1.37 < |\eta| < 1.52$ .

channel	name	description	frequency	$m$ [GeV]	$\sigma$ [GeV]	events outside $\pm 2\sigma$	FWHM [GeV]
$\mu\mu\mu\mu$	all	all events	1.00	$124.51 \pm 0.02$	$2.00 \pm 0.02$	0.13	4.0
$\mu\mu\mu\mu$	bbbb	all muons in the barrel	0.19	$124.48 \pm 0.05$	$1.81 \pm 0.05$	0.12	3.5
$\mu\mu\mu\mu$	bbb	three muons in the barrel	0.28	$124.54 \pm 0.05$	$1.92 \pm 0.05$	0.14	3.5
$\mu\mu\mu\mu$	bb	two muons in the barrel	0.26	$124.52 \pm 0.05$	$2.06 \pm 0.05$	0.13	3.5
$\mu\mu\mu\mu$	other	any other event	0.26	$124.62 \pm 0.06$	$2.26 \pm 0.06$	0.11	5.0
$\mu\mu ee$	all	all events	1.00	$123.97 \pm 0.05$	$2.38 \pm 0.04$	0.17	5.0
$\mu\mu ee$	any_onecrk	at least one electron in the crack region	0.10	$123.71 \pm 0.19$	$3.20 \pm 0.05$	0.12	7.5
$\mu\mu ee$	bb_bb	all leptons in the barrel	0.29	$124.11 \pm 0.07$	$1.96 \pm 0.06$	0.17	4.0
$\mu\mu ee$	other_bb	electrons in the barrel, at least a muon in the endcap	0.35	$124.04 \pm 0.07$	$2.34 \pm 0.07$	0.16	4.5
$\mu\mu ee$	other_other	any other event	0.26	$123.65 \pm 0.11$	$2.63 \pm 0.10$	0.16	4.5
$ee\mu\mu$	all	all events	1.00	$123.94 \pm 0.04$	$2.10 \pm 0.04$	0.22	5.0
$ee\mu\mu$	onecrk_any	at least one electron in the crack region	0.10	$122.90 \pm 0.20$	$3.65 \pm 0.17$	0.14	7.5
$ee\mu\mu$	bb_bb	all leptons in the barrel	0.31	$124.14 \pm 0.06$	$1.81 \pm 0.05$	0.21	3.5
$ee\mu\mu$	bb_other	electrons in the barrel, at least a muon in the endcap	0.25	$124.06 \pm 0.07$	$1.82 \pm 0.06$	0.21	3.5
$ee\mu\mu$	other_other	any other event	0.34	$123.67 \pm 0.07$	$2.43 \pm 0.06$	0.22	5.0
$eeee$	all	all events	1.00	$123.11 \pm 0.06$	$2.70 \pm 0.05$	0.19	6.0
$eeee$	bbbb	all electrons in the barrel	0.46	$123.39 \pm 0.07$	$2.26 \pm 0.06$	0.19	5.0
$eeee$	onecrk	at least one electron in the crack region	0.18	$123.32 \pm 0.17$	$3.36 \pm 0.15$	0.20	9.0
$eeee$	bbb	three electrons in the barrel (none in the crack)	0.22	$122.72 \pm 0.12$	$2.60 \pm 0.07$	0.19	6.5
$eeee$	other	any other event	0.15	$122.54 \pm 0.15$	$2.77 \pm 0.15$	0.21	7.5

**Table 5.5.** Resolution on the four lepton invariant mass after Z mass constraint, estimated from a signal MC sample ( $m_H = 125\text{GeV}$ ), in different detector reconstruction regions. Barrel for muons is defined as  $|\eta| < 1.05$ ; for electrons, barrel is defined as  $|\eta| < 1.37$ , crack region as  $1.37 < |\eta| < 1.52$ .

channel	name	description	frequency	$m$ [GeV]	$\sigma$ [GeV]	events outside $\pm 2\sigma$	FWHM [GeV]
$\mu\mu\mu\mu$	all	all events	1.00	$124.89 \pm 0.02$	$1.64 \pm 0.02$	0.15	3.0
$\mu\mu\mu\mu$	bbbb	all muons in the barrel	0.19	$124.81 \pm 0.04$	$1.42 \pm 0.04$	0.16	2.5
$\mu\mu\mu\mu$	bbb	three muons in the barrel	0.28	$124.86 \pm 0.04$	$1.69 \pm 0.04$	0.14	3.0
$\mu\mu\mu\mu$	bb	two muons in the barrel	0.26	$124.91 \pm 0.04$	$1.56 \pm 0.04$	0.17	3.0
$\mu\mu\mu\mu$	other	any other event	0.26	$125.05 \pm 0.04$	$1.74 \pm 0.05$	0.17	3.5
$\mu\mu ee$	all	all events	1.00	$124.24 \pm 0.04$	$2.15 \pm 0.04$	0.19	4.5
$\mu\mu ee$	any_onecrk	at least one electron in the crack region	0.10	$124.15 \pm 0.18$	$2.97 \pm 0.04$	0.19	6.5
$\mu\mu ee$	bb_bb	all leptons in the barrel	0.29	$124.40 \pm 0.06$	$1.73 \pm 0.06$	0.22	3.0
$\mu\mu ee$	other_bb	electrons in the barrel, at least a muon in the endcap	0.35	$124.32 \pm 0.07$	$2.08 \pm 0.06$	0.17	4.0
$\mu\mu ee$	other_other	any other event	0.26	$124.05 \pm 0.08$	$2.28 \pm 0.08$	0.21	4.5
$ee\mu\mu$	all	all events	1.00	$124.22 \pm 0.03$	$1.85 \pm 0.03$	0.25	4.5
$ee\mu\mu$	onecrk_any	at least one electron in the crack region	0.10	$124.05 \pm 0.14$	$2.62 \pm 0.14$	0.23	4.5
$ee\mu\mu$	bb_bb	all leptons in the barrel	0.31	$124.34 \pm 0.05$	$1.58 \pm 0.04$	0.25	3.0
$ee\mu\mu$	bb_other	electrons in the barrel, at least a muon in the endcap	0.25	$124.32 \pm 0.06$	$1.64 \pm 0.05$	0.24	4.5
$ee\mu\mu$	other_other	any other event	0.34	$124.03 \pm 0.07$	$2.10 \pm 0.06$	0.25	5.0
$eeee$	all	all events	1.00	$123.37 \pm 0.05$	$2.54 \pm 0.05$	0.20	5.5
$eeee$	bbbb	all electrons in the barrel	0.46	$123.66 \pm 0.07$	$2.08 \pm 0.06$	0.22	5.0
$eeee$	onecrk	at least one electron in the crack region	0.18	$123.59 \pm 0.16$	$3.05 \pm 0.13$	0.20	5.5
$eeee$	bbb	three electrons in the barrel (none in the crack)	0.22	$123.15 \pm 0.12$	$2.80 \pm 0.12$	0.20	5.5
$eeee$	other	any other event	0.15	$122.91 \pm 0.14$	$2.60 \pm 0.13$	0.23	5.0

## 5.4 Reducible Background Estimation

The normalization of the reducible  $\ell\ell + jj$  and  $t\bar{t}$  backgrounds is evaluated using data-driven methods. As discussed in Sec. 4.1.3, the composition of the reducible backgrounds depends on the flavour of the  $Z_2$  decay leptons: different methods are used for the estimate of reducible backgrounds in the  $\ell\ell + \mu\mu$  and  $\ell\ell + ee$  final states.

Due to the few statistics in data control regions, the shape of the reducible background is obtained from Monte Carlo simulation. A control region is used, where impact parameter and calorimetric isolation requirements are not applied on leptons from  $Z_2$ , while a relative track isolation of less than 30% is required. Shape systematics are assigned by using two other control regions, namely one where the nominal track isolation requirement, a relative calorimeter isolation of less than 30% and a transverse impact parameter significance  $d_0/\sigma(d_0) < 6.5$  are applied, and one where the requirement on the impact parameter significance is inverted.

### 5.4.1 $\ell\ell + \mu\mu$ Background

Two are the control regions in which the  $Z + jj$ ,  $Z + b\bar{b}$  and  $t\bar{t}$  backgrounds are estimated: a control region with enriched  $b\bar{b}$  contribution and suppressed  $\pi/K$  in-flight decays, and the other enriched in both components.

#### $b\bar{b}$ Control Region

The  $b\bar{b}$ -enhanced control region is obtained by removing the isolation requirement for the  $Z_2$  decay leptons, and requiring at least one of these two leptons to fail the impact parameter significance requirement. In this way, contamination from the  $ZZ$  background is reduced, and both the  $Z + jj$  and  $t\bar{t}$  components can be estimated.

The estimation is performed using the fact that the invariant mass distribution of  $Z_1$  is flat for the  $t\bar{t}$  component and shows a peak at  $m_1 \approx m_Z$  for the  $Z + jj$  component. Fig. 5.10 shows this distribution in the control region, which is then fitted using a second order Chebychev polynomial for the  $t\bar{t}$  component and the convolution of a Breit-Wigner and a Crystal Ball resolution function for the  $Z + jj$  component; parameters for these functions are fitted on MC and allowed to vary by 10% in the fit to the experimental data.

The number of events in this control region is obtained from the fit and then extrapolated to the signal region, using a transfer factor which uses the efficiency of the impact parameter significance and isolation requirements obtained from  $Z + b\bar{b}$  simulation. This transfer factor is checked using a data-driven control region in which events with a  $Z$  boson plus exactly one muon are selected;  $Z$  decay leptons must fulfil the same requirements used for leptons from  $Z_1$ . Variations of about 10% are observed between transfer factors determined from MC and this  $Z + \mu$  control region, and a corresponding systematic uncertainty is assigned on the number of background events in the signal region.

#### $\pi/K$ Control Region

To obtain a sample enriched in  $\pi/K$  decays, a control region is defined removing the impact parameter and isolation requirements on muons from  $Z_2$  and requiring

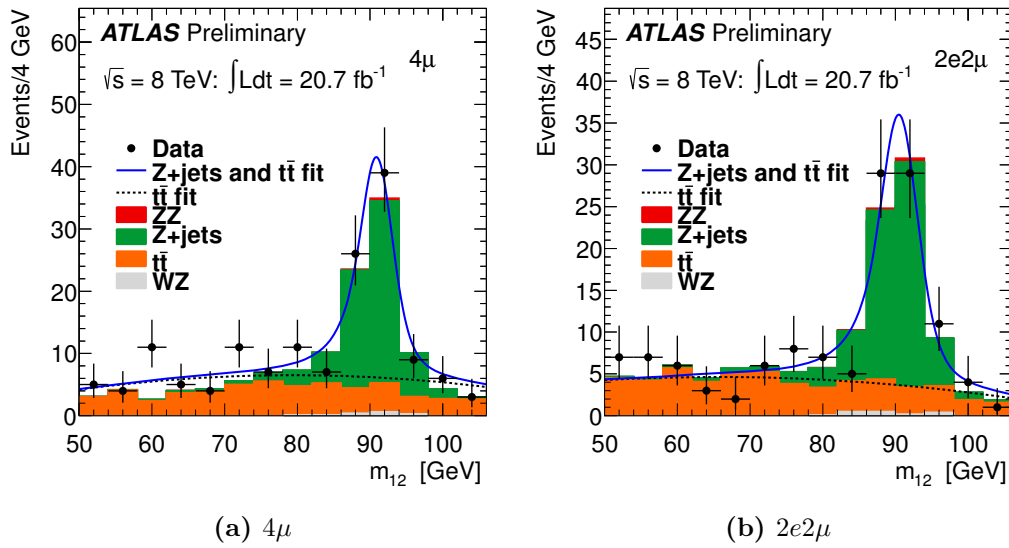


**Figure 5.10.** Distribution of  $m_1$ , for the two  $\ell\ell + \mu\mu$  final states, in the control region where the isolation requirements are not applied to the decay muons from  $Z_2$ , and at least one of these muons is required to fail the impact parameter significance requirement.

that at least one of the two decay muons fails the track isolation requirement. The contribution from  $\pi/K$  decays is obtained performing a fit on the  $m_1$  distribution to which the contribution from  $Z + b\bar{b}$  — determined as described above — is removed, and is found to be about 20% of the total  $Z + jj$  estimate.

### $t\bar{t}$ Control Region

A cross-check of the  $t\bar{t}$  background estimate is obtained using a control region in which four-lepton events with  $e^\pm\mu^\mp$  pairs are selected, if they satisfy the requirement  $50 < m_{e\mu} < 106$  GeV and if the two additional leptons are opposite charge muons with  $m_{\mu\mu}$  which satisfies the same selection criteria used for  $m_2$ . Events with  $Z \rightarrow ee, \mu\mu$  decays are rejected, and isolation and impact parameter requirements are applied only to the opposite-charge opposite-flavour lepton pair. An estimate consistent with the one from the  $b\bar{b}$  control region is obtained.

### 5.4.2 $\ell\ell + ee$ Background

Reconstructed electrons can come from different sources: true isolated electrons, electrons from heavy flavour decays (Q), electrons from photons conversions ( $\gamma$ ), electron fakes from jets (f). At reconstruction level it is possible to select *reconstruction categories* of electrons which are electron-like (E) or fake-like (E), using as discriminating variables the fraction of high threshold hits in the TRT ( $R_{\text{TRT}}$ ), the fraction of electron energy in the first ECAL layer ( $f_1$ ) and the lateral containment of the electromagnetic cluster in the azimuthal direction ( $R_\phi$ , measured using the second ECAL layer). Four control regions are used for the background estimate.

**$ll + e^\pm e^\mp$ , Relaxed Cuts**

The  $ll + ee$  control region is formed by relaxing the selection criteria on the  $Z_2$  decay electrons. Contributions to this control region from each of the sources described above are obtained using the classification in reconstruction categories. For each category, the extrapolation efficiency to the signal region is obtained from MC and cross-checked with data.

 **$ll + e^\pm e^\mp$ , Inverted Cuts**

An additional control region, which is in this case orthogonal to the signal region, is also obtained inverting isolation and impact parameter requirements; classification in reconstruction categories is applied. The extrapolation efficiency is in this case estimated using a  $Z + \ell$  data sample in  $p_T$  and  $\eta$  bins, and is found to be in good agreement with the other method. An additional cross-check is also performed, applying the same two methods to similar control regions where  $Z + e^\pm e^\pm$  events are selected.

 **$3\ell + \ell$  Same-Charge**

An additional estimate is obtained using a control region where the electrons from  $Z_2$  have same charge, the three highest  $p_T$  leptons satisfy the full analysis requirements and the remaining electron is only required to have at least 1 pixel, 7 silicon hits and to pass the  $R_\eta$  selection criteria.

The different yields for each of the truth components  $f$ ,  $\gamma$  and  $Q$  are obtained performing a simultaneous fit to the distributions of the number of B-layer hits and of  $R_{\text{TRT}}$ . Each component is modeled using templates from Monte Carlo simulation. A systematic uncertainty on the estimated yields is obtained with the result of the fit obtained replacing  $R_{\text{TRT}}$  with  $f_1$  or using instead the distance in  $\eta$  between the extrapolated impact point of the track on the calorimeter and the cluster barycenter obtained using the first ECAL layer ( $\Delta\eta_1$ ).

**Same-charge, Full Analysis**

An additional control region is defined performing the full analysis but selecting same-charge electrons in the case of  $Z_2$ . A  $m_{4\ell} < 160$  GeV requirement is applied to remove contamination from  $ZZ$  background events with mismeasured charge; contamination from  $Z + b\bar{b}$  is expected to be small. The resulting estimate is 6 (2) events in the  $4e$  ( $2\mu 2e$ ) channels, in good agreement within statistical uncertainties with the other estimates.

**5.4.3 Summary of Reducible Background Estimates**

Table 5.6 reports the results of all the reducible background estimation methods; the estimate used for the background normalization is denoted with a “†” symbol. The fraction of background events in the  $m_{4\ell} < 160$  GeV region is approximately 80% of the total.

Fig. 5.11 shows the  $m_1$  and  $m_2$  distributions for events selected applying all analysis criteria, apart from isolation and impact parameter requirements on leptons

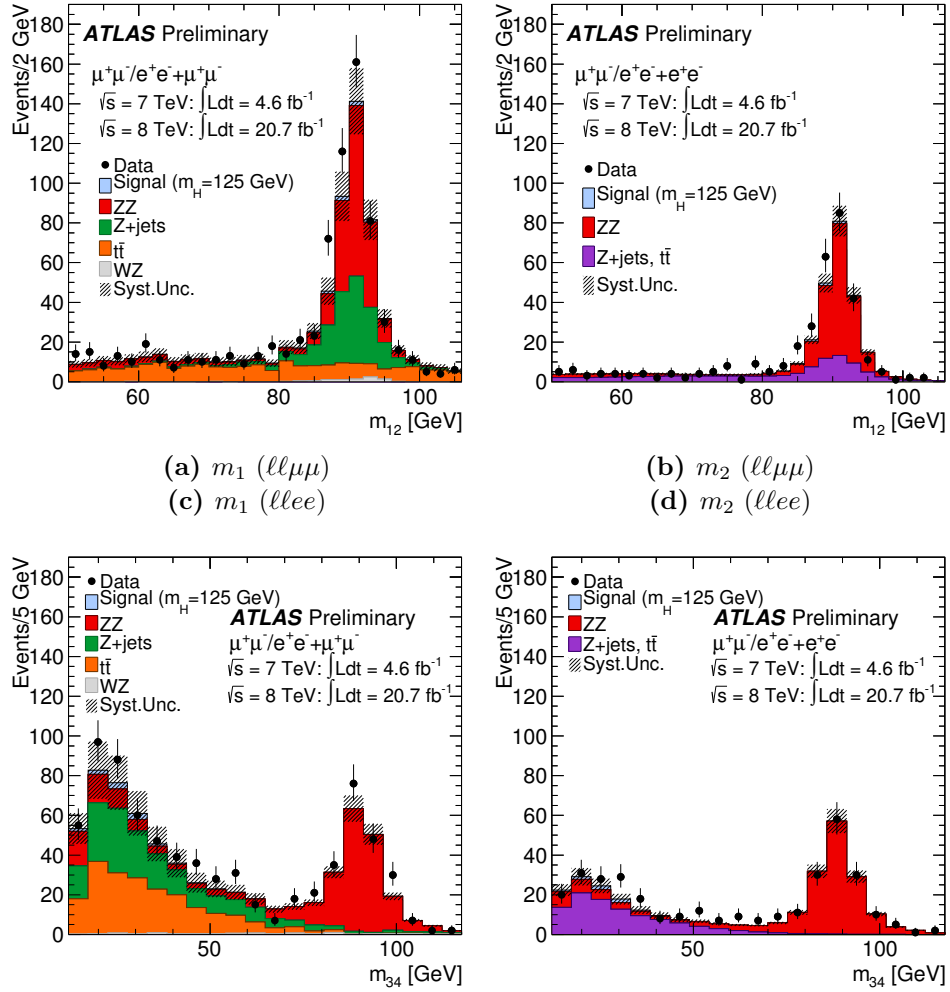


**Figure 5.11.** Distributions of  $m_1$  and  $m_2$  for events where isolation and impact parameter requirements on the  $Z_2$  decay leptons are relaxed, for the  $ll + \mu\mu$  and  $ll + ee$  final states. Data are compared with Monte Carlo simulation for a 125 GeV Higgs signal and for reducible background, for which normalizations obtained from data-driven methods are applied.

Method	Estimate for $\sqrt{s} = 8$ TeV	Estimate for $\sqrt{s} = 7$ TeV
	$4\mu$	$4\mu$
$m_{12}$ fit: $Z + jj$ contribution	$2.4 \pm 0.5 \pm 0.6^\dagger$	$0.22 \pm 0.07 \pm 0.02^\dagger$
$m_{12}$ fit: $t\bar{t}$ contribution	$0.14 \pm 0.03 \pm 0.03^\dagger$	$0.03 \pm 0.01 \pm 0.01^\dagger$
$t\bar{t}$ from $e\mu + \mu\mu$	$0.10 \pm 0.05 \pm 0.004$	-
	$2e2\mu$	$2e2\mu$
$m_{12}$ fit: $Z + jj$ contribution	$2.5 \pm 0.5 \pm 0.6^\dagger$	$0.19 \pm 0.06 \pm 0.02^\dagger$
$m_{12}$ fit: $t\bar{t}$ contribution	$0.10 \pm 0.02 \pm 0.02^\dagger$	$0.03 \pm 0.01 \pm 0.01^\dagger$
$t\bar{t}$ from $e\mu + \mu\mu$	$0.12 \pm 0.07 \pm 0.005$	-
	$2\mu2e$	$2\mu2e$
$\ell\ell + e^\pm e^\mp$ relaxed cuts	$5.2 \pm 0.4 \pm 0.5^\dagger$	$1.8 \pm 0.3 \pm 0.4$
$\ell\ell + e^\pm e^\mp$ inverted cuts	$3.9 \pm 0.4 \pm 0.6$	-
$3\ell + \ell$ (same-charge)	$4.3 \pm 0.6 \pm 0.5$	$2.8 \pm 0.4 \pm 0.5^\dagger$
same-charge, full analysis	4	0
	$4e$	$4e$
$\ell\ell + e^\pm e^\mp$ relaxed cuts	$3.2 \pm 0.5 \pm 0.4^\dagger$	$1.4 \pm 0.3 \pm 0.4$
$\ell\ell + e^\pm e^\mp$ inverted cuts	$3.6 \pm 0.6 \pm 0.6$	-
$3\ell + \ell$ (same-charge)	$4.2 \pm 0.5 \pm 0.5$	$2.5 \pm 0.3 \pm 0.5^\dagger$
same-charge, full analysis	3	2

**Table 5.6.** Summary of the estimated yields of reducible background events for the  $20.7 \text{ fb}^{-1}$  of  $\sqrt{s} = 8$  TeV data and for the  $4.6 \text{ fb}^{-1}$  of  $\sqrt{s} = 7$  TeV data for the full  $m_{4\ell}$  range of the analysis (see the text for details). Events for the  $\ell\ell + ee$  control region with same-sign electrons are given only for  $m_{4\ell} < 160$  GeV, to reduce contamination from  $ZZ$  events with charge mismeasurements; approximately 80% of the reducible background events is in this region. The methods used for the final background estimates are indicated with a “ $\dagger$ ” symbol. The first uncertainty is statistical, the second is systematic.

from  $Z_2$ , for  $\ell\ell + \mu\mu$  and  $\ell\ell + ee$  final states. Good agreement in shape and normalization is observed with data.

## 5.5 Systematic Uncertainties

Various sources of systematic uncertainties on signal and background yields are considered:

**Muon Identification and Reconstruction** Uncertainties on muon identification and reconstruction efficiency scale factors, as estimated for signal and irreducible background, are uniform in the full  $m_{4\ell}$  range and amount to  $\pm 0.8\%$  ( $\pm 0.4\% / \pm 0.4\%$ ) for the  $4\mu$  ( $2\mu 2e / 2e 2\mu$ ) channel.

**Electron Identification and Reconstruction** Uncertainties on electron identification and reconstruction efficiency scale factors result in an uncertainty on the signal yields of  $\pm 2.4\%$  ( $\pm 1.8\% / \pm 1.6\%$ ) for the  $4e$  ( $2\mu 2e / 2e 2\mu$ ) channel at  $m_{4\ell} = 1$  TeV and  $\pm 9.4\%$  ( $\pm 8.7\% / \pm 2.4\%$ ) at  $m_{4\ell} = 125$  GeV.

**Isolation and Impact Parameter Requirements** The uncertainty on the efficiencies of the isolation and impact parameter requirements is evaluated by measuring the efficiency of these criteria on a di-jet sample enriched in non-isolated leptons from  $b, c$ -quark decays, and is found to be negligible.

**Higgs  $p_T$  Reweighting** The uncertainty on the corrections to the NNLO Higgs  $p_T$  spectrum described in Sec. 4.1 is taken into account and an additional  $\pm 1\%$  uncertainty is added in the ggF case, to account for parton density functions and QCD scale uncertainties.

**Luminosity** The overall uncertainty on the integrated luminosity is  $\pm 1.8\%$  for the 7 TeV dataset and 3.6% for the 8 TeV dataset[18], and is assigned as corresponding uncertainty for normalizations coming from Monte Carlo.

**Theory Uncertainties** All theory-related systematic uncertainties for signal and irreducible background described in Sec. 5.1.2 are taken into account.

**Electron Energy Scale** The uncertainty on the electron energy scale is determined from  $Z \rightarrow ee$  decays, yields an uncertainty over the measured Higgs mass  $m_H$  of less than  $\pm 0.4\%$  ( $\pm 0.2\%$ ) for the  $4e$  ( $2e 2\mu$ ) channel, and is negligible for  $2\mu 2e$  (where the electrons have lower momenta). This uncertainty is verified for  $p_T < 15$  GeV using  $J/\psi$  decays: at 10 GeV measurements and predictions agree to better than 1%, which leads to a contribution to the overall uncertainty on  $m_H$  of less than 0.1%. Similarly, the effect of uncertainties on final-state QED radiation modelling and background contamination are below 0.1%.

**Muon Momentum Scale** The contribution to the uncertainty on  $m_H$  due to uncertainties on the determination of the muon momentum scale is evaluated using  $J/\psi, \Upsilon$  and  $Z$  decays, and is estimated to be  $\pm 0.2\%$  ( $\pm 0.1\%$ ) for the  $4\mu(2\mu 2e)$  channels.

## 5.6 Results

The overall signal reconstruction and selection efficiency for  $m_H = 125$  GeV for the 2012 (2011) data analysis is 39% (39%) for the  $4\mu$  channel, 26% (21%) for  $2\mu 2e + 2e 2\mu$  and 19% (15%) for  $4e$ .

	$4\mu$		$2\mu 2e/2e2\mu$		$4e$	
	low mass	high mass	low mass	high mass	low mass	high mass
$\sqrt{s} = 8 \text{ TeV}$ integrated luminosity $20.7 \text{ fb}^{-1}$						
$ZZ^{(*)}$	$12.4 \pm 0.6$	$92.6 \pm 6.7$	$14.7 \pm 0.9$	$144 \pm 11$	$5.4 \pm 0.5$	$55.9 \pm 4.5$
$Z, Zb\bar{b}$ , and $t\bar{t}$	$1.9 \pm 0.6$	$0.5 \pm 0.2$	$6.1 \pm 1.5$	$1.5 \pm 0.4$	$2.5 \pm 0.6$	$0.6 \pm 0.2$
total background	$14.3 \pm 0.8$	$93.1 \pm 6.7$	$20.8 \pm 1.8$	$145 \pm 11$	$8.0 \pm 0.8$	$56.5 \pm 4.5$
data	27	93	28	169	13	55
$m_H = 123 \text{ GeV}$	$4.4 \pm 0.6$		$5.4 \pm 0.8$		$2.2 \pm 0.4$	
$m_H = 125 \text{ GeV}$	$5.8 \pm 0.7$		$7.0 \pm 0.9$		$2.9 \pm 0.4$	
$m_H = 127 \text{ GeV}$	$6.7 \pm 0.9$		$8.4 \pm 1.2$		$3.4 \pm 0.5$	
$\sqrt{s} = 7 \text{ TeV}$ integrated luminosity $4.6 \text{ fb}^{-1}$						
$ZZ^{(*)}$	$2.2 \pm 0.1$	$16.8 \pm 1.2$	$2.5 \pm 0.2$	$26.6 \pm 2.0$	$0.8 \pm 0.1$	$9.4 \pm 0.8$
$Z, Zb\bar{b}$ , and $t\bar{t}$	$0.2 \pm 0.1$	$0.05 \pm 0.02$	$2.4 \pm 0.5$	$0.6 \pm 0.1$	$2.0 \pm 0.5$	$0.48 \pm 0.1$
total background	$2.4 \pm 0.1$	$16.9 \pm 1.2$	$4.9 \pm 0.6$	$27.1 \pm 2.0$	$2.8 \pm 0.5$	$9.8 \pm 0.8$
data	8	23	5	23	2	13
$m_H = 123 \text{ GeV}$	$0.7 \pm 0.1$		$0.8 \pm 0.1$		$0.3 \pm 0.1$	
$m_H = 125 \text{ GeV}$	$1.0 \pm 0.1$		$1.1 \pm 0.2$		$0.4 \pm 0.1$	
$m_H = 127 \text{ GeV}$	$1.0 \pm 0.2$		$1.2 \pm 0.2$		$0.4 \pm 0.1$	

**Table 5.7.** Number of observed and expected events in “low mass” ( $100 < m_{4\ell} < 160 \text{ GeV}$ ) and “high mass” ( $m_{4\ell} \geq 160 \text{ GeV}$ ) regions. Uncertainties on expected signal and background yields are reported.

Table 5.7 shows the number of event observed in each final state and the number of expected events for backgrounds. Expectations are given for  $100 < m_{4\ell} < 160 \text{ GeV}$  and  $m_{4\ell} \geq 160 \text{ GeV}$ , for the  $20.7 \text{ fb}^{-1}$  at  $\sqrt{s} = 8 \text{ TeV}$  and the  $4.6 \text{ fb}^{-1}$  at  $\sqrt{s} = 7 \text{ TeV}$  data sets and the combined dataset. Expectations in a window of  $\pm 5 \text{ GeV}$  around  $m_H = 125 \text{ GeV}$  are presented in table 5.8. Seven out of the 225 events with  $Z_1 \rightarrow \mu\mu$  undergo FSR recovery; one of them is within  $120 < m_{4\ell} < 130 \text{ GeV}$ . The overall signal to background ratio is about 1.4.

Four-lepton invariant mass distributions, corresponding to the combined luminosity from 2011 and 2012, are shown in Fig. 5.12a for the mass range  $80 < m_{4\ell} < 170 \text{ GeV}$  and in Fig. 5.12b for the mass range  $170 < m_{4\ell} < 900 \text{ GeV}$ . For the selected candidates with  $120 < m_{4\ell} < 130 \text{ GeV}$ , the distribution of  $m_2$  as a function of  $m_1$  is shown in Fig. 5.13a, while the distribution of  $m_{4\ell}$  versus  $m_1$  for  $90 < m_{4\ell} < 135 \text{ GeV}$  is shown in Fig. 5.13b; no  $Z$  mass constraint is applied in both cases. Mass distributions for each final state are shown in the range  $80 < m_{4\ell} < 170 \text{ GeV}$  in Fig. 5.14.

### 5.6.1 Upper Limit and Signal Significance

As discussed, the discriminating variable between signal and backgrounds is  $m_{4\ell}$ . To set upper limits at 95% CL on the Higgs boson production cross-section, as a function of its mass  $m_H$ , the  $CL_s$  modified frequentist formalism is used[68] with the profile likelihood ratio test statistic[69]. A maximum likelihood fit of signal and background models to the observed  $m_{4\ell}$  distribution is performed to evaluate the test statistic.

	total signal full mass range	signal	$ZZ^*$	$Z + jj, t\bar{t}$	S/B	expected	observed
$\sqrt{s} = 8 \text{ TeV}$							
$4\mu$	$5.8 \pm 0.7$	$5.3 \pm 0.7$	$2.3 \pm 0.1$	$0.50 \pm 0.13$	1.9	$8.1 \pm 0.9$	11
$2\mu 2e$	$3.0 \pm 0.4$	$2.6 \pm 0.4$	$1.2 \pm 0.1$	$1.01 \pm 0.21$	1.2	$4.8 \pm 0.7$	4
$2e 2\mu$	$4.0 \pm 0.5$	$3.4 \pm 0.4$	$1.7 \pm 0.1$	$0.51 \pm 0.16$	1.5	$5.6 \pm 0.7$	6
$4e$	$2.9 \pm 0.4$	$2.3 \pm 0.3$	$1.0 \pm 0.1$	$0.62 \pm 0.16$	1.4	$3.9 \pm 0.6$	6
total	$15.7 \pm 2.0$	$13.7 \pm 1.8$	$6.2 \pm 0.4$	$2.62 \pm 0.34$	1.6	$22.5 \pm 2.9$	27
$\sqrt{s} = 7 \text{ TeV}$							
$4\mu$	$1.0 \pm 0.1$	$0.97 \pm 0.13$	$0.49 \pm 0.02$	$0.05 \pm 0.02$	1.8	$1.5 \pm 0.2$	2
$2\mu 2e$	$0.4 \pm 0.1$	$0.39 \pm 0.05$	$0.21 \pm 0.02$	$0.55 \pm 0.12$	0.5	$1.2 \pm 0.1$	1
$2e 2\mu$	$0.7 \pm 0.1$	$0.57 \pm 0.08$	$0.33 \pm 0.02$	$0.04 \pm 0.01$	1.5	$0.9 \pm 0.1$	2
$4e$	$0.4 \pm 0.1$	$0.29 \pm 0.04$	$0.15 \pm 0.01$	$0.49 \pm 0.12$	0.5	$0.9 \pm 0.1$	0
total	$2.5 \pm 0.4$	$2.2 \pm 0.3$	$1.17 \pm 0.07$	$1.12 \pm 0.17$	1.0	$4.5 \pm 0.5$	5
$\sqrt{s} = 8 \text{ TeV}$ and $\sqrt{s} = 7 \text{ TeV}$							
$4\mu$	$6.8 \pm 0.8$	$6.3 \pm 0.8$	$2.8 \pm 0.1$	$0.55 \pm 0.15$	1.9	$9.6 \pm 1.0$	13
$2\mu 2e$	$3.4 \pm 0.5$	$3.0 \pm 0.4$	$1.4 \pm 0.1$	$1.56 \pm 0.33$	1.0	$6.0 \pm 0.8$	5
$2e 2\mu$	$4.7 \pm 0.6$	$4.0 \pm 0.5$	$2.1 \pm 0.1$	$0.55 \pm 0.17$	1.5	$6.6 \pm 0.8$	8
$4e$	$3.3 \pm 0.5$	$2.6 \pm 0.4$	$1.2 \pm 0.1$	$1.11 \pm 0.28$	1.1	$4.9 \pm 0.8$	6
total	$18.2 \pm 2.4$	$15.9 \pm 2.1$	$7.4 \pm 0.4$	$3.74 \pm 0.93$	1.4	$27.1 \pm 3.4$	32

**Table 5.8.** Number of observed and expected events in the region  $120 < m_{4\ell} < 130 \text{ GeV}$ .

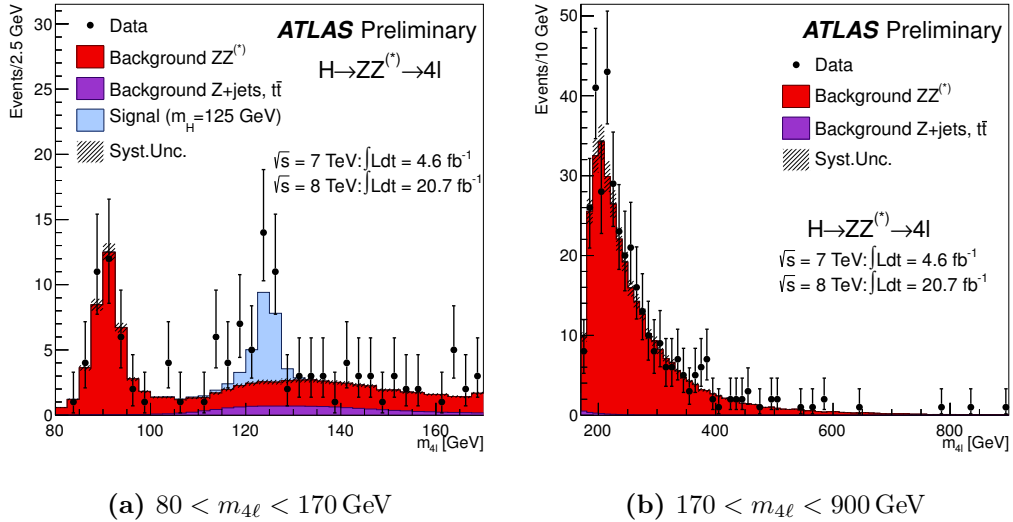


**Figure 5.12.** Distribution of the four-lepton invariant mass for observed events, together with expectation from a  $m_H = 125 \text{ GeV}$  signal and from backgrounds.

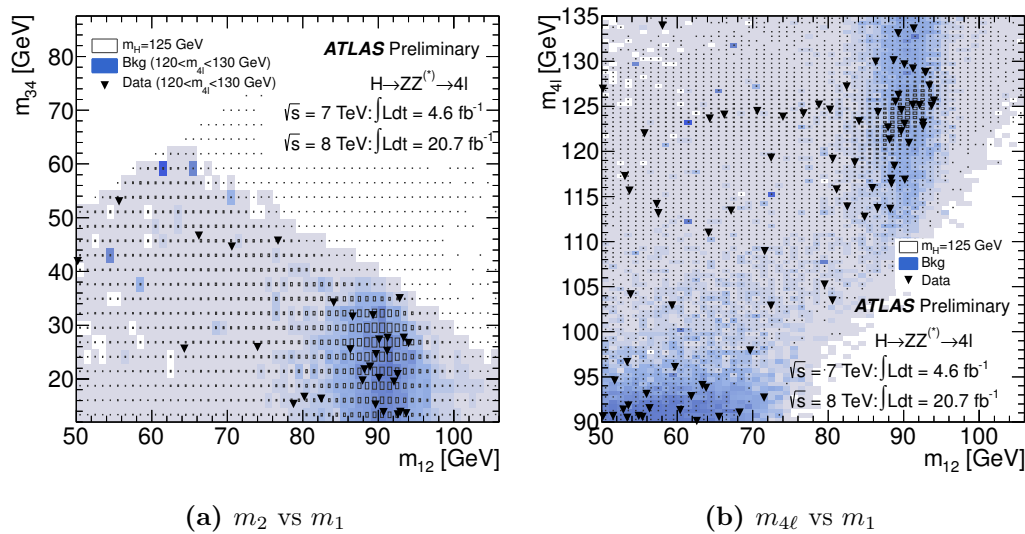


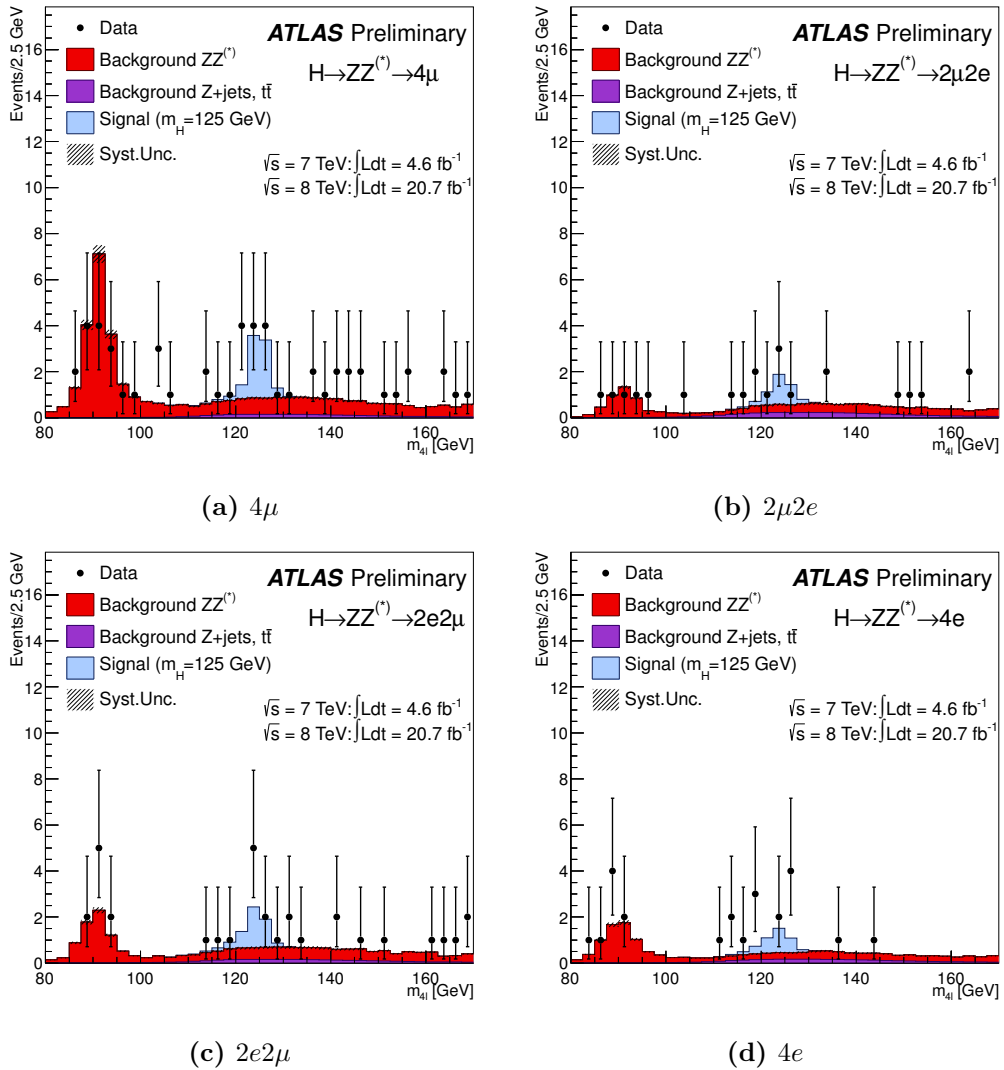
**Figure 5.13.** **a:** Distribution of  $m_2$  versus  $m_1$ , for events with  $120 < m_{4\ell} < 130$  GeV. **b:** Distribution of  $m_{4\ell}$  versus  $m_1$  for events with  $90 < m_{4\ell} < 135$  GeV. All masses are calculated without applying the  $Z$  mass constraint fit.

data set	observed			expected	
	min $p_0$	significance [ $\sigma$ ]	$m_H(p_0)$	min $p_0(m_H)$	significance [ $\sigma$ ]
$\sqrt{s} = 7$ TeV	$2.5 \times 10^{-3}$	2.8	125.6 GeV	$3.5 \times 10^{-2}$	1.8
$\sqrt{s} = 8$ TeV	$8.8 \times 10^{-10}$	6.0	124.1 GeV	$2.8 \times 10^{-5}$	4.0
combined	$2.7 \times 10^{-11}$	6.6	124.3 GeV	$5.7 \times 10^{-6}$	4.4

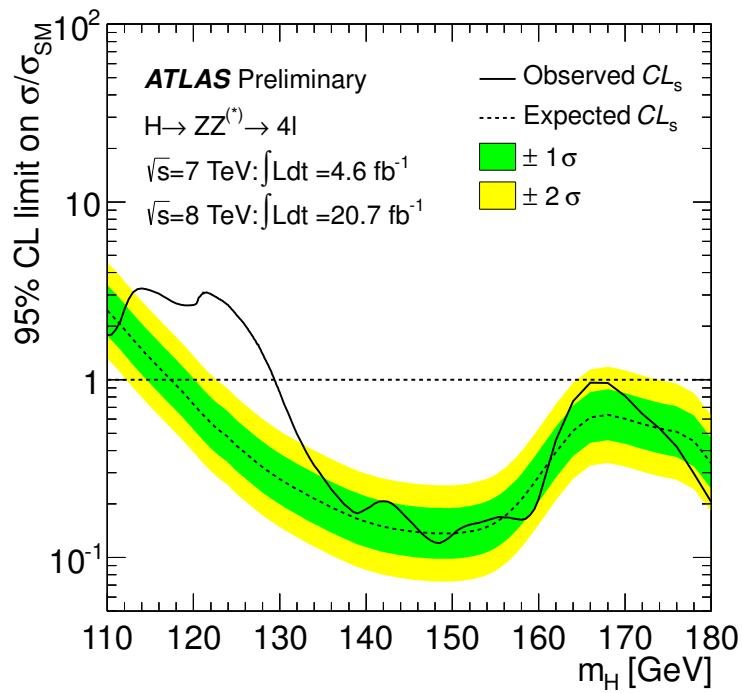
**Table 5.9.** Observed and expected values of  $p_0$  for the  $\sqrt{s} = 7$  TeV,  $\sqrt{s} = 8$  TeV data sets and their combination. The expected  $p_0$  is quoted at the value of  $m_H$  of the observed minimum.

Fig. 5.15 shows the observed and expected 95% CL cross-section upper limits, as a function of  $m_H$ , for the combined  $\sqrt{s} = 8$  TeV and  $\sqrt{s} = 7$  TeV data sets. An excess is observed at 125 GeV, which does not allow to exclude a Higgs boson below 130 GeV.

The significance of this excess is given in Fig. 5.16 by the probability  $p_0$  to obtain, in the background only hypothesis, a test statistics more signal-like than the one observed in data; nuisance parameters are fixed to their best fit values in the background only hypothesis. Asymptotic approximations[69] are used in the calculation of  $p_0$ , which is given as a function of  $m_H$  in the  $110 \div 180$  GeV range for the individual 2011 and 2012 datasets and their combination. Lowest observed local values of  $p_0$ , and the corresponding expected values, are shown in Table 5.9. A significance of  $6.6\sigma$  is observed for  $m_H = 124.3$  GeV.



**Figure 5.14.** Four-lepton invariant mass distributions for the four final states, in the range  $80 < m_{4\ell} < 170 \text{ GeV}$ . Error bars represent 68.3% central confidence intervals.



**Figure 5.15.** Expected (dashed) and observed (full line) 95% CL upper limit on the Higgs boson production cross-section, divided by the cross-section expected in the SM, as a function of  $m_H$ , in the low mass region. The green and yellow bands indicate the expected limits with  $\pm 1\sigma$  and  $\pm 2\sigma$  fluctuations, respectively.

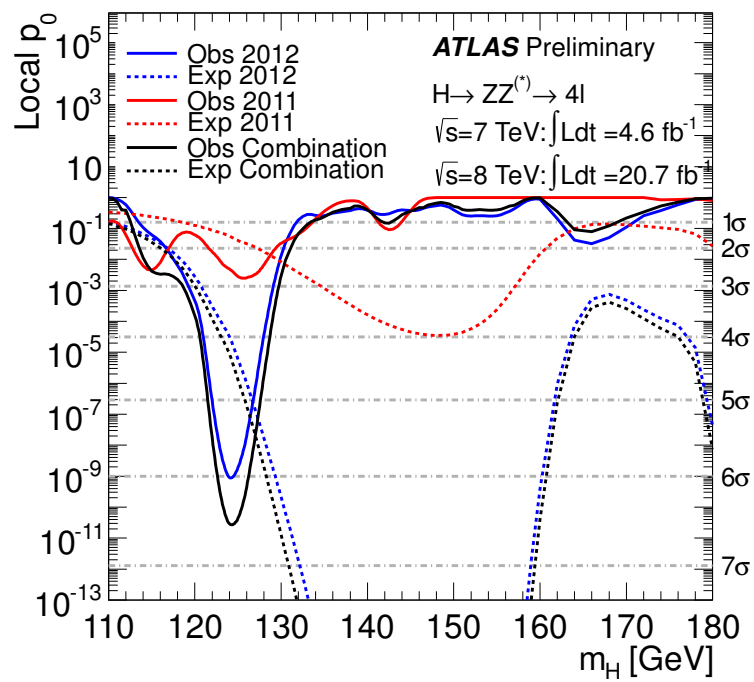


**Figure 5.16.** The observed local  $p_0$  for the combination of the 2011 and 2012 datasets (solid black line); the results for  $\sqrt{s} = 7 \text{ TeV}$  and  $\sqrt{s} = 8 \text{ TeV}$  are shown in red and blue solid lines. The dashed curves show the expected median local  $p_0$  for the signal hypothesis when tested at the corresponding  $m_H$ .

### 5.6.2 Mass Measurement

The mass of the new particle at 125 GeV can be measured using a  $m_H$ -dependent signal  $m_{4\ell}$  model. Four-lepton mass distributions are obtained from Monte Carlo and described by probability density functions obtained using the kernel density estimation technique[70]. The kernel density estimation technique uses sums of gaussian kernels with variable width over the unbinned set of input points, to smooth the input distribution in a non-parametric way. Probability density functions for different simulated mass points are then combined together, using the fact that the  $m_{4\ell}$  distribution shifts approximately linearly with  $m_H$ . B-splines are used to obtain a p.d.f. which is a function of  $m_H$ : for a given value of  $m_H$ , the resulting  $m_{4\ell}$  shape is in this way a weighted superposition of all shapes obtained from simulated  $m_H$  values in Monte Carlo. Signal and background shapes are varied in shape from the nominal expectation to allow for shape systematics due to all relevant effects described in Sec. 5.5.

Within this likelihood model,  $m_H$  is a free parameter of the fit and is a parameter of interest of the problem. Fig. 5.17a shows the profile likelihood as a function of  $m_H$ , with and without applying electron and muon mass scale systematic uncertainties (MSS(e) and MSS( $\mu$ ), respectively<sup>12</sup>). Fig. 5.17b shows the corresponding profile likelihood curves as a function of  $m_H$  for each of the four final states: results for  $ee + \ell\ell$  and  $\mu\mu + \ell\ell$  final states, in which electrons and muons respectively dominate the mass scale, are in good agreement within uncertainties. The best fit mass is

$$m_H = 124.3^{+0.6}_{-0.5} (\text{stat})^{+0.5}_{-0.3} (\text{syst}) \text{GeV},$$

with a systematic uncertainty which is dominated by the energy and momentum scale uncertainties.

### 5.6.3 Signal Strength

The signal strength scale factor  $\mu$ , defined as the ratio between the observed and the expected yield of signal events, is a free parameter of the fit and can be treated as a parameter of interest together with  $m_H$ . Fig. 5.18 shows the best fit of the profile likelihood ratio in the  $\mu$  versus  $m_H$  plane, together with the 68% and 95% CL confidence regions obtained in the asymptotic approximation. The value of the signal strength  $\mu$  at the best fit value for  $m_H$  (124.3 GeV) is  $\mu = 1.7^{+0.5}_{-0.4}$ .

## 5.7 Combination with Other Channels

### 5.7.1 Mass Measurement

A combined mass measurement for the new resonance[71] is performed using data from the channels with high resolution on  $m_H$ ,  $H \rightarrow \gamma\gamma$ , and  $H \rightarrow ZZ^{(*)} \rightarrow 4\ell$ . Hypothesized values of  $m_H$  are tested with the profile likelihood ratio

$$\Lambda(m_H) = \frac{L(m_H, \hat{\mu}_{\gamma\gamma}(m_H), \hat{\mu}_{4\ell}(m_H), \hat{\theta}(m_H))}{L(\hat{m}_H, \hat{\mu}_{\gamma\gamma}, \hat{\mu}_{4\ell}, \hat{\theta})},$$

<sup>12</sup>When a systematic effect is not applied, the corresponding nuisance parameters are fixed to their best fit values.

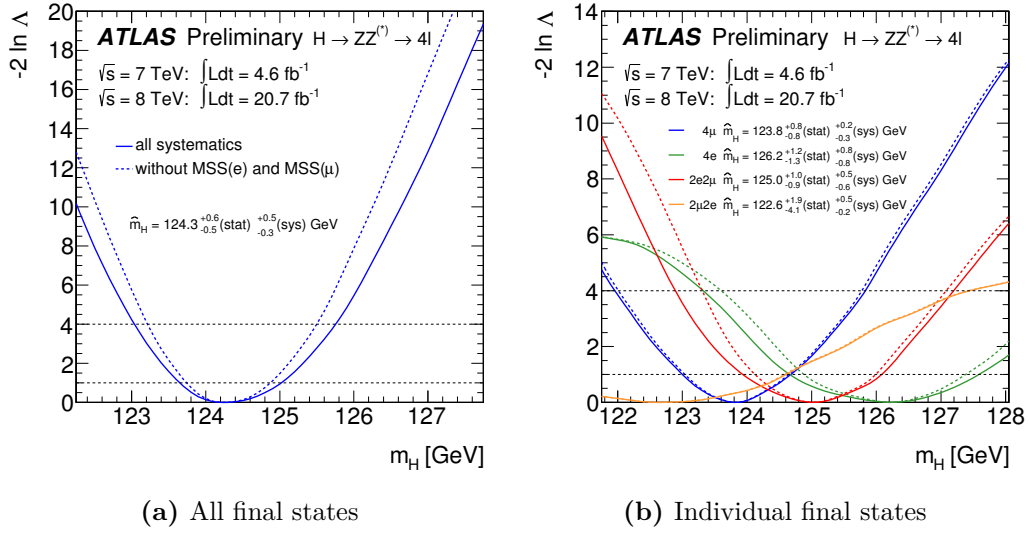


**Figure 5.17.** Profile likelihood as a function of  $m_H$  **a** for the combination of all final states and **b** for the individual final states for the combined  $\sqrt{s} = 8$  TeV and  $\sqrt{s} = 7$  TeV data samples, with (solid curve) and without (dashed curve) applying the mass scale systematics for electrons (MSS(e)) and muons (MSS( $\mu$ )). The 68% (95%) CL confidence interval on  $m_H$  is determined by the points where the profile likelihood curve is below 1 (4).

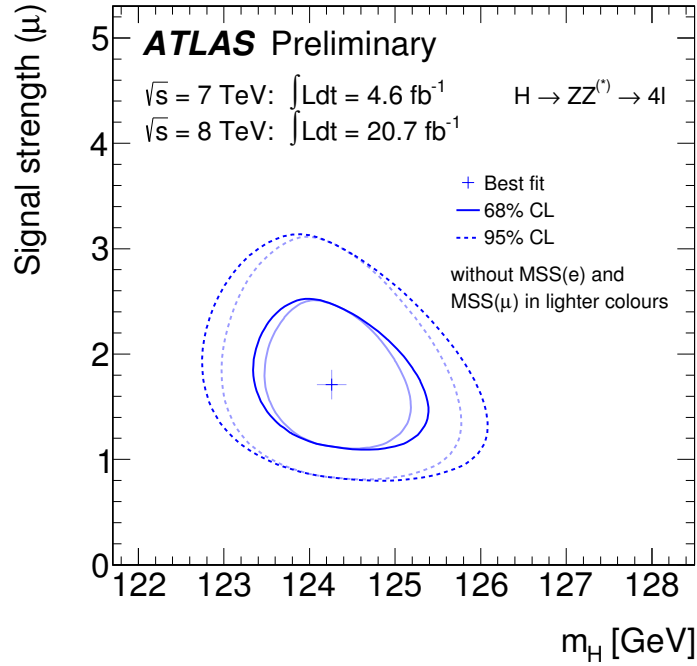


**Figure 5.18.** Likelihood ratio contours in the  $(\mu, m_H)$  plane that, in the asymptotic limit, correspond to 68% and 95% CL contours. In lighter colour, results obtained without using electron and muon mass scale uncertainties are shown.

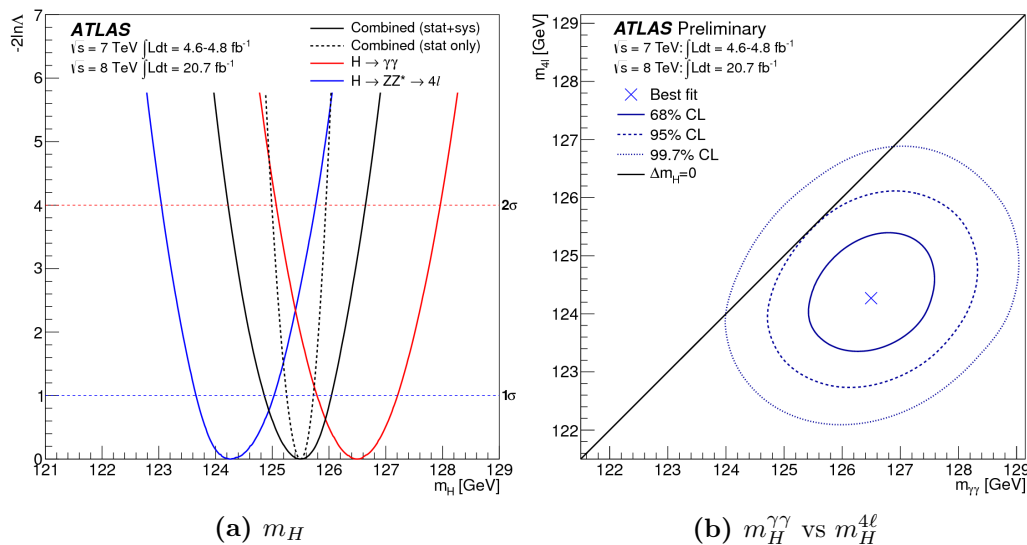


**Figure 5.19.** **a:** Profile likelihood ratio as a function of  $m_H$  for the  $H \rightarrow \gamma\gamma$  and  $H \rightarrow ZZ^{(*)} \rightarrow 4\ell$  channels and their combination. **b:** Likelihood contours as a function of  $m_H^{\gamma\gamma}$  and  $m_H^{4\ell}$ , the individual mass measurements performed in the two channels.

where  $\theta$  is the set of nuisance parameters of the model and the single and double circumflex denote the unconditional and conditional maximum likelihood estimates of the parameters, respectively. The leading source of systematic uncertainty in the mass measurement comes from mass scale uncertainties, which yield small correlation between the two measurements (Fig. 5.19b). Individual and combined measurements are shown in Fig. 5.19a, where the combined mass is measured to be

$$m_H = 125.5 \pm 0.2(\text{stat})_{-0.6}^{+0.5}(\text{sys}) \text{ GeV}.$$

### 5.7.2 Signal Strengths

The combined measurement of the signal strength parameter  $\mu$ , using all decay channels ( $W, ZH \rightarrow bb, H \rightarrow \tau\tau, H \rightarrow WW^* \rightarrow \ell\nu\ell\nu, H \rightarrow \gamma\gamma$  and  $H \rightarrow ZZ^{(*)} \rightarrow 4\ell$ ) for an integrated luminosity of up to  $25 \text{ fb}^{-1}$ , is performed for a fixed mass hypothesis of  $125.5 \text{ GeV}$ , by using the profile likelihood ratio

$$\Lambda(\mu) = \frac{L(\mu, \hat{\theta}(\mu))}{L(\hat{\mu}, \hat{\theta})},$$

where  $\mu$  is the vector of signal strength factors. Results are shown in Fig. 5.20: the measured global signal yield is

$$\hat{\mu} = 1.30 \pm 0.13(\text{stat}) \pm 0.1(\text{sys}),$$

and is consistent with the SM expectation  $\mu = 1$  at 9% level (40% when using rectangular pdfs for the dominant theory systematic uncertainties). The agreement between the individual signal strengths and the combined value is 13%. The value of  $\hat{\mu}$  changes by about 4% by varying the assumed  $m_H$  of  $\pm 1 \text{ GeV}$ .

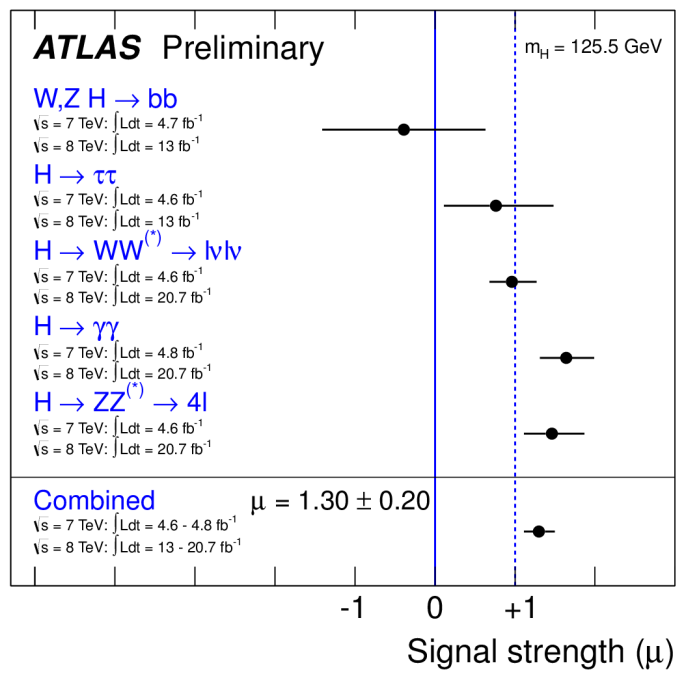


**Figure 5.20.** Measurements of the signal strength parameter  $\mu$  for  $m_H = 125.5 \text{ GeV}$  for the individual channels and their combination.

## Chapter 6

# Spin–parity Measurements

In the Standard Model, the Higgs boson is predicted to be a spin zero particle with even parity — a  $0^+$  state. Discriminant–based techniques which exploit the full final state information from the  $H \rightarrow ZZ^{(*)} \rightarrow 4\ell$  decay can be used to test this hypothesis against alternative scenarios, in order to establish which model the observed data are more likely to be described by. In this chapter, the  $J^P$ –MELA technique is introduced, and results on the hypothesis testing with the 2011 and 2012 collision data are presented.

### 6.1 Analysis Method

Different pairs of hypotheses on the spin–parity state of the new particle are tested, using a multivariate technique based on the matrix element description of the  $X \rightarrow ZZ$  decay: the full information on the final state, based on the 7 masses and angles defined in Sec. 4.2.1, is projected on a single dimension, the  $J^P$ –MELA *discriminant*. The new particle is assumed to have a mass  $m_H = 125$  GeV.

#### 6.1.1 Hypothesis Testing

The following hypotheses on the quantum numbers of the new particle are considered:

- $0^+$  the Standard Model Higgs Boson (following Sec. 4.2.3,  $g_1 = 2i, g_2 = g_3 = g_4 = 0$ );
- $0^-$  a pure pseudoscalar state ( $g_1 = g_2 = g_3 = 0, g_4 = 1$ );
- $1^+$  the vector state of Sec. 4.2.3 with  $b_1 = 1, b_2 = 0$ ;
- $1^-$  the pseudovector state of Sec. 4.2.3 with  $b_1 = 0, b_2 = 1$ ;
- $2^+$  a minimal coupling parity–even spin 2 state, equivalent to a Kaluza–Klein graviton ( $g_1 = g_5 = 1, g_{i \neq 1,5} = 0$  of Sec. 4.2.3);
- $2^-$  a parity–odd state with higher order operators ( $g_8 = g_9 = 1, g_{i \neq 8,9} = 0$ ).

The spin 2 states can in principle be produced both in gluon fusion and  $q\bar{q}$  annihilation. For example, the dominant contribution to the production of the considered  $2^+$  state comes from the ggF process; the contribution from  $q\bar{q}$  annihilation

is about 4% at LO QCD, but might be significantly modified from higher order QCD corrections. The production mechanism affects the kinematic distributions of the final state, since in the boson rest frame the projection of its polarization states onto the parton collision axis can take only the values  $\pm 2$  for ggF and  $\pm 1$  for  $q\bar{q}$  production. Five values of fraction of ggF production  $f_{qq} = 0, 25\%, 50\%, 75\%$  and 100% are considered for both  $2^+$  and  $2^-$  models, by mixing at generator level events simulated under the  $f_{qq} = 0$  and  $f_{qq} = 1$  hypotheses<sup>1</sup>.

### 6.1.2 Data and Monte Carlo Samples

The same data and background Monte Carlo samples of the analysis described in Chapter 5 are used.

As for the signal simulation, the JHU leading–order generator[42] is used to simulate the decay of a boson with  $m_H = 125$  GeV under the hypotheses defined in the previous section, both at  $\sqrt{s} = 7$  TeV and 8 TeV. The Pythia MC generator is employed for the parton showers, using the CTEQ6L1 parton density functions and the AU2 underlying event tuning[72]. A generator level comparison of kinematic distributions between JHU and POWHEG generators is shown in Fig. 6.1. Events generated by JHU under the spin 0 hypotheses are weighted in such a way to account for differences in the Higgs  $p_T$  spectrum with respect to POWHEG simulation. Fig. 6.2 shows the generator level comparison between gluon fusion and  $q\bar{q}$  annihilation production mechanisms for the spin  $2^+$  model.

The normalization and shapes of the  $J^P$ –MELA discriminant for the reducible background are obtained from data control regions, as explained in Sec. 5.4.

### 6.1.3 Event Selection

The event selection criteria described in Sec. 5.2 are applied. An additional requirement on the reconstructed four–lepton invariant mass,

$$115 < m_{4\ell} < 130 \text{ GeV}$$

is applied, in order to select a narrow signal region around the 125 GeV peak with low background contamination.

It has to be noted that, in the case of  $4\mu$  and  $4e$  final states, the selection criteria can in principle produce a reconstructed lepton quadruplet where the assignment of leptons to  $Z$  bosons is wrong (*wrong–pairing*), i.e.

$$\left(\ell_{Z_1}^+, \ell_{Z_1}^-, \ell_{Z_2}^+, \ell_{Z_2}^-\right)_{\text{reco}} \neq \left(\ell_{Z_1}^+, \ell_{Z_1}^-, \ell_{Z_2}^+, \ell_{Z_2}^-\right)_{\text{true}}.$$

Wrong–pairing affects both signal and backgrounds, typically for events with both  $Z_1$  and  $Z_2$  which in reality are off the mass shell. This effect can be evaluated on Monte Carlo: Table 6.1 shows the fraction of mis–paired selected candidates for signal and background simulation.

<sup>1</sup>The two samples can be mixed as no interference effect is present between the ggF and the  $q\bar{q}$  production processes.

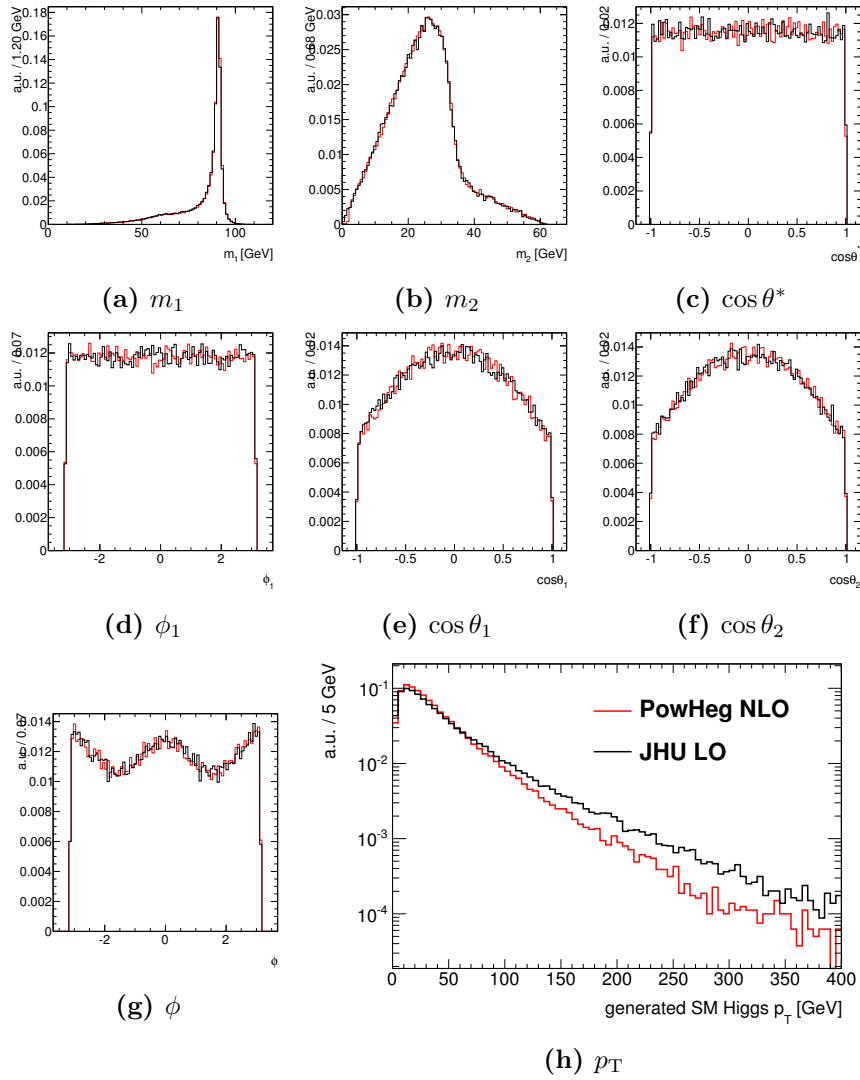


**Figure 6.1.** Comparison between JHU (LO) and POWHEG (NLO) Monte Carlo signal samples for the SM  $0^+$  model, at generator level. Residual differences between Higgs  $p_T$  spectra are accounted for by applying a correction weight to JHU spin-zero events (this weight is not applied in the shown distributions).

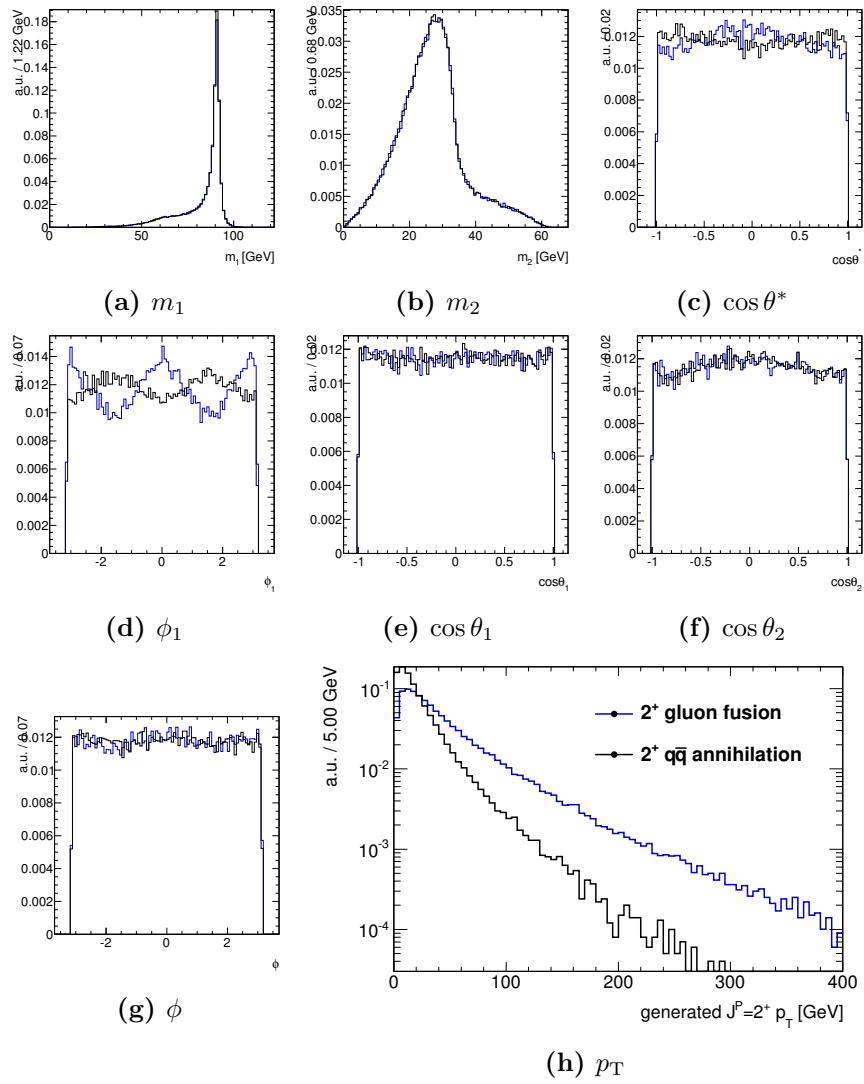


**Figure 6.2.** Comparison between  $J^P = 2^+$  Monte Carlo signal samples with gluon-fusion and  $q\bar{q}$  annihilation production mechanisms, at generator level.

Sample	Fraction of mis-paired candidates (%)	
channel	$4\mu$	$4e$
POWHEG $gg, J^P = 0^+$	$9.4 \pm 0.4$	$11.0 \pm 0.7$
JHU $gg, J^P = 0^+$	$9.2 \pm 0.5$	$10.9 \pm 0.7$
JHU $gg, J^P = 0^-$	$13.5 \pm 0.6$	$13.9 \pm 0.8$
JHU $qq, J^P = 1^+$	$3.5 \pm 0.3$	$4.1 \pm 0.5$
JHU $qq, J^P = 1^-$	$6.8 \pm 0.3$	$6.9 \pm 0.5$
JHU $gg, J^P = 2^+$	$6.3 \pm 0.4$	$6.5 \pm 0.5$
JHU $qq, J^P = 2^+$	$6.0 \pm 0.4$	$6.5 \pm 0.6$
JHU $gg, J^P = 2^-$	$16.7 \pm 0.6$	$15.9 \pm 0.8$
JHU $qq, J^P = 2^-$	$13.2 \pm 0.7$	$16.8 \pm 1.3$
POWHEG $pp \rightarrow ZZ$	$17.8 \pm 0.3$	$16.4 \pm 0.4$

**Table 6.1.** Fraction of events with wrong-pairing selected in JHU and POWHEG simulation, for signals and irreducible background, in the mass window 115 GeV to 130 GeV.

The analysis is performed in four final states ( $4\mu, 2\mu 2e, 2e 2\mu, 4e$ ), two center-of-mass energies ( $\sqrt{s} = 7$  TeV and 8 TeV) and two bins of four-leptons mass,

$$121 \text{ GeV} < m_{4\ell} < 127 \text{ GeV},$$

$$115 \text{ GeV} < m_{4\ell} < 121 \text{ GeV} \cup 127 \text{ GeV} < m_{4\ell} < 130 \text{ GeV},$$

which are denoted as “high” and “low” signal to background ratio (S/B) bins. Monte Carlo studies show that the choice of the two mass bins, which aims at reducing the impact of backgrounds on the measurement, allows for an improvement in the separation between pairs of hypotheses of about 5%.

The expected yields in each of these  $4 \times 2 \times 2$  channels are shown in Table 6.2 and Table 6.3.

Final State and bin	Signal	$ZZ$	Reducible
$4\mu$ High	4.62	1.42	0.29
$4\mu$ Low	0.93	1.92	0.39
$4e$ High	1.95	0.58	0.32
$4e$ Low	0.77	0.83	0.43
$2e 2\mu$ High	3.01	1.02	0.31
$2e 2\mu$ Low	0.79	1.41	0.42
$2\mu 2e$ High	2.22	0.68	0.44
$2\mu 2e$ Low	0.65	0.94	0.61

**Table 6.2.** Expected yields for signal,  $ZZ$  background and reducible backgrounds for the 8 TeV data analysis ( $20.7 \text{ fb}^{-1}$ ).

Final State and bin	Signal	$ZZ$	Reducible
$4\mu$ High	0.83	0.27	0.06
$4\mu$ Low	0.17	0.40	0.09
$4e$ High	0.24	0.09	0.07
$4e$ Low	0.11	0.12	0.10
$2e2\mu$ High	0.51	0.20	0.07
$2e2\mu$ Low	0.13	0.28	0.09
$2\mu2e$ High	0.33	0.11	0.10
$2\mu2e$ Low	0.09	0.17	0.14

**Table 6.3.** Expected yields for signal,  $ZZ$  background and reducible backgrounds for the 7 TeV data analysis ( $4.6 \text{ fb}^{-1}$ ).

### 6.1.4 Kinematic Distributions

Fig. 6.3 shows the distributions for  $m_1, m_2$  and the five production and decay angles in the full mass range  $115 \text{ GeV} < m_{4\ell} < 130 \text{ GeV}$ , for the 8 TeV dataset. Expectations for the  $0^+$  and  $0^-$  hypotheses are shown.

## 6.2 The $J^P$ -MELA Discriminant

As discussed in Sec. 4.2.1, the final state information can be conveniently expressed in terms of eight degrees of freedom — the Higgs mass  $m_H$ , the masses of the two intermediate bosons  $m_1, m_2$  and the five production and decay angles  $\Omega = \{\cos \theta^*, \phi_1, \cos \theta_1, \cos \theta_2, \phi\}$ . In the case of signal, Eq. (4.1) describes the distribution of seven of these observables as a function of parameters which characterize (and define) each of the signal models. Indeed, one can treat Eq. (4.1) as a probability density function (pdf) in this 7D space for a given model  $H$ ,

$$p(m_1^{(\text{true})}, m_2^{(\text{true})}, \Omega^{(\text{true})} | H),$$

where the superscript “true” is to underline that this pdf will provide a *parton level* description of the process, i.e. only the *true* masses and angles will strictly be distributed according to this pdf. Reconstruction effects such as detector acceptance in  $p_T, \eta$  and — to less extent — detector resolution, as well as selection effects which both imply kinematic cuts and induce wrong–pairing, need to be parametrized in an effective way, in order to obtain a pdf  $p_S$  which optimally describes *reconstructed* observables. Such a model can be easily extended to the 8D space, by writing

$$p_S(m_{4\ell}, m_1, m_2, \Omega | H) = p_S(m_{4\ell} | H) \cdot p_S(m_1, m_2, \Omega | H), \quad (6.1)$$

under the assumption that no correlations are present between the reconstructed Higgs mass and the spin–parity sensitive observables.

This information can be used effectively to build a discriminant between two different hypotheses  $H_0$  and  $H_1$ , i.e. a one–dimensional observable which condensates the full final state observation, and whose probability distribution is deeply different

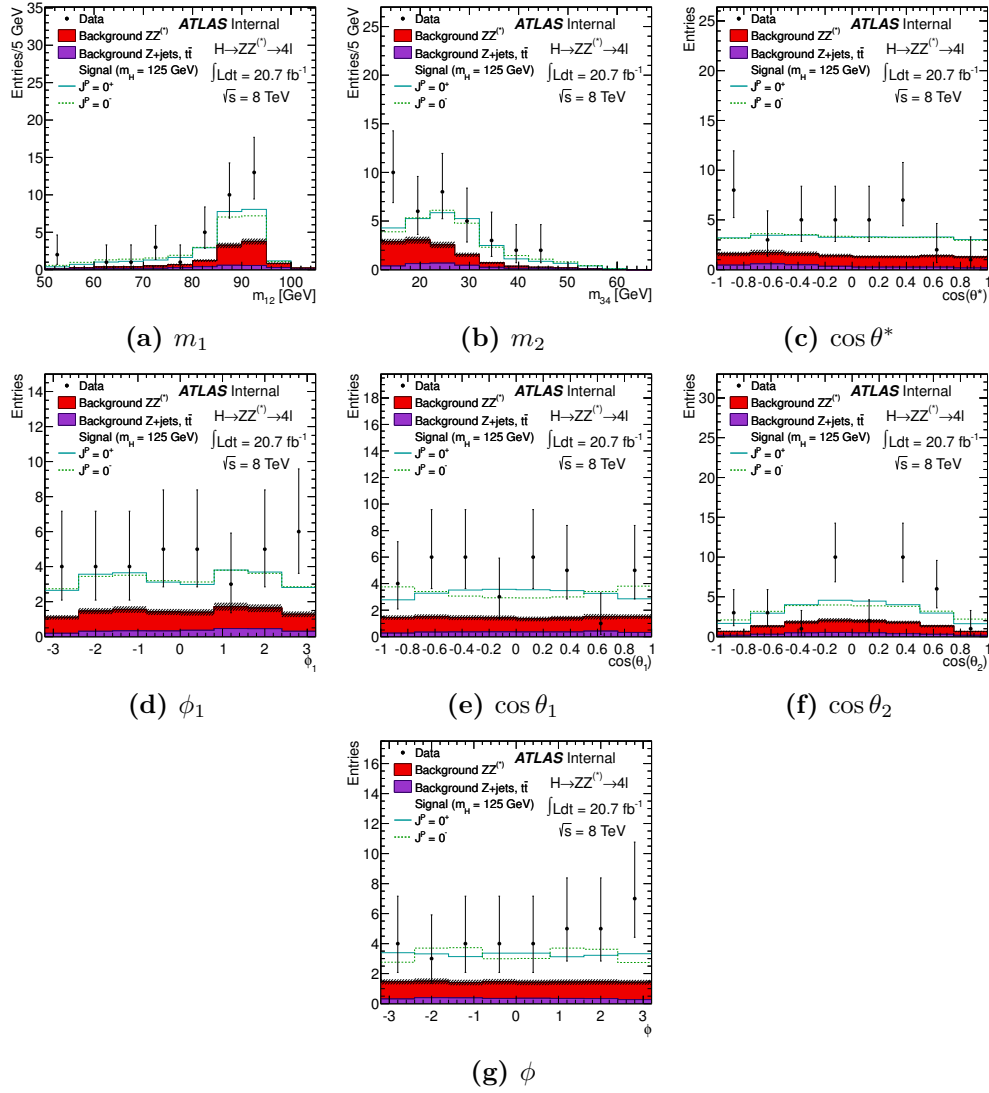


Figure 6.3. Kinematic distributions for the full mass range and the 8 TeV dataset.

between  $H_0$  and  $H_1$ . The  $J^P$ –MELA discriminant is defined as

$$J^P\text{-MELA}_{H_0,H_1}(m_{4\ell}, m_1, m_2, \Omega) = \frac{p_S(m_{4\ell}, m_1, m_2, \Omega|H_0)}{p_S(m_{4\ell}, m_1, m_2, \Omega|H_0) + p_S(m_{4\ell}, m_1, m_2, \Omega|H_1)}, \quad (6.2)$$

and is indeed a number associated to each event<sup>2</sup>, defined in terms of the likelihood of that event to occur when the hypothesis  $H_0$  is true and of the corresponding likelihood for  $H_1$ . By construction, its value is 0 for a purely- $H_1$  event and 1 for a purely- $H_0$  event. It can be proved that the discriminant defined in Eq. (6.2) provides the optimal separation between the two hypotheses, provided that the pdfs  $p$  give an accurate description of the actual observables and their correlations.

### 6.2.1 Signal Description

The likelihood  $p_S$ , which describes the probability of an event to occur under a given signal hypothesis  $H$ , is defined as follows<sup>3</sup>:

$$p_S(m_{4\ell}, m_1, m_2, \Omega|H) = f_{RP} \cdot p_S(m_{4\ell}) \cdot p(m_1, m_2, \Omega|H) \cdot A(m_1, m_2, \Omega|H) + (1 - f_{RP}) \cdot p_S(m_{4\ell}) \cdot p_{WP}(m_1, m_2, \Omega|H), \quad (6.3)$$

where  $f_{RP}$  is the fraction of events in which selection preserved the correct lepton pairing<sup>4</sup>,  $p$  is defined by Eq. (6.1),  $A$  is the *acceptance function* which allows to correct for the fact that Eq. (6.1) is a parton level description of  $m_1, m_2, \Omega$ , and  $p_{WP}$  is a pdf which describes events where the lepton pairing is wrong.

### Mass Parametrization

The mass distribution  $p(m_{4\ell}|H)$  is obtained by fitting a model composed by the sum of a Crystal Ball function and a Gaussian distribution to full simulation Monte Carlo. The same model is used to describe both events with correct and with wrong lepton pairing.

### Acceptance Functions

The acceptance function  $A$  is written as

$$A(m_1, m_2, \Omega) = A(m_1, m_2) \cdot A(\cos \theta^*) \cdot A(\phi_1) \cdot A(\cos \theta_1) \cdot A(\cos \theta_2) \cdot A(\phi),$$

i.e. as a product of individual 1D terms for each of the production and decay angles, and a 2D term for the two dilepton masses. Acceptance functions are determined on half of the statistics of the available signal Monte Carlo samples, as follows.

The individual terms for the five angular variables are obtained by fitting with an empirical model the ratio between the distributions of each angle obtained from full simulation MC (numerator) and from pseudo–data generated according to the

<sup>2</sup>The dependence on  $p_S(m_{4\ell})$  accounts for possible differences in four–lepton mass resolution between different signal hypotheses.

<sup>3</sup>One has to note that  $p$ , which comes from Eq. (4.1) and has its complete form in Sec. A.3, is here evaluated using the *reconstructed* observables.

<sup>4</sup>It is identically 0 for  $2\mu 2e$  and  $2e 2\mu$  final states.

parton-level pdf  $p$  (denominator). The fit functions for a single observable  $\xi$  are in the general form

$$f(\xi) = (a + b\xi) \cdot \sum_{i=0}^4 p_i \cdot \cos(2i \cdot \xi) \quad (6.4)$$

where  $a, b, p_1, p_2, p_3, p_4$  are free parameters of the fit to the ratio of Monte Carlo and data histograms of  $\xi$ .

The 2D term  $A(m_1, m_2)$  is obtained with an iterative procedure. First, all other acceptance corrections are applied, and pseudo-events are generated according to the  $p_S$  model<sup>5</sup>. Then, the ratio between the  $m_2$  distributions in full simulation Monte Carlo and in these pseudo-data (which is an histogram) is fitted with an empirical model. Lastly, the procedure is repeated, this time adding this 1D acceptance correction on  $m_2$ , to obtain the correction term for  $m_1$ .

**Wrong-pairing** The pdf describing the wrong-paired events is obtained from half of the statistics of the available signal Monte Carlo samples, in the form

$$p_{WPP}(m_{4\ell}, m_1, m_2, \Omega) = p_S(m_{4\ell}) \cdot p_{WPP}(m_1, m_2) \cdot p(\cos \theta^*) \cdot p(\phi_1) \cdot p(\cos \theta_1) \cdot p(\cos \theta_2) \cdot p(\phi).$$

The 2D term  $p_{WPP}(m_1, m_2)$  is described by a 2D template obtained from Monte Carlo simulation. In a way analogous to the acceptance functions  $A$ , an empirical parametrization is used to describe the 1D angular distributions for wrong-paired events, in the form

$$f(\xi) = (a + b\xi) \cdot \sum_{i=0}^8 p_i \cdot \cos(2i \cdot \xi). \quad (6.5)$$

### 6.2.2 Closure Tests

Closure tests for the likelihood (6.3) are performed using half of the full simulation Monte Carlo samples, the other half having been used to determine the functional form of acceptance functions and wrong-pairing parametrization. Comparison are done using 1D projections, over each of the eight dimensions, of the full likelihood model, which is compared to simulation for all the considered signal hypotheses.

The projections of the signal likelihood and full MC simulation are in good agreement, indicating that the chosen parametrizations are adequate for a general description of the considered spin-parity states. Comparisons are shown in the case of a SM Higgs boson in Fig. 6.4 to 6.11, while the distributions for all other models are shown in App. B. Any residual discrepancy observed between pdf and MC samples is not expected to introduce any bias in the hypothesis testing procedure.

### 6.2.3 Spin Two: Admixtures between $gg$ and $q\bar{q}$ Production

The pdf for a  $J = 2$  particle with a given fraction of  $q\bar{q}$  annihilation production  $f_{qq}$  is defined in terms of the pdfs of the pure  $q\bar{q}$  and  $gg$  states, already corrected for

<sup>5</sup>For this purpose  $f_{RP} \equiv 1$ .

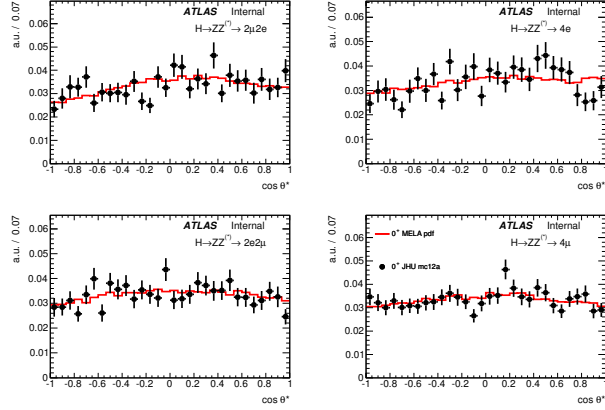


**Figure 6.4.** Comparison of the likelihood projection for a  $0^+$  Higgs-like resonance (red curve) and the corresponding JHU (black points) MC simulation for the  $\cos \theta^*$  observable. From left to right and top to bottom:  $2\mu 2e$ ,  $4e$ ,  $2e2\mu$  and  $4\mu$  channels.

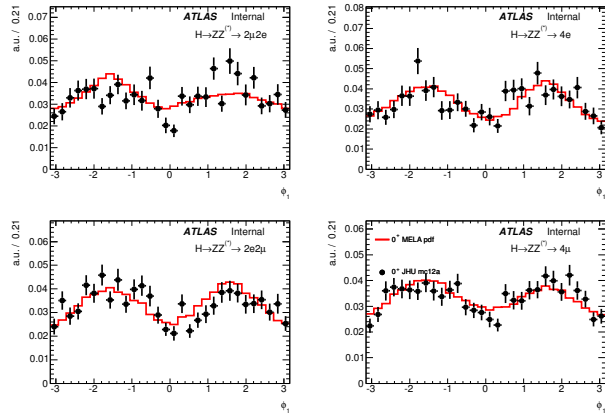


**Figure 6.5.** Comparison of the likelihood projection for a  $0^+$  Higgs-like resonance (red curve) and the corresponding JHU (black points) MC simulation for the  $\phi_1$  observable. From left to right and top to bottom:  $2\mu 2e$ ,  $4e$ ,  $2e2\mu$  and  $4\mu$  channels.

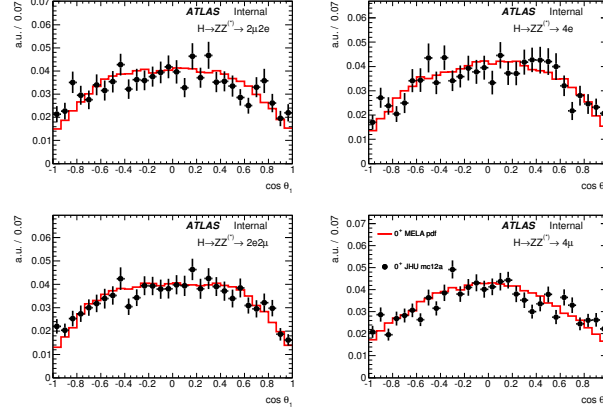


**Figure 6.6.** Comparison of the likelihood projection for a  $0^+$  Higgs-like resonance (red curve) and the corresponding JHU (black points) MC simulation for the  $\cos \theta_1$  observable. From left to right and top to bottom:  $2\mu 2e$ ,  $4e$ ,  $2e 2\mu$  and  $4\mu$  channels.

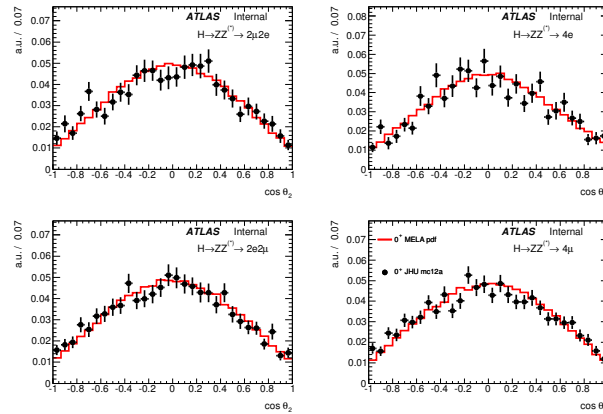


**Figure 6.7.** Comparison of the likelihood projection for a  $0^+$  Higgs-like resonance (red curve) and the corresponding JHU (black points) MC simulation for the  $\cos \theta_2$  observable. From left to right and top to bottom:  $2\mu 2e$ ,  $4e$ ,  $2e 2\mu$  and  $4\mu$  channels.

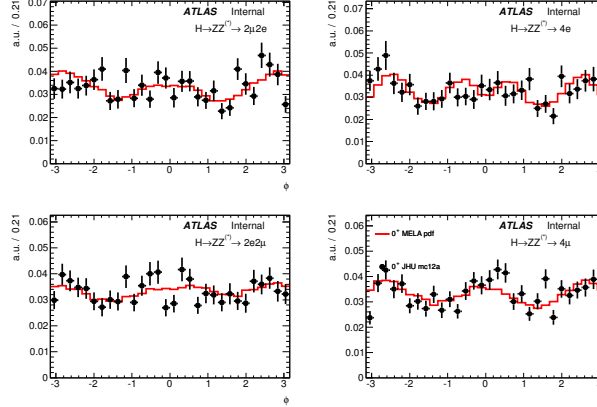


**Figure 6.8.** Comparison of the likelihood projection for a  $0^+$  Higgs-like resonance (red curve) and the corresponding JHU (black points) MC simulation for the  $\phi$  observable. From left to right and top to bottom:  $2\mu 2e$ ,  $4e$ ,  $2e 2\mu$  and  $4\mu$  channels.

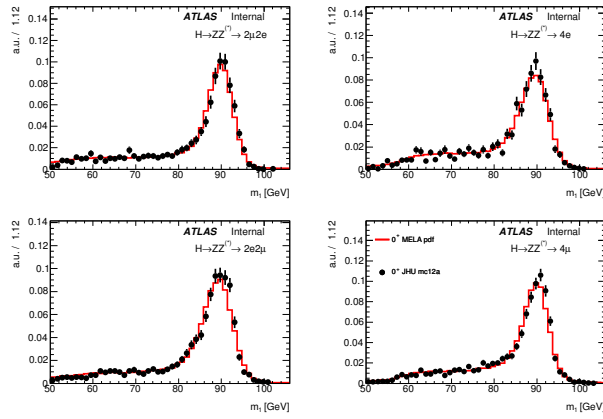


**Figure 6.9.** Comparison of the likelihood projection for a  $0^+$  Higgs-like resonance (red curve) and the corresponding JHU (black points) MC simulation for the  $m_{Z_1}$  observable. From left to right and top to bottom:  $2\mu 2e$ ,  $4e$ ,  $2e 2\mu$  and  $4\mu$  channels.

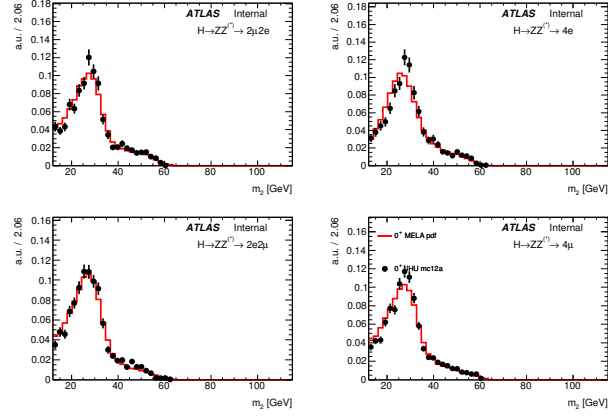


**Figure 6.10.** Comparison of the likelihood projection for a  $0^+$  Higgs-like resonance (red curve) and the corresponding JHU (black points) MC simulation for the  $m_{Z_2}$  observable. From left to right and top to bottom:  $2\mu 2e$ ,  $4e$ ,  $2e 2\mu$  and  $4\mu$  channels.

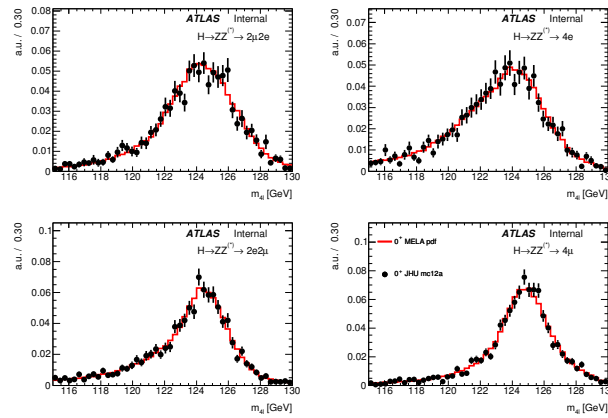


**Figure 6.11.** Comparison of the likelihood projection for a  $0^+$  Higgs-like resonance (red curve) and the corresponding JHU (black points) MC simulation for the  $m_{A_1}$  observable. From left to right and top to bottom:  $2\mu 2e$ ,  $4e$ ,  $2e 2\mu$  and  $4\mu$  channels.

$J^P$	Production mechanism	Decay channel	Selection efficiency
$2^+$	$gg \rightarrow X$	$X \rightarrow 4\mu$	$0.346 \pm 0.003$
$2^+$		$X \rightarrow 2\mu 2e$	$0.216 \pm 0.003$
$2^+$		$X \rightarrow 2e 2\mu$	$0.279 \pm 0.003$
$2^+$		$X \rightarrow 4e$	$0.181 \pm 0.002$
$2^+$	$q\bar{q} \rightarrow X$	$X \rightarrow 4\mu$	$0.315 \pm 0.002$
$2^+$		$X \rightarrow 2\mu 2e$	$0.193 \pm 0.002$
$2^+$		$X \rightarrow 2e 2\mu$	$0.254 \pm 0.002$
$2^+$		$X \rightarrow 4e$	$0.165 \pm 0.002$
$2^-$	$gg \rightarrow X$	$X \rightarrow 4\mu$	$0.356 \pm 0.003$
$2^-$		$X \rightarrow 2\mu 2e$	$0.218 \pm 0.003$
$2^-$		$X \rightarrow 2e 2\mu$	$0.278 \pm 0.003$
$2^-$		$X \rightarrow 4e$	$0.193 \pm 0.002$
$2^-$	$q\bar{q} \rightarrow X$	$X \rightarrow 4\mu$	$0.233 \pm 0.003$
$2^-$		$X \rightarrow 2\mu 2e$	$0.140 \pm 0.002$
$2^-$		$X \rightarrow 2e 2\mu$	$0.112 \pm 0.002$
$2^-$		$X \rightarrow 4e$	$0.180 \pm 0.002$

**Table 6.4.** Selection efficiencies for the spin 2 hypothesis, for the  $gg$  and  $q\bar{q}$  production mechanisms.

acceptance and wrong–pairing effects: one has

$$\begin{aligned}
 p_S(m_{4\ell}, m_1, m_2, \Omega | J = 2, f_{qq}) &= f_{qq}^{\text{eff}} \cdot p_S(m_{4\ell}, m_1, m_2, \Omega | J = 2, f_{qq} = 0) \\
 &\quad + (1 - f_{qq}^{\text{eff}}) \cdot p_S(m_{4\ell}, m_1, m_2, \Omega | J = 2, f_{qq} = 1),
 \end{aligned} \tag{6.6}$$

where the effective fraction  $f_{qq}^{\text{eff}}$  is defined in terms of the selection efficiencies  $\epsilon_{gg,qq}$  for the two production mechanisms, as

$$f_{qq}^{\text{eff}} = \frac{f_{qq} \cdot \epsilon_{qq}}{f_{qq} \cdot \epsilon_{qq} + (1 - f_{qq}) \cdot \epsilon_{gg}}.$$

Table 6.4 shows these selection efficiencies for the four final states, as evaluated from Monte Carlo.

Closure tests for this procedure are shown in Appendix B for all the considered values of  $f_{qq}$  for the  $J = 2$  states. Good agreement is found between the fully simulated MC events and the 1D projections of Eq. (6.6), proving the validity of the linear combination described above.

### 6.3 Signal and Background Parametrization

Signal and background models are obtained from the distributions of the  $J^P$ –MELA discriminant computed on Monte Carlo samples for signal and irreducible background,

and on data control regions for the reducible background. Histograms obtained in this way are used as likelihood components for a binned maximum likelihood approach.

### 6.3.1 Likelihood Model

The total binned likelihood can be written in the form

$$L(\epsilon, \mu) = \prod_{ij} \text{Pois}(N_{ij}^{\text{obs}} | N_{ij}^{\text{exp}}),$$

where the sum runs over the 16 channels<sup>6</sup>  $i$  and the bin  $j$  of the  $i$ -th distribution.  $N_{ij}^{\text{obs}}$  is the number of events observed in the  $j$ -th bin of the  $i$ -th channel, while the corresponding expected number of events is

$$N_{ij}^{\text{exp}} = \mu N_S^{ij} [\epsilon \cdot p_{ij}(H_0) + (1 - \epsilon) \cdot p_{ij}(H_1)] + \sum_{k=ZZ, \text{red}} N_{B_k}^{ij} p_{ij}(B_k),$$

where  $N_{S,ZZ, \text{red}}^{ij}$  is the expected number of events from signal, irreducible and reducible backgrounds, and  $p_{ij}$  is the value in that bin of the pdf describing the  $J^P$ -MELA discriminant for a given signal or background hypothesis.

The signal strength  $\mu$  is taken at its best fit value (*profiled*).  $H_0$  and  $H_1$  are the two hypotheses under test: discrimination is performed computing the ratio of profile likelihoods test statistics

$$\log \frac{L(H_0)}{L(H_1)} \equiv \log \frac{L(\epsilon = 0, \mu = \hat{\mu})}{L(\epsilon = 1, \mu = \hat{\mu})}. \quad (6.7)$$

Distributions of the test statistics are computed generating a series of pseudo-experiments in the  $H_0$  and  $H_1$  hypotheses.

### 6.3.2 Discriminant Distributions

$J^P$ -MELA distributions (histograms), from which  $p_{ij}$  are computed, are obtained:

- in the case of signal and irreducible background, on full simulation MC;
- in the case of reducible background, by smoothing using a Kernel Density method the  $J^P$ -MELA distribution computed on the inclusive data-driven control region, i.e. the same distribution is used for all the 16 channels.

Distributions for the various discriminants are shown in Fig. 6.12–6.15.

<sup>6</sup>(7 TeV, 8 TeV)  $\times$  (4 $\mu$ , 2 $\mu$ 2e, 2e2 $\mu$ , 4e)  $\times$  (“low”, “high”)

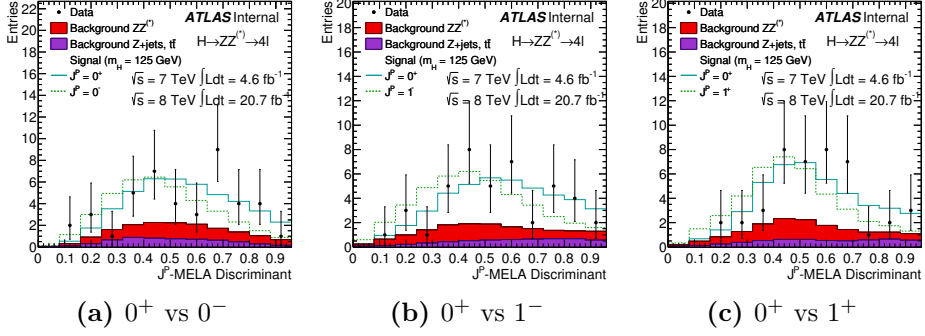


**Figure 6.12.** Distribution of the  $J^P$ -MELA discriminant between the  $0^+$  and the  $0^-, 1^+$  and  $1^-$  hypotheses, in data and Monte Carlo.

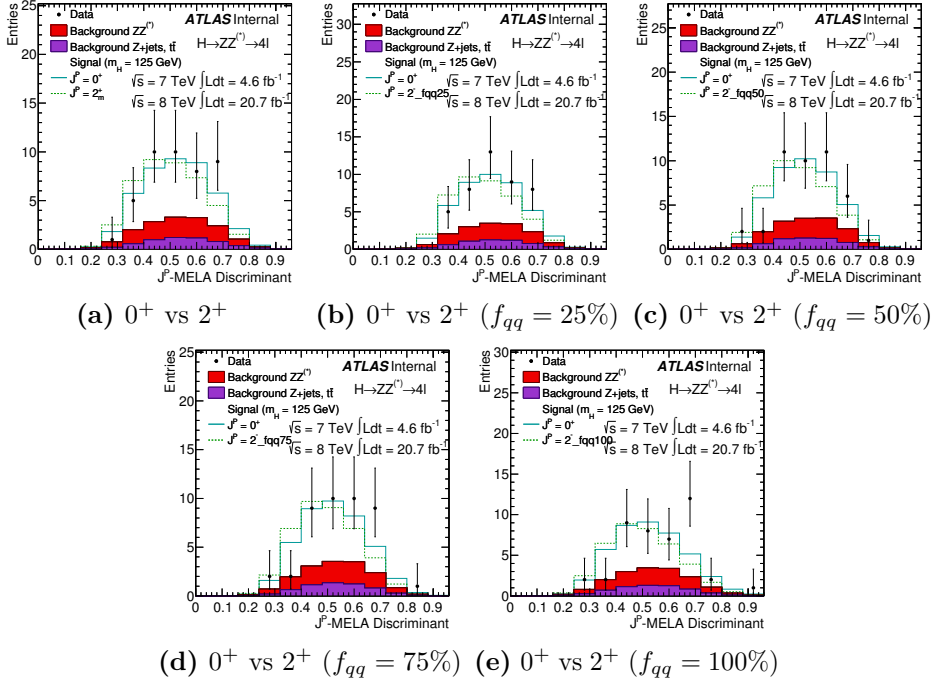


**Figure 6.13.** Distribution of the  $J^P$ -MELA discriminant between the  $0^+$  and the  $2^+$  hypothesis with different values of  $f_{qq}$ , in data and Monte Carlo.

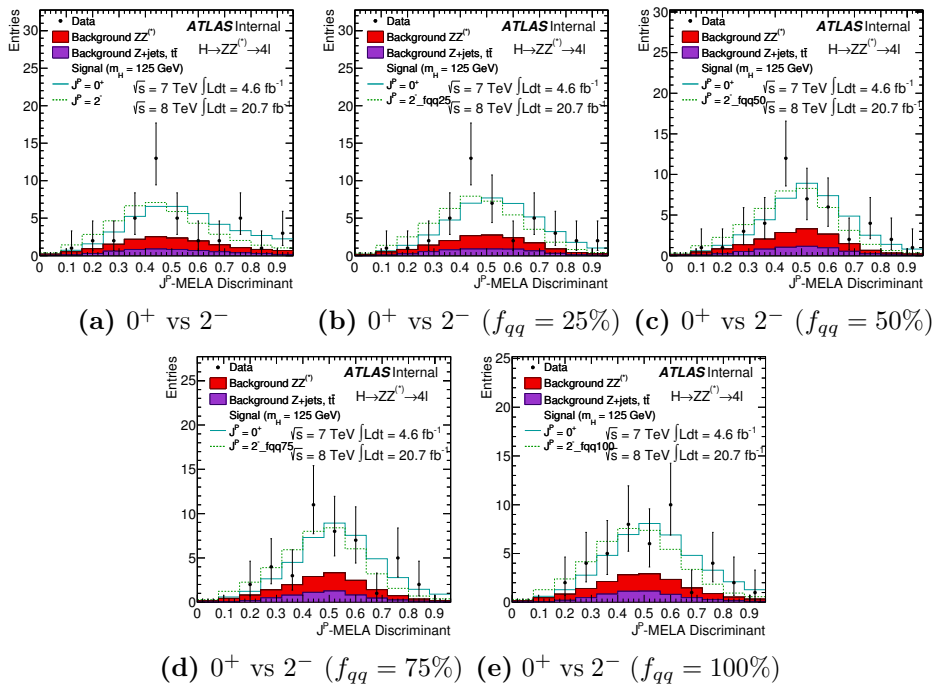


**Figure 6.14.** Distribution of the  $J^P$ -MELA discriminant between the  $0^+$  and the  $2^-$  hypothesis with different values of  $f_{qq}$ , in data and Monte Carlo.

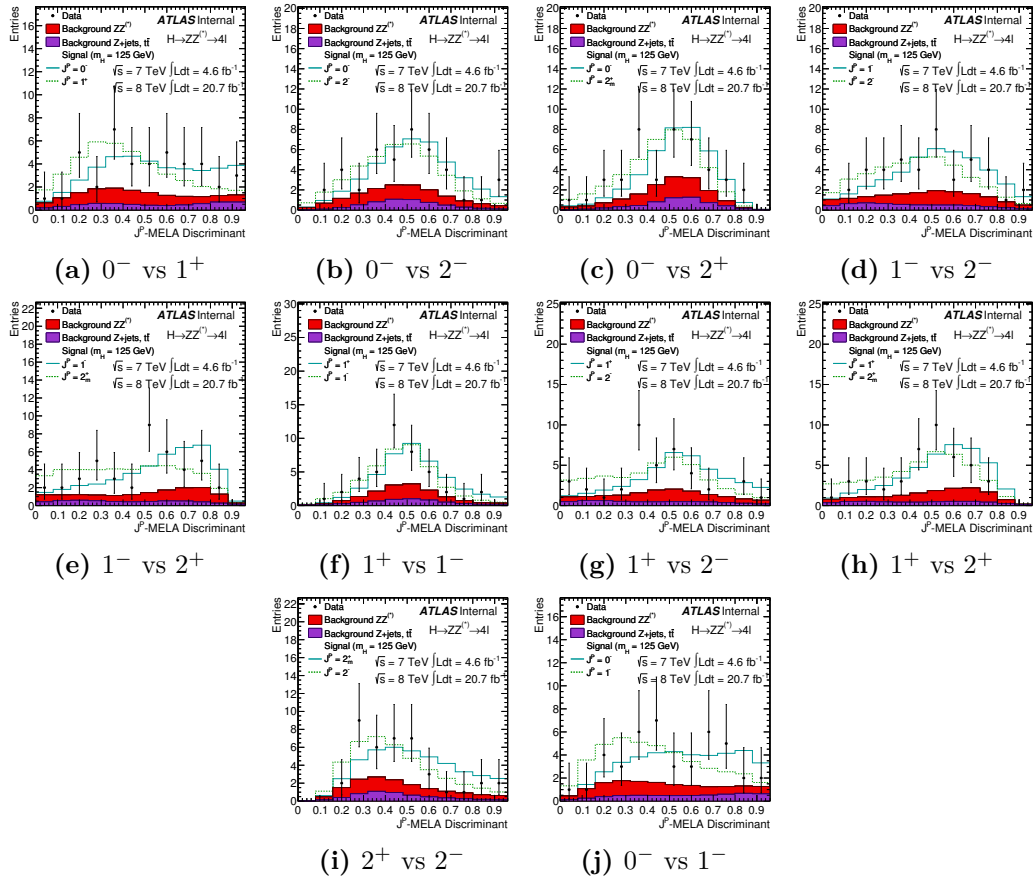


Figure 6.15. Distribution of the  $J^P$ -MELA discriminant between various hypotheses, in data and Monte Carlo.

### 6.3.3 Systematic Uncertainties

Systematic uncertainties are included to the likelihood model of Sec. 6.3.1 in the form of nuisance parameters, which allow the description of effects both on the normalization of each of the 16 analysis sub-channels and on the shape of the  $J^P$ -MELA discriminant.

#### Normalization Systematics

The following effects on normalization are taken into account:

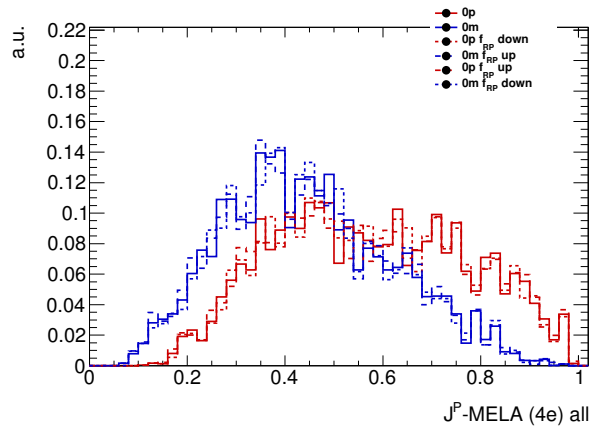
- the systematic uncertainty on the luminosity measurement, which affects the overall normalization of signal and irreducible background, described in Sec. 5.5;
- the effect of assuming a different value for the hypothesized  $m_H$ , which leads less than 10% variations in the relative normalization of “low” and “high” S/B bins;
- the effect of muon and electron energy scale and resolution systematics, which is conservatively evaluated as a 10% effect on the relative normalization of the two S/B bins;
- the overall normalization uncertainties on the event yields for irreducible and reducible background, described in Sec. 5.5.

#### Shape Systematics

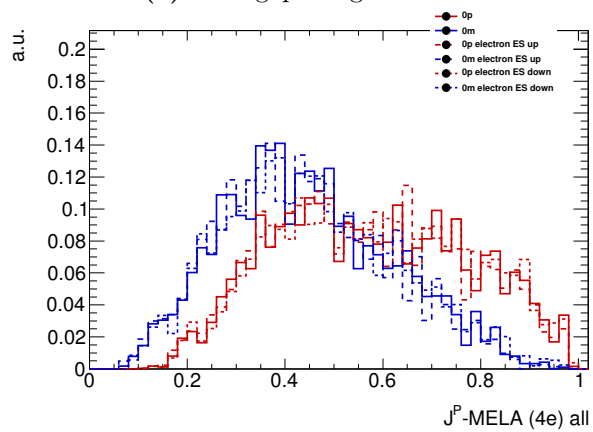
Additional systematic effects can affect the shapes of the  $J^P$ -MELA discriminant. The following have been taken into account:

- an uncertainty on the fraction of candidates with wrong lepton pairing is assigned to all spin hypotheses from the half-difference between the  $0^+$  wrong-pairing fraction obtained from POWHEG and JHU simulations (Table 6.1);
- the statistical uncertainty on the reducible background shape, due to the low statistics available on data, is taken from the 95% CL upper and lower variations of the nominal Kernel Density pdf;
- the effect on the discriminant shapes of the uncertainty on the corrections to the Higgs  $p_T$  spectrum;
- the effect of muon and electron energy scale and resolution systematics.

The effect on the  $J^P$ -MELA discriminant of some of the shape systematics is illustrated in Fig. 6.16, while Fig. 6.17 shows two examples of the shape uncertainty associated to the reducible backgrounds.

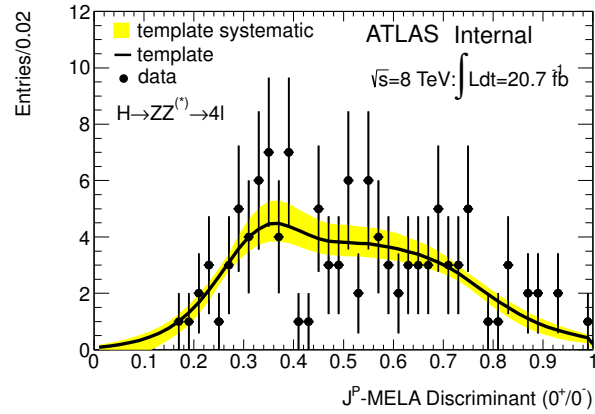
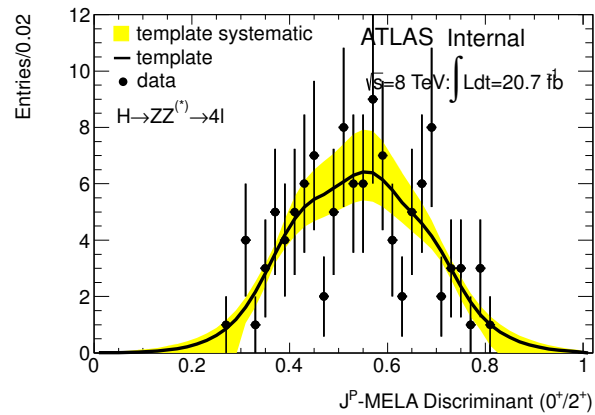


(a) Wrong–pairing fraction



(b) Electron energy scale systematics

**Figure 6.16.** Distributions of the  $J^P$ –MELA discriminant between the  $0^+$  and the  $0^-$  hypotheses, with the shape systematics associated to the fraction of wrong–paired events and to the electron energy scale systematics in the  $4e$  final state.

(a)  $0^+$  vs  $0^-$ (b)  $0^+$  vs  $2^+$ 

**Figure 6.17.** Distributions  $J^P$ -MELA discriminant distributions for the reducible background obtained for the  $0^+$  vs  $0^-$  and  $0^+$  vs  $2^+$  hypotheses tests, and the corresponding systematic uncertainties. Due to the lack of data statistics, all the four final states are combined together.

tested	assumed	$0^+$	$0^-$	$1^+$	$1^-$	$2^+$	$2^-$
$0^+$	-	-	0.0025 (2.8116)	0.0046 (2.6015)	0.0009 (3.1167)	0.0676 (1.4936)	0.0043 (2.6291)
$0^-$	0.0011 (3.0647)	-	-	0.0004 (3.3715)	0.0004 (3.3580)	0.0044 (2.6176)	0.0096 (2.3408)
$1^+$	0.0031 (2.7376)	0.0004 (3.3876)	-	-	0.0074 (2.4391)	0.0031 (2.7328)	0.0005 (3.2664)
$1^-$	0.0010 (3.0883)	0.0005 (3.2777)	0.0067 (2.4727)	-	-	0.0003 (3.4183)	0.0044 (2.6232)
$2^+$	0.0639 (1.5232)	0.0073 (2.4432)	0.0040 (2.6503)	0.0004 (3.3876)	-	-	0.0023 (2.8291)
$2^-$	0.0032 (2.7247)	0.0082 (2.4015)	0.0011 (3.0490)	0.0028 (2.7730)	0.0013 (3.0015)	-	-

**Table 6.5.** Expected separations between different spin hypotheses combining 7 TeV and 8 TeV results.

tested	assumed	$0^+$	$2^+(f_{qq} = 25\%)$	$2^+(f_{qq} = 50\%)$	$2^+(f_{qq} = 75\%)$	$2^+(f_{qq} = 100\%)$
$0^+$	-	-	0.0750 (1.4397)	0.0775 (1.4220)	0.0734 (1.4512)	0.0817 (1.3937)
$2^+(f_{qq} = 25\%)$	0.0674 (1.4955)					
$2^+(f_{qq} = 50\%)$	0.0678 (1.4922)					
$2^+(f_{qq} = 75\%)$	0.0686 (1.4863)					
$2^+(f_{qq} = 100\%)$	0.0652 (1.5122)					

**Table 6.6.** Expected separations between the  $0^+$  and the  $2^+$  hypotheses for different values of  $f_{qq}$ , combining 7 TeV and 8 TeV results.

## 6.4 Hypothesis Testing Results

Distributions for the test statistics of Eq. (6.7), generated using more than 500k pseudo–experiments for each hypothesis, are shown in Fig. 6.18–6.21. Maximum likelihood estimates of the nuisance parameters are obtained from a fit of the likelihood model to the data. In each pseudo–experiment, the expected number of signal and background events is fixed to the yield observed on data. All systematic uncertainties described in Sec. 6.3.3 are taken into account; the signal strength  $\mu$  is profiled.

### 6.4.1 Expected Separations

Expected separations between pairs of alternative hypotheses are shown in terms of  $p_0$ –values and the corresponding number of Gaussian  $\sigma$ s (between parentheses) in Tables 6.5–6.7, for the combined 7 TeV and 8 TeV dataset.

### 6.4.2 Observed Separations

Observed separations between pairs of alternative hypotheses are shown in terms of  $p_0$ –values and the corresponding number of Gaussian  $\sigma$ s (between parentheses<sup>7</sup>) in Tables 6.8–6.10, for the combined 7 TeV and 8 TeV dataset.

<sup>7</sup>Negative values for Gaussian sigmas occur when  $p_0 > 0.50$ .

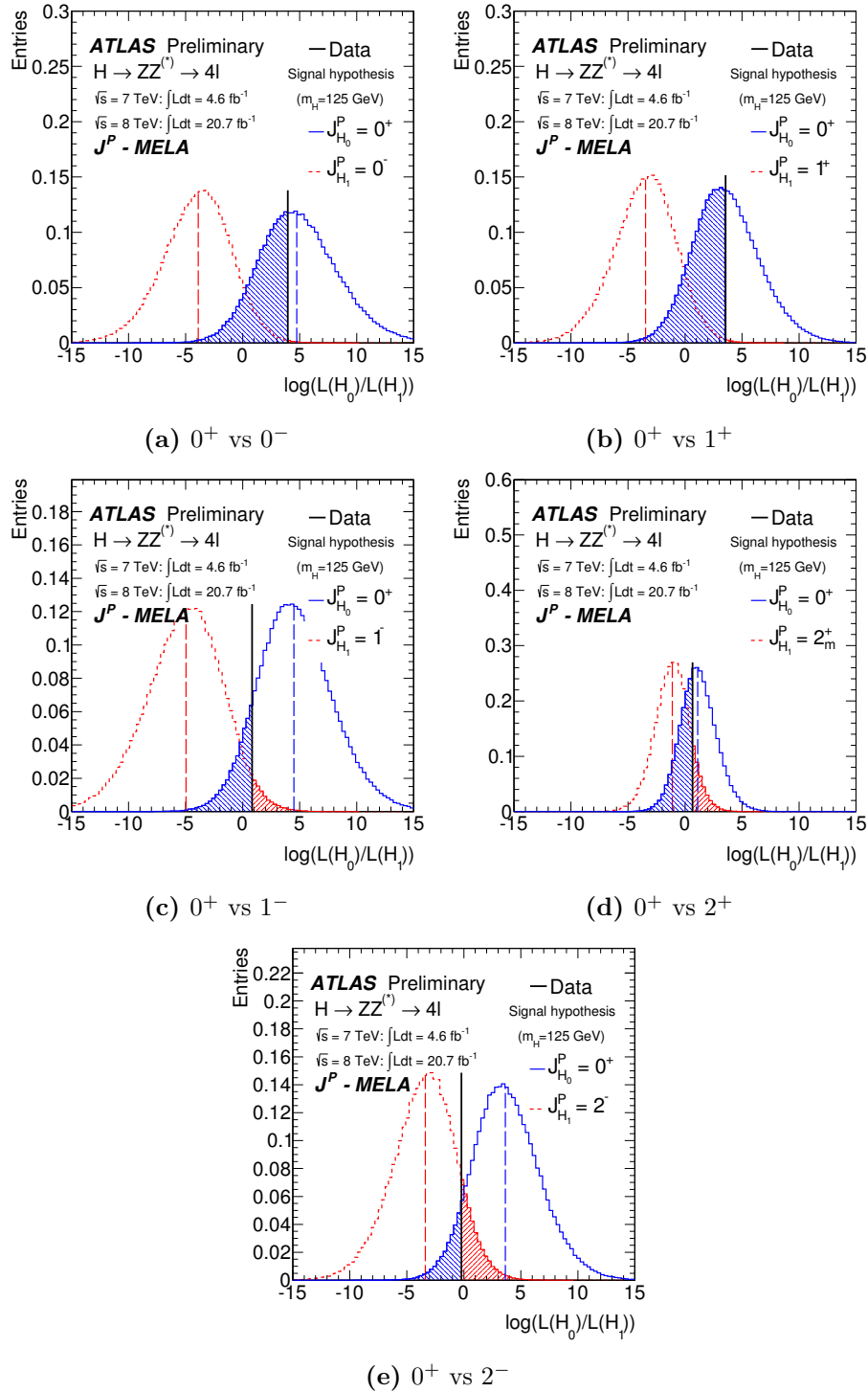


**Figure 6.18.** Distributions of the test statistics for each pair of spin and parity hypotheses, compared with the observed value of the test statistics in data.

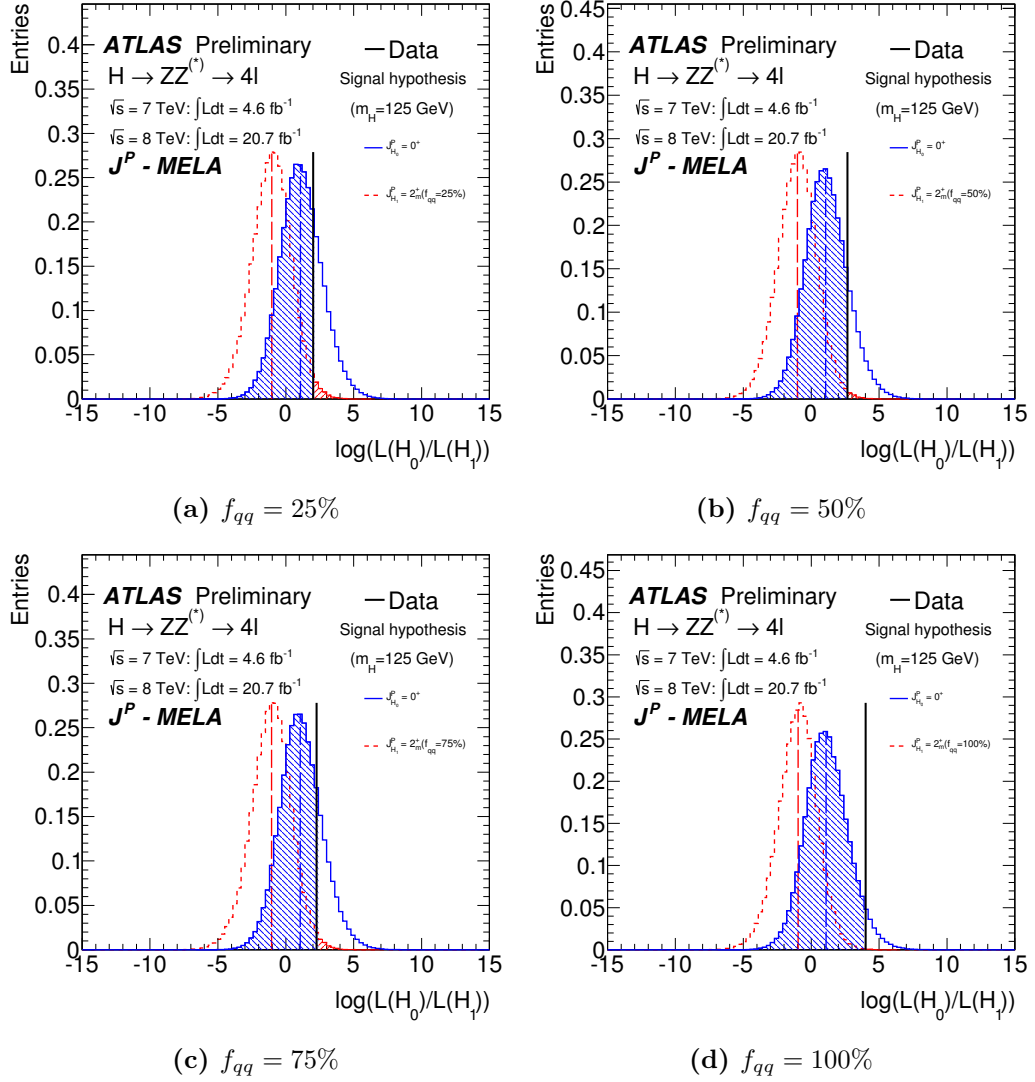


**Figure 6.19.** Distributions of the test statistics for the hypothesis test between  $0^+$  vs  $2^+$  with  $f_{qq} \neq 0$ , compared with the observed value of the test statistics in data.

tested	assumed	$0^+$	$2^-(f_{qq} = 25\%)$	$2^-(f_{qq} = 50\%)$	$2^-(f_{qq} = 75\%)$	$2^-(f_{qq} = 100\%)$
$0^+$	-	-	0.0043 (2.6239)	0.0078 (2.4196)	0.0065 (2.4828)	0.0045 (2.6133)
$2^-(f_{qq} = 25\%)$	0.0039 (2.6637)					
$2^-(f_{qq} = 50\%)$	0.0065 (2.4829)					
$2^-(f_{qq} = 75\%)$	0.0057 (2.5300)					
$2^-(f_{qq} = 100\%)$	0.0034 (2.7108)					

**Table 6.7.** Expected separations between the  $0^+$  and the  $2^+$  hypotheses for different values of  $f_{qq}$ , combining 7 TeV and 8 TeV results.

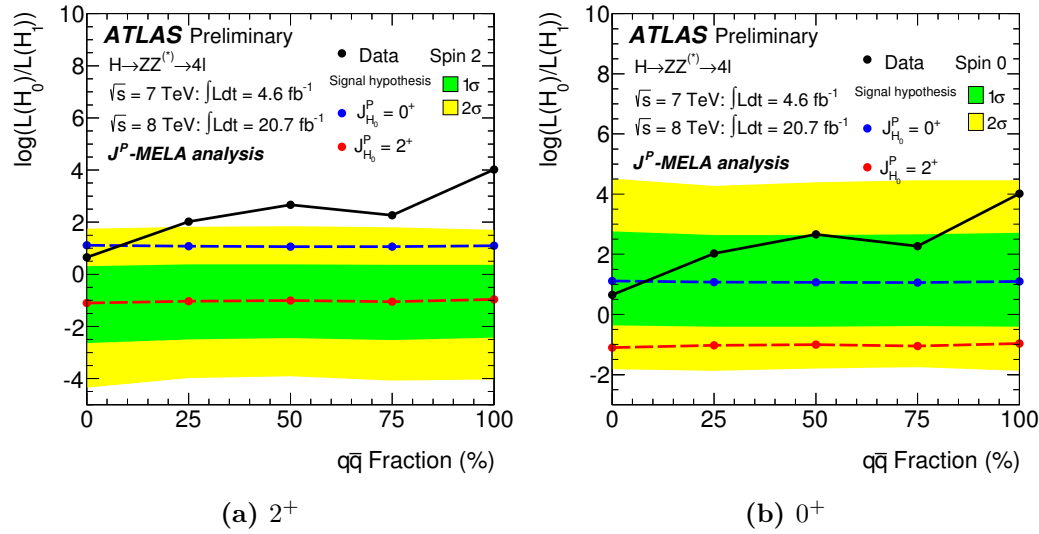


**Figure 6.20.** Median of the distributions of the test statistics for the assumed ( $H_0 = 0^+$ ) and the alternative ( $H_1 = 2^+$ ) hypotheses, together with  $\pm 1\sigma$  and  $\pm 2\sigma$  bands around either hypothesis, for  $0^+$  vs  $2^+$  with different values of  $f_{qq}$ , compared with the observation in data.

tested assumed	$0^+$	$0^-$	$1^+$	$1^-$	$2^+$	$2^-$
$0^+$	-	0.4046 (0.2416)	0.5075 (-0.0188)	0.1123 (1.2143)	0.3793 (0.3074)	0.0766 (1.4286)
$0^-$	0.0022 (2.8445)	-	0.1019 (1.2707)	0.0105 (2.3093)	0.0378 (1.7766)	0.1681 (0.9616)
$1^+$	0.0028 (2.7690)	0.0134 (2.2153)	-	0.0874 (1.3567)	0.0204 (2.0451)	0.0013 (3.0158)
$1^-$	0.0274 (1.9204)	0.1288 (1.1320)	0.1360 (1.0986)	-	0.0300 (1.8810)	0.1680 (0.9621)
$2^+$	0.1127 (1.2122)	0.2126 (0.7976)	0.2499 (0.6747)	0.0498 (1.6470)	-	0.0504 (1.6414)
$2^-$	0.1070 (1.2428)	0.0778 (1.4202)	0.3875 (0.2859)	0.0373 (1.7830)	0.0995 (1.2844)	-

**Table 6.8.** Observed separations between different spin hypotheses combining 7 TeV and 8 TeV results.

tested assumed	$0^+$	$2^+(25\%qq)$	$2^+(50\%qq)$	$2^+(75\%qq)$	$2^+(100\%qq)$
$0^+$	-	0.7309 (-0.6154)	0.8411 (-0.9988)	0.7789 (-0.7685)	0.9550 (-1.6952)
$2^+(25\%qq)$	0.0166 (2.1297)				
$2^+(50\%qq)$	0.0056 (2.5346)				
$2^+(75\%qq)$	0.0115 (2.2748)				
$2^+(100\%qq)$	0.0005 (3.3048)				

**Table 6.9.** Observed separations between the  $0^+$  and the  $2^+$  hypotheses for different values of  $f_{qq}$ , combining 7 TeV and 8 TeV results.

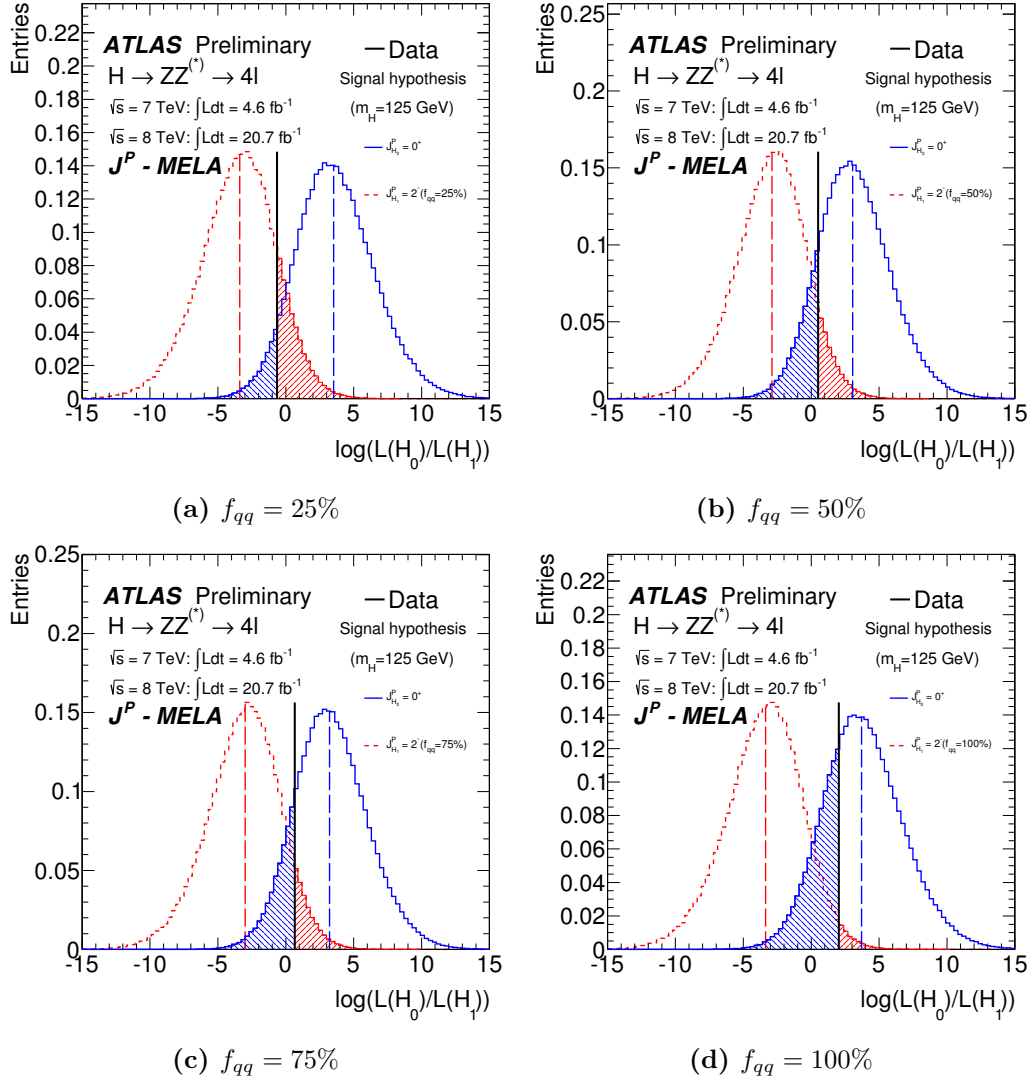


**Figure 6.21.** Distributions of the test statistics for the hypothesis test between  $0^+$  vs  $2^-$  with  $f_{qq} \neq 0$ , compared with the observed value of the test statistics in data.

tested	assumed	$0^+$	$2^- (25\%qq)$	$2^- (50\%qq)$	$2^- (75\%qq)$	$2^- (100\%qq)$
$0^+$	-	-	0.0568 (1.5823)	0.1521 (1.0275)	0.1539 (1.0200)	0.2729 (0.6042)
$2^- (25\%qq)$	0.1446 (1.0600)					
$2^- (50\%qq)$	0.0765 (1.4290)					
$2^- (75\%qq)$	0.0680 (1.4912)					
$2^- (100\%qq)$	0.0180 (2.0980)					

**Table 6.10.** Observed separations between the  $0^+$  and the  $2^-$  hypotheses for different values of  $f_{qq}$ , combining 7 TeV and 8 TeV results.

		$J^P$ -MELA analysis			
		tested $J^P$ for an assumed $0^+$		tested $0^+$ for an assumed $J^P$	$CL_s$
		expected	observed	observed	
$0^-$	$p_0$	0.0011	0.0022	0.40	0.004
$1^+$	$p_0$	0.0031	0.0028	0.51	0.006
$1^-$	$p_0$	0.0010	0.027	0.11	0.031
$2^+$	$p_0$	0.064	0.11	0.38	0.182
$2^-$	$p_0$	0.0032	0.11	0.08	0.116

**Table 6.11.** Values of the expected and observed  $p_0$  for an assumed  $0^+$  hypothesis  $H_0$  and different tested  $H_1 = J^P$  hypotheses, together with the observed  $p_0$  values when  $H_0$  and  $H_1$  are inverted, for the combined 8 TeV and 7 TeV dataset. The  $CL_s$  confidence level obtained from these  $p_0$  values is also shown. The production mode for  $2^+$  and  $2^-$  states is assumed to be 100% ggF.

### 6.4.3 Summary

Table 6.11 shows the observed values of  $p_0$  for all hypothesis tests in which the assumed hypothesis is the Standard Model  $0^+$  model. The statistical separation between the hypothesis pairs is also provided in terms of  $CL_s$ , defined as

$$CL_s = \frac{p_0(\text{data}|H_1 = J^P)}{1 - p_0(\text{data}|H_0 = 0^+)},$$

where  $p_0$  is computed from the test statistics distribution in the  $H_0(H_1)$  hypothesis, as the right-tail integral from the test statistics value on data to infinity. The expected separation between  $H_0$  and  $H_1$  is obtained using the median of the  $H_0$  distribution instead of the value of the test statistics on data.

The expected separation between the SM hypothesis and the  $0^-, 1^+, 1^-$  and  $2^-$  hypotheses is above the  $2.5\sigma$  level, while the expected separation against  $2^+$  is about  $1.5\sigma$ . The expected separation is, for the  $2^+$  and  $2^-$  hypotheses, found to be independent on the production fraction  $f_{qq}$ .

The observed  $p_0$  values allow to exclude the  $0^-, 1^+$  and  $1^-$  hypotheses against the SM  $0^+$  with a  $CL_s$  value of 99.6%, 99.4% and 96.9%. As for the exclusion of the  $2^+$  and  $2^-$  hypotheses against the SM, the observed  $CL_s$  values make the result inconclusive.

## 6.5 Combination with Other Channels

A combination of spin-parity measurements from  $H \rightarrow ZZ^{(*)} \rightarrow 4\ell$ ,  $H \rightarrow \gamma\gamma$  and  $H \rightarrow WW^{(*)} \rightarrow \ell\nu\ell\nu$  is presented in Ref. [73]. Results, as shown in Fig. 6.22, exclude the specific  $J^P = 2^+$  hypothesis against the Standard Model expectation with a confidence level of more than 99.9%, independently on assumed the value of the fraction  $f_{qq}$ .

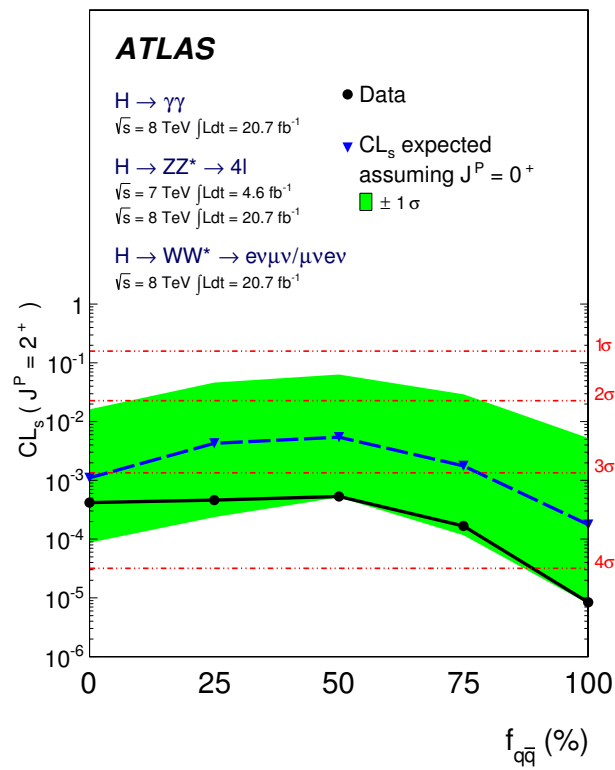


**Figure 6.22.** Combination of spin–parity studies in  $H \rightarrow ZZ^{(*)} \rightarrow 4\ell$ ,  $H \rightarrow \gamma\gamma$  and  $H \rightarrow WW^{(*)} \rightarrow \ell\nu\ell\nu$  analyses, for the  $0^+$  versus  $2^+$  hypothesis testing. From Ref. [73].

## Chapter 7

# Probing the $HZZ$ Tensor Structure

Direct information on the decay amplitude of the new particle into two vector bosons can be obtained by studying the final state distributions of the decay leptons. If the spin of this particle is assumed to be zero, four coupling parameters  $g_i$  define the most general  $X \rightarrow ZZ$  decay amplitude. In the Standard Model only the first one,  $g_1$ , is non-zero: admixtures between  $CP$ -even and  $CP$ -odd components or contributions from new physics in loops can be probed looking for deviations from zero of  $g_4$  and  $g_2$ , by using the matrix element description of the final state. In this chapter, prospects on the measurement of  $g_4$  and  $g_2$  with data from the foreseen HL-LHC are discussed.

### 7.1 Decay Amplitude in the Scalar Boson Assumption

Let us take again Eq. (4.4):

$$A(X \rightarrow Z_1 Z_2) = v^{-1} \left( g_1 m_Z^2 \epsilon_1^* \epsilon_2^* + g_2 f_{\mu\nu}^{*(1)} f^{*(2),\mu\nu} + g_3 f^{*(1),\mu\nu} f_{\mu\alpha}^{*(2)} \frac{q_\nu q^\alpha}{\Lambda^2} + g_4 f_{\mu\nu}^{*(1)} \tilde{f}^{*(2),\mu\nu} \right). \quad (7.1)$$

We recognize that:

$g_1$  is equal to  $2i$  in the SM<sup>1</sup>;

$g_2$  obtains a non-zero value in the SM only after electroweak radiative corrections,  $g_2 = \mathcal{O}(10^{-2})$ ;

$g_3$  multiplies a term which is suppressed by the square of the scale of new physics  $\Lambda \gtrsim 10 \text{ TeV}$ , and therefore is neglected in the following discussion;

---

<sup>1</sup>In the following we will usually adopt the convention where  $g_1 = 1 \in \mathbb{R}$  is used to denote the SM model, since an overall complex phase does not affect angular distributions and overall normalization effects can be absorbed in the signal strength modifier  $\mu$ .

$g_4$  is the only term multiplying a  $CP$ -odd component<sup>2</sup>, and is zero in the SM up to three loop corrections.

Different theoretical models (a review of which can be found in Ref. [74]) predict  $CP$  violation when both  $CP$ -even and  $CP$ -odd terms in Eq. (4.5) are present[75]. For example, within the context of Two-Higgs-Doublet-Models,  $CP$  violation arises from the mixing of the neutral Higgs sector, composed by two scalar bosons and a pseudoscalar, and might be responsible for the baryon asymmetry observed in Nature[76]. However, in many models the coupling between a pseudoscalar state and a pair of  $Z$  bosons is allowed only at loop level. As a consequence, one expects that the contribution to the amplitude due to the  $CP$ -even component is dominant, i.e. that phenomenologically the interesting region to probe is  $|g_4/g_1| \ll 1$ . On the other hand, the observation of a value of the  $g_2$  parameter significantly different from the SM prediction might hint at new physics contributions to loop processes other than the SM ones.

### 7.1.1 Measurement Strategy

The measurement of the value of any of the coupling parameters can be performed by fitting for  $\text{Re}(g_4), \text{Im}(g_4)$  and  $\mu$  assuming  $g_1 = 1$ , or by fitting for  $\text{Re}(g_2), \text{Im}(g_2)$  and  $\mu$  still with  $g_1 = 1$ . In this way, one is sensitive to the ratio of couplings

$$\text{Re}(g_2/g_1), \quad \text{Im}(g_2/g_1) \quad \text{or} \quad \text{Re}(g_4/g_1), \quad \text{Im}(g_4/g_1) \quad (7.2)$$

while modifications of the overall signal cross-section are still taken into account with the signal strength factor  $\mu$ .

An alternative parametrization of Eq. (7.2) is given by

$$f_{a_i} = \frac{|a_i|^2 \sigma_i}{|a_i|^2 \sigma_1 + |a_i|^2 \sigma_i}, \quad \phi_{a_i} = \text{Arg} \left( \frac{a_i}{a_1} \right), \quad (7.3)$$

where  $\sigma_i$  is the cross-section associated to the  $a_i$  term of Eq. (4.6), computed for all  $a_{j \neq 1} = 0$ . The value of  $\sigma_i$  depends on the acceptance of the analysis and can be computed from Monte Carlo. Applying the same event selection of Chapter 5, one gets

$$f_{a_i} = \frac{r_{i1}^2}{1 + r_{i1}^2}, \quad \text{where } r_{31}^2 \approx 0.16 \frac{|g_4|^2}{|g_1|^2} \quad \text{and} \quad r_{21}^2 \approx 0.382 \frac{|g_2|^2}{|g_1|^2}. \quad (7.4)$$

To uniform the notation, in the following we will call  $f_{g_2} = f_{a_2}$  and  $f_{g_4} = f_{a_3}$ .

### 7.1.2 Interpretation of $g_4/g_1$ vs $\langle f_{CP} \rangle$

Event by event, the fraction of  $CP$ -odd component introduced in Eq. (4.12)

$$f_{CP} = \frac{|A_\perp|^2}{|A_0|^2 + |A_\parallel|^2 + |A_\perp|^2},$$

<sup>2</sup>The fact that  $g_4$  is responsible for a  $CP$ -odd component can be seen expressing the amplitude in the transversity base, as done in Sec. 4.2.4.

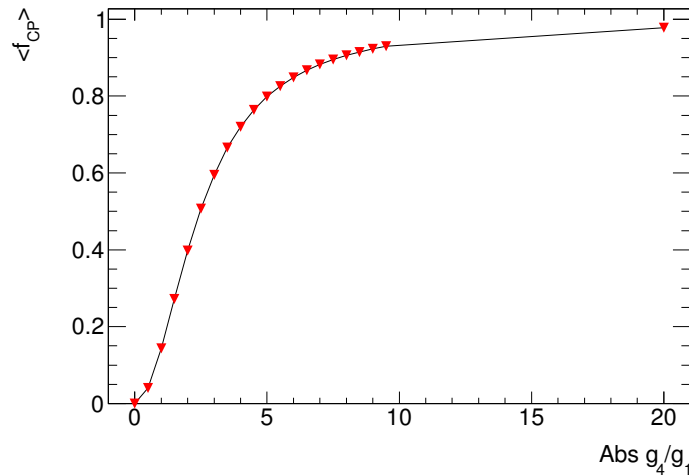


**Figure 7.1.** Relation between  $\langle f_{CP} \rangle$  and  $|g_4/g_1|$ .

is, through the dependence on transversity amplitudes, a function of the intermediate vector boson masses  $m_1, m_2$ . To interpret a given value of  $g_4/g_1$  in terms of  $CP$ -even/odd components, an *effective* parameter

$$\langle f_{CP} \rangle = \int_{C_{m_1, m_2}} dm_1 dm_2 f_{CP}(m_1, m_2)$$

is introduced, where the integral is taken on the surface  $C_{m_1, m_2}$  determined by the event kinematics and selection criteria. Fig. 7.1 shows the relation between  $\langle f_{CP} \rangle$  and  $|g_4/g_1|$ . The relation

$$\langle f_{CP} \rangle \approx f_{a_3} \equiv f_{g_4}$$

holds.

### 7.1.3 Sensitivity on $g_4/g_1, g_2/g_1$

The effect on one-dimensional mass and angular distributions of non-zero values of  $g_2$  and  $g_4$ , when  $g_1$  is assumed to be equal to unity, is shown in Fig. 7.2, in the case of  $g_4$ , and Fig. 7.3 in the case of  $g_2$ . As for the pseudoscalar term, the sensitivity is mainly on the absolute value  $|g_4/g_1|$ : if one assumes that  $g_4/g_1$  is real, discrimination between positive and negative values ( $+3$ , in red, and  $-3$ , in green) is obtained only from the azimuthal angle  $\phi$ , while imaginary values ( $3i$ , in blue, and  $-3i$ , in magenta) induce asymmetries in the  $\cos \theta_{1,2}$  distributions. As for  $g_2$ , most of the separation with respect to the SM is obtained from  $m_2, \cos \theta_{1,2}, \phi$  for negative values of  $g_2/g_1$  ( $-1$ , in green).

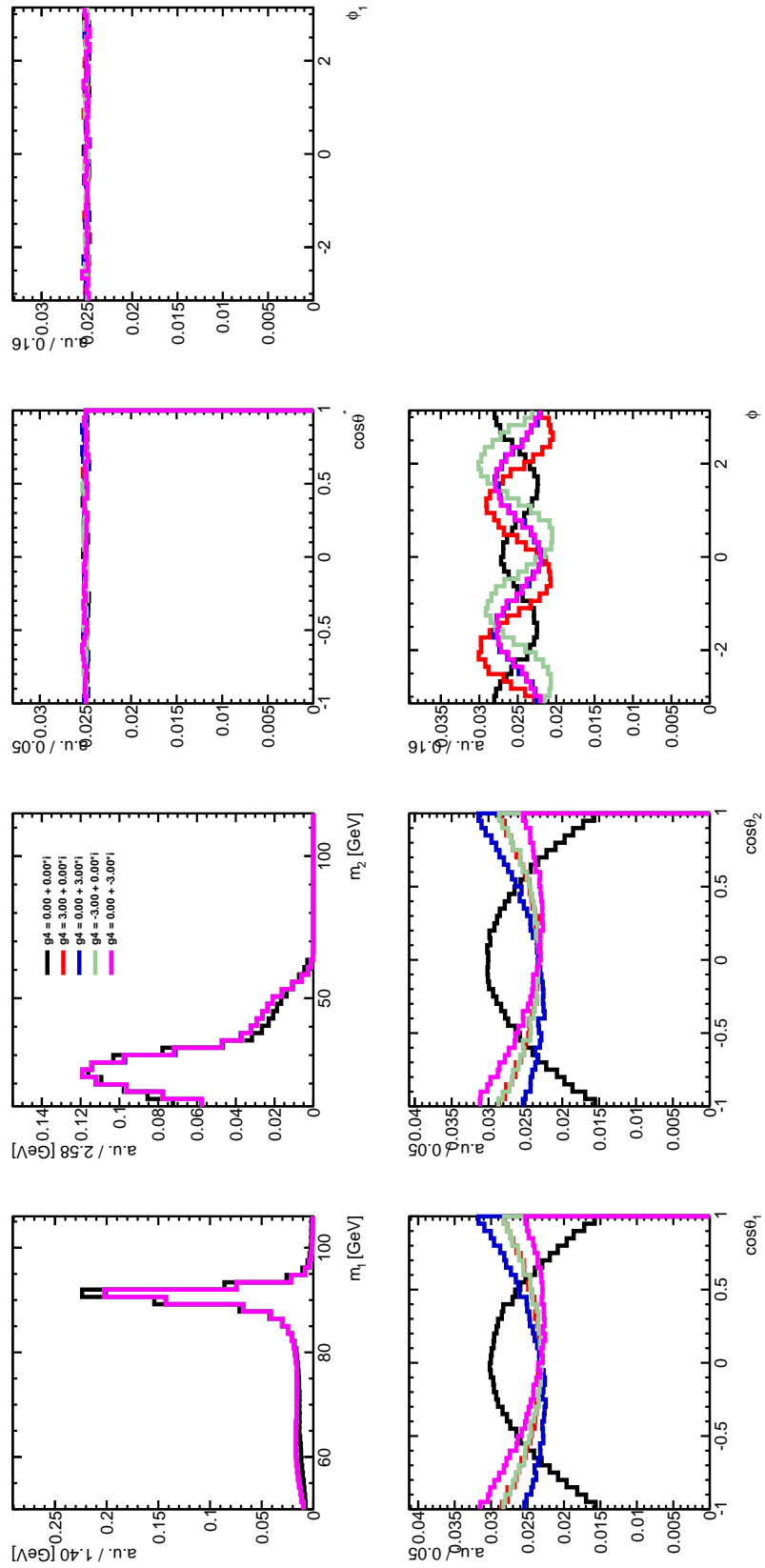


**Figure 7.2.** Distribution of the mass and angular observables, at parton level, for different  $g_4$  hypotheses, when  $g_1 = 1, g_2 = g_3 = 0$ .

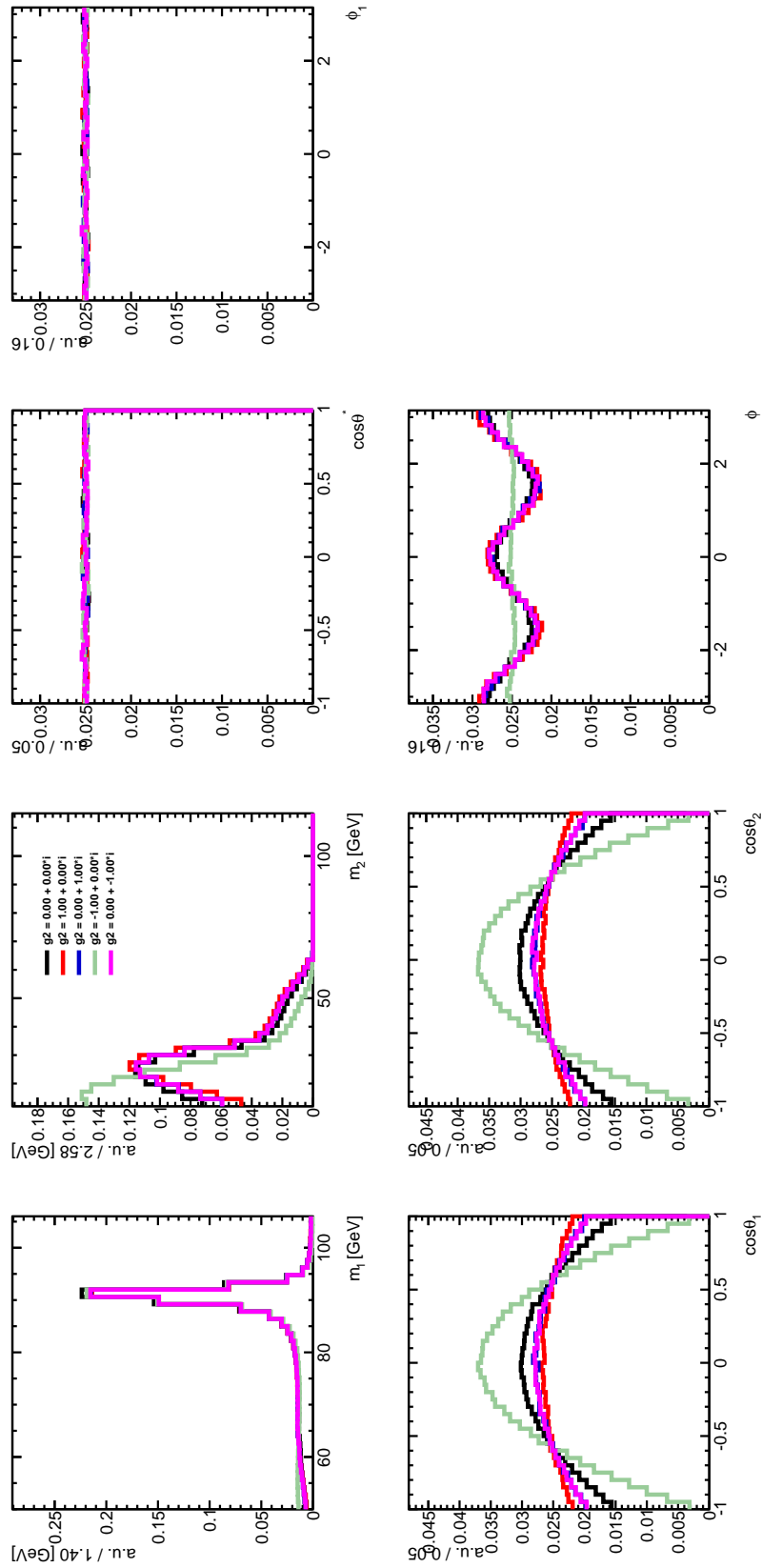


**Figure 7.3.** Distribution of the mass and angular observables, at parton level, for different  $g_2$  hypotheses, when  $g_1 = 1, g_3 = g_4 = 0$ .

### 7.1.4 Analysis Techniques

Two parallel approaches can be used to probe the  $g_2$  and  $g_4$  complex couplings:

- a full fit to the 8D final state of a signal plus background model;
- a discriminant-based approach, in which a 2D analysis is performed in a space where one dimension aims at discriminating signal from backgrounds, and the other dimension provides separation between different signal ( $g_2/g_1, g_4/g_1$ ) hypotheses.

These two approaches are somewhat complementary. On one hand, the 8D fit method allows to probe the tensor structure of the  $HZZ$  vertex in an optimal way, since all available information on the final state is used in the fitting procedure: the interesting coupling is a free parameter of the fit. On the other hand, this technique relies on an accurate description of detector and selection effects and on an accurate parametrization of irreducible and reducible backgrounds. These are complex goals, given the high dimensionality of the observable space, and assumptions must be made on the way acceptance effects and backgrounds are parametrized. The 2D approach is used as a cross-check of the validity this method: it is an extension of the  $J^P$ -MELA hypothesis testing technique, in which the likelihood model for signal and backgrounds is built directly from the 2D distribution of two discriminants computed on full simulation Monte Carlo, and therefore does not require a parametrization of detector and acceptance effects. It provides the possibility to define the set of values of the interesting parameter ( $g_2/g_1, g_4/g_1$ ) which are expected to be excluded with respect to the SM hypothesis  $g_2 = g_4 = 0$ .

In this chapter, these two approaches are introduced, and preliminary sensitivity projections on the real and imaginary parts of  $g_2/g_1$  and  $g_4/g_1$  for  $300\text{ fb}^{-1}$  and  $3000\text{ fb}^{-1}$  at the HL-LHC at 14 TeV are studied with Monte Carlo simulation. Confidence intervals on the complex amplitude parameters, and equivalently on the fractions  $f_{g_i}$  and the argument of  $g_i$ , are shown in the assumption of a Standard Model Higgs boson.

#### Sample Reweighting

Signal samples are simulated, as discussed in Chapter 6, with the JHU generator, in the SM  $0^+$  hypothesis.

A reweighting procedure is applied to obtain full simulation Monte Carlo samples for any ( $g_1 = 1, g_2, g_4$ ) hypothesis. Reconstructed events from the Standard Model  $0^+$  sample are weighted with a factor

$$w(m_1, m_2, \Omega|\tilde{g}_i) = \frac{p(m_1, m_2, \Omega|g_i = \tilde{g}_i)}{p(m_1, m_2, \Omega|g_i = 0)} \quad (i = 2, 4), \quad (7.5)$$

which represents the ratio between the probabilities of that event to occur in the  $\tilde{g}_i \neq 0$  and in the SM hypothesis.

The validity of this procedure is based on the fact that the phase space covered by the pdf is the same for all possible spin zero hypotheses. Fig. 7.4–7.7 show the validation at reconstruction level of sample reweighting, where the  $0^-$  sample fully

simulated with JHU MC is compared to the  $0^+$  sample reweighted according to Eq. 7.5. Good agreement between the two sets of distributions of the final state masses and production and decay angles is observed within the MC statistical uncertainty.

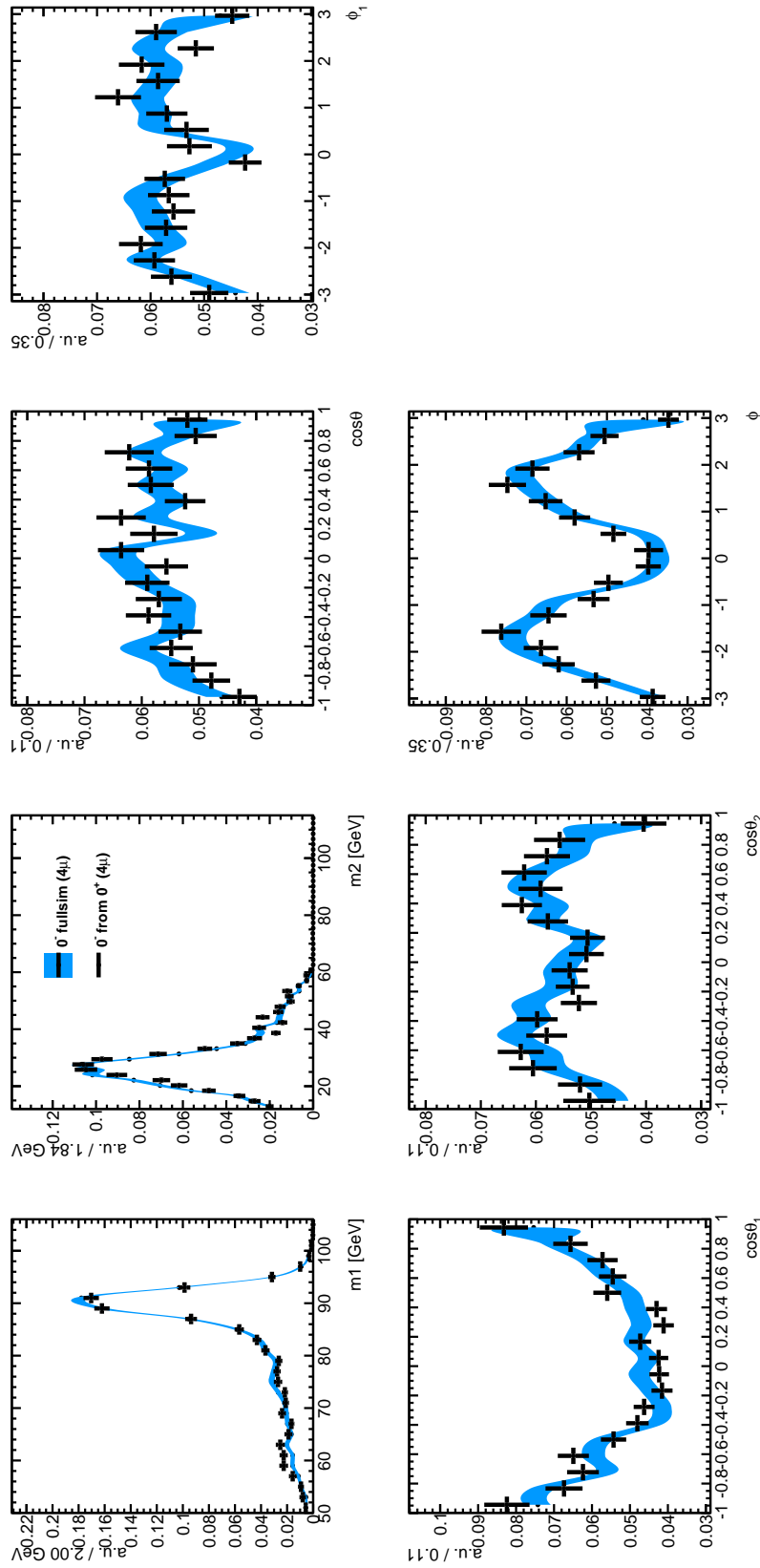


**Figure 7.4.** Distribution of the mass and angular observables, at reconstruction level, for the  $4\mu$  final state for a fully simulated  $0^-$  model (blue band) and the fully simulated SM  $0^+$  model reweighted to  $0^-$  using the matrix element.

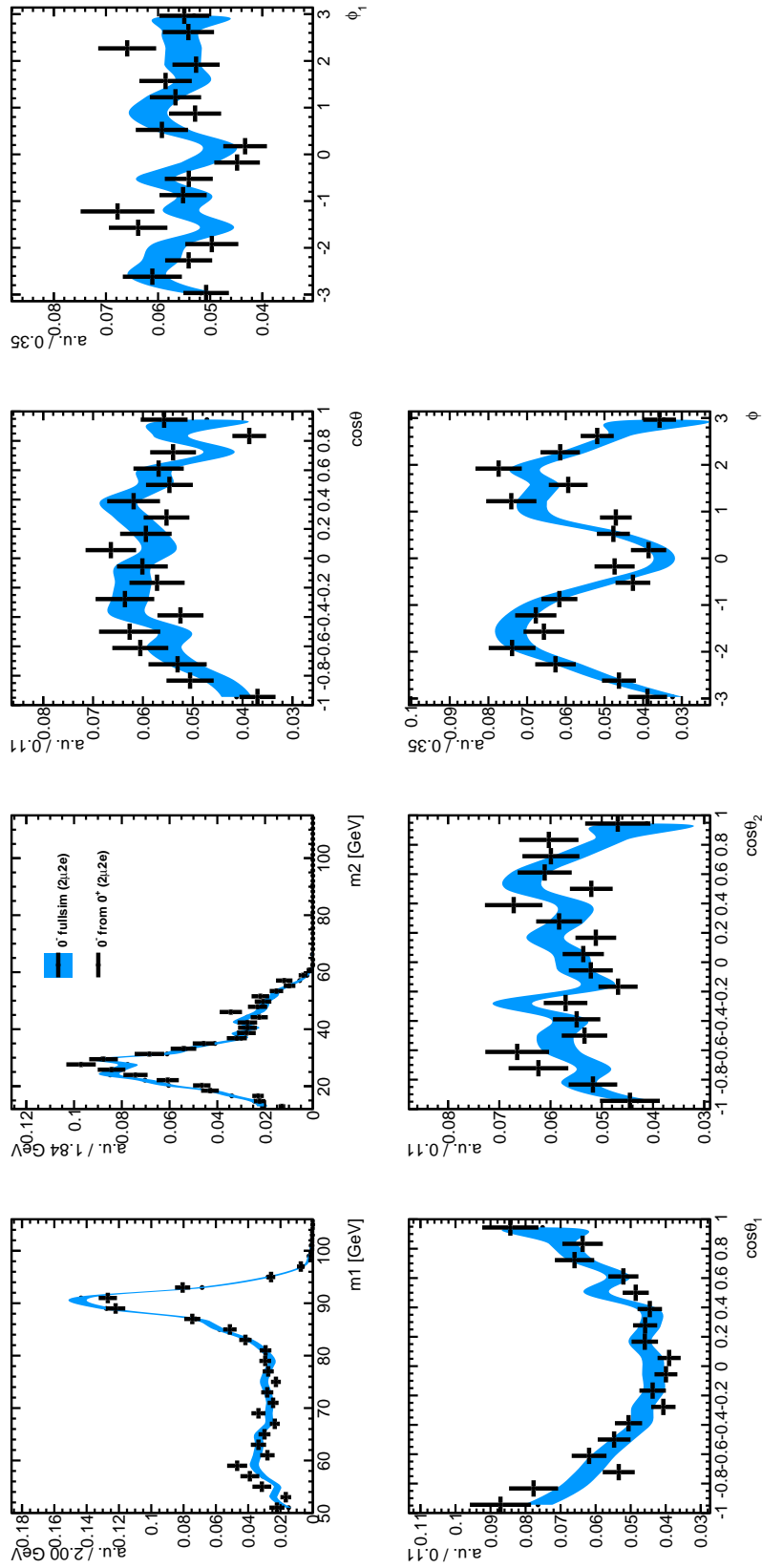


**Figure 7.5.** Distribution of the mass and angular observables, at reconstruction level, for the  $2\mu 2e$  final state for a fully simulated  $0^-$  model (blue band) and the fully simulated SM  $0^+$  model reweighted to  $0^-$  using the matrix element.

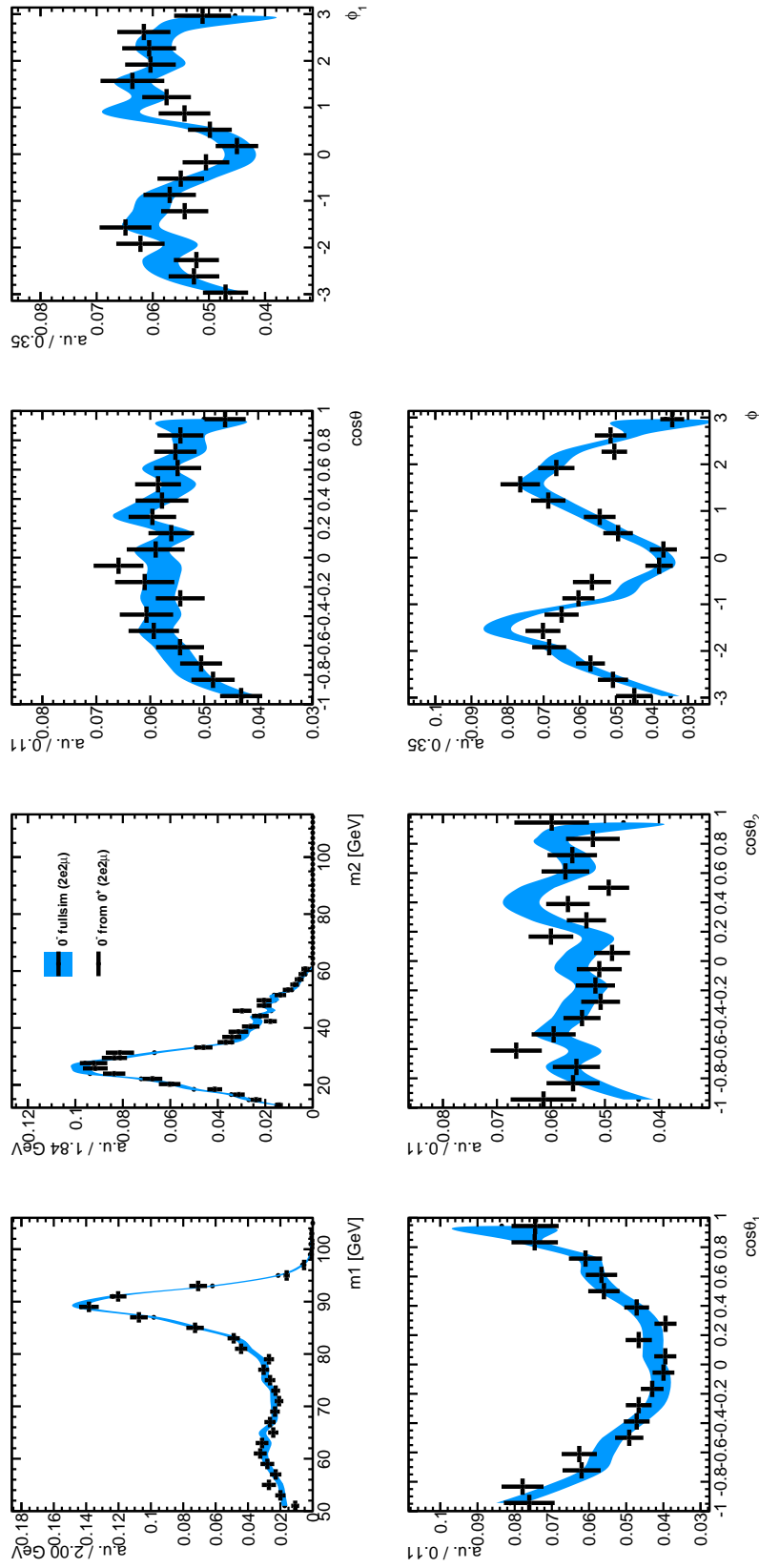


**Figure 7.6.** Distribution of the mass and angular observables, at reconstruction level, for the  $2e2\mu$  final state for a fully simulated  $0^-$  model (blue band) and the fully simulated SM  $0^+$  model reweighted to  $0^-$  using the matrix element.

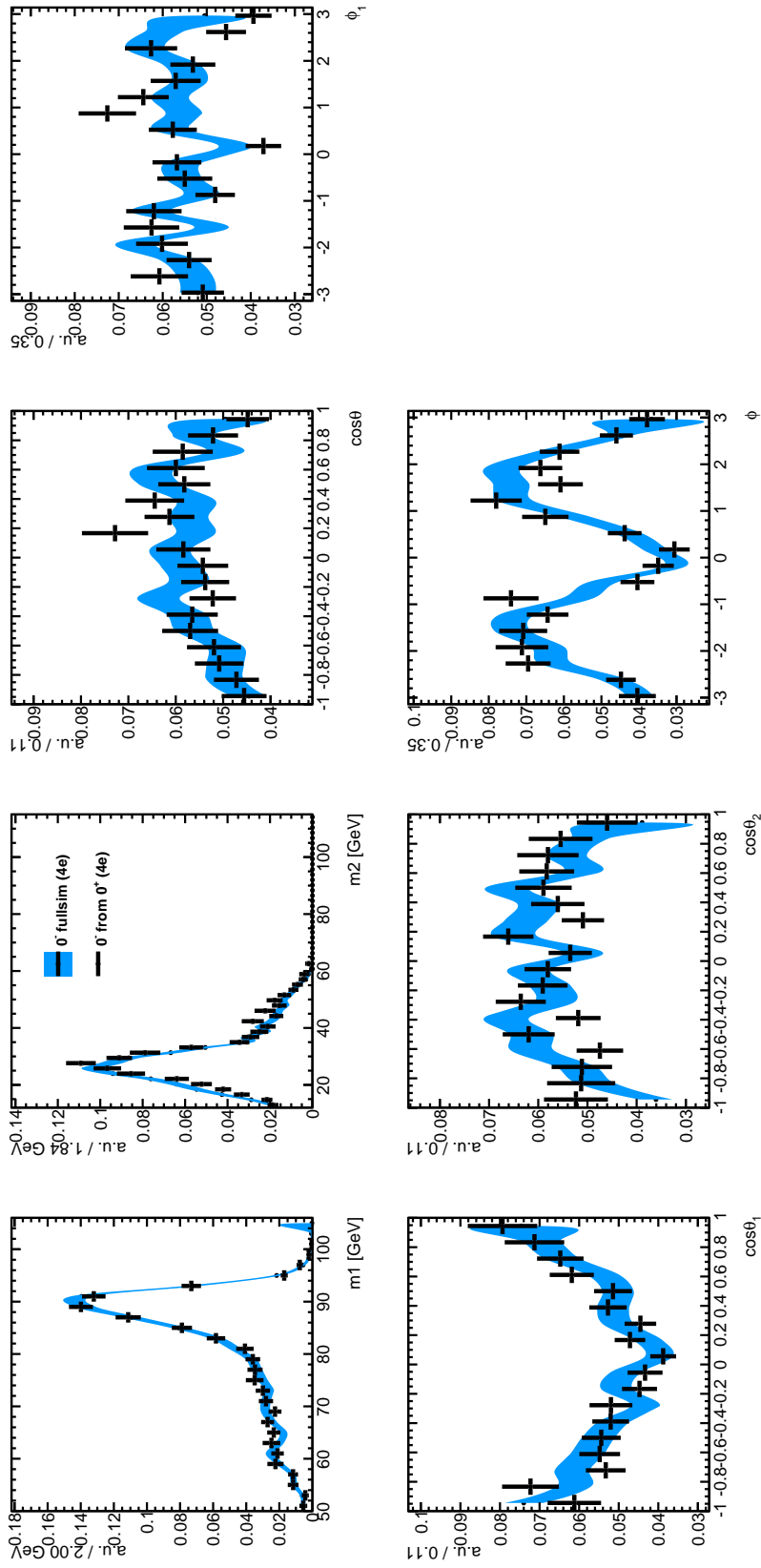


**Figure 7.7.** Distribution of the mass and angular observables, at reconstruction level, for the  $4e$  final state for a fully simulated  $0^-$  model (blue band) and the fully simulated SM  $0^+$  model reweighted to  $0^-$  using the matrix element.

Final State	Signal	$ZZ^*$	Reducible Backgrounds
$4\mu$	1186	427	214
$2\mu 2e$	867	287	144
$2e 2\mu$	1035	383	191
$4e$	871	317	158

**Table 7.1.** Event yields expected in the selected mass region for signal and backgrounds with  $3000 \text{ fb}^{-1}$  collected at a high luminosity LHC.

### Event Yields and Systematic Uncertainties

Events are selected using the same criteria presented in Chapter 5. Signal and background cross-sections for  $\sqrt{s} = 14 \text{ TeV}$  are used<sup>3</sup>, and event yields are computed with fast simulation studies which take into account the harsher experimental conditions at the HL-LHC. Table 7.1 shows the expectations for signal, irreducible and reducible backgrounds, in the four final states, for  $3000 \text{ fb}^{-1}$ ; the  $300 \text{ fb}^{-1}$  expectation is obtained by rescaling these numbers for the different luminosity. The sum of the yields of the reducible and irreducible backgrounds is assigned to the  $ZZ^*$  simulated events.

Systematic uncertainties are assigned on this yield estimation:

- 3% luminosity uncertainty, correlated between signal and background;
- 5% lepton reconstruction efficiency;
- 9.4% (7.4%) combined uncertainty on the  $ZZ^*$  production cross-section and on the reducible background yield for 300 (3000)  $\text{fb}^{-1}$ .

An additional systematic uncertainty of 10% on signal and background normalization is applied in the case of the 8D fit, correlated between signal and background, to conservatively take into account possible uncertainties in the description of detector acceptance and resolution and in parametrization of backgrounds.

## 7.2 8D Fit

The 8D fit approach uses the full final state information,

$$m_{4\ell}, m_1, m_2, \cos \theta^*, \phi_1, \cos \theta_1, \cos \theta_2, \phi,$$

which is described using the same signal model used to build the  $J^P$ -MELA discriminant, which comes from matrix element calculation corrected for acceptance and selection effects (see Sec. 6.2.1), and an empirical background model based on MC simulation.

<sup>3</sup>In the case of the signal, which is simulated with  $m_H = 125 \text{ GeV}$ , one has  $\sigma \times BR = 15.85 \text{ fb}$ .

### 7.2.1 Likelihood Model

The likelihood model in the 8D case is written as

$$L(\text{Re}(g_4/g_1), \text{Im}(g_4/g_1), \mu, \theta) = \prod_{k=4\mu, 2\mu 2e, 2e 2\mu, 4e} \prod_{i=1}^N \text{Pois}(N | \mu N_s^{(k)} + N_b^{(k)}) \cdot \left\{ \frac{N_s^{(k)}}{N_s^{(k)} + N_b^{(k)}} p_S^{(k)}(m_{4\ell}^{(i)}, m_1^{(i)}, m_2^{(i)}, \Omega^{(i)} | \text{Re}(g_4/g_1), \text{Im}(g_4/g_1)) + \frac{N_b^{(k)}}{N_s^{(k)} + N_b^{(k)}} p_{ZZ}^{(k)}(m_1^{(i)}, m_2^{(i)}, \Omega^{(i)}) \right\}, \quad (7.6)$$

(and equivalent for  $g_2$ ) where  $p_S$  is the full signal description introduced in Eq. (6.3), which corrects the matrix element calculation for acceptance and selection effects in each of the four final states. To ease the notation, gaussian constraints on nuisance parameters  $\theta$  associated to the normalization systematic uncertainties presented in Sec. 7.1.4 are not shown.

### 7.2.2 Background Description

For the description of the irreducible background, the factorization

$$p_{ZZ}(m_1, m_2, \Omega) = p_{ZZ}(m_1, m_2) \cdot p_{ZZ}(\cos \theta^*) \cdot p_{ZZ}(\phi_1) \cdot p_{ZZ}(\cos \theta_1) \cdot p_{ZZ}(\cos \theta_2) \cdot p_{ZZ}(\phi)$$

is used, where each  $p_{ZZ}$  term is obtained from full simulation MC. One-dimensional distributions of the five angles are parametrized empirically as in Sec. 6.2.1, while a 2D histogram template is used for  $m_1, m_2$ . Fig. 7.8 shows the level of agreement between full simulation  $ZZ$  MC and  $p_{ZZ}$ .

### 7.2.3 Statistical Procedure

A 2D scan of the likelihood of Eq. (7.6) is performed in the complex plane to obtain a confidence interval on the measured parameter  $g_i/g_1$ , which in the asymptotic assumption is equivalent to the set of  $\tilde{g}_i/g_1 = (\text{Re}(g_i/g_1), \text{Im}(g_i/g_1))$  values for which

$$\begin{aligned} -2\Delta LL &= 2 \log \frac{L(\tilde{g}_i/g_1)}{L(\hat{g}_i/g_1)} \propto \chi^2(\text{ndof} = 2) \\ &\leq 2.28(5.99) \text{ for } 68\% (95\%) \text{ CL.} \end{aligned}$$

The two parameters of interest are the real and imaginary parts of  $g_4/g_1$  ( $g_2/g_1$ ); the signal strength  $\mu$  is profiled. Expected limits are obtained by fitting an Asimov dataset[69] generated in the Standard Model hypothesis, and quoting the corresponding confidence intervals. The granularity with which the likelihood is evaluated in the complex plane is  $\text{Re}(g_i/g_1) \times \text{Im}(g_i/g_1) = 0.05 \times 0.05$ .

### 7.2.4 Closure Tests

In order to test the correct implementation of the method and the validity of signal and background parametrizations, a series of closure tests has been performed.

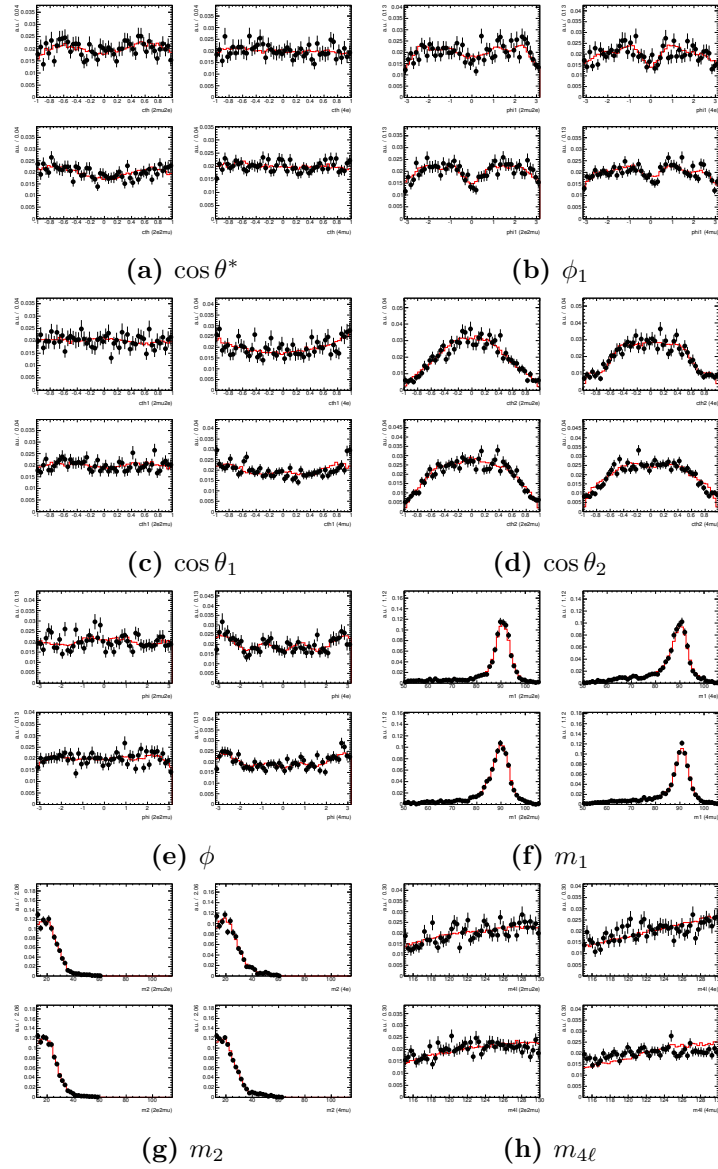


**Figure 7.8.** Comparison of the likelihood projection for the  $pp \rightarrow ZZ^{(*)} \rightarrow 4\ell$  irreducible background (red curve) and the corresponding POWHEG (black points) MC simulation for the eight observables. From left to right and top to bottom for each observable:  $2\mu 2e$ ,  $4e$ ,  $2e 2\mu$  and  $4\mu$  channels.

Channel	Eq. Stat. ( $\text{fb}^{-1}$ )	Pull Mean	Pull $\sigma$
$4\mu$	30	$-0.01 \pm 0.03$	$0.91 \pm 0.02$
$2\mu 2e$	30	$-0.01 \pm 0.03$	$0.93 \pm 0.02$
$2e 2\mu$	30	$-0.03 \pm 0.03$	$0.93 \pm 0.02$
$4e$	30	$0.00 \pm 0.03$	$0.91 \pm 0.02$
$4\mu$	3000	$0.01 \pm 0.03$	$1.07 \pm 0.02$
$2\mu 2e$	3000	$0.04 \pm 0.03$	$1.02 \pm 0.02$
$2e 2\mu$	3000	$0.00 \pm 0.03$	$1.05 \pm 0.02$
$4e$	3000	$0.05 \pm 0.03$	$1.02 \pm 0.02$

**Table 7.2.** Mean and width of gaussian pulls for the  $\text{Re}(g_4)$  parameter ( $g_1 = 1$ ), obtained by performing 1000 functional toy experiments using the full 8D likelihood to generate signal plus background samples with an equivalent statistic of  $30 \text{ fb}^{-1}$  and  $3000 \text{ fb}^{-1}$ .

Dedicated test samples, obtained either from pseudo-experiments (*toys*) generated from the likelihood itself to test its correct implementation, or from full simulation MC, have been used to study possible biases induced by the fitting procedure.

To validate the fitting procedure, toy experiments have been performed generating 1000 samples with a number of events Poisson-distributed around the expectations for  $30 \text{ fb}^{-1}$  and  $3000 \text{ fb}^{-1}$ . Pulls of the  $\text{Re}(g_4/g_1) = x$  parameter, defined as

$$\text{pull}(x)_i = \frac{x_i - x^{(\text{true})}}{\sigma(x_i)}$$

have been studied. Table 7.2 shows the mean and width of gaussian fits to the pull distributions (some examples of which are reported in Fig. 7.9). Mean and standard deviation of the distributions are compatible with the expectations of 0 and 1, respectively, indicating that no significant bias is observed.

Table 7.3 shows the mean and width of gaussian fits to the pull distributions obtained by injecting multiple samples from the SM MC events corresponding to an equivalent statistic<sup>4</sup> of about  $30 \text{ fb}^{-1}$ . In all cases pull distributions are consistent within statistical uncertainty with normal distributions.

A high-statistics test has been performed by fitting the full SM sample, which corresponds to a luminosity of more than  $3000 \text{ fb}^{-1}$ , reweighted to different values of the  $g_4$  and  $g_2$  parameters. The distributions of the fitted values of  $\text{Re}(g_i/g_1)$  and  $\text{Im}(g_i/g_1)$  versus their true values are shown in Fig. 7.10. No significant bias is observed for any of the tested values.

Finally, Fig. 7.11 shows  $-2\Delta LL$  sensitivity contours at 68% and 95% CL in the  $(\text{Re}(g_i/g_1), \text{Im}(g_i/g_1))$  planes, as obtained by fitting three injected samples with  $g_1 = 1$  and  $g_4 = -1 + i$ ,  $g_4 = 2 + 2i$  and  $g_2 = -1 + i$ , for an integrated luminosity of  $300 \text{ fb}^{-1}$ .

<sup>4</sup>The equivalent statistics is limited by the available full simulation MC statistics.

Channel	Eq. Stat. ( $\text{fb}^{-1}$ )	Pull mean	Pull sigma
$4\mu$	30	$0.02 \pm 0.04$	$0.83 \pm 0.03$
$2\mu 2e$	30	$0.00 \pm 0.06$	$0.92 \pm 0.04$
$2e 2\mu$	30	$0.09 \pm 0.05$	$0.96 \pm 0.04$
$4e$	30	$0.07 \pm 0.06$	$0.95 \pm 0.05$

**Table 7.3.** Mean and width of gaussian pulls for the  $\text{Re}(g_4)$  parameter ( $g_1 = 1$ ), obtained by fitting multiple pseudo-experiments sampled from full simulation Standard Model MC events, corresponding to an equivalent statistic of  $30 \text{fb}^{-1}$  each.

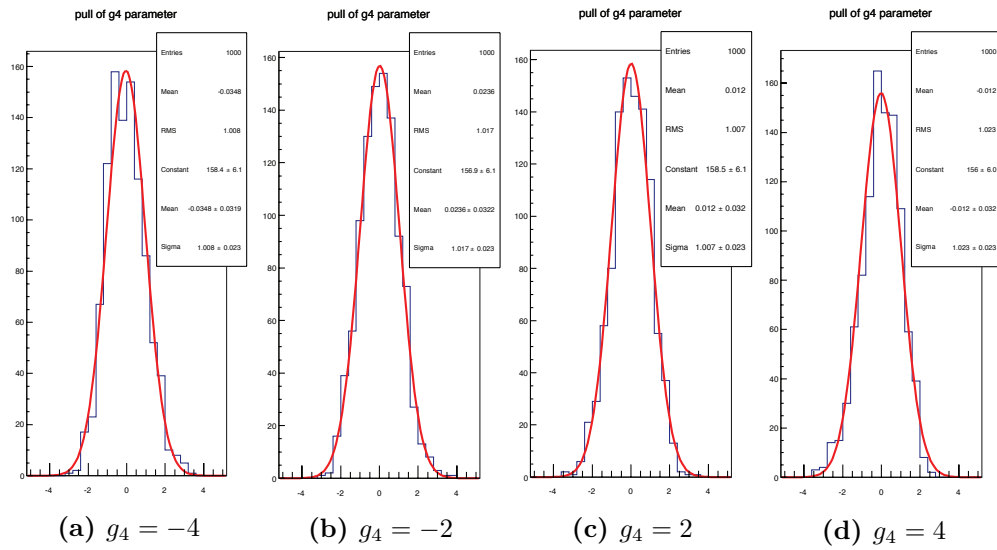


**Figure 7.9.** Pull distributions for the  $g_4$  parameter ( $g_1 = 1$ ) obtained in toy experiments corresponding to an equivalent statistic of  $3000 \text{fb}^{-1}$  each.

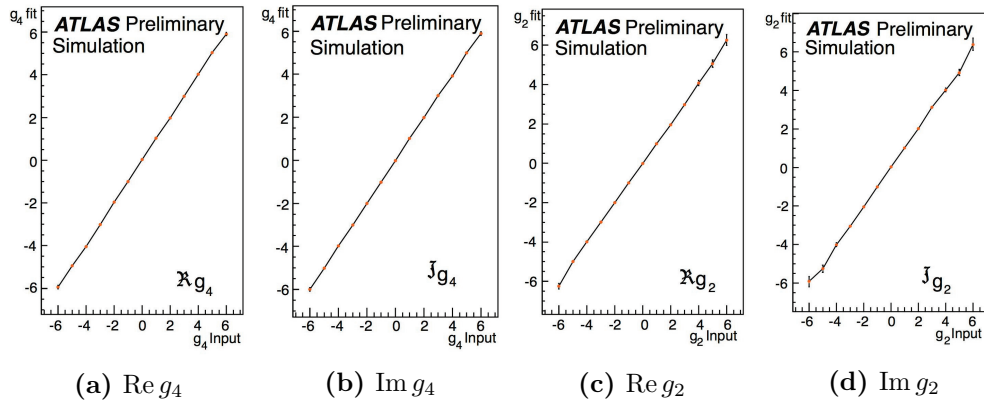


**Figure 7.10.** Distributions of the measured values of  $g_4$  ( $g_2$ ) ( $y$ -axis) from fits to samples with generated values  $g_4$  ( $g_2$ ) and  $g_1 = 1$  ( $x$ -axis). Each sample is obtained by reweighting the the full simulation Standard Model sample to the corresponding hypotheses.

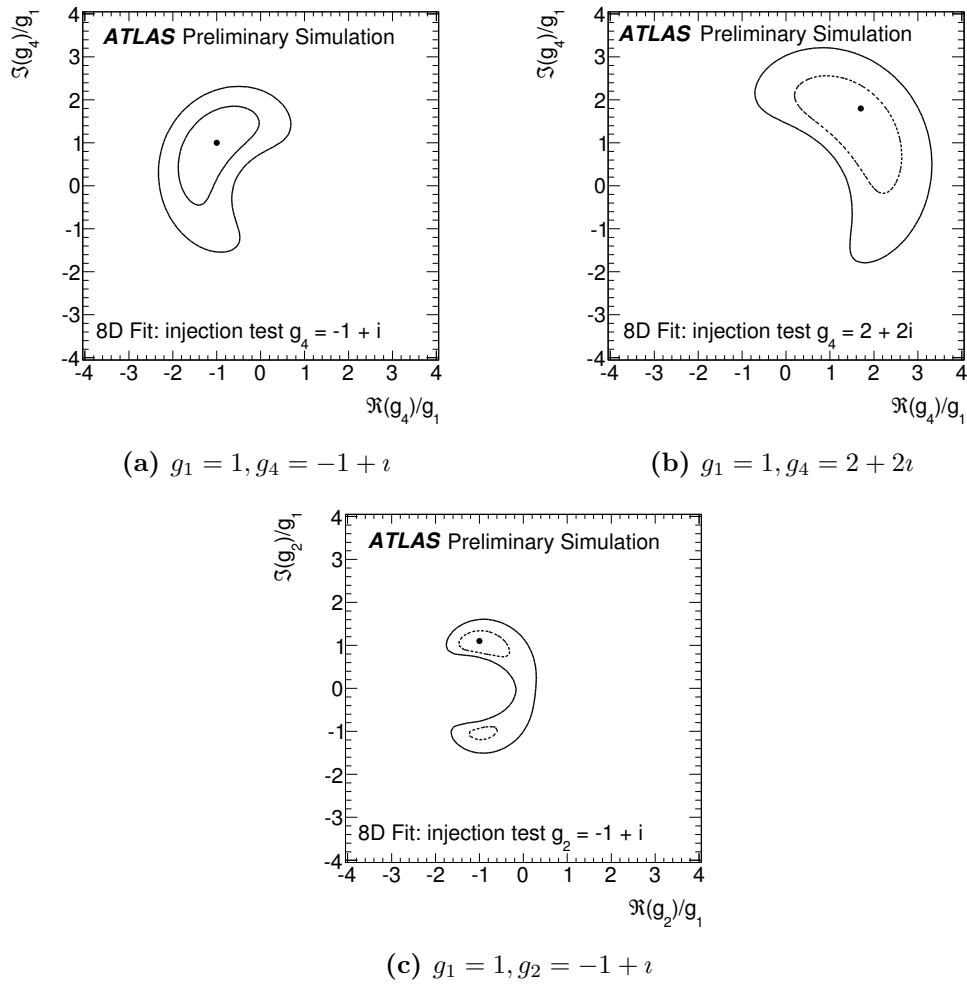


**Figure 7.11.** Contours corresponding to 68% and 95% CL of the distribution of  $-2\Delta LL$  in the  $(\text{Re}(g_i/g_1), \text{Im}(g_i/g_1))$  plane, obtained when samples different from the SM one are injected, for the 8D fit and the  $g_4$  and  $g_2$  parameters. The tests assume an integrated luminosity of  $300 \text{ fb}^{-1}$ .

### 7.2.5 Results

Fig. 7.12 and 7.13 show the distribution of  $-2\Delta LL$ , in the  $(\text{Re}(g_4/g_1), \text{Im}(g_4/g_1))$  and  $(\text{Re}(g_2/g_1), \text{Im}(g_2/g_1))$  planes when a Standard Model signal is assumed, for integrated luminosities of  $300 \text{ fb}^{-1}$  (upper plots) and  $3000 \text{ fb}^{-1}$  (lower plots). The 68% and 95% CL contours are reported as well.

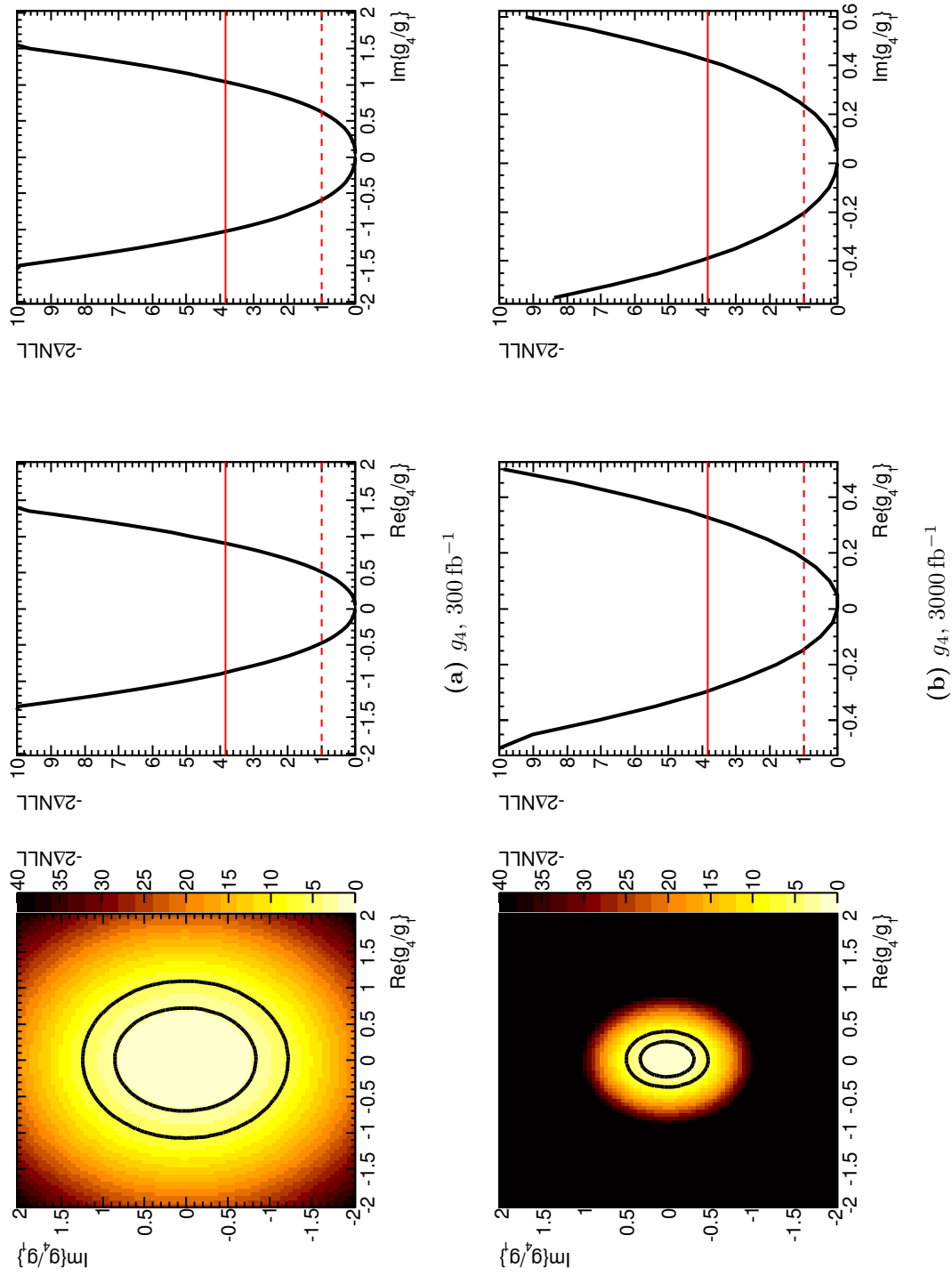


**Figure 7.12.** Left: distribution of  $-2\Delta LL$  from the 8D fit to the SM Asimov dataset, in the  $g_4/g_1$  complex plane, for 300 fb<sup>-1</sup> and 3000 fb<sup>-1</sup> of integrated luminosity. The 68% and 95% CL contours are reported as well. Center and right: likelihood projections as a function of one parameter, when the other is profiled.

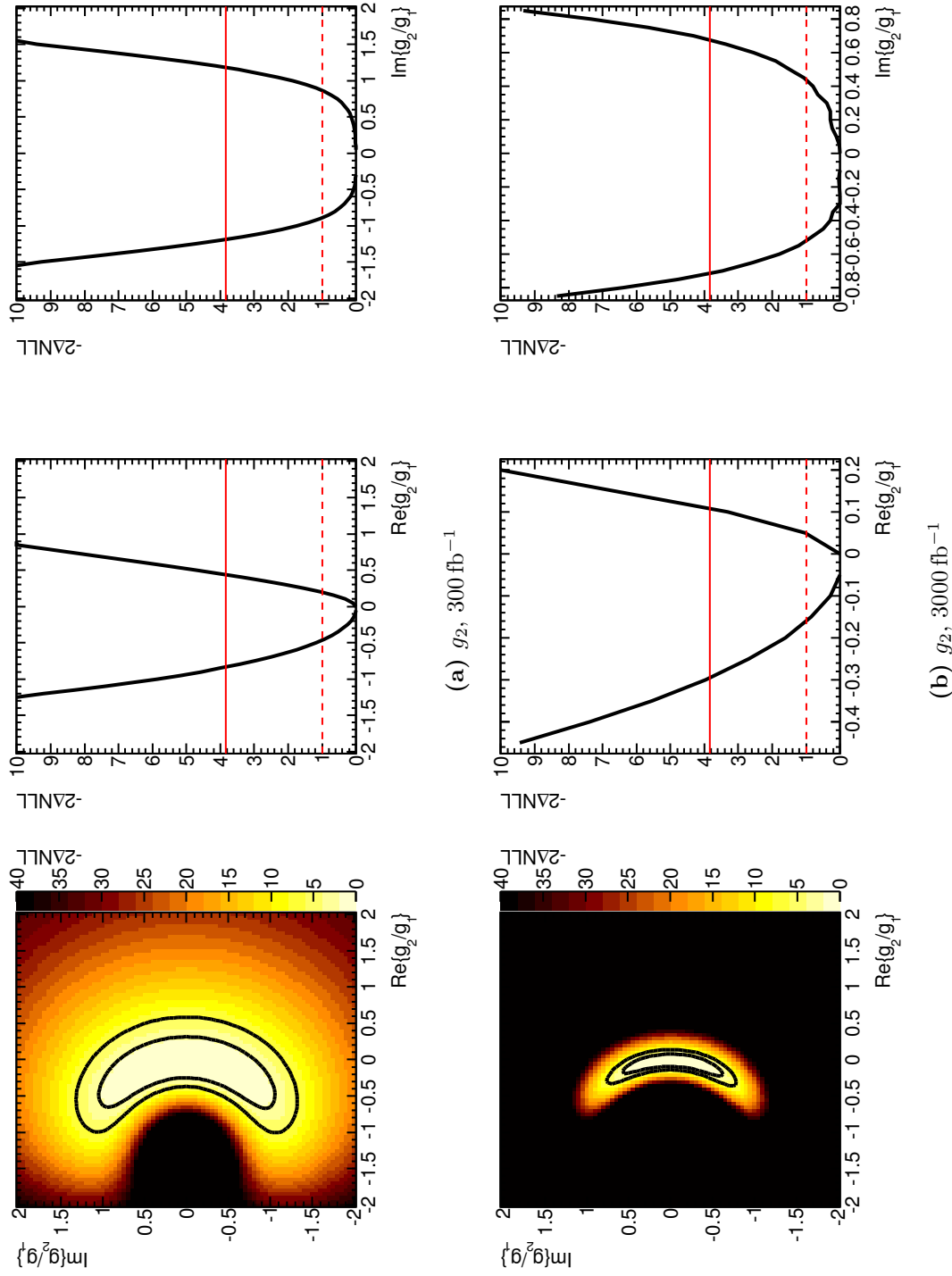


**Figure 7.13.** Left: distribution of  $-2\Delta LL$  from the 8D fit to the SM Asimov dataset, in the  $g_2/g_1$  complex plane, for  $300 \text{ fb}^{-1}$  and  $3000 \text{ fb}^{-1}$  of integrated luminosity. The 68% and 95% CL contours are reported as well. Center and right: likelihood projections as a function of one parameter, when the other is profiled.

### 7.3 2D Discriminant Analysis

A complementary 2D discriminant method is developed, as an extension of the  $J^P$ -MELA technique. Hypothesis testing is performed between the SM hypothesis and the tested  $g_1$  hypothesis ( $i = 1, 2$ ), in the two dimensional space where one dimension is given by

$$D_{\tilde{g}_i}(m_1, m_2, \Omega) = \frac{p(m_1, m_2, \Omega | g_1 = 1, g_i = 0)}{p(m_1, m_2, \Omega | g_1 = 1, g_i = 0) + p(m_1, m_2, \Omega | g_1 = 1, g_i = \tilde{g}_i)}, \quad (7.7)$$

and the other dimension is

$$D_{ZZ} = m_{4\ell},$$

and aims at separating signal and background. It can be noted that the discriminant of Eq. (7.7) is the analogous of Eq. (6.2), this time separating the SM hypothesis from the  $g_i \neq 0$  ones.

#### 7.3.1 Likelihood Model

For each point of the complex plane ( $\text{Re}(g_i/g_1), \text{Im}(g_i/g_1)$ ), an hypothesis test is performed between that specific hypothesis and the SM one, using the likelihood model

$$L(\epsilon, \mu, \theta) = \prod_{k=4\mu, 2\mu 2e, 2e 2\mu, 4e} \prod_{i=1}^N \text{Pois}(N | \mu N_s^{(k)} + N_b^{(k)}) \cdot \left\{ \frac{N_s^{(k)}}{N_s^{(k)} + N_b^{(k)}} \left[ \epsilon f_{\text{sig}}^{(k)}(D_{\tilde{g}_4}^{(i)}, m_{4\ell}^{(i)} | \tilde{g}_4/g_1) \right. \right. \\ \left. \left. + (1 - \epsilon) f_{\text{sig}}^{(k)}(D_{\tilde{g}_4}^{(i)}, m_{4\ell}^{(i)} | g_4/g_1 = 0) \right] + \frac{N_b^{(k)}}{N_s^{(k)} + N_b^{(k)}} f_{\text{bkg}}^{(k)}(D_{\tilde{g}_4}^{(i)}, m_{4\ell}^{(i)}) \right\}$$

(and analogous for  $g_2$ ), where the second product runs over events  $i$  and, again, gaussian constraints associated to nuisance parameters  $\theta$  to account for normalization systematics in signal and background are not shown. The parameter  $\epsilon$  is 1 in the case of the hypothesis  $\tilde{g}_4$  and 0 in the case of the SM hypothesis.

The functions  $f_{\text{sig}}^{(k)}$  are obtained using 2D distributions computed on Monte Carlo samples (an example of which is shown in Fig. 7.14), in the case of signal after the reweighting described in Sec. 7.1.4. Discriminant distributions are smoothed using a 2D kernel density estimation technique.

#### 7.3.2 Statistical Procedure

The hypothesis testing is performed using the profile likelihood test statistics, where  $\epsilon$  is treated as parameter of interest and  $\mu$  is profiled. In each point of the complex plane, the corresponding hypothesis on  $g_i/g_1$  is tested against the SM hypothesis, using the  $CL_s$  method and the asymptotic calculation[69]. The CL of exclusion of the alternative hypothesis with respect to the SM one is reported, for each point of the plane, by using an Asimov dataset generated according to the SM hypothesis. This procedure is performed with a granularity  $\text{Re}(g_i/g_1) \times \text{Im}(g_i/g_1) = 0.05 \times 0.05$  in the complex plane.

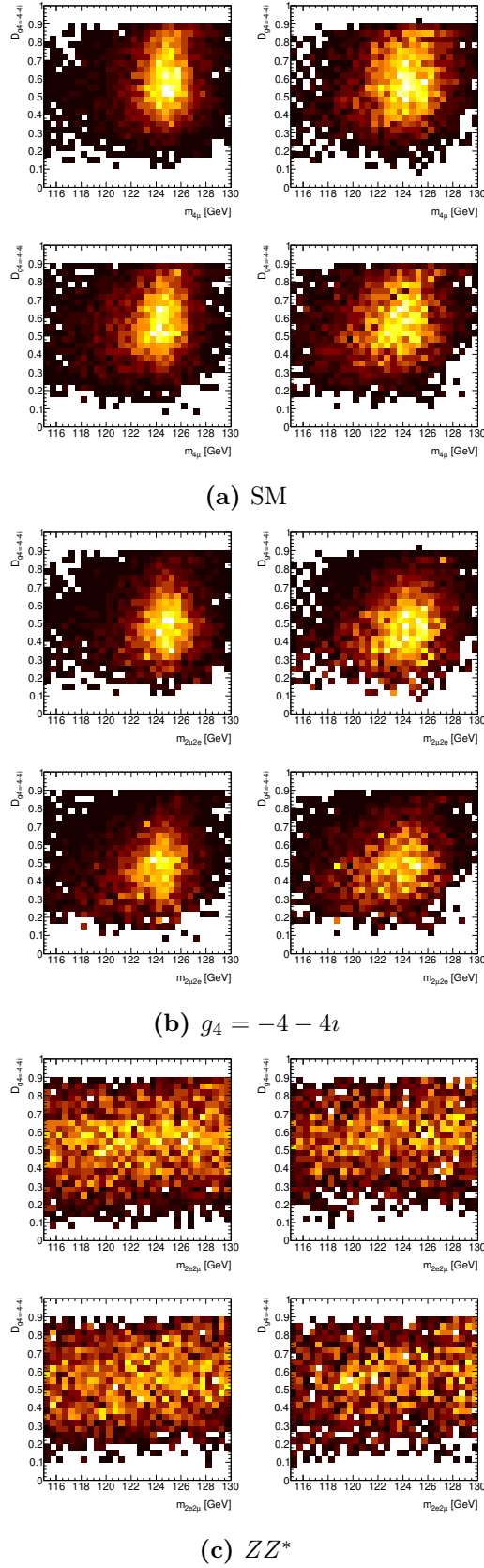


**Figure 7.14.** Example of the distribution, for the four final states, of the 2D discriminant computed on full simulation events, for SM signal, SM signal reweighted to  $g_4 = -4 - 4i$  and  $ZZ^*$  continuum background.

Luminosity (fb <sup>-1</sup> )	Re( $g_4/g_1$ )	Im( $g_4/g_1$ )	Re( $g_2/g_1$ )	Im( $g_2/g_1$ )
300	(-0.88, 0.91)	(-1.02, 1.05)	(-0.84, 0.44)	(-1.19, 1.18)
3000	(-0.30, 0.33)	(-0.39, 0.42)	(-0.30, 0.11)	(-0.71, 0.68)

**Table 7.4.** Expected sensitivities, expressed in terms of the expected 95% CL intervals for  $\text{Re}(g_4/g_1)$ ,  $\text{Im}(g_4/g_1)$ ,  $\text{Re}(g_2/g_1)$  and  $\text{Im}(g_2/g_1)$  when the other parameter is profiled, that can be obtained with the 8D fit method in the presence of a SM signal.

Luminosity (fb <sup>-1</sup> )	$ \text{Re}(g_4/g_1) $	$ \text{Im}(g_4/g_1) $	$ \text{Re}(g_2/g_1) $	$ \text{Im}(g_2/g_1) $
300	0.80	0.90	0.69	1.05
3000	0.32	0.41	0.26	0.65

**Table 7.5.** Expected sensitivities, expressed as 95% CL expected upper limits on the  $|\text{Re}(g_4/g_1)|$ ,  $|\text{Im}(g_4/g_1)|$ ,  $|\text{Re}(g_2/g_1)|$  and  $|\text{Im}(g_2/g_1)|$  parameters, that can be obtained in the presence of a SM signal with the 2D hypothesis testing method.

### 7.3.3 Results

Fig. 7.15 shows the expected sensitivity in number of gaussian sigmas, to exclude a given point in the  $(\text{Re}(g_4/g_1), \text{Im}(g_4/g_1))$  (upper plots), and  $(\text{Re}(g_2/g_1), \text{Im}(g_2/g_1))$  (lower plots) planes, for a Standard Model signal, estimated with the 2D hypothesis testing method. Left plots assume an integrated luminosity of  $300 \text{ fb}^{-1}$ , while the right plots assume  $3000 \text{ fb}^{-1}$ .

## 7.4 Summary

A summary of the expected sensitivities on  $g_4/g_1$  and  $g_2/g_1$ , that can be reached with  $300 \text{ fb}^{-1}$  and  $3000 \text{ fb}^{-1}$ , with the 8D fitting technique is reported in Table 7.4. Results are compatible with those obtained with the cross-check 2D hypothesis testing technique (shown in Table 7.5) within the uncertainty associated to the granularity of the scan of the complex plane<sup>5</sup>.

A summary of the expected sensitivities for the fractions  $f_{g_4}$  and  $f_{g_2}$  for  $300 \text{ fb}^{-1}$  and  $3000 \text{ fb}^{-1}$  obtained with the 8D fit technique is reported in Table 7.6, while contours at 68% and 95% CL are shown in Fig. 7.16. Results are compatible with those obtained with the cross-check 2D hypothesis testing technique (shown in Table 7.7 and Fig. 7.16) within the uncertainty associated to the granularity of the scan of the  $f_{g_i}$  versus  $\text{Arg}(g_i/g_1)$  plane, which is  $0.02 \times 0.02$ . Further precision on the measurement of  $f_{g_2}, f_{g_4}$  might be achieved in the future applying similar techniques at the foreseen  $e^+e^-$  colliders[77].

<sup>5</sup>In the 8D case, intervals on the real and imaginary parts of the coupling factors are given profiling the other parameter. In the 2D case the one-dimensional interval, obtained from the same plane, containing points not excluded at 95% CL is given. In both cases, the procedure is applied on the 2D histograms shown in Fig. 7.12, 7.13, 7.15 (for the  $(\text{Re} g_i/g_1, \text{Im} g_i/g_1)$  plane) and Fig. 7.16, 7.17 (for the  $(f_{g_i}, \text{Arg}(g_i/g_1))$  plane), and is therefore affected by the granularity of the scan

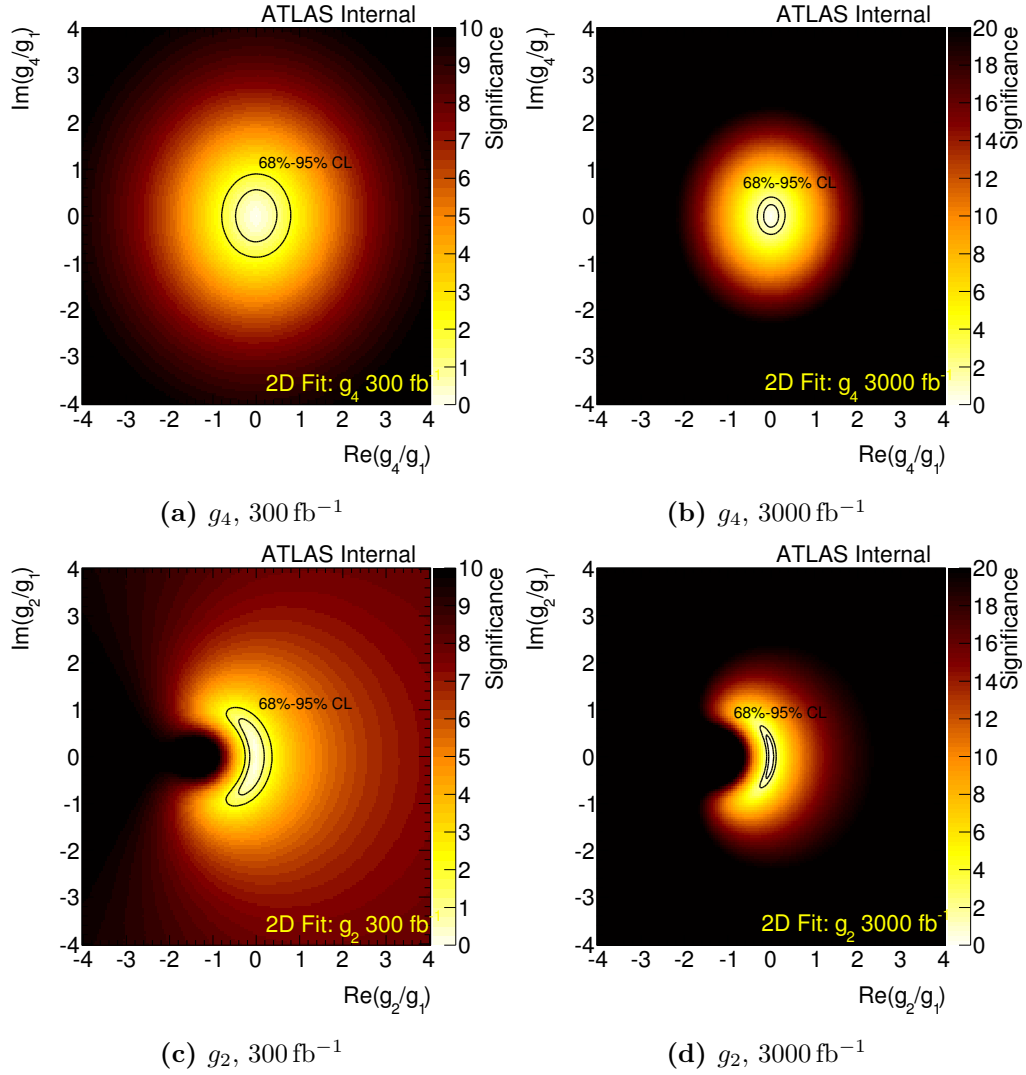


**Figure 7.15.** Expected sensitivity in number of equivalent gaussian sigmas, to exclude a given point in the  $(\text{Re}(g_4/g_1), \text{Im}(g_4/g_1))$  and  $(\text{Re}(g_2/g_1), \text{Im}(g_2/g_1))$  planes, for a Standard Model signal, estimated with the 2D hypothesis testing method. The 68% and 95% CL contours are reported as well.

Luminosity ( $\text{fb}^{-1}$ )	$f_{g_4}$	$f_{g_2}$
300	0.20	0.29
3000	0.06	0.12

**Table 7.6.** Expected sensitivities for  $f_{g_4}$  and  $f_{g_2}$ , for  $300 \text{ fb}^{-1}$  and  $3000 \text{ fb}^{-1}$ , with the 2D fit method. Numbers are expressed as 95% CL upper limits on the  $f_{g_4}$  and  $f_{g_2}$  parameters, which can be obtained in the presence of a Standard Model signal.

Luminosity ( $\text{fb}^{-1}$ )	$f_{g_4}$	$f_{g_2}$
300	0.12	0.34
3000	0.04	0.15

**Table 7.7.** Expected sensitivities for  $f_{g_4}$  and  $f_{g_2}$ , for  $300 \text{ fb}^{-1}$  and  $3000 \text{ fb}^{-1}$ , with the 2D hypothesis testing method. Numbers are expressed as 95% CL upper limits on the  $f_{g_4}$  and  $f_{g_2}$  parameters, which can be obtained in the presence of a Standard Model signal.

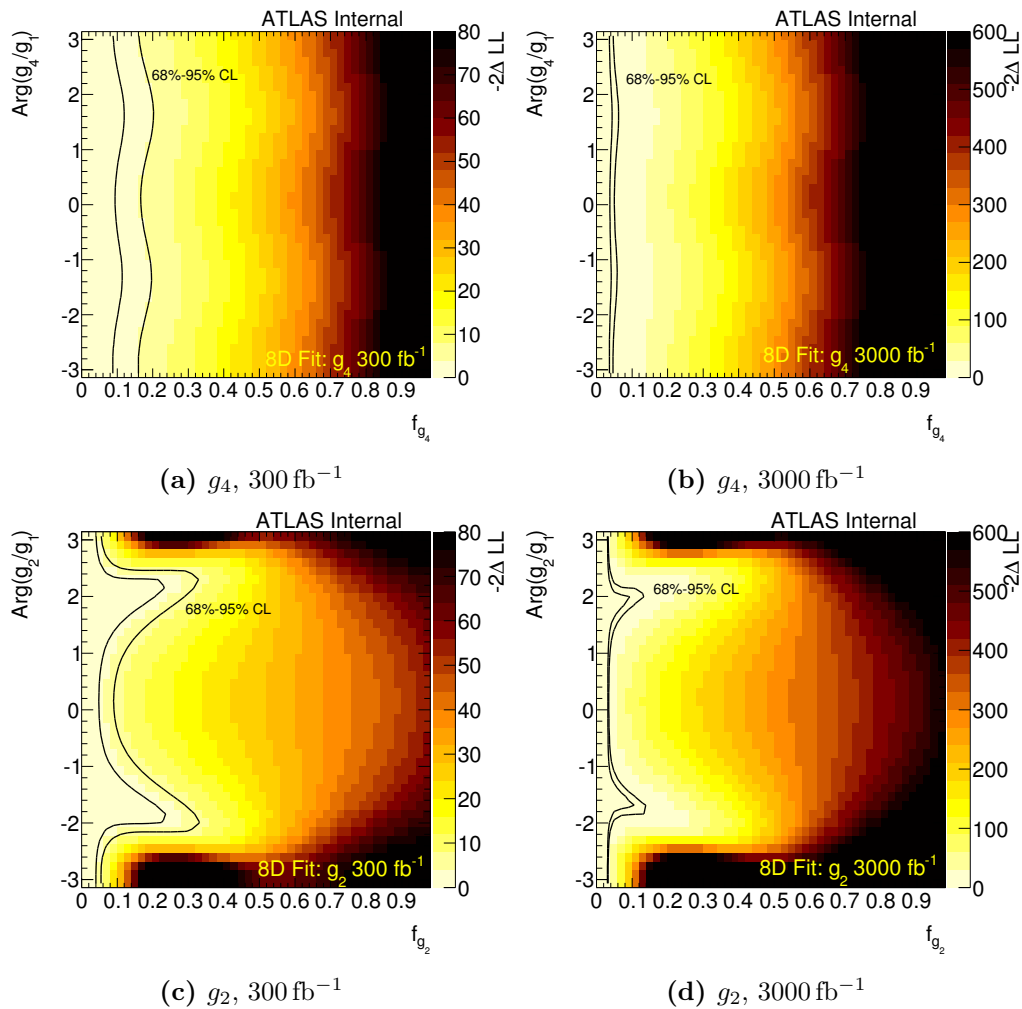


**Figure 7.16.** Distribution of  $-2\Delta LL$  of the 8D fit in the  $f_{g_4}$  versus  $\text{Arg}(g_4/g_1)$  and  $f_{g_2}$  versus  $\text{Arg}(g_2/g_1)$  planes, when the Standard Model hypothesis is assumed.

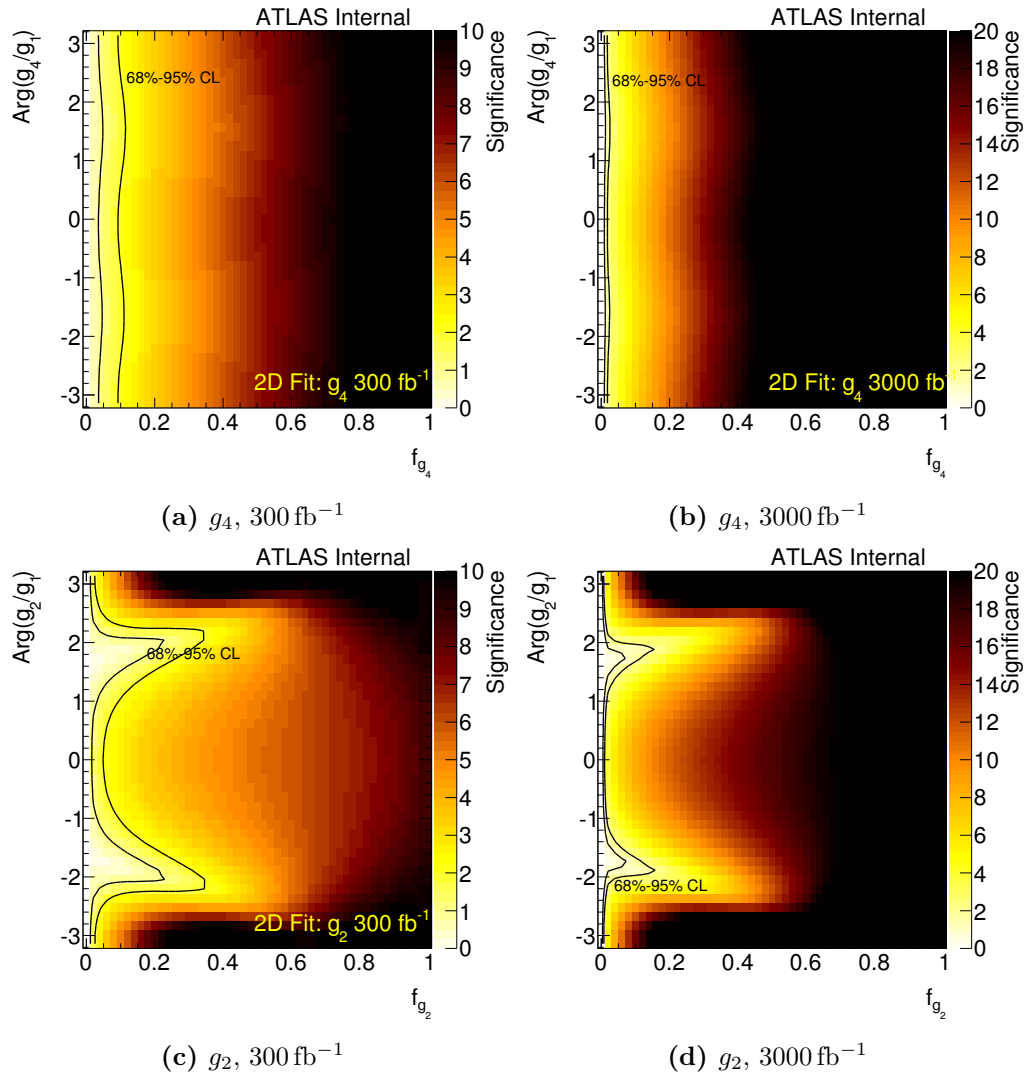


**Figure 7.17.** Expected sensitivity in number of equivalent gaussian sigmas, to exclude a given point in the  $f_{g_4}$  versus  $\text{Arg}(g_4/g_1)$  and  $f_{g_2}$  versus  $\text{Arg}(g_2/g_1)$  planes, when the Standard Model hypothesis is assumed, estimated with the 2D hypothesis testing method.

---

in each of the planes.



## Chapter 8

# Conclusions

A search for the Standard Model Higgs boson in the  $H \rightarrow ZZ^{(*)} \rightarrow 4\ell$  decay channel has been presented in this thesis, with about  $25 \text{ fb}^{-1}$  of data collected in  $pp$  collisions at  $\sqrt{s} = 7 \text{ TeV}$  and  $8 \text{ TeV}$  by the ATLAS experiment at the LHC. Event selection criteria and lepton and four-lepton mass resolution performance have been discussed. A new particle has been observed within this search in  $H \rightarrow ZZ^{(*)} \rightarrow 4\ell$ , with a local significance against background of about  $6.6\sigma$ . This observation has been confirmed by decays in other channels with rates consistent with the Standard Model expectation. Combined results from all ATLAS searches show that this particle has a mass of  $125.5 \pm 0.2(\text{stat})_{-0.6}^{+0.5}(\text{sys}) \text{ GeV}$  and a signal strength of  $1.30 \pm 0.13(\text{stat}) \pm 0.1(\text{sys})$  compatible with the Standard Model expectation of unity.

The Standard Model prediction for the quantum numbers of this new particle,  $J^P = 0^+$ , has been tested against different alternative hypotheses, using a matrix-element-based method. The  $J^P$ -MELA multivariate technique for the description of final state kinematics in terms of the most general parametrization of the  $H \rightarrow ZZ$  decay amplitude, corrected for acceptance and selection effects studied on Monte Carlo simulation, has been presented. The hypothesis testing method against  $J^P = 0^-, 1^+, 1^-, 2^+$  and  $2^-$  specific models has been described. Results show that the  $0^+$  hypothesis is clearly preferred, and  $0^-, 1^+$  and  $1^-$  models are excluded at more than 95% CL with the  $CL_s$  method. Combination with searches in  $H \rightarrow \gamma\gamma$  and  $H \rightarrow WW^{(*)} \rightarrow \ell\nu\ell\nu$  decay channels allows to exclude also the  $2^+$  hypothesis at more than 99.9% CL, independently on the assumed fraction of gluon fusion and  $q\bar{q}$  annihilation production processes.

Finally, two techniques, based on the same description of the final state kinematics, for the determination of the coupling parameters which characterize the most general  $H \rightarrow ZZ$  decay amplitude, have been described. A 2D hypothesis testing method in the complex plane of the complex coupling parameters  $g_2/g_1$  and  $g_4/g_1$  has been presented, as well as a 8D fitting method based on the full analytic signal description and an empirical background model. Sensitivity prospects for a High Luminosity LHC at  $\sqrt{s} = 14 \text{ TeV}$  have been discussed: a fractional CP-odd component of more than 20% (6%) can be excluded at 95% CL with  $300 \text{ fb}^{-1}$  ( $3000 \text{ fb}^{-1}$ ). An analysis of the ATLAS Run I dataset is currently ongoing; preliminary projections show that an expected sensitivity on  $\langle f_{CP} \rangle$  comparable to the result by the CMS collaboration

reported in Ref. [78] can be reached with the proposed techniques.

## Appendix A

# Decay Amplitudes and Differential Distributions

In this Appendix, the full functional form for the differential distributions of a particle with spin  $J = 0, 1, 2$  decaying via  $X \rightarrow Z_1 Z_2 \rightarrow 4\ell$  is given[42].

### A.1 Spin One

The helicity amplitudes in the spin-one case corresponding to Eq. (4.7) are the following:

$$\begin{aligned}
 A_{00} &= b_1 \frac{(m_1^2 - m_2^2)}{m_X} \sqrt{x}, \\
 A_{++} &= i b_2 \frac{(m_1^2 - m_2^2)}{m_X}, \\
 A_{--} &= -i b_2 \frac{(m_1^2 - m_2^2)}{m_X}, \\
 A_{+0} &= b_1 m_1 \sqrt{x} + i b_2 \frac{m_2}{m_X^2} \left[ \frac{1}{2} (m_X^2 - m_1^2 + m_2^2) \left( \frac{m_1^2}{m_2^2} - 1 \right) + 2m_1^2 x \right], \\
 A_{0+} &= -b_1 m_2 \sqrt{x} - i b_2 \frac{m_1}{m_X^2} \left[ \frac{1}{2} (m_X^2 + m_1^2 - m_2^2) \left( \frac{m_2^2}{m_1^2} - 1 \right) + 2m_2^2 x \right], \\
 A_{-0} &= b_1 m_1 \sqrt{x} - i b_2 \frac{m_2}{m_X^2} \left[ \frac{1}{2} (m_X^2 - m_1^2 + m_2^2) \left( \frac{m_1^2}{m_2^2} - 1 \right) + 2m_1^2 x \right], \\
 A_{0-} &= -b_1 m_2 \sqrt{x} + i b_2 \frac{m_1}{m_X^2} \left[ \frac{1}{2} (m_X^2 + m_1^2 - m_2^2) \left( \frac{m_2^2}{m_1^2} - 1 \right) + 2m_2^2 x \right].
 \end{aligned}$$

### A.2 Spin Two

The scattering amplitude of Eq. (4.8) can be written as

$$\begin{aligned}
A(X \rightarrow Z_1 Z_2) = \Lambda^{-1} e_1^{*\mu} e_2^{*\nu} \left[ c_1 (q_1 q_2) t_{\mu\nu} + c_2 g_{\mu\nu} t_{\alpha\beta} \tilde{q}^\alpha \tilde{q}^\beta + c_3 \frac{q_{2\mu} q_{1\nu}}{m_X^2} t_{\alpha\beta} \tilde{q}^\alpha \tilde{q}^\beta \right. \\
+ 2c_{41} q_{1\nu} q_2^\alpha t_{\mu\alpha} + 2c_{42} q_{2\mu} q_1^\alpha t_{\nu\alpha} + c_5 t_{\alpha\beta} \frac{\tilde{q}^\alpha \tilde{q}^\beta}{m_X^2} \epsilon_{\mu\nu\rho\sigma} q_1^\rho q_2^\sigma \\
\left. + c_6 t^{\alpha\beta} \tilde{q}_\beta \epsilon_{\mu\nu\alpha\rho} q^\rho + \frac{c_7 t^{\alpha\beta} \tilde{q}_\beta}{m_X^2} (\epsilon_{\alpha\mu\rho\sigma} q^\rho \tilde{q}^\sigma q_\nu + \epsilon_{\alpha\nu\rho\sigma} q^\rho \tilde{q}^\sigma q_\mu) \right].
\end{aligned}$$

The eight coefficients  $c_i$  can be expressed through the couplings  $g_i$  by

$$\begin{aligned}
c_1 &= 2g_1 + 2g_2 \frac{s}{\Lambda^2} \left(1 + \frac{m_1^2}{s}\right) \left(1 + \frac{m_2^2}{s}\right) + 2g_5 \frac{m_Z^2}{s}, \\
c_2 &= -\frac{g_1}{2} + g_3 \frac{s}{\Lambda^2} \left(1 - \frac{m_1^2 + m_2^2}{2s}\right) + 2g_4 \frac{s}{\Lambda^2} + g_7 \frac{m_Z^2}{\Lambda^2}, \\
c_3 &= -\left(\frac{g_2}{2} + g_3 + 2g_4\right) \frac{m_X^2}{\Lambda^2}, \\
c_{41} &= -g_1 - g_2 \frac{s + m_1^2}{\Lambda^2} - g_3 \frac{m_2^2}{\Lambda^2} - g_6 \frac{m_V^2}{\Lambda^2}, \\
c_{42} &= -g_1 - g_2 \frac{s + m_2^2}{\Lambda^2} - g_3 \frac{m_1^2}{\Lambda^2} - g_6 \frac{m_V^2}{\Lambda^2}, \\
c_5 &= 2g_8 \frac{m_X^2}{\Lambda^2}, \\
c_6 &= g_9 \frac{m_V^2}{\Lambda^2}, \\
c_7 &= g_{10} \frac{m_X^2 m_V^2}{\Lambda^4}.
\end{aligned}$$

The helicity amplitudes are as follows:

$$\begin{aligned}
\Lambda^2 A_{00} &= \frac{m_X^4}{m_1 m_2 \sqrt{6}} \frac{c_1}{8} + \frac{m_1 m_2}{\sqrt{6}} \left[ c_1 \frac{1}{2} (1+x) - c_2 2x + c_{41} 2x + c_{42} 2x \right] \\
&\quad - \frac{(m_1^4 + m_2^4)}{m_1 m_2 \sqrt{6}} \frac{c_1}{4} + \frac{m_1 m_2 (m_1^2 - m_2^2)}{m_X^2 \sqrt{6}} (c_{41} - c_{42}) 2x \\
&\quad + \frac{(m_1^8 + m_2^8)}{m_X^4 m_1 m_2 \sqrt{6}} \frac{c_1}{8} + \frac{m_1^3 m_2^3}{m_X^4 \sqrt{6}} \left[ c_1 \left(\frac{3}{4} + x\right) - c_2 (4x + 8x^2) - c_3 8x^2 \right] \\
&\quad + \frac{m_1 m_2 (m_1^4 + m_2^4)}{m_X^4 \sqrt{6}} \left[ -c_1 \frac{1}{2} (1+x) + c_2 2x \right], \\
\Lambda^2 A_{++} &= \frac{m_X^2}{\sqrt{6}} \frac{c_1}{4} - \frac{(m_1^4 + m_2^4)}{m_X^2 \sqrt{6}} \frac{c_1}{4} + \frac{m_1^2 m_2^2}{m_X^2 \sqrt{6}} \left[ c_1 \left(\frac{1}{2} + x\right) + c_2 8x \right] - i \frac{m_1 m_2}{\sqrt{6}} c_6 4\sqrt{x} \\
&\quad + i \frac{m_1^3 m_2^3}{m_X^4 \sqrt{6}} c_5 8x\sqrt{x}, \\
\Lambda^2 A_{--} &= \frac{m_X^2}{\sqrt{6}} \frac{c_1}{4} - \frac{(m_1^4 + m_2^4)}{m_X^2 \sqrt{6}} \frac{c_1}{4} + \frac{m_1^2 m_2^2}{m_X^2 \sqrt{6}} \left[ c_1 \left(\frac{1}{2} + x\right) + c_2 8x \right] + i \frac{m_1 m_2}{\sqrt{6}} c_6 4\sqrt{x}
\end{aligned}$$

$$\begin{aligned}
& -\imath \frac{m_1^3 m_2^3}{m_X^4 \sqrt{6}} c_5 8x \sqrt{x}, \\
\Lambda^2 A_{+0} &= \frac{m_X^3}{m_2 \sqrt{2}} \frac{c_1}{8} + \frac{m_X m_2}{\sqrt{2}} \left(1 - \frac{m_1^2}{m_2^2}\right) \frac{c_1}{8} + \frac{m_1^2 m_2}{m_X \sqrt{2}} \left[ c_1 \left( \frac{1}{4} + \frac{1}{2}x - \frac{m_2^2}{8m_1^2} - \frac{m_1^2}{8m_2^2} \right) + c_{41} 2x \right] \\
& + \frac{m_1^2 m_2^3}{m_X^3 \sqrt{2}} c_1 \left[ \frac{1}{8} \left( \frac{m_1^4}{m_2^4} - \frac{m_2^2}{m_1^2} \right) + \left(1 - \frac{m_1^2}{m_2^2}\right) \left( \frac{3}{8} + \frac{1}{2}x \right) \right] - \imath \frac{m_X m_1}{\sqrt{2}} c_6 \sqrt{x} \\
& + \imath \frac{m_1^3}{m_X \sqrt{2}} c_6 \left(1 - \frac{m_2^2}{m_1^2}\right) \sqrt{x} - \imath \frac{m_1^3 m_2^2}{m_X^3 \sqrt{2}} c_7 4x \sqrt{x}, \\
\Lambda^2 A_{0+} &= \frac{m_X^3}{m_1 \sqrt{2}} \frac{c_1}{8} + \frac{m_X m_1}{\sqrt{2}} \left(1 - \frac{m_2^2}{m_1^2}\right) \frac{c_1}{8} + \frac{m_1 m_2^2}{m_X \sqrt{2}} \left[ c_1 \left( \frac{1}{4} + \frac{1}{2}x - \frac{m_2^2}{8m_1^2} - \frac{m_1^2}{8m_2^2} \right) + c_{42} 2x \right] \\
& + \frac{m_1^3 m_2^2}{m_X^3 \sqrt{2}} c_1 \left[ \frac{1}{8} \left( \frac{m_2^4}{m_1^4} - \frac{m_1^2}{m_2^2} \right) + \left(1 - \frac{m_2^2}{m_1^2}\right) \left( \frac{3}{8} + \frac{1}{2}x \right) \right] - \imath \frac{m_X m_2}{\sqrt{2}} c_6 \sqrt{x} \\
& + \imath \frac{m_2^3}{m_X \sqrt{2}} c_6 \left(1 - \frac{m_1^2}{m_2^2}\right) \sqrt{x} - \imath \frac{m_1^2 m_2^3}{m_X^3 \sqrt{2}} c_7 4x \sqrt{x}, \\
\Lambda^2 A_{-0} &= \frac{m_X^3}{m_2 \sqrt{2}} \frac{c_1}{8} + \frac{m_X m_2}{\sqrt{2}} \left(1 - \frac{m_1^2}{m_2^2}\right) \frac{c_1}{8} + \frac{m_1^2 m_2}{m_X \sqrt{2}} \left[ c_1 \left( \frac{1}{4} + \frac{1}{2}x - \frac{m_2^2}{8m_1^2} - \frac{m_1^2}{8m_2^2} \right) + c_{41} 2x \right] \\
& + \frac{m_1^2 m_2^3}{m_X^3 \sqrt{2}} c_1 \left[ \frac{1}{8} \left( \frac{m_1^4}{m_2^4} - \frac{m_2^2}{m_1^2} \right) + \left(1 - \frac{m_1^2}{m_2^2}\right) \left( \frac{3}{8} + \frac{1}{2}x \right) \right] + \imath \frac{m_X m_1}{\sqrt{2}} c_6 \sqrt{x} \\
& - \imath \frac{m_1^3}{m_X \sqrt{2}} c_6 \left(1 - \frac{m_2^2}{m_1^2}\right) \sqrt{x} + \imath \frac{m_1^3 m_2^2}{m_X^3 \sqrt{2}} c_7 4x \sqrt{x}, \\
\Lambda^2 A_{0-} &= \frac{m_X^3}{m_1 \sqrt{2}} \frac{c_1}{8} + \frac{m_X m_1}{\sqrt{2}} \left(1 - \frac{m_2^2}{m_1^2}\right) \frac{c_1}{8} + \frac{m_1 m_2^2}{m_X \sqrt{2}} \left[ c_1 \left( \frac{1}{4} + \frac{1}{2}x - \frac{m_2^2}{8m_1^2} - \frac{m_1^2}{8m_2^2} \right) + c_{42} 2x \right] \\
& + \frac{m_1^3 m_2^2}{m_X^3 \sqrt{2}} c_1 \left[ \frac{1}{8} \left( \frac{m_2^4}{m_1^4} - \frac{m_1^2}{m_2^2} \right) + \left(1 - \frac{m_2^2}{m_1^2}\right) \left( \frac{3}{8} + \frac{1}{2}x \right) \right] + \imath \frac{m_X m_2}{\sqrt{2}} c_6 \sqrt{x} \\
& - \imath \frac{m_2^3}{m_X \sqrt{2}} c_6 \left(1 - \frac{m_1^2}{m_2^2}\right) \sqrt{x} + \imath \frac{m_1^2 m_2^3}{m_X^3 \sqrt{2}} c_7 4x \sqrt{x}, \\
\Lambda^2 A_{+-} &= A_{-+} = m_X^2 \frac{c_1}{4} + \frac{m_1^2 m_2^2}{m_X^2} c_1 x - \frac{(m_1^2 - m_2^2)^2}{m_X^2} \frac{c_1}{4}.
\end{aligned}$$

### A.3 Differential Distributions

Let  $J$  be the spin of the boson  $X$ ; we will use all symbols defined in Sec. 4.2. The helicity amplitudes  $A_{\alpha\beta} = A_{\alpha\beta}(m_1, m_2)$  of Eq. 4.3 are presented in Eq. (4.6) for  $J = 0$ , Eq. (A.1) for  $J = 1$  and Eq. (A.2) for  $J = 2$ . Since they are complex amplitudes, we can express them using their absolute value  $|A_{\alpha\beta}|$  and the phase  $\phi_{\alpha\beta} = \arg(A_{\alpha\beta}/A_{00})$ .

The differential angular and mass distribution, expressed in terms of the helicity amplitudes, is

$$\frac{\mathcal{N}_J d\Gamma_J(m_1, m_2, \cos \theta^*, \Psi, \cos \theta_1, \cos \theta_2, \Phi)}{d \cos \theta^* d\Psi d \cos \theta_1 d \cos \theta_2 d\Phi} =$$

$$\begin{aligned}
& F_{0,0}^J(\theta^*) \times \left[ 4|A_{00}|^2 \sin^2 \theta_1 \sin^2 \theta_2 \right. \\
& \quad + |A_{++}|^2 \left( 1 + 2A_{f_1} \cos \theta_1 + \cos^2 \theta_1 \right) \left( 1 + 2A_{f_2} \cos \theta_2 + \cos^2 \theta_2 \right) \\
& \quad + |A_{--}|^2 \left( 1 - 2A_{f_1} \cos \theta_1 + \cos^2 \theta_1 \right) \left( 1 - 2A_{f_2} \cos \theta_2 + \cos^2 \theta_2 \right) \\
& \quad + 4|A_{00}||A_{++}|(A_{f_1} + \cos \theta_1) \sin \theta_1 (A_{f_2} + \cos \theta_2) \sin \theta_2 \cos(\Phi + \phi_{++}) \\
& \quad + 4|A_{00}||A_{--}|(A_{f_1} - \cos \theta_1) \sin \theta_1 (A_{f_2} - \cos \theta_2) \sin \theta_2 \cos(\Phi - \phi_{--}) \\
& \quad \left. + 2|A_{++}||A_{--}| \sin^2 \theta_1 \sin^2 \theta_2 \cos(2\Phi - \phi_{--} + \phi_{++}) \right] \\
& + F_{1,1}^J(\theta^*) \times \left[ 2|A_{+0}|^2(1 + 2A_{f_1} \cos \theta_1 + \cos^2 \theta_1) \sin^2 \theta_2 \right. \\
& \quad + 2|A_{0-}|^2 \sin^2 \theta_1 (1 - 2A_{f_2} \cos \theta_2 + \cos^2 \theta_2) \\
& \quad + 2|A_{-0}|^2(1 - 2A_{f_1} \cos \theta_1 + \cos^2 \theta_1) \sin^2 \theta_2 \\
& \quad + 2|A_{0+}|^2 \sin^2 \theta_1 (1 + 2A_{f_2} \cos \theta_2 + \cos^2 \theta_2) \\
& \quad + 4|A_{+0}||A_{0-}|(A_{f_1} + \cos \theta_1) \sin \theta_1 (A_{f_2} - \cos \theta_2) \sin \theta_2 \cos(\Phi + \phi_{+0} - \phi_{0-}) \\
& \quad \left. + 4|A_{0+}||A_{-0}|(A_{f_1} - \cos \theta_1) \sin \theta_1 (A_{f_2} + \cos \theta_2) \sin \theta_2 \cos(\Phi + \phi_{0+} - \phi_{-0}) \right] \\
& + F_{1,-1}^J(\theta^*) \times \left[ 4|A_{+0}||A_{0+}|(A_{f_1} + \cos \theta_1) \sin \theta_1 (A_{f_2} + \cos \theta_2) \sin \theta_2 \cos(2\Psi - \phi_{+0} + \phi_{0+}) \right. \\
& \quad + 4|A_{+0}||A_{-0}| \sin^2 \theta_1 \sin^2 \theta_2 \cos(2\Psi - \Phi - \phi_{+0} + \phi_{-0}) \\
& \quad + 4|A_{0-}||A_{0+}| \sin^2 \theta_1 \sin^2 \theta_2 \cos(2\Psi + \Phi - \phi_{0-} + \phi_{0+}) \\
& \quad \left. + 4|A_{0-}||A_{-0}|(A_{f_1} - \cos \theta_1) \sin \theta_1 (A_{f_2} - \cos \theta_2) \sin \theta_2 \cos(2\Psi - \phi_{0-} + \phi_{-0}) \right] \\
& + F_{2,2}^J(\theta^*) \times \left[ |A_{+-}|^2(1 + 2A_{f_1} \cos \theta_1 + \cos^2 \theta_1)(1 - 2A_{f_2} \cos \theta_2 + \cos^2 \theta_2) \right. \\
& \quad \left. + |A_{-+}|^2(1 - 2A_{f_1} \cos \theta_1 + \cos^2 \theta_1)(1 + 2A_{f_2} \cos \theta_2 + \cos^2 \theta_2) \right] \\
& + F_{2,-2}^J(\theta^*) \times \left[ 2|A_{+-}||A_{-+}| \sin^2 \theta_1 \sin^2 \theta_2 \cos(4\Psi - \phi_{+-} + \phi_{-+}) \right] \\
& + F_{0,1}^J(\theta^*) \times \left[ 4\sqrt{2}|A_{00}||A_{+0}|(A_{f_1} + \cos \theta_1) \sin \theta_1 \sin^2 \theta_2 \cos(\Psi - \Phi/2 - \phi_{+0}) \right. \\
& \quad + 4\sqrt{2}|A_{00}||A_{0-}| \sin^2 \theta_1 (A_{f_2} - \cos \theta_2) \sin \theta_2 \cos(\Psi + \Phi/2 - \phi_{0-}) \\
& \quad + 2\sqrt{2}|A_{--}||A_{+0}| \sin^2 \theta_1 (A_{f_2} - \cos \theta_2) \sin \theta_2 \cos(-\Psi + 3\Phi/2 + \phi_{+0} - \phi_{--}) \\
& \quad + 2\sqrt{2}|A_{--}||A_{0-}|(A_{f_1} - \cos \theta_1) \sin \theta_1 (1 - 2A_{f_2} \cos \theta_2 + \cos^2 \theta_2) \\
& \quad \cdot \cos(-\Psi + \Phi/2 + \phi_{0-} - \phi_{--}) \\
& \quad + 2\sqrt{2}|A_{++}||A_{+0}|(1 + 2A_{f_1} \cos \theta_1 + \cos^2 \theta_1)(A_{f_2} + \cos \theta_2) \sin \theta_2 \\
& \quad \cdot \cos(\Psi + \Phi/2 - \phi_{+0} + \phi_{++}) \\
& \quad \left. + 2\sqrt{2}|A_{++}||A_{0-}|(A_{f_1} + \cos \theta_1) \sin \theta_1 \sin^2 \theta_2 \cos(\Psi + 3\Phi/2 - \phi_{0-} + \phi_{++}) \right] \\
& + F_{0,-1}^J(\theta^*) \times \left[ 4\sqrt{2}|A_{00}||A_{0+}| \sin^2 \theta_1 (A_{f_2} + \cos \theta_2) \sin \theta_2 \cos(\Psi + \Phi/2 + \phi_{+0}) \right. \\
& \quad + 4\sqrt{2}|A_{00}||A_{-0}|(A_{f_1} - \cos \theta_1) \sin \theta_1 \sin^2 \theta_2 \cos(\Psi - \Phi/2 + \phi_{-0}) \\
& \quad + 2\sqrt{2}|A_{--}||A_{0+}|(A_{f_1} - \cos \theta_1) \sin \theta_1 \sin^2 \theta_2 \cos(\Psi + 3\Phi/2 + \phi_{0+} - \phi_{--}) \\
& \quad \left. + 2\sqrt{2}|A_{--}||A_{-0}|(1 - 2A_{f_1} \cos \theta_1 + \cos^2 \theta_1)(A_{f_2} - \cos \theta_2) \sin \theta_2 \right]
\end{aligned}$$

$$\begin{aligned}
& \cdot \cos(\Psi + \Phi/2 + \phi_{-0} - \phi_{--}) \\
& + 2\sqrt{2}|A_{++}||A_{0+}|(A_{f_1} + \cos\theta_1) \sin\theta_1(1 + 2A_{f_2} \cos\theta_2 + \cos^2\theta_2) \\
& \cdot \cos(\Psi - \Phi/2 + \phi_{0+} - \phi_{++}) \\
& + 2\sqrt{2}|A_{++}||A_{-0}| \sin^2\theta_1(A_{f_2} + \cos\theta_2) \sin\theta_2 \cos(-\Psi + 3\Phi/2 - \phi_{-0} + \phi_{++}) \Big] \\
& + F_{0,2}^J(\theta^*) \times \Big[ 4|A_{00}||A_{+-}|(A_{f_1} + \cos\theta_1) \sin\theta_1(A_{f_2} - \cos\theta_2) \sin\theta_2 \cos(2\Psi - \phi_{+-}) \\
& + 2|A_{--}||A_{+-}| \sin^2\theta_1(1 - 2A_{f_2} \cos\theta_2 + \cos^2\theta_2) \cos(2\Psi - \Phi + \phi_{--} - \phi_{+-}) \\
& + 2|A_{++}||A_{+-}|(1 + 2A_{f_1} \cos\theta_1 + \cos^2\theta_1) \sin^2\theta_2 \cos(2\Psi + \Phi + \phi_{++} - \phi_{+-}) \Big] \\
& + F_{0,-2}^J(\theta^*) \times \Big[ 4|A_{00}||A_{-+}|(A_{f_1} - \cos\theta_1) \sin\theta_1(A_{f_2} + \cos\theta_2) \sin\theta_2 \cos(2\Psi + \phi_{-+}) \\
& + 2|A_{--}||A_{-+}|(1 - 2A_{f_1} \cos\theta_1 + \cos^2\theta_1) \sin^2\theta_2 \cos(2\Psi + \Phi - \phi_{--} + \phi_{-+}) \\
& + 2|A_{++}||A_{-+}| \sin^2\theta_1(1 + 2A_{f_2} \cos\theta_2 + \cos^2\theta_2) \cos(2\Psi - \Phi - \phi_{++} + \phi_{-+}) \Big] \\
& + F_{1,2}^J(\theta^*) \times \Big[ 2\sqrt{2}|A_{+0}||A_{+-}|(1 + 2A_{f_1} \cos\theta_1 + \cos^2\theta_1)(A_{f_2} - \cos\theta_2) \sin\theta_2 \cos(\Psi + \Phi/2 + \phi_{+0} - \phi_{+-}) \\
& + 2\sqrt{2}|A_{0-}||A_{+-}|(A_{f_1} + \cos\theta_1) \sin\theta_1(1 - 2A_{f_2} \cos\theta_2 + \cos^2\theta_2) \cos(\Psi - \Phi/2 + \phi_{0-} - \phi_{+-}) \\
& - 2\sqrt{2}|A_{+0}||A_{-+}|(A_{f_1} - \cos\theta_1) \sin\theta_1(1 + 2A_{f_2} \cos\theta_2 + \cos^2\theta_2) \cos(-\Psi + \Phi/2 + \phi_{+0} - \phi_{-+}) \\
& - 2\sqrt{2}|A_{-0}||A_{-+}|(1 - 2A_{f_1} \cos\theta_1 + \cos^2\theta_1)(A_{f_2} + \cos\theta_2) \sin\theta_2 \cos(\Psi + \Phi/2 + \phi_{-0} - \phi_{-+}) \Big] \\
& + F_{1,-2}^J(\theta^*) \times \Big[ 2\sqrt{2}|A_{+0}||A_{-+}| \sin^2\theta_1(A_{f_2} + \cos\theta_2) \sin\theta_2 \cos(3\Psi - \Phi/2 - \phi_{+0} + \phi_{-+}) \\
& + 2\sqrt{2}|A_{0-}||A_{-+}|(A_{f_1} - \cos\theta_1) \sin\theta_1 \sin^2\theta_2 \cos(3\Psi + \Phi/2 - \phi_{0-} + \phi_{-+}) \\
& - 2\sqrt{2}|A_{+0}||A_{-+}|(A_{f_1} + \cos\theta_1) \sin\theta_1 \sin^2\theta_2 \cos(3\Psi + \Phi/2 + \phi_{+0} - \phi_{-+}) \\
& - 2\sqrt{2}|A_{-0}||A_{-+}| \sin^2\theta_1(A_{f_2} - \cos\theta_2) \sin\theta_2 \cos(3\Psi - \Phi/2 + \phi_{-0} - \phi_{-+}) \Big],
\end{aligned}$$

where  $\mathcal{N}_J$  is a normalization constant, and  $A_{f_i}$  is a parameter<sup>1</sup> which characterizes the decay of  $Z_i$ , and is approximately 0.15.

The functions  $F_{i,j}^J(\theta^*)$  are defined through the Wigner  $d$ -functions as

$$F_{i,j}^J(\theta^*) = \sum_{m=0,\pm 1,\pm 2} f_m d_{im}^J(\theta^*) d_{jm}^J(\theta^*), \quad (\text{A.3})$$

where  $f_m$  are linked to the fractions  $f_{zi}$  of spin two  $X$  resonance production with projections of the spin over the  $z$  axis of  $0, \pm 1, \pm 2$ , by the relations

$$f_0 = f_{z0}, \quad f_{\pm 2} = \frac{f_{z2}}{2}, \quad f_{\pm 1} = \frac{f_{z1} \pm \Delta f_{z1}}{2}.$$

For a spin zero particle, only  $F_{00}^0 \neq 0$ ; for a spin one particle, only  $F_{11}^1$  and  $F_{-11}^1$  are non-zero. All contributions are in principle present for a spin two particle.

### A.3.1 The Effect of the Production Mechanism

The production mechanism of the resonance  $X$  influences the decay angular distributions through the terms of Eq. (A.3). In the case of  $q\bar{q}$  annihilation, the resonance

<sup>1</sup>It is defined by  $A_f = 2\bar{g}_V^f \bar{g}_A^f / (\bar{g}_V^{f2} + \bar{g}_A^{f2})$ .

$X$  can be produced only by  $m = \pm 1$ , while in  $gg$  fusion one can have either  $m = \pm 2$  or  $m = 0$ . The relative fractions of  $m = \pm 2$  versus  $m = 0$  are determined by the helicity amplitudes of Eq. (A.2). The relative fraction  $f_{q\bar{q}}$  of  $q\bar{q} \rightarrow X$  production is determined by the ratio of cross-sections: This leads to

$$\begin{aligned}
 f_{+1} = f_{-1} &= \frac{f_{z1}}{2} = \frac{f_{q\bar{q}}}{2}, \\
 f_{+2} = f_{-2} &= \frac{f_{z2}}{2} = (1 - f_{q\bar{q}}) \frac{|A_{+-}^{gg}|^2}{\sum_{\alpha,\beta=\pm 1} |A_{\alpha\beta}^{gg}|^2} = (1 - f_{q\bar{q}}) \frac{|A_{-+}^{gg}|^2}{\sum_{\alpha,\beta=\pm 1} |A_{\alpha\beta}^{gg}|^2}, \\
 f_0 &= f_{z0} = (1 - f_{q\bar{q}}) \frac{|A_{++}^{gg}|^2 + |A_{--}^{gg}|^2}{\sum_{\alpha,\beta=\pm 1} |A_{\alpha\beta}^{gg}|^2}.
 \end{aligned} \tag{A.4}$$

For a  $J = 0$  resonance,  $f_{q\bar{q}} = 0$  and  $f_0 = 1$ . For a  $J = 1$  resonance  $f_{q\bar{q}} = 1$ . For a  $J = 2$  resonance, all polarizations are in general possible. The minimal coupling configuration corresponds to  $f_0 = 0$ .

## Appendix B

# Closure Tests for Signal Parametrization

In this appendix, closure tests for the likelihood description of signal Monte Carlo presented in Chapter 6 are shown.

### B.1 Closure Tests

In figures B.1 to B.13 the comparisons for all the eight final state observables for all the tested production models are shown. An overall good agreement is observed, confirming that the pdf accurately describes the processes studied for all the spin hypotheses considered.

#### B.1.1 $J^P = 0^-$

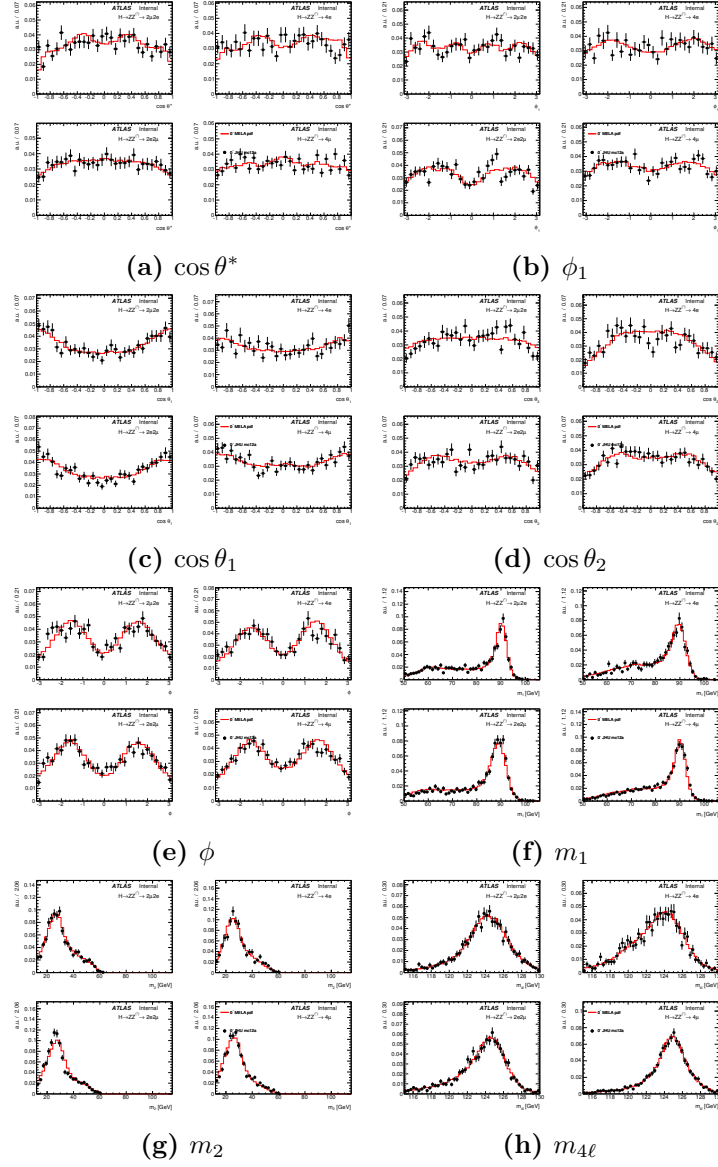


**Figure B.1.** Comparison of the likelihood projection for a  $0^-$  Higgs-like resonance (red curve) and the corresponding JHU (black points) MC simulation for the eight observables. From left to right and top to bottom for each observable:  $2\mu 2e$ ,  $4e$ ,  $2e 2\mu$  and  $4\mu$  channels.

B.1.2  $J^P = 1^+$

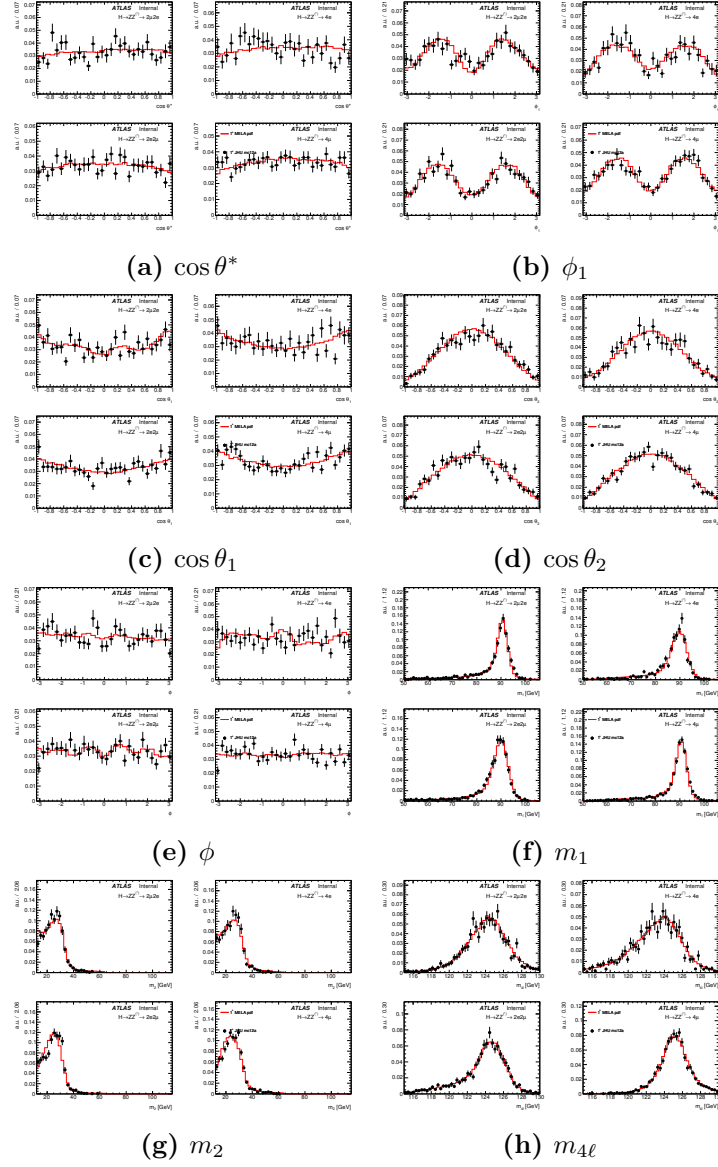


**Figure B.2.** Comparison of the likelihood projection for a  $1^+$  Higgs-like resonance (red curve) and the corresponding JHU (black points) MC simulation for the eight observables. From left to right and top to bottom for each observable:  $2\mu 2e$ ,  $4e$ ,  $2e 2\mu$  and  $4\mu$  channels.

**B.1.3**  $J^P = 1^-$

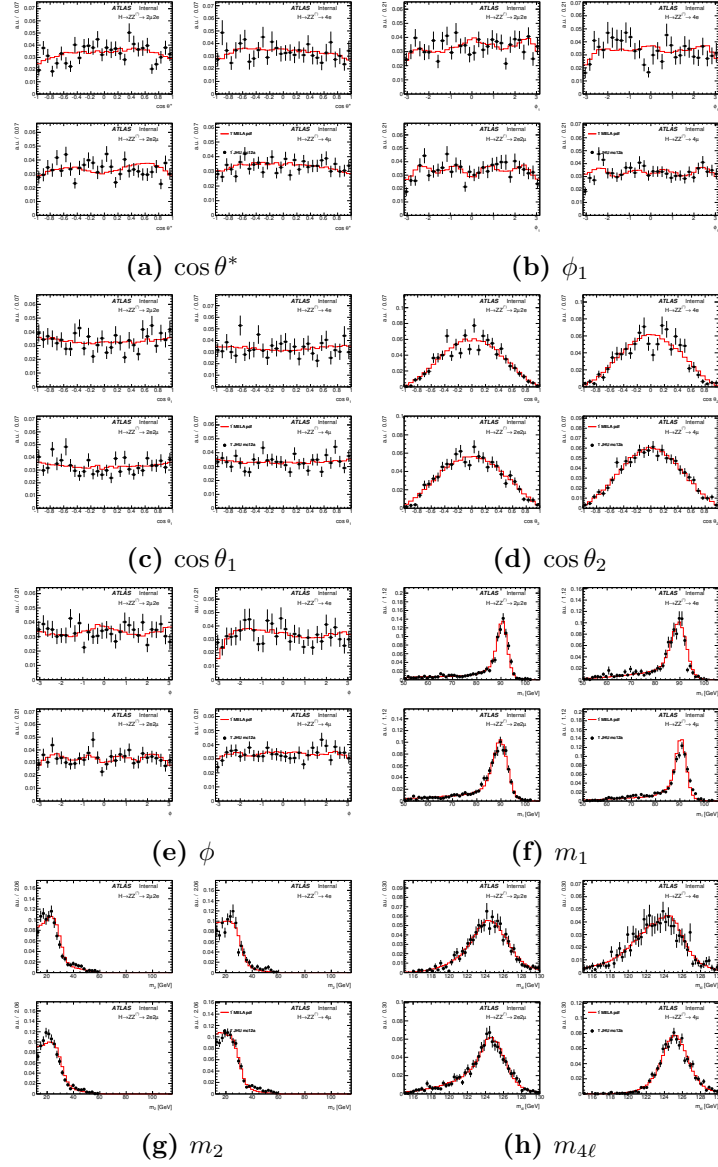


**Figure B.3.** Comparison of the likelihood projection for a  $1^-$  Higgs-like resonance (red curve) and the corresponding JHU (black points) MC simulation for the eight observables. From left to right and top to bottom for each observable:  $2\mu 2e$ ,  $4e$ ,  $2e 2\mu$  and  $4\mu$  channels.

B.1.4  $J^P = 2^+$

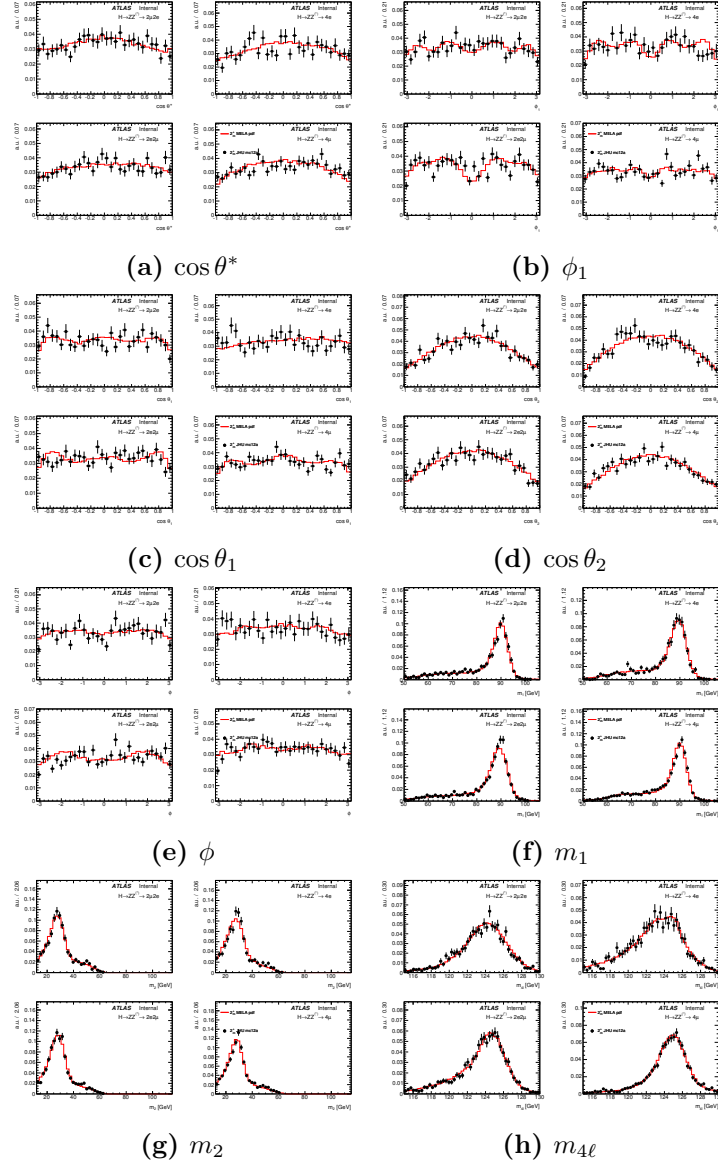


**Figure B.4.** Comparison of the likelihood projection for a  $2^+$  Higgs-like resonance (red curve) and the corresponding JHU (black points) MC simulation for the eight observables. From left to right and top to bottom for each observable:  $2\mu 2e$ ,  $4e$ ,  $2e2\mu$  and  $4\mu$  channels.

B.1.5  $J^P = 2^-$

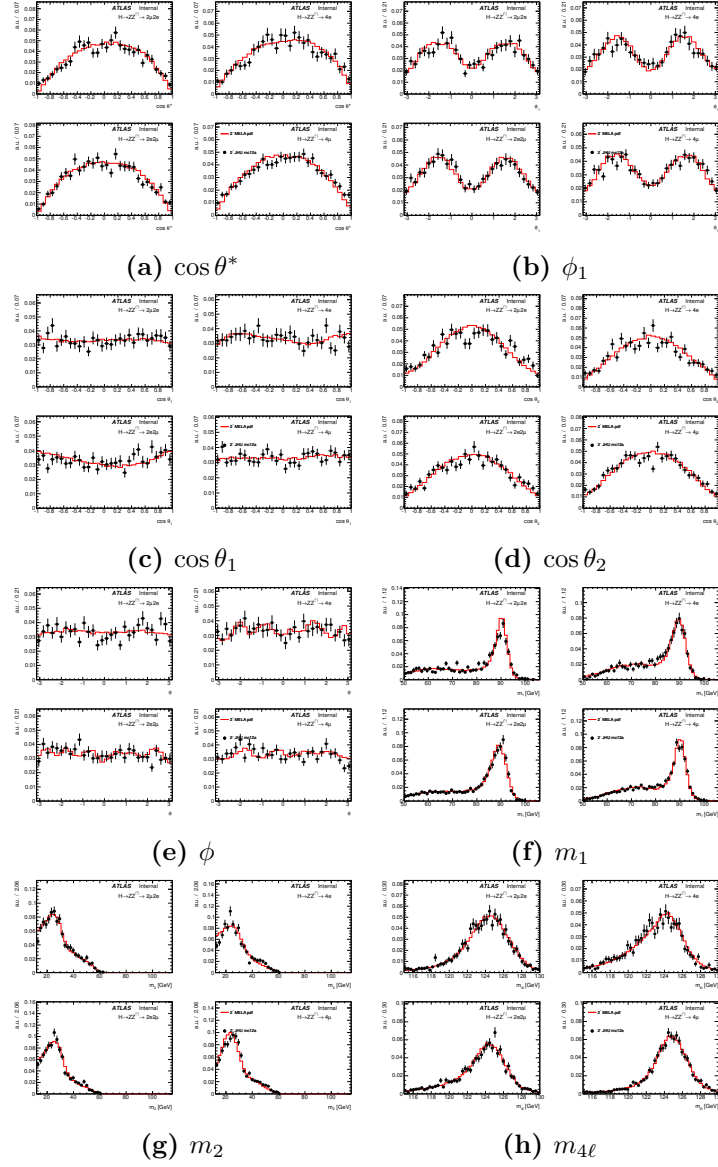


**Figure B.5.** Comparison of the likelihood projection for a  $2^-$  Higgs-like resonance (red curve) and the corresponding JHU (black points) MC simulation for the eight observables. From left to right and top to bottom for each observable:  $2\mu 2e$ ,  $4e$ ,  $2e 2\mu$  and  $4\mu$  channels.

**B.1.6**  $J^P = 2^+$  (25%  $qq$  production)

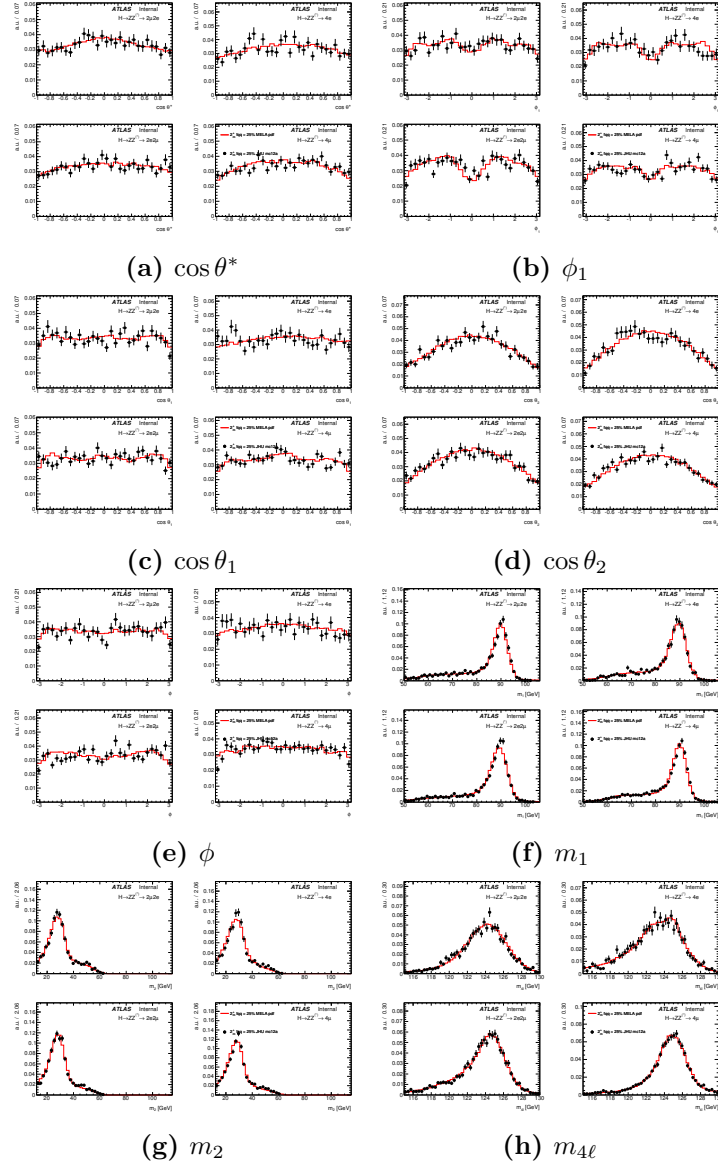


**Figure B.6.** Comparison of the likelihood projection for a  $2^+ f_{qq} = 25\%$  Higgs-like resonance (red curve) and the corresponding JHU (black points) MC simulation for the eight observables. From left to right and top to bottom for each observable:  $2\mu 2e$ ,  $4e$ ,  $2e 2\mu$  and  $4\mu$  channels.

**B.1.7**  $J^P = 2^+$  (50%  $qq$  production)

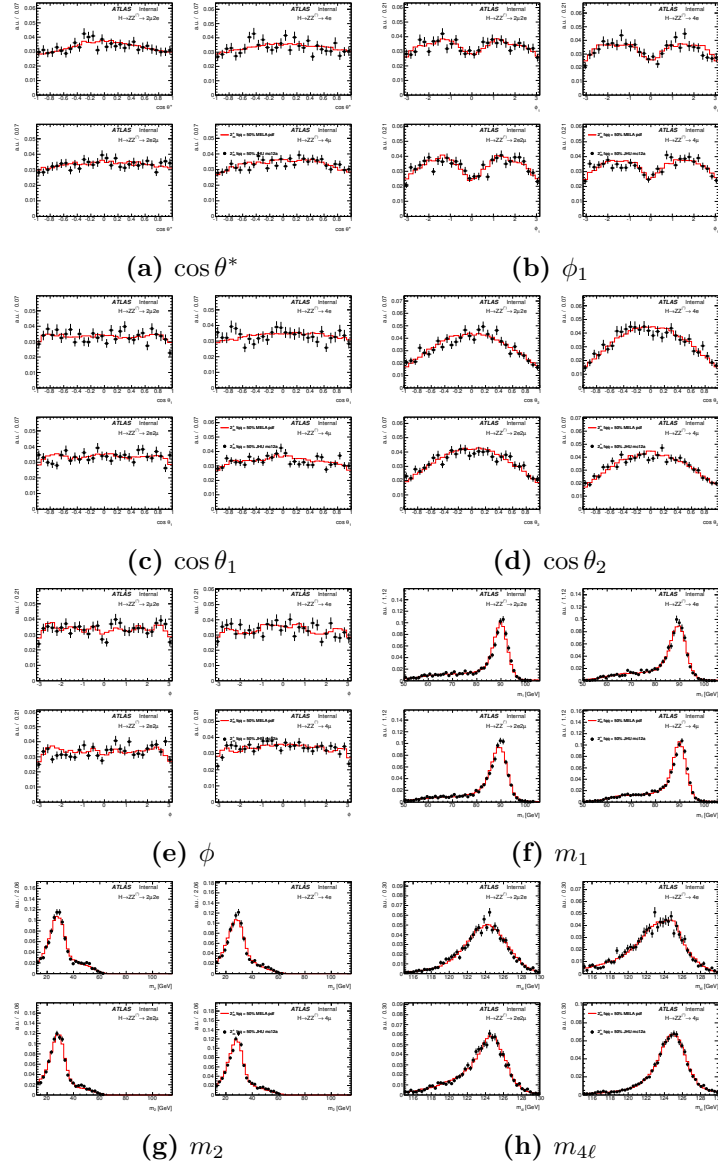


**Figure B.7.** Comparison of the likelihood projection for a  $2^+ f_{qq} = 50\%$  Higgs-like resonance (red curve) and the corresponding JHU (black points) MC simulation for the eight observables. From left to right and top to bottom for each observable:  $2\mu 2e$ ,  $4e$ ,  $2e 2\mu$  and  $4\mu$  channels.

**B.1.8**  $J^P = 2^+$  (75%  $qq$  production)

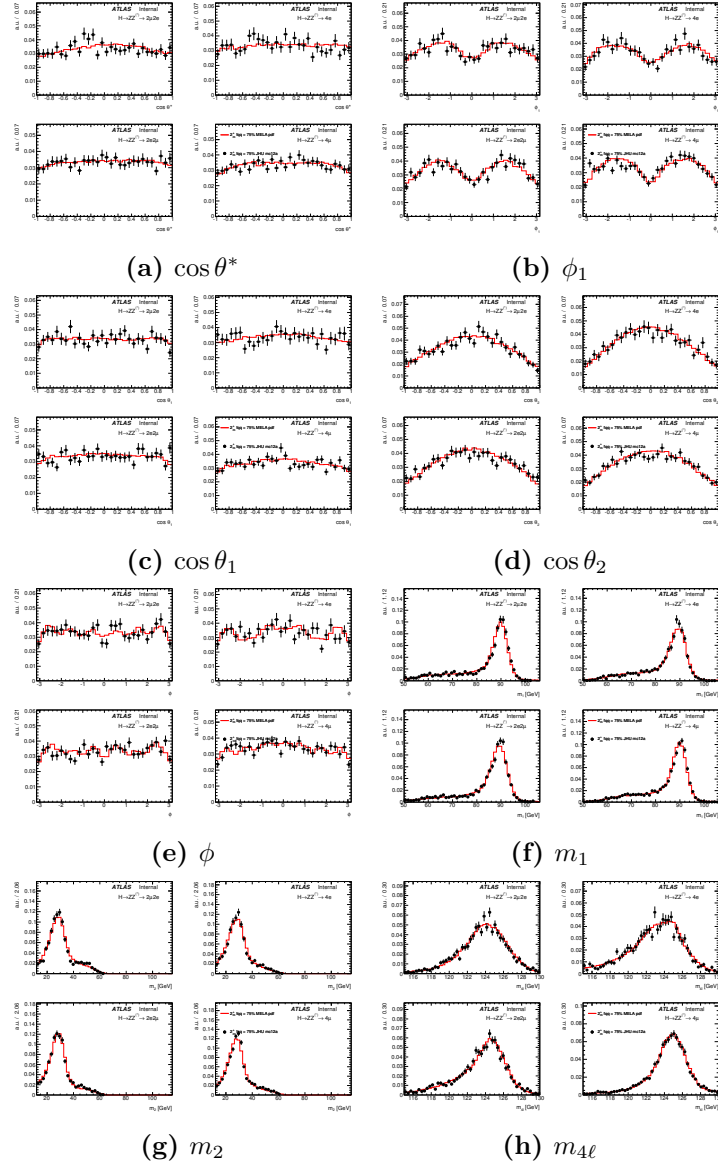


**Figure B.8.** Comparison of the likelihood projection for a  $2^+ f_{qq} = 75\%$  Higgs-like resonance (red curve) and the corresponding JHU (black points) MC simulation for the eight observables. From left to right and top to bottom for each observable:  $2\mu 2e$ ,  $4e$ ,  $2e 2\mu$  and  $4\mu$  channels.

**B.1.9**  $J^P = 2^+$  (100%  $qq$  production)

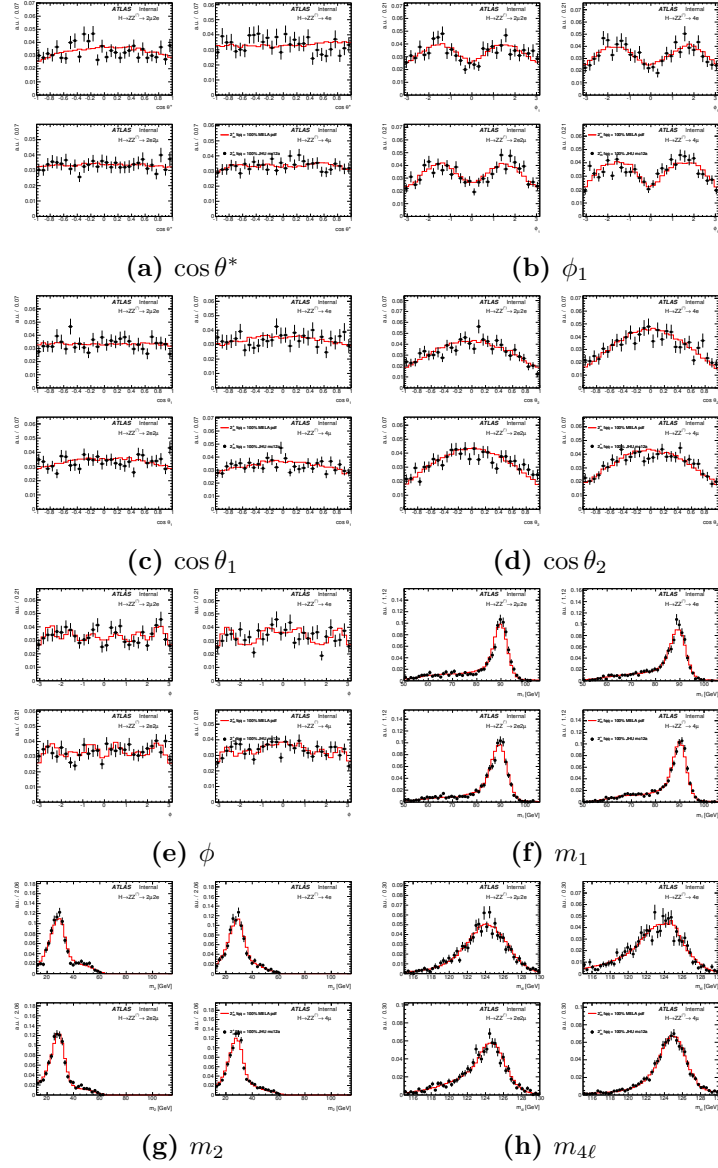


**Figure B.9.** Comparison of the likelihood projection for a  $2^+ f_{qq} = 100\%$  Higgs-like resonance (red curve) and the corresponding JHU (black points) MC simulation for the eight observables. From left to right and top to bottom for each observable:  $2\mu 2e$ ,  $4e$ ,  $2e 2\mu$  and  $4\mu$  channels.

**B.1.10**  $J^P = 2^-$  (25%  $qq$  production)

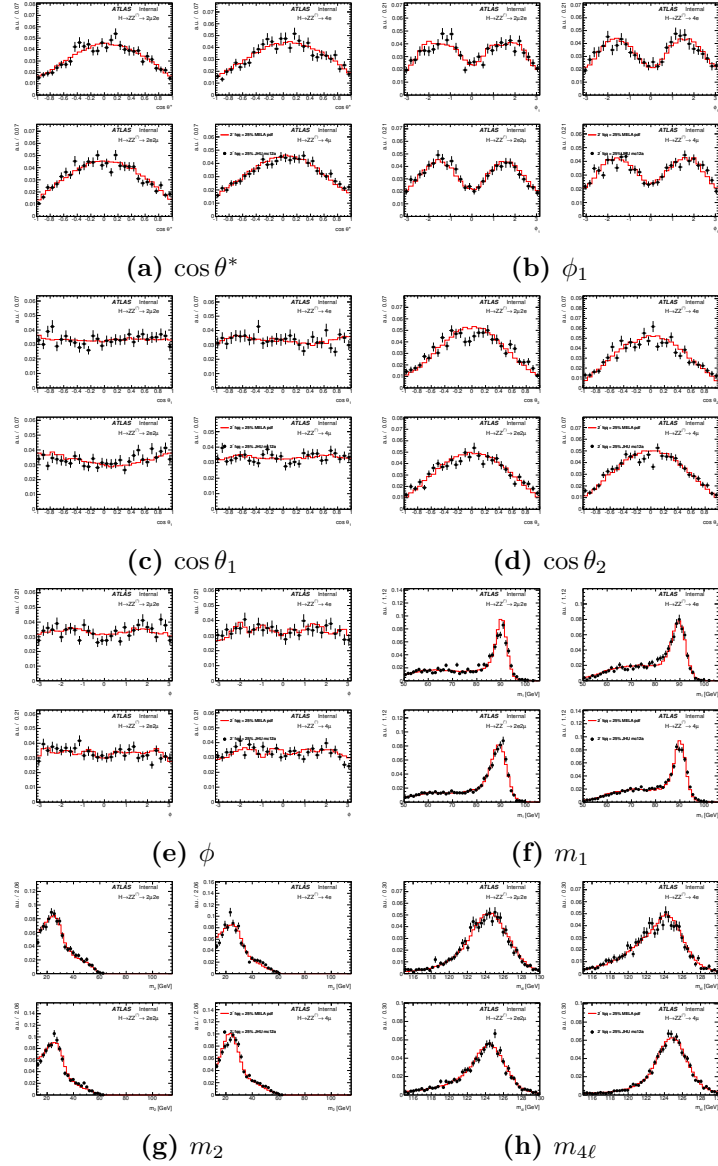


**Figure B.10.** Comparison of the likelihood projection for a  $2^- f_{qq} = 25\%$  Higgs-like resonance (red curve) and the corresponding JHU (black points) MC simulation for the eight observables. From left to right and top to bottom for each observable:  $2\mu 2e$ ,  $4e$ ,  $2e 2\mu$  and  $4\mu$  channels.

**B.1.11**  $J^P = 2^-$  (50%  $qq$  production)

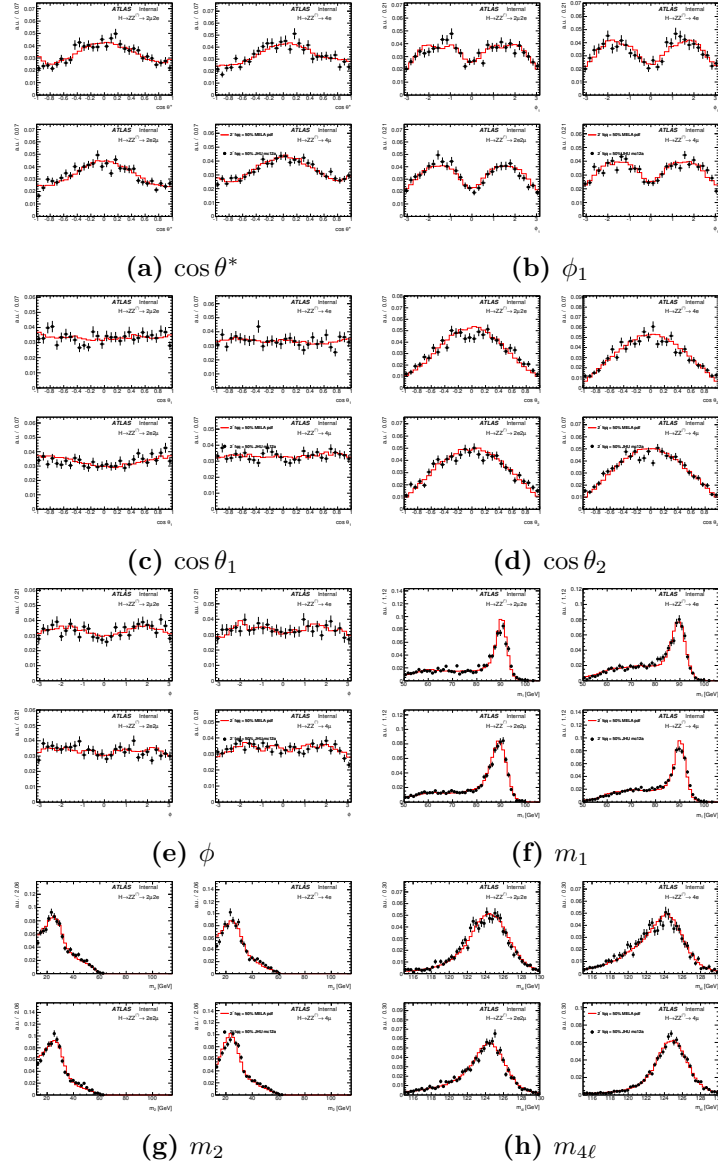


**Figure B.11.** Comparison of the likelihood projection for a  $2^- f_{qq} = 50\%$  Higgs-like resonance (red curve) and the corresponding JHU (black points) MC simulation for the eight observables. From left to right and top to bottom for each observable:  $2\mu 2e$ ,  $4e$ ,  $2e 2\mu$  and  $4\mu$  channels.

**B.1.12**  $J^P = 2^-$  (75%  $qq$  production)

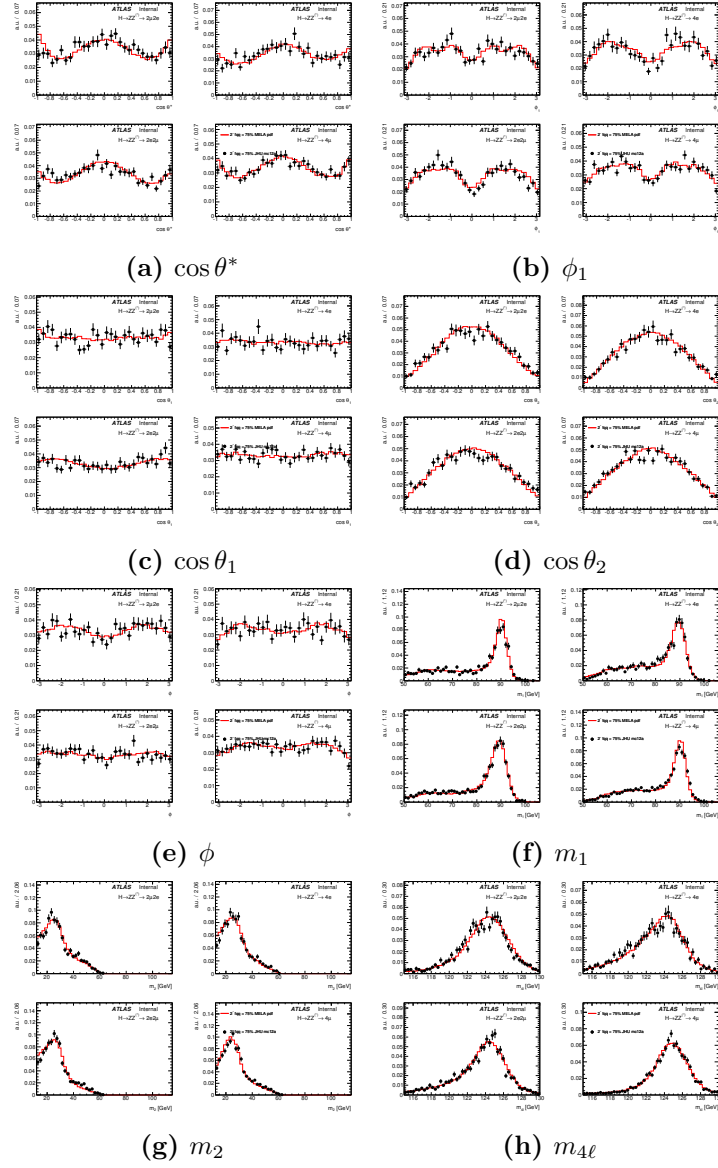


**Figure B.12.** Comparison of the likelihood projection for a  $2^- f_{qq} = 75\%$  Higgs-like resonance (red curve) and the corresponding JHU (black points) MC simulation for the eight observables. From left to right and top to bottom for each observable:  $2\mu 2e$ ,  $4e$ ,  $2e 2\mu$  and  $4\mu$  channels.

**B.1.13**  $J^P = 2^-$  (100%  $qq$  production)

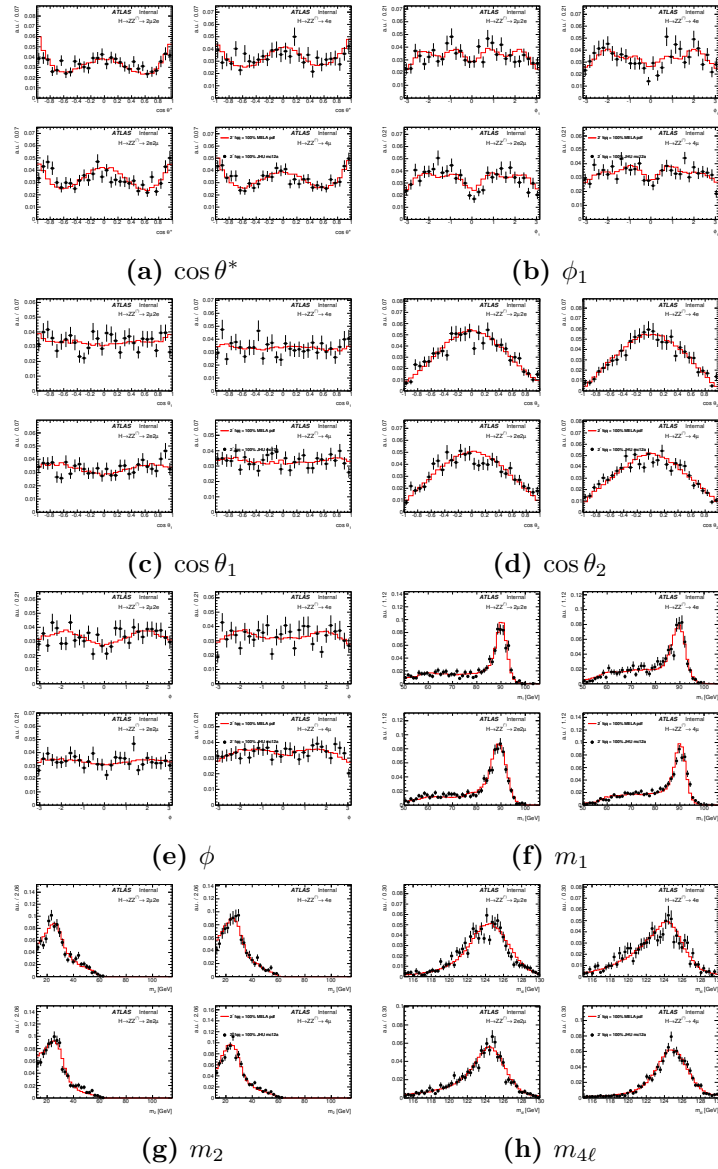


**Figure B.13.** Comparison of the likelihood projection for a  $2^- f_{qq} = 100\%$  Higgs-like resonance (red curve) and the corresponding JHU (black points) MC simulation for the eight observables. From left to right and top to bottom for each observable:  $2\mu 2e$ ,  $4e$ ,  $2e 2\mu$  and  $4\mu$  channels.

# Bibliography

- [1] E. Fermi, *Tentativo di una Teoria Dei Raggi  $\beta$* , Il Nuovo Cimento (1924-1942) **11** (1934) 1–19.
- [2] F. Englert and R. Brout, *Broken Symmetry and the Mass of Gauge Vector Mesons*, Phys. Rev. Lett. **13** (1964) 321–323.  
P. W. Higgs, *Broken Symmetries and the Masses of Gauge Bosons*, Phys. Rev. Lett. **13** (1964) 508–509.
- [3] A. Wingerter, *Implications of the Stability and Triviality Bounds on the Standard Model with Three and Four Chiral Generations*, [arXiv:1109.5140](#).
- [4] J. Ellis *et al.*, *The Probable Fate of the Standard Model*, [arXiv:0906.5140](#).
- [5] N. Cabibbo, L. Maiani, G. Parisi, R. Petronzio, *Bounds on the fermions and Higgs boson masses in grand unified theories*, Nucl. Phys. B **158** (1979) 295–305.
- [6] C. Kolda and H. Murayama, *The Higgs Mass and New Physics Scales in the Minimal Standard Model*, [arXiv:hep-ph/0003170](#).
- [7] LHC Higgs Cross Section Working Group, S. Dittmaier, C. Mariotti, G. Passarino, and R. Tanaka (Eds.), *Handbook of LHC Higgs Cross Sections: 1. Inclusive Observables*, CERN-2011-002 (CERN, Geneva, 2011), [arXiv:1101.0593](#).  
LHC Higgs Cross Section Working Group, *Handbook of LHC Higgs Cross Sections: 2. Differential Distributions*, CERN-2012-002 (CERN, Geneva, 2012), [arXiv:1201.3084](#).  
LHC Higgs Cross Section Working Group, *Handbook of LHC Higgs Cross Sections: 3. Higgs Properties*, [arXiv:1307.1347](#).
- [8] A. Djouadi, M. Spira and P. M. Zerwas, *Production of Higgs bosons in proton colliders: QCD corrections*, Phys. Lett. B **264** (1991) 440–446.  
M. Spira, *QCD effects in Higgs physics*, Fortsch. Phys. **46** (1998) 203–284, [arXiv:hep-ph/9705337](#).  
A. Pak, M. Rogal, and M. Steinhauser, *Finite top quark mass effects in NNLO Higgs boson production at LHC*, JHEP **1002** (2010) 025, [arXiv:0911.4662](#).  
R. V. Harlander, H. Mantler, S. Marzani, and K. J. Ozeren, *Higgs production in gluon fusion at next-to-next-to-leading order QCD for finite top mass*, Eur. Phys. J. C **66** (2010) 359–372, [arXiv:0912.2104](#).

- [9] R. Barate *et al.* [LEP Working Group for Higgs boson searches and ALEPH and DELPHI and L3 and OPAL Collaborations], *Search for the standard model Higgs boson at LEP*, Phys. Lett. B **565** (2003) 61, [arXiv:hep-ex/0306033](#).
- [10] The ALEPH, DELPHI, L3, OPAL Collaborations, the LEP Electroweak Working Group, *Electroweak Measurements in Electron-Positron Collisions at W-Boson-Pair Energies at LEP*, CERN-PH-EP-2013-022 (CERN, Geneva, 2013), [arXiv:1302.3415](#).
- M. Baak *et al.*, *Updated Status of the Global Electroweak Fit and Constraints on New Physics*, Eur. Phys. J. C **72** (2012) 2003, [arXiv:1107.0975](#).
- [11] CDF, D0 collaborations, *Higgs Boson Studies at the Tevatron*, [arXiv:1303.6346](#).
- [12] ATLAS collaboration, *Observation of a New Particle in the Search for the Standard Model Higgs Boson with the ATLAS Detector at the LHC*, Phys. Lett. B **716** (2012) 1–29.
- [13] CMS collaboration, *Observation of a new boson at a mass of 125 GeV with the CMS experiment at the LHC*, Phys. Lett. B **716** (2012) 30.
- [14] ATLAS Collaboration, *Combined coupling measurements of the Higgs-like boson with the ATLAS detector using up to 25 fb<sup>-1</sup> of proton-proton collision data*, [ATLAS-CONF-2013-034](#).
- [15] CMS Collaboration, *Combination of standard model Higgs boson searches and measurements of the properties of the new boson with a mass near 125 GeV*, [CMS-PAS-HIG-13-005](#).
- [16] O. Brüning *et al.*, *LHC Design Report*, [CERN-2004-003-V-1](#).
- [17] <http://hilumilhc.web.cern.ch/HiLumiLHC/index.html>
- [18] ATLAS Collaboration, *Luminosity Determination in pp Collisions at  $\sqrt{s} = 7$  TeV Using the ATLAS Detector at the LHC*, Eur. Phys. J. C **71** 1630, 2011, [arXiv:1101.2185](#).
- ATLAS Collaboration, *Improved luminosity determination in pp collisions at  $\sqrt{s} = 7$  TeV using the ATLAS Detector at the LHC*, [arXiv:1302.4393](#).
- [19] ATLAS Collaboration, *The ATLAS Experiment at the CERN Large Hadron Collider*, JINST **3** (2008) [S08003](#).
- [20] R. L. Gluckstern, *Uncertainties in track momentum and direction, due to multiple scattering and measurement errors*, Nucl. Inst. Meth. **24** (1963) 381–389.
- [21] ATLAS Collaboration, *ATLAS detector and physics performance: Technical Design Report, 1*, [ATLAS-TDR-14](#).

- [22] ATLAS Collaboration, *ATLAS magnet system: Technical Design Report*, [CERN-LHCC-97-018](#).  
ATLAS Collaboration, *ATLAS central solenoid: Technical Design Report*, [CERN-LHCC-97-021](#).  
ATLAS Collaboration, *ATLAS barrel toroid: Technical Design Report*, [CERN-LHCC-97-019](#).  
ATLAS Collaboration, *ATLAS end-cap toroids: Technical Design Report*, [CERN-LHCC-97-20](#).
- [23] ATLAS Collaboration, *ATLAS inner detector: Technical Design Report*, [CERN-LHCC-97-016](#).  
ATLAS Collaboration, *ATLAS inner detector: Technical Design Report, 2*, [CERN-LHCC-97-017](#).  
ATLAS Collaboration, *The ATLAS Inner Detector commissioning and calibration*, Eur. Phys. J. C **70** (2010) 787–821, [arXiv:1004.5293](#).
- [24] ATLAS Collaboration, *ATLAS calorimeter performance: Technical Design Report*, [CERN-LHCC-96-040](#).  
ATLAS Collaboration, *ATLAS liquid-argon calorimeter: Technical Design Report*, [CERN-LHCC-96-041](#).  
ATLAS Collaboration, *ATLAS tile calorimeter: Technical Design Report*, [CERN-LHCC-96-042](#).
- [25] ATLAS Collaboration, *ATLAS muon spectrometer: Technical Design Report*, [CERN-LHCC-97-022](#).
- [26] ATLAS Collaboration, *ATLAS level-1 trigger: Technical Design Report*, [CERN-LHCC-98-014](#).  
ATLAS Collaboration, *ATLAS high-level trigger, data-acquisition and controls: Technical Design Report*, [CERN-LHCC-2003-022](#).
- [27] ATLAS Collaboration, *Performance of the ATLAS Electron and Photon Trigger in pp Collisions at  $\sqrt{s} = 7$  TeV in 2011*, [ATLAS-CONF-2012-048](#).
- [28] ATLAS Collaboration, *Performance of the ATLAS muon trigger in 2011*, [ATLAS-CONF-2012-099](#).
- [29] ATLAS Collaboration, *Performance of the ATLAS Inner Detector Track and Vertex Reconstruction in the High Pile-Up LHC Environment*, [ATLAS-CONF-2012-042](#).  
T. Cornelissen *et al.*, *Concepts, Design and Implementation of the ATLAS New Tracking (NEWT)*, [ATL-SOFT-PUB-2007-007](#).
- [30] R. Fruehwirth, W. Waltenberger, P. Vanlaer, *Adaptive vertex fitting*, J. Phys. G **34** (2007) [N343](#).  
ATLAS Collaboration, *Performance of primary vertex reconstruction in proton-proton collisions at  $\sqrt{s} = 7$  TeV in the ATLAS experiment*, [ATLAS-CONF-2010-069](#).

- [31] ATLAS Collaboration, *Preliminary results on the muon reconstruction efficiency, momentum resolution, and momentum scale in ATLAS 2012 pp collision data*, [ATLAS-CONF-2013-088](#).
- [32] S. Hassani *et al.*, *A muon identification and combined reconstruction procedure for the ATLAS detector at the LHC using the (MUONBOY, STACO, MuTag) reconstruction packages*, Nucl. Instr. Meth. A **572** (2007) 77–79.
- [33] H. Bethe and W. Heitler, *On the Stopping of Fast Particles and on the Creation of Positive Electrons*, Proc. R. Soc. Lond. A **146** (1934) 83–112.  
A. Schaelicke *et al.*, *Improved Description of Bremsstrahlung for High-Energy Electrons in Geant4*, IEEE Nucl. Sci. Symp. Conf. Rec. N37-1 (2008) 2788.
- [34] ATLAS Collaboration, *Improved electron reconstruction in ATLAS using the Gaussian Sum Filter-based model for bremsstrahlung*, [ATLAS-CONF-2012-047](#).
- [35] W. Lampl *et al.*, *Calorimeter Clustering Algorithms: Description and Performance*, [ATL-LARG-PUB-2008-002](#).  
ATLAS Collaboration, *Electron performance measurements with the ATLAS detector using the 2010 LHC proton–proton collision data*, Eur. Phys. J. C **72** (2012) 1909, [arXiv:1110.3174](#).
- [36] J. Beringer *et al.* (Particle Data Group), Phys. Rev. D **86**, 010001 (2012).
- [37] T. Sjostrand, S. Mrenna, and P. Z. Skands, *PYTHIA 6.4 physics and manual*, JHEP **05** (2006) 026, [arXiv:hep-ph/0603175](#).  
T. Sjostrand, S. Mrenna, and P. Z. Skands, *A brief introduction to PYTHIA 8.1*, Comput. Phys. Commun. **178** (2008) 852–867, [arXiv:0710.3820](#).
- [38] S. Alioli, P. Nason, C. Oleari, and E. Re, *NLO Higgs boson production via gluon fusion matched with shower in POWHEG*, JHEP **04** (2009) 002, [arXiv:0812.0578](#).  
P. Nason and C. Oleari, *NLO Higgs boson production via vector-boson fusion matched with shower in POWHEG*, JHEP **02** (2010) 037, [arXiv:0911.5299](#).
- [39] D. de Florian, G. Ferrera, M. Grazzini, and D. Tommasini, *Transverse-momentum resummation: Higgs boson production at the Tevatron and the LHC*, [arXiv:1109.2109](#).
- [40] J. Campbell and K. Ellis, *MCFM—Monte Carlo for FeMtobarn processes*, <http://mcfm.fnal.gov>, 2010.  
J. Campbell and K. Ellis, *An update on vector boson pair production at hadron colliders*, Phys. Rev. D **60** (1999) 113006, [arXiv:hep-ph/9905386](#).  
J. Campbell, K. Ellis and C. Williams, *Vector boson pair production at the LHC*, JHEP **07** (2011) 018, [arXiv:1105.0020](#).
- [41] C. N. Yang, *Selection Rules for the Dematerialization of a Particle into Two Photons*, Phys. Rev. **77** (1950) 242–245.

- R. H. Dalitz, *On an Alternative Decay Process for the Neutral  $\pi$ -Meson*, Proc. Phys. Soc. A **64** (1951) 667.
- [42] Y. Y. Gao *et al.*, *Spin determination of single-produced resonances at hadron colliders*, Phys. Rev. D **81** 075022 (2010).  
S. Bolognesi *et al.*, *Spin and parity of a single-produced resonance at the LHC*, Phys. Rev. D **86** 095031 (2012).
- [43] L. D. Landau, *The moment of a 2-photon system*, Dokl. Akad. Nauk. USSR **60** (1948) 207.  
C. N. Yang, *Selection Rules for the Dematerialization of a Particle into Two Photons*, Phys. Rev. **77** (1950) 242–245.
- [44] J. F. Gunion, Y. Jiang, and S. Kraml, *Could two NMSSM Higgs bosons be present near 125 GeV?*, [arXiv:1207.1545](#).
- [45] P. Golonka, and Z. Was, *PHOTOS Monte Carlo: A Precision tool for QED corrections in Z and W decays*, Eur. Phys. J. C **45** (2006) 97–107, [arXiv:hep-ph/0506026](#).
- [46] S. Jadach, Z. Was, R. Decker, J. H. Juhn, *The tau decay library TAUOLA: Version 2.4*, Comput. Phys. Commun. **76** (1993) 361–380.  
P. Golonka *et al.*, *The tauola-photos-F environment for the TAUOLA and PHOTOS packages, release II*, Comput. Phys. Commun. **174** (2006) 818–835, [arXiv:hep-ph/0312240](#).
- [47] S. Dawson, *Radiative corrections to Higgs boson production*, Nucl. Phys. B **359** (1991) 283–300.  
M. Spira, A. Djouadi, D. Graudenz, and P. M. Zerwas, *Higgs boson production at the LHC*, Nucl. Phys. B **453** (1995) 17–82, [arXiv:hep-ph/9504378](#).
- [48] K. Melnikov and F. Petriello, *Electroweak gauge boson production at hadron colliders through  $O(\alpha_s^2)$* , Phys. Rev. D **74** (2006) 114017, [arXiv:hep-ph/0909070](#).  
C. Anastasiou *et al.*, *High precision QCD at hadron colliders: electroweak gauge boson rapidity distributions at NNLO*, Phys. Rev. D **69** (2004) 094008, [arXiv:hep-ph/0312266](#).
- [49] M. Aliev *et al.*, *HATHOR: hadronic top and heavy quarks cross section calculator*, Comput. Phys. Commun. **182** (2011) 1034, [arXiv:1007.1327](#).
- [50] R. V. Harlander and W. B. Kilgore, *Next-to-next-to-leading order Higgs production at hadron colliders*, Phys. Rev. Lett. **88** (2002) 201801, [arXiv:hep-ph/0201206](#).  
C. Anastasiou and K. Melnikov, *Higgs boson production at hadron colliders in NNLO QCD*, Nucl. Phys. B **646** (2002) 220–256, [arXiv:hep-ph/0207004](#).  
V. Ravindran, J. Smith, and W. L. van Neerven, *NNLO corrections to the total cross section for Higgs boson production in hadron hadron collisions*, Nucl. Phys. B **665** (2003) 325–366, [arXiv:hep-ph/0302135](#).

- [51] S. Catani, D. de Florian, M. Grazzini, and P. Nason, *Soft-gluon resummation for Higgs boson production at hadron colliders*, JHEP **07** (2003) 028, [arXiv:hep-ph/0306211](#).
- [52] U. Aglietti, R. Bonciani, G. Degrossi, and A. Vicini, *Two-loop light fermion contribution to Higgs production and decays*, Phys. Lett. B **595** (2004) 432–441, [arXiv:hep-ph/0404071](#).
- S. Actis, G. Passarino, C. Sturm, and S. Uccirati, *NLO Electroweak Corrections to Higgs Boson Production at Hadron Colliders*, Phys. Lett. B **670** (2008) 12–17, [arXiv:0809.1301](#).
- [53] M. Ciccolini, A. Denner, and S. Dittmaier, *Strong and electroweak corrections to the production of Higgs+2jets via weak interactions at the LHC*, Phys. Rev. Lett. **99** (2007) 161803, [arXiv:0707.0381](#).
- M. Ciccolini, A. Denner, and S. Dittmaier, *Electroweak and QCD corrections to Higgs production via vector-boson fusion at the LHC*, Phys. Rev. D **77** (2008) 013002, [arXiv:0710.4749](#).
- K. Arnold *et al.*, *VBFNLO: A parton level Monte Carlo for processes with electroweak bosons*, Comput. Phys. Commun. **180** (2009) 1661–1670, [arXiv:0811.4559](#).
- [54] P. Bolzoni, F. Maltoni, S.-O. Moch, and M. Zaro, *Higgs production via vector-boson fusion at NNLO in QCD*, Phys. Rev. Lett. **105** (2010) 011801, [arXiv:1003.4451](#).
- [55] T. Han and S. Willenbrock, *QCD correction to the  $pp \rightarrow WH$  and  $ZH$  total cross-sections*, Phys. Lett. B **273** (1991) 167–172.
- [56] O. Brein, A. Djouadi, and R. Harlander, *NNLO QCD corrections to the Higgs-strahlung processes at hadron colliders*, Phys. Lett. B **579** (2004) 149–156, [arXiv:hep-ph/0307206](#).
- [57] M. L. Ciccolini, S. Dittmaier, and M. Kramer, *Electroweak radiative corrections to associated  $WH$  and  $ZH$  production at hadron colliders*, Phys. Rev. D **68** (2003) 073003, [arXiv:hep-ph/0306234](#).
- [58] A. Bredenstein, A. Denner, S. Dittmaier, and M. M. Weber, *Precise predictions for the Higgs-boson decay  $H \rightarrow WW/ZZ \rightarrow 4\text{leptons}$* , Phys. Rev. D **74** (2006) 013004, [arXiv:hep-ph/0604011](#).
- A. Bredenstein, A. Denner, S. Dittmaier, and M. M. Weber, *Radiative corrections to the semileptonic and hadronic Higgs-boson decays  $H \rightarrow WW/ZZ \rightarrow 4\text{fermions}$* , JHEP **02** (2007) 080, [arXiv:hep-ph/0611234](#).
- [59] T. Melia, P. Nason, R. Rontsch, and G. Zanderighi,  *$W^+W^-$ ,  $WZ$  and  $ZZ$  production in the POWHEG BOX*, JHEP **1111** (2011) 078, [arXiv:1107.5051](#).
- [60] T. Binoth, N. Kauer, and P. Mertsch, *Gluon-induced QCD corrections to  $pp \rightarrow ZZ \rightarrow \ell\bar{\ell}\ell'\bar{\ell}'$* , [arXiv:0807.0024](#).

- [61] ATLAS Collaboration, *The ATLAS simulation Infrastructure*, Eur. Phys. J. C **70** (2010) 823–874, [arXiv:1005.4568](#).
- [62] S. Agostinelli *et al.*, *GEANT4: A simulation toolkit*, Nucl. Instrum. Meth. A **506** (2003) 250–303.
- [63] M. L. Mangano *et al.*, *ALPGEN, a generator for hard multiparton processes in hadronic collisions*, JHEP **07** (2003) 001, [arXiv:hep-ph/0206293](#).
- [64] S. Frixione, P. Nason, and B. R. Webber, *Matching NLO QCD and parton showers in heavy flavour production*, JHEP **08** (2003) 007, [arXiv:hep-ph/0305252](#).
- [65] G. Corcella *et al.*, *HERWIG 6: an event generator for hadron emission reactions with interfering gluons (including super-symmetric processes)*, JHEP **01** (2001) 010, [arXiv:hep-ph/0011363](#).
- [66] J. M. Butterworth, J. R. Forshaw, and M. H. Seymour, *Multiparton interactions in photoproduction at HERA*, Z. Phys. C **72** (1996) 637–646, [arXiv:hep-ph/9601371](#).
- [67] ATLAS Collaboration, *Reconstruction of collinear final-state-radiation photons in Z decays to muons in  $\sqrt{s} = 7$  TeV proton-proton collisions*, ATLAS-CONF-2012-143.
- [68] A. L. Read, *Presentation of search results: The CL(s) technique*, J. Phys. G **28** (2002) 2693–2704.
- [69] G. Cowan, K. Cranmer, E. Gross, and O. Vitells, *Asymptotic formulae for likelihood-based tests of new physics*, Eur. Phys. J. C **71** (2011) 1554, [arXiv:1007.1727](#).
- [70] K. S. Cranmer, *Kernel estimation in high-energy physics*, Comput. Phys. Commun. **136** (2001) 198–207, [arXiv:hep-ex/0011057](#).
- [71] ATLAS Collaboration, *Combined measurements of the mass and signal strength of the Higgs-like boson with the ATLAS detector using up to  $25 \text{ fb}^{-1}$  of proton-proton collision data*, ATLAS-CONF-2013-014.  
ATLAS Collaboration, *Measurements of Higgs boson production and couplings in diboson final states with the ATLAS detector at the LHC*, Phys. Lett. B **726** (2013) 88–119.
- [72] ATLAS Collaboration, *Summary of ATLAS Pythia 8 tunes*, ATL-PHYS-PUB-2012-003.  
ATLAS Collaboration, *ATLAS tunes of PYTHIA 6 and Pythia 8 for MC11*, ATL-PHYS-PUB-2011-009.
- [73] ATLAS Collaboration, *Study of the spin of the new boson with up to  $25 \text{ fb}^{-1}$  of ATLAS data*, ATLAS-CONF-2013-040.  
ATLAS Collaboration, *Evidence for the spin-0 nature of the Higgs boson using ATLAS data*, Phys. Lett. B **726** (2013) 120–144.

- [74] S. Kraml *et al.* (Eds.), *CP Studies and Non-Standard Higgs Physics*, CERN-2006-009, [arXiv:hep-ph/0608079](#).
- [75] R. Godbole, D. J. Miller and M. M. Muehlleitner, *Aspects of CP violation in the HZZ coupling at the LHC*, JHEP **0712** (2007) 031, [arXiv:0708.0458](#).
- [76] W. Bernreuther, P. Gonzalez and M. Wiebusch, *Pseudoscalar Higgs Bosons at the LHC: Production and Decays into Electroweak Gauge Bosons Revisited*, [arXiv:1003.5585](#).  
J. Shu and Y. Zhang, *Impact of a CP Violating Higgs: from LHC to Baryogenesis*, [arXiv:1304.0773](#).
- [77] I. Anderson *et al.*, *Constraining anomalous HVV interactions at proton and lepton colliders*, [arXiv:1309.4819](#).
- [78] CMS Collaboration, *Properties of the Higgs-like boson in the decay  $H \rightarrow ZZ \rightarrow 4\ell$  in  $pp$  collisions at  $\sqrt{s} = 7$  TeV and 8 TeV*, [CMS-PAS-HIG-13-002](#).